CHARACTERIZATION OF LUNAR CRUST WITH MOON MINERALOGY MAPPER DATA

Ying Sun

Submitted to the faculty of the University Graduate School
in partial fulfillment of the requirements
for the degree
Doctor of Philosophy
in the Department of Earth Sciences,
Indiana University

August 2015

Accepted by the Graduate Faculty, Indiana University, in partial
fulfillment of the requirements for the degree of Doctor of Philosophy.

Lin Li Ph.D., Chair

Doctoral Committee

Broxton Bird Ph.D.

June 9, 2015

Daniel Johnson Ph.D.

Kathy Licht Ph.D.

William P Gilhooly Ⅲ Ph.D.

ACKNOWLEDGEMENTS

I would like to express the deepest gratitude to my committee chair Dr. Lin Li. Without his expert guidance, full support, incredible patience, and encouragement, my dissertation would have never been accomplished and been frustrating and overwhelming. All my current expertise are associated with his generous teaching and selfless help in the past five years. He is one of the most knowledgeable scientists I have known and provides a great opportunity for me to involve in the scientific field of planetary geology. He is not only a teacher for me, but also a friend, a family. When I have any difficulties on research or life, he will do everything to help me. My appreciation is more than words I can say. I hope that one day I can be an excellent scientist and advisor like him.

I am so grateful to all my committee members, Dr. Broxton Bird, Dr. Daniel Johnson, Dr. Kathy Licht and Dr. William P Gilhooly Ⅲ for their professional guidance and valuable suggestions.

I would also like to thank our department, the Department of Earth Sciences, to provide all the assistance and facilities. Thanks to all the faculties, staff and students in our department for their friendship.

Specially thanks to all my colleagues, Igor Ogashawara, Dawei Liu, Jia Du and Kaishan Song. They spend a lot of times for helping me improve the skill on scientific presentation and writing.

Finally, I would like to thank my parents for raising me and always standing behind me, believing in me.

Ying Sun

CHARACTERIZATION OF LUNAR CRUST WITH MOON MINERALOGY MAPPER DATA

This dissertation has three main focuses: (1) identify the distribution of a new rock type (Mg-spinel lithology) on the Moon and explore the likely petrogenesis of Mg-spinel; (2) investigate the presence of olivine in the crater central peaks and analyze the sources of olivine; (3) determine the compositional variations of lunar crust with depth, and establish a new model to describe the structure of the lunar crust.

Lin Li Ph.D., Chair

TABLE OF CONTENTS

CURRICULUM VITAE

CHAPTER 1

INTRODUCTION

1. General overview

The Moon provides the best opportunity to characterize early fundamental formation processes of a planetary body including the early differentiation of magma, the development of an early crust, and evolution of the late stage. The lunar crust which represents the product of lunar evolution provides the most direct evidence for the origin and evolution of the Moon. Determining the composition and evolution of the lunar crust is critical for us to better understand early planetary evolution and crustal genesis. Synthesizing data from both remote sensing and sample analysis reveals that the lunar crust is compositionally heterogeneous in both horizontal and vertical dimensions [e.g. Jolliff et al., 2000; Tompkins and Pieters, 1999]. The compositional diversity and evolution of the lunar crust are broadly understood within the framework of the lunar magma ocean (LMO) and post-LMO activities, in which the ancient crust formed through the flotation of anorthosites in a global differentiation event [e.g. Wood et al., 1970; Shirley, 1983; Warren, 1985]. Other lithologies such as Mg-suite rocks are thought to have formed through subsequent post-LMO magmatism [e.g. Wieczorek et al., 2006]. However, this understanding is limited by the under representative lunar sample collection and by previous remote sensing techniques that had relatively low spatial and spectral resolution. Details of lunar crustal structure and evolution therefore remain contentious. A global investigation of lunar crustal composition with up-to-date data (e.g. the Moon Mineralogy Mapper [M^3]) is necessary.

2. Magmatic evolution of the lunar crust

A simple framework of the magmatic evolution of the lunar crust has been reconstructed and grouped into following multiple stages [e.g. Shearer and Papike, 1999].

Stage 1 is the formation, crystallization and the initial differentiation of a lunar magma ocean (LMO). The Moon experienced a global or partial melting to form the LMO in its early history [e.g. Wood et al., 1970; Shirley, 1983; Warren, 1985]. Crystallization of the LMO produced a ferroan anorthositic crust by floatation and a wide variety of mafic cumulates sinking into the mantle [e.g. Warren, 1985]. In a dynamically simple LMO, the crystallization sequence is olivine → orthopyroxene ± olivine → olivine +clinopyroxene ± plagioclase → clinopyroxene + plagioclase → clinopyroxene + plagioclase +ilmenite [Shearer et al., 2006]. Stage 2 is gravitational overturn of LMO cumulates. Based on the LMO crystallization sequence, the mantle cumulate stratigraphy is unstable in density. The Mg-rich olivine is the first phase to crystallize and occupies greater than 90% of early cumulate piles [Elardo et al., 2011], leading to a scenario that the Mg' [Mg/(Mg+Fe)]of the upper (late) portions of the cumulate pile is lower than that of lower (early) portions of cumulates. In particular, the Mg' of the ilmenite-bearing cumulates should be substantially lower [Shearer and Papike, 1999]. This gravitational instability results in a large-scale overturn of cumulate assemblages to a stable state. The overturn event transported the late-forming cumulates into the deep lunar mantle and the early cumulates into the upper mantle, mixing of LMO cumulates on a variety of scales in both spatial and temporal. Stage 3 is post-LMO magmatism. The decompressional melting of LMO mafic cumulates generated by gravitational overturn provides a potential source for the parent magmas of post-LMO magmatism. The KREEP is the LMO final residues enriched in potassium (K), rare earth elements (REE), and phosphorus (P). The post-LMO rocks (e.g. Mg-suite rocks) crystallize from the high Mg' magma which is generated by LMO cumulates with the incorporation of KREEP and anorthositic crust through assimilation or mixing. The above description of the magmatic evolution of the lunar crust is admittedly simplified, and many questions about the details still remain uncertain. For example, what are the exact extents and duration of each stage? Did each stage of crustal magmatic evolution occur in a sequence or overlap in time between stages? In order to answer these questions and refine the magmatic processes of the lunar crust, the compositional characteristics of the lunar crust need to be better understand including what the major rock types are, the abundance and distribution of common minerals and the variations of chemical elements within these rock and mineral types.

3. Lunar crustal composition

3.1. Lunar crustal rocks

The analysis of lunar samples returned by the Apollo and Luna missions (1969-1976) provided an initial first-hand perspective about the mineralogy and lithology of the Moon's principal crustal rock types (Figure 1-3). These samples have been divided into two main groups including ferroan anorthosite suite (FAN) and magnesium suite (Mg-suite) on the basis of their major mineral compositions and bulk rock molar ratios Na/(Na+Ca) vs. Mg/(Mg+Fe) shown in Figure 1-1 [e.g. Warren 1985, 1986; Shearer and Papike, 1999].

Rocks in the ferroan anorthosite suite (FAN) are found among the Apollo 15 samples and dominate samples of the Apollo 16 and Luna 20. Two features make the FAN mineralogically and chemically distinct from other igneous rocks [e.g. Wieczorek et al., 2006]. First, the rocks in FAN are highly anorthositic. Second, mafic silicates in FAN rocks are ferroan in composition. The FAN rocks usually contain more than 95% plagioclase (a content generally > 94 %), < 5% mafic minerals and few to none of the common minor or accessory minerals in anorthosites such as ilmenite, spinel, phosphates, or zircon. Most of the FAN rocks are highly calcic and aluminous, and the mafic minerals in FAN rocks usually have relatively high Fe/Mg values (low Mg'). The FAN rocks are also deficient in incompatible elements, which indicates they formed from a relatively unevolved melt. The composition of the FAN rocks coupled with the relatively coarse relict grain size, cumulus texture, and extremely old ages clearly imply that the FAN rocks could represent primitive crust produced during LMO initial differentiation in Stage 1 [e.g. Wieczorek et al., 2006].

The magnesian suite (Mg-suite) rocks are found among the samples from all of the Apollo landing sites and are most abundant in the Apollo 15 and 17 samples [e.g. Wieczorek et al., 2006]. One of the most important features of Mg-suite rocks is high Mg' compared to FAN rocks. The main rock types are norite, gabbro, troctolite, more feldspathic variations, such as noritic anorthosite, and several "ultramafic" assemblages, such as dunite (nearly pure olivine). The major minerals of Mg-suite rocks are plagioclase, low-Ca pyroxene (orthopyroxene), high-Ca pyroxene (clinopyroxene), and olivine. Major element compositions of the Mg-suite rocks vary widely. For instance, MgO ranges from 7 wt. % (an anorthositic norite) to 45 wt. % (dunite) and Al_2O_3 from <2 wt. % (dunite) to nearly 29 wt. % (troctolitic anorthosite). However, there are still numerous compositional features to distinguish the Mg-suite rocks from other igneous rocks. Values of Mg/(Mg+Fe) (Mg') negatively correlate with Na/(Na+Ca) (Figure 1-1), and TiO_2 values are typically low [Shearer and Papike, 1999]. Most of the Mg-suite rocks also show significant trace element enrichment. The ages of Mg-suite rocks are commonly younger than FAN, but the overlap exists between the ages of Mg-suite and FAN. The Mg-suite rocks do not necessarily have a petrogenetic relationship among all members. Currently, the Mg-suite rocks are considered to represent intrusions into early lunar crust (FAN) (Stage 3) [e.g.

Wieczorek et al., 2006].

In addition to FAN and Mg-suite, other more evolved plutonic rocks also exist in the lunar crust. For example, alkali suite rocks are highly enriched in Na and K contents compared to Mg-suite rocks. However, these rock types are not common in the crust, and it is difficult to distinguish them from Mg-suite using remote sensing data. The spectra feature of common lunar minerals is mainly based on the abundance of Fe content and the position of Fe in the crystal structure rather than Na and K. Therefore, only two common groups (FAN and Mg-suite) are taken into account in this study.

3.2. Lunar crustal minerals

The common minerals within the lunar crust, which are detectable by spectroscopy, are plagioclase, olivine and pyroxene (orthopyroxene, clinopyroxene) [Lucey et al., 2006]. The abundance and distribution of these common minerals, as well as their petrogenesis, provide direct evidence to improve our understanding of the lunar crustal evolution.

Plagioclase is the most common mineral in the lunar crust [Heiken et al., 1991]. The plagioclase series consist of solid solutions between albite ($NaAlSi_3O_8$) and anorthite ($CaAl_2Si_2O_8$). The lunar plagioclases are depleted in Na (albite) relative to terrestrial plagioclases. Most of the lunar plagioclase is Ca-rich (anorthite [An]) and rare in incompatible elements. The rock type of nearly pure plagioclase (>95%) is usually named as crystalline plagioclase bearing material, pure anorthosite (PAN) or ferroan anorthosite (FAN).

Olivine, $(Mg, Fe)_2SiO_4$, is typically the first mafic mineral to crystallize from a mafic magma and occurs in the lunar crust and mantle [Lucey et al., 2006]. The major compositional variation of olivine is caused by exchange of Fe and Mg resulting in two distinct endmembers: the Mg endmember (Mg_2SiO_4) is forsterite (Fo) and the Fe endmember (Fe_2SiO_4) is fayalite (Fa). According to the crystallization sequence of the LMO (in section 2), Mg-rich olivine crystallize earlier than Fe-rich olivine, which might be used to indicate the origin of olivine [e.g. Shearer and Papike, 1999]. The olivine dominated rock types include dunite (almost pure olivine [Fo90]) and troctolite (the mixture of plagioclase, pyroxene, and olivine).

Pyroxene is the most compositionally complex of the major silicate phases in lunar rocks and is extensively distributed in the lunar crust and mantle. Pyroxene is primarily defined in terms of the endmember components including $Mg_2Si_2O_6$ (enstatite), $Ca_2Si_2O_6$ (wollastonite), and $Fe_2Si_2O_6$ (ferrosilite) (Figure 1-2). Pyroxene is also divided into two groups on the basis of crystal structure including orthopyroxene (orthorhombic system) and clinopyroxene (monoclinic system). Orthopyroxene, $(Mg, Fe)_2Si_2O_6$, containing almost no Ca, is usually referred to as low-Ca pyroxene. Clinopyroxene, $(Ca, Mg, Fe)_2Si_2O_6$, represents high-Ca pyroxene. The common pyroxene-bearing rock types include norite (orthopyroxene+plagioclase) and gabbro (clinopyroxene+plagioclase).

Another critical member of the lunar minerals considered in this study is Mg-spinel because of its new discovery and compositional uniqueness [e.g. Pieter et al., 2011]. Mg-spinel (transparent $MgAl_2O_4$ spinel) only exists in some small fragments of lunar samples and is always associated with mafic materials (e.g. olivine). However, Mg-spinel lithologies lacking mafic minerals have been recently discovered with the Moon Mineralogy Mapper (M^3) image along the innermost ring of the Moscoviense basin on the lunar farside [Pieters et al., 2010; 2011]. The Mg-spinel lithologies differ from spinel bearing rocks in the lunar sample due to their distinct compositional features including

~20-30 % $MgAl_2O_4$ spinel [Dhingra et al., 2011], less than 5% mafic minerals such as pyroxene or olivine [Pieters et al., 2011], and less than 5% FeO content [Jackson et al., 2012]. Mg-spinel lithologies have not been found in any lunar samples. Note Mg-spinel is also named as pink spinel, Mg-Al spinel, and $MgAl_2O_4$ spinel. The Mg-spinel bearing lithologies (Mg-spinel+plagioclase) are also named as Mg-spinel anorthosite, pink spinel anorthosite (PSA).

3.3. Lunar crustal chemistry

The knowledge of the bulk chemical composition of the lunar crust is important for unraveling the details of crustal evolution. Lunar equatorial gamma-ray data obtained from orbit during the Apollo missions, global gamma-ray and neutron flux data from the Lunar Prospector (LP) mission, and Ultraviolet–Visible (UVVIS) images from the Clementine mission provide us the opportunities to estimate the abundance and distribution of some critical elements on the Moon, such as Al, Th, and Fe.

According to geochemical information obtained from orbit, Jolliff et al. [2000] classified lunar crust into three distinct provinces including the Procellarum KREEP Terrane (PKT), the Feldspathic Highlands Terrane (FHT), and the South Pole-Aitken Terrane (SPAT). Currently, these three terranes have been accepted as a reasonable classification for understanding the origin and evolution of the lunar crust. The PKT is distinguished from other terranes primarily by its KREEP-rich geochemistry and extensive mare basalts related to volcanic history. Data from the LP mission shows that the surface abundances of incompatible elements (Th, K, Gd, Sm, and by inference the other elements that make up KREEP) are highly concentrated in several regions including Oceanus Procellarum, Maria Imbrium, Frigoris, Cognitum, Insularum, Vaporum, Nubium, and

Humorum (~20°E-80°W, 70°S-70°N) [Lawrence et al., 1998, 2000; Jolliff et al., 2000]. Additionally, the PKT accounts for only about 16% of the surface area of the Moon, but more than 60% of the mare basalts by area are located in this region [Wieczorek et al., 2006]. Moreover, the FeO map derived from Clementine UVVIS data by Lucey et al. [1998] reveals that the PKT contains a high concentration of FeO. The thin crust underneath the PKT is also considered to be enriched in FeO and KREEP based on the analysis of basin ejecta composition [Jolliff et al., 2000; Wieczorek et al., 2006]. The FHT is characterized by its ancient age, high albedo, highly feldspathic composition, limited post magma-ocean magmatism, low abundances of incompatible elements and extensive cratering [Jolliff et al. 2000]. The FHT occupies over 60% of the lunar surface and centered around 40°N, 180°E. The thick crust underneath the FHT is highly anorthositic and low in FeO concentration [Jolliff et al. 2000]. The SPAT is regarded as a separate terrane because the SPA is the largest basin on the Moon, as well as its compositional anomaly. SPAT has high FeO concentration relative to the typical nonmare lunar crust and is rare in KREEP [Jolliff et al. 2000].

4. Crustal variations with depth

The structure and composition of the lunar crust serve as a window to understanding and exploring the crustal evolution. Many lines of evidence suggest that the composition of the lunar crust varies with depth. Ryder and Wood [1977] proposed the lunar crust could be composed of two or three compositional layers increasing mafic materials with depth based on the analysis of lunar samples. Spudis et al. [1984] and Spudis and Davis [1986] described a ferroan anorthositic upper layer (Al_2O_3 ~26-28 wt. %) at depths from ~10 to 35 km overlaying a mafic noritic lower layer (Al_2O_3 ~20 wt. %). Through analyzing

Clementine multispectral UVVIS images of 109 crater central peaks, Tompkins and Pieters [1999] suggested the upper lunar crust is extremely anorthositic (An ~82%) (~5-30 km) and the lower crust is mafic (An ~75%) (~25-55 km). Some studies advocated that the lunar crust can be better characterized by three-layer models in terms of crustal composition. Spudis et al. [1999] and Bussey and Spudis [2000] proposed a three-layer crustal model on the basis of analysis of large impact basins. In this model, the lunar crust has a noritic upper layer (FeO ~4-6 wt. %, Al_2O_3 ~26 wt. %) down to depths of ~15-20 km, a pure anorthositic middle layer (FeO <2 wt. %, Al_2O_3 >33 wt. %) at depths between ~15 and ~35 km and a more mafic lower layer (FeO ~9-12 wt. %, Al_2O_3 ~18-20 wt. %) at depth of ~ 35 to 65 km. Recently, the lunar bulk chemical composition for three-layer crust models was redefined by Taylor and Wieczorek [2014]. However, two analyses of central peak mineral composition with Clementine [Cahill et al., 2009] and Diviner data [Song et al., 2013] did not find systematic compositional heterogeneity in the vertical direction of the lunar crust.

5. Limitations in previous studies

The lunar crustal structure and evolution have been investigated for decades. However, details of the lunar crust remain contentious for following reasons:

1) Lunar samples were returned from only six manned American Apollo missions (1969–1972) and three automated former Soviet Union Luna missions (1970–1976). All the samples were collected from the lunar nearside (Figure 1-3), and no samples have been obtained from crater central peaks which could represent the composition of deep layers. Even though the samples could reflect the composition of the lunar crust, the spatially restricted subset of lunar samples cannot fully represent the entire crust.

2) The past remote sensing data used to interpret the composition of the lunar crust

have relatively low spatial or spectral resolution. For example, the images acquired by the Clementine mission has a spatial resolution of 100 m but only 9 spectral bands (low spectral resolution). This low spectral resolution is not enough to identify new minerals (Mg-spinel) and confidently distinguish different minerals.

3) The average crustal thickness has been recently revised to 34-43 km through Gravity Recovery and Interior Laboratory (GRAIL) data [Wieczorek et al., 2013], which is much thinner than previous estimates (50-60 km). The new estimation of crustal thickness implies the previous crustal models may have misclassified part of the upper lunar mantle as the lunar crust.

4) To date, there is no consensus on the structure of the lunar crust which impacts on explanations of the crustal evolution. For example, the precise extent of the Mg-suite magmatism cannot be determined based on previous studies [e.g. Tompkins and Pieters, 1999; Spudis et al., 1999; Bussey and Spudis, 2000; Cahill et al., 2009]. The Mg-suite probably exists in layers at depths from ~25-55 km on the basis of a study by Tompkins and Pieters [1999]. Moreover, Spudis et al. [1999] and Bussey and Spudis [2000] suggested Mg-suite present at a depth of ~ 35 to 65 km. However, Cahill et al. [2009] proposed that the Mg-suite should be ubiquitous throughout the entire crust based on mineralogy analysis of 55 crater central peaks.

5) The LP gamma-ray data collected from orbit only senses the upper meter of the regolith and show that the surface abundance of incompatible elements is concentrated within the PKT [Jolliff et al., 2000]. Moreover, the FeO map derived from Clementine data also represents the surface FeO concentration [Lucey et al., 1998]. These observations led the questions: Is the surface distribution of KREEP representative of the underlying crust?

Is the classification of three crustal terranes mainly based on the concentration of Th and Fe really applicable to the underlying crust?

To address the limitations mentioned above, an updated investigation of the lunar crustal composition and structure with recent data is necessary, which can advance our understanding of its thermal and magmatic evolution.

6. Objectives

The main objectives of this study are: (1) to investigate the presence of Mg-spinel bearing central peaks globally with M^3 images and explore the petrogenesis of new Mg-spinel lithologies, (2) to identify the presence of olivine in the crater central peaks originated from crustal layers or mantle in order to shed light on the origin of olivine, (3) to conduct detection of crystalline plagioclase, orthopyroxene and clinopyroxene on lunar crater central peaks on the global scale with M^3 reflectance images, and (4) to integrate detection results of five minerals (Mg-spinel, olivine, crystalline plagioclase, orthopyroxene, and clinopyroxene) and to characterize the compositional variations of the lunar crust in both lateral and vertical dimensions. (5) To establish a new compositional model for the lunar crust and explore the crustal evolution.

7. Outline of studies

According to the description in the previous sections, the characteristics of new minerals (e.g. Mg-spinel) and the first crystallized mineral (olivine) play very important role in understanding the structure and evolution of the lunar crust. If Mg-spinel is considered as a common member of lunar crust minerals, what is the petrogenesis of Mg-spinel and how is the Mg-spinel origin related to the evolution of the crust? What is the origin of olivine (e.g. mantle or crust)? If olivine is generated in the crust, how did the olivine formation impact the crustal evolution? Due to the most controversial nature with respect to the origin of Mg-spinel and olivine, we first focus on the analysis of Mg-spinel and olivine in Chapters 2 and 3.

In Chapter 2, results from a systematic screening of lunar crater central peaks for the presence of the new mineral Mg-spinel are described to address the distribution and petrogenesis of Mg-spinel. The presence of Mg-spinel has been identified in 38 central peaks out of 166 investigated craters. Through analysis of the vertical and lateral variations of Mg-spinel within the crust, we observed that Mg-spinel is more common in the lunar crust than previously expected. Mg-spinel is present in all three terranes and in both shallow and deep layers of the lunar crust. Moreover, Mg-spinel appears to be more extensive in the middle part of the lunar crust underneath PKT. However, Mg-spinel does not necessarily coexist with olivine or pyroxene. There are nine investigated central peaks, which only contain Mg-spinel and plagioclase and no detectable mafic materials. Exogenic and endogenic origins of Mg-spinel have been thoroughly discussed on the basis of our observations in Chapter 2. This study indicates that the origin of Mg-spinel is related to Mg-suite plutonism and assimilation between high Mg' magma with anorthositic crust. The extensive distribution of Mg-spinel and Mg-suite related petrogenesis indicate that Mg-spinel bearing lithologies might represent a new member of Mg-suite lunar rocks.

In Chapter 3, the presence of olivine on crater central peaks is investigated with M^3 images. Results show that ~5% of investigated central peaks contain olivine, and the olivine-rich areas are concentrated in the middle layer of the lunar crust underneath the PKT. The presence of crystalline plagioclase has been identified in the most of Ol-bearing central peaks. Some Ol-bearing central peaks also contain Mg-spinel and pyroxene. Three possible scenarios for the origin of olivine are discussed including impact origin, mantle uplift, and magmatic origin. The results of this study suggest that the magmatic origin is the most probable scenario because the impact origin and mantle uplift cannot fully explain the observations of Ol-bearing central peaks. We propose a hybrid magmatic scenario to unravel the petrogenesis of olivine in the central peaks. The crust underneath PKT was permanently thinned and fractured by Procellarum and Insularum basin formation processes, which could have led to a potential magma upwelling into the lunar crust. Olivine-rich materials could be generated through plutonic events or be transported from depth by magma and emplaced in relatively shallow layers. Olivine-rich materials may then finally have been excavated by impact craters and rebounded to the central peaks.

The presence of other common minerals including crystalline plagioclase, clinopyroxene and orthopyroxene have been investigated with M^3 images and are described in Chapter 4, which is built upon the results presented in Chapter 2 and Chapter 3 to determine the compositional variation of the lunar crust. Mg-spinel is considered a common lunar crustal mineral on the basis of results presented in Chapter 2, and both Mg-spinel and olivine appear to be concentrated in the middle part of the lunar crust on the basis of the observations described in Chapter 2 and 3. All these are used to refine the compositional diversity of the lunar crust and develop a new three-layer model for the lunar crust in Chapter 4. The ratio of the origin depth of the central peak (D) to the average crustal thickness (T) is used to describe the vertical structure of the lunar crust. The uppermost layer ($D/T < 0.3$) is anorthositic or noritic megaregolith that has been heavily modified by the impact cratering. The middle layer ($D/T = 0.3\text{-}0.6$) contains Mg-suite rock equivalent (mafic materials and Mg-spinel anorthosite), which indicates the post-LMO magmatism frequently occurred within this layer. All the mafic materials and Mg-spinel are concentrated within PKT revealing that secondary magmatism frequently occurred underneath PKT. For the lowermost layer (D/T > 0.6), we speculate the presence of a global pure anorthositic layer which might represent the primitive crustal composition produced by the LMO.

Figure captions

Figure 1-1. Compositional variability of the various lunar highland magmatic suites illustrated in a plot of molar Na/(Na+Ca) *100 vs. Mg/(Mg+Fe) *100 for bulk rock compositions (revised figure in Warren [1986]).

Figure 1-2. The composition of pyroxene shows in triangle of three endmembers [Papike et al., 1991]

Figure 1-3. Six Apollo missions (1969–1972) and three Soviet unmanned missions (1970–1976) returned more than 380 kg of samples from nine localities on the near side of the Moon.

Figures

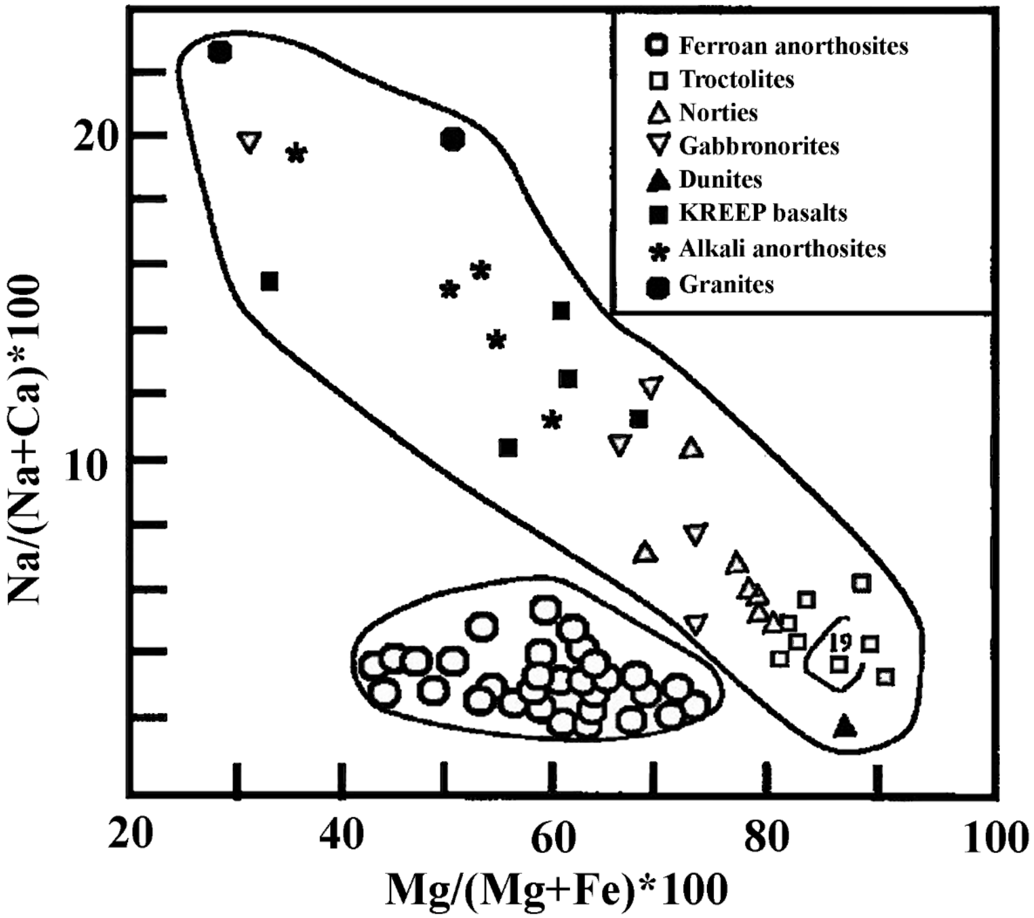

Figure 1-1.

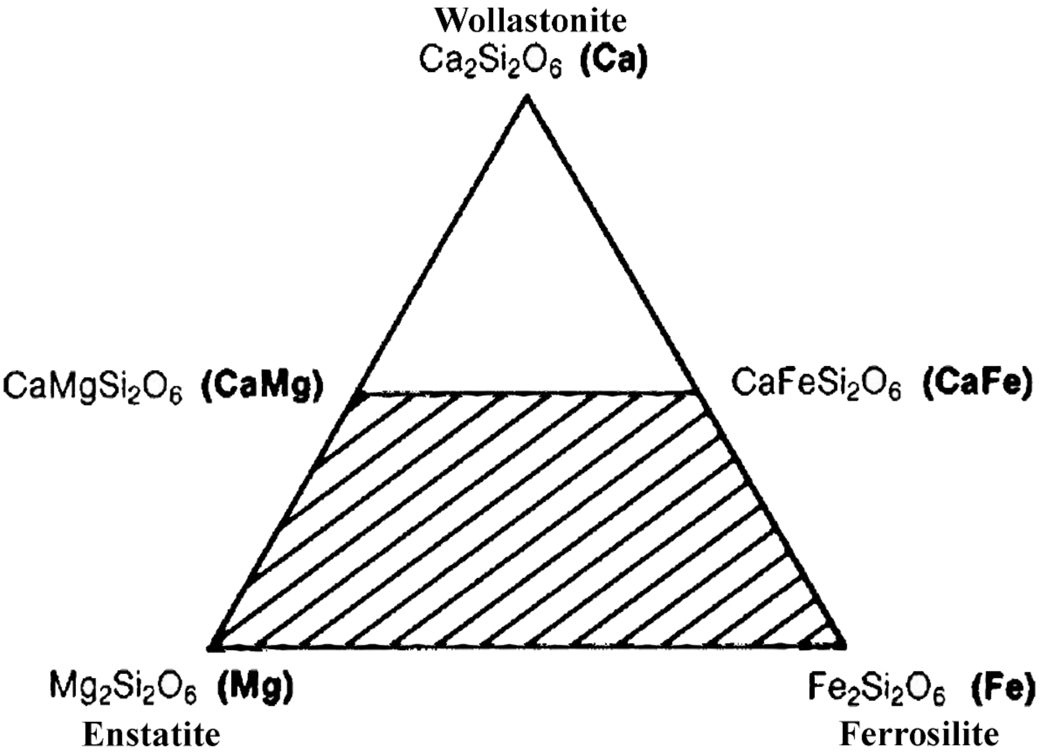
Wollastonite
$Ca_2Si_2O_6$ (Ca)
$CaMgSi_2O_6$ (CaMg)
$CaFeSi_2O_6$ (CaFe)
$Mg_2Si_2O_6$ (Mg)
Enstatite
$Fe_2Si_2O_6$ (Fe)
Ferrosilite

Figure 1-2.

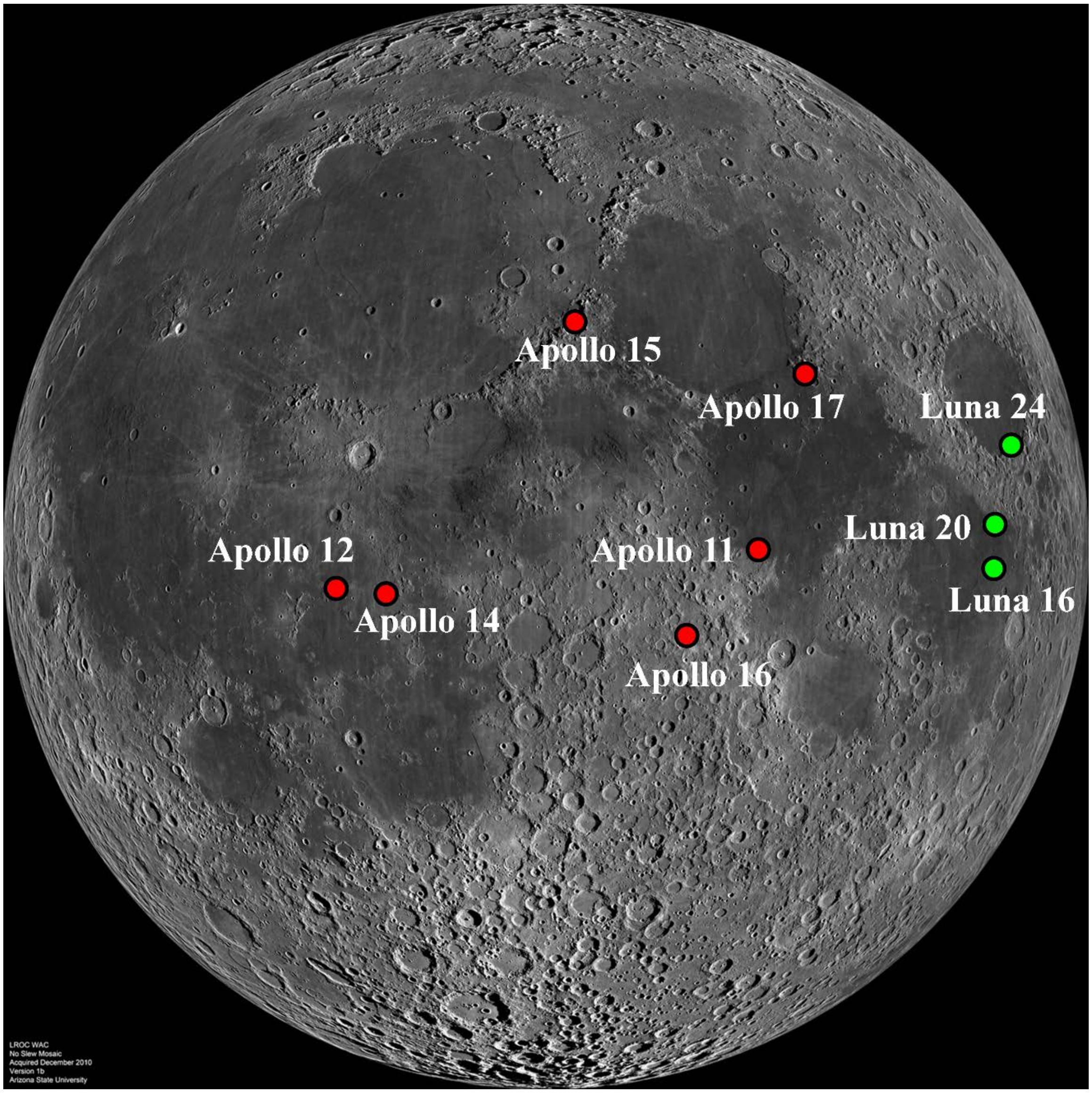
Apollo 15
Apollo 17
Luna 24
Luna 20
Apollo 12
Apollo 11
Apollo 14
Luna 16
Apollo 16
LROC WAC
No Slew Mosaic
Acquired December 2010
Version 1b
Arizona State University

Figure 1-3.

References

Bussey, D. B. J., and Spudis, P. D., (2000). Compositional studies of the Orientale, Humorum, Nectaris, and Crisium lunar basins. *Journal of Geophysical Research* 105:4235-4243

Cahill, J. T. S., et al., (2009). Compositional variations of the lunar crust: Results from radiative transfer modeling of central peak spectra, *Journal of Geophysical Research*, 114(E9), 1–17. doi:10.1029/2008JE003282.

Dhingra, D., et al., (2011). Non-linear spectral un-mixing using Hapke Modeling: Application to remotely acquired M^3 spectra of spinel bearing lithologies on the moon. *In Lunar and Planetary Science Conference* (Vol. 42, p. 2431).

Elardo, S. M., et al., (2011). Lunar Magma Ocean crystallization revisited: Bulk composition, early cumulate mineralogy, and the source regions of the highlands Mg-suite. *Geochimica et Cosmochimica Acta*, 75(11), 3024-3045.

Jackson, C. R. M., et al., (2012). Compositional constraints on lunar spinel anorthosite: Synthesis of spinel with variable iron content. *In Lunar and Planetary Science Conference* (Vol. 43, p. 2335).

Jolliff, B. L., et al., (2000). Major lunar crustal terranes: Surface expressions and crust-mantle origins. *Journal of Geophysical Research: Planets* (1991–2012), 105(E2), 4197-4216.

Lawrence, D. J., et al., (1998). Global elemental maps of the Moon: The Lunar Prospector gamma-ray spectrometer. *Science*, 281(5382), 1484-1489.

Lawrence, D. J., et al., (2000). Thorium abundances on the lunar surface. *Journal of Geophysical Research: Planets* (1991–2012), 105(E8), 20307-20331.

Lucey, P. G., et al., (1998). FeO and TiO_2 concentrations in the South Pole-Aitken basin: Implications for mantle composition and basin formation. *Journal of Geophysical Research: Planets* (1991–2012), 103(E2), 3701-3708.

Papike, J., et al., (1991). Lunar minerals. *Lunar sourcebook*, 121-181.

Pieters, C. M., et al., (2010). Identification of a new spinel-rich lunar rock type by the Moon Mineralogy Mapper (M^3). *In Lunar and Planetary Science Conference* (Vol. 41, p. 1854).

Pieters, C. M., et al., (2011). Mg-spinel lithology: A new rock type on the lunar farside. *Journal of Geophysical Research: Planets* (1991–2012), 116(E6).

Ryder, G., and Wood, J. A., (1977). Serenitatis and Imbrium impact melts-Implications for large-scale layering in the lunar crust. *In Lunar and Planetary Science Conference* (Vol. 8, pp. 655-668).

Shearer, C. K., and Papike, J. J., (1999). Magmatic evolution of the Moon. *American Mineralogist*, 84, 1469-1494

Shearer, C. K., et al., (2006). Thermal and magmatic evolution of the Moon. *Reviews in Mineralogy and Geochemistry*, 60(1), 365-518.

Shirley, D. N. (1983). A partially molten magma ocean model. *Journal of Geophysical Research: Solid Earth* (1978–2012), 88(S02), A519-A527.

Song, E., et al., (2013). Bulk mineralogy of lunar crater central peaks via thermal infrared spectra from the Diviner Lunar Radiometer: A study of the Moon's crustal composition at depth. *Journal of Geophysical Research: Planets*, 118(4), 689-707.

Spudis, P. D., et al., (1984). Composition of Orientale basin deposits and implications for the lunar basin-forming process. *Journal of Geophysical Research: Solid Earth* (1978-

2012), 89(S01), C197-C210.

Spudis, P. D., and Davis, P. A., (1986). A chemical and petrological model of the lunar crust and implications for lunar crustal origin. *Journal of Geophysical Research: Solid Earth* (1978–2012), 91(B13), E84-E90.

Spudis, P. D., et al., (1999). Structure and composition of the lunar crust. *In New Views of the Moon 2: Understanding the Moon through the Integration of Diverse Dataset*s (Vol. 1, p. 61).

Taylor, G. J., and Wieczorek, M. A., (2014). Lunar bulk chemical composition: a post-Gravity Recovery and Interior Laboratory reassessment. *Philosophical Transactions of the Royal Society A: Mathematical, Physical and Engineering Sciences*, 372(2024), 20130242.

Tompkins, S., and Pieters, C. M., (1999). Mineralogy of the lunar crust: Results from Clementine. *Meteoritics and Planetary Science*, 34(1), 25-41.

Warren, P. H., (1985). The magma ocean concept and lunar evolution. *Annual Review of Earth and Planetary Sciences*, 13, 201-240.

Warren, P. H. (1986). Anorthosite assimilation and the origin of the Mg/Fe-related bimodality of pristine moon rocks: Support for the magmasphere hypothesis. *Journal of Geophysical Research: Solid Earth* (1978–2012), 91(B4), 331-343.

Wieczorek, M. A., et al., (2006). The constitution and structure of the lunar interior. *Reviews in Mineralogy and Geochemistry*, 60(1), 221-364.

Wieczorek, M. A., et al., (2013). The crust of the Moon as seen by GRAIL. *Science*, 339(6120), 671-675.

Wood, J. A., et al., (1970). Lunar anorthosites and a geophysical model of the moon. *Geochimica et Cosmochimica Acta Supplement*, 1, 965.

CHAPTER 2

DETECTION OF MG-SPINEL BEARING CENTRAL PEAKS USING M^3 IMAGES:

IMPLICATIONS FOR THE PETROGENESIS OF MG-SPINEL

Abstract

Mg-spinel bearing lithologies, lacking abundant mafic materials, have been discovered with images acquired by the Moon Mineralogy Mapper (M^3) aboard Chandrayaan-1. We conducted a systematic screening of lunar crater central peaks for the presence of Mg-spinel to address its distribution and petrogenesis. 38 Mg-spinel bearing crater central peaks were identified in this study out of 166 craters investigated. The results suggest that Mg-spinel is common in the lunar crust and appears to be extensive in the middle part of the lunar crust underneath Procellarum KREEP Terrane (PKT). Mg-spinel neither is exclusively originated from deep layers (>10 km) nor necessarily coexist with the appearance of olivine or pyroxene. 15 Mg-spinel bearing central peaks originated from a depth less than 10 km. Nine investigated central peaks only contain Mg-spinel and plagioclase without any detectable mafic materials. All those observations imply that the origin of Mg-spinel is possibly related to Mg-suite plutonism and assimilation between high Mg' magma with anorthositic crust. The extensive distribution and Mg-suite related petrogenesis indicate that Mg-spinel bearing lithologies might represent a new member of Mg-suite rocks.

1. Introduction

Integrated analysis of lunar samples returned by the Apollo and Luna missions, lunar meteorites, and remote sensing data leads to the recognition that the lunar crust is laterally and vertically heterogeneous. This compositional diversity and complexity of the lunar crust have been explained by Lunar Magma Ocean (LMO) and post-LMO magmatism processes [Shirley, 1983; Warren, 1985; Shearer and Papike, 1999]. In the LMO process, a large portion of the Moon was initially molten, the dense material (mafic cumulates) would sink to the bottom as the lunar mantle and the light material (anorthosite) would go up to the upper layer as floatation crust. The post-LMO magmatism process is mainly referred to as decompressional melting of mafic cumulates triggered by gravitational overturn due to density difference among the mantle cumulates. The post-LMO magma is thought to have intruded into primitive anorthositic crust and formed Mg-suite rocks to boost the compositional variety of the lunar crust. Mg-spinel lithologies (hereafter referred to simply as Mg-spinel) recently discovered with the Moon Mineralogy Mapper (M^3) image along the innermost ring of the Moscoviense basin on the lunar farside [Pieters et al., 2010; 2011] are testimony to the compositional diversity of the crust. Since the discovery by Pieters et al. [2010; 2011], Mg-spinel has drawn much attention of the lunar science community with the hope of deciphering the origin of this unusual mineral.

Mg-spinel lithologies are characterized by three key petrological features based on spectral observations and experimental studies: (1) ~20-30 % $MgAl_2O_4$ spinel [Dhingra et al., 2011a]; (2) less than 5% mafic minerals such as pyroxene or olivine [Pieters et al., 2011]; (3) less than 5% FeO content [Jackson et al., 2012]. The characteristics of spinel identified in the lunar sample collections have been summarized in Prissel et al. [2014b].

Most spinels found in lunar rock samples are in forms of Fe-, Cr-, Ti- rich opaque minerals. Even if a small amount of transparent Mg-Al spinel exists, it is always associated with mafic minerals (e.g. olivine). The unique feature of the new Mg-spinel rock type identified with M^3 images lies in its high Mg' and lack of mafic minerals, which have not been observed in any of returned lunar samples. The distinct petrological characteristics of Mg-spinel have triggered substantial investigations of its presence and distribution in order to understand its petrogenesis process within the context of lunar crustal evolution.

Numerous Mg-spinel bearing regions have been found based on spectral analyses of M^3 images [Dhingra et al., 2011b; Dhingra and Pieters, 2011; Lal et al., 2011, 2012; Bhattacharya et al., 2012; Kaur et al., 2012; Kaur and Chauhan, 2013a; 2013b; 2014; Srivastava and Gupta, 2012; 2013; Sun et al., 2013; Pieters et al., 2013; 2014] and Selenological and Engineering Explorer (SELENE) Spectral Profiler (SP) data [Yamamoto et al., 2013a]. Mg-spinel exhibits a strong diagnostic absorption around 2 µm due to the presence of Fe^{2+} in tetrahedral sites [Burns, 1993; Cloutis et al., 2004]. Geological settings where Mg-Spinel has been identified include impact basins [e.g. Yamamoto et al., 2013a], thin crust [e.g. Pieters et al., 2014] or the central peak of large craters (Theophilus [e.g. Dhingra et al., 2011b], Tycho [e.g. Kaur et al., 2012], Copernicus [e.g. Dhingra and Pieters 2011]). Mg-spinel bearing lithology was also found in the Sinus Aestuum region associated with pyroclastic deposits [Sunshine et al., 2010], the floor-fractured crater Dalton [Pieters et al., 2014], and the Hansteen Alpha region [Kaur et al., 2013b] which is related to nonmare volcanism [Hawke et al., 2003].

Several possible hypotheses for the petrogenesis of Mg-spinel based on exogenic or endogenic processes have been proposed. Yue et al. [2013] suggested that unusual materials, such as Mg-spinel, could be projectile remnants of the impactor survived in the impact process. Gross et al. [2014] and Treiman et al. [2015] proposed that Mg-spinel originated from impact melts of anorthosite and troctolite at near-surface low pressures. However, Pieters et al. [2011] suggested the origin of Mg-spinel is related to one or more magmatic intrusions into the lower crust or the crust-mantle interface. This hypothesis has gained support from numerous studies which concluded that Mg-spinel, which is a deep-seated material, was excavated by impact basins and emplaced to the lunar surface [e.g., Dhingra et al., 2011b; Srivastava and Gupta, 2012; Yamamoto et al., 2013a]. Alternatively, Prissel et al. [2012; 2013; 2014a; 2014b] proposed that Mg-spinel resulted from assimilation of high-Mg, low-Fe magma with wall-rock anorthosite at a wide range of pressures on the basis of petrological experiments. Taylor and Pieters [2013] further emphasized that this high- Mg, low - Fe magma could have Very-High-Potassium (VHK) basaltic composition in order to produce such high Mg' spinel.

Currently, many questions regarding Mg-spinel are still unresolved. Is the Mg-spinel a major rock type in the crust? What are the spatial extents of Mg-spinel, both vertically and laterally? What is the relationship between Mg-spinel and other common lunar minerals? What is the most possible origin of Mg-spinel? How is the petrogenesis of Mg-spinel related to the evolution of the lunar crust? In order to answer above questions, a global screening of Mg-spinel bearing central peaks has been conducted in this study. The association between our observations and previous studies reveals important implications for distribution and petrogenesis of Mg-spinel.

2. Methods

2.1. Crater central peak

Lunar crater central peaks originate from the crust or mantle and offer an informative window for the detection of lunar crustal variations in lateral and vertical dimensions. In this study, we examined 166 lunar crater central peaks (Figure 2-1) which were selected from 1559 lunar craters listed in the USGS crater database (http://planetarynames.wr.usgs.gov/). The selection of these lunar craters was based on the following criteria: (1) craters are larger than 35 km in diameter; (2) craters should exhibit an apparent topographic peak based on M^3 images and Lunar Orbiter Laser Altimeter (LOLA) elevation data; (3) Central peaks are entirely covered with M^3 L2 reflectance images; (4) central peaks should show significantly strong spectral absorption features; (5) each central peak was observed with high spatial resolution images (Lunar Reconnaissance Orbiter (LRO) Wide Angle Camera (WAC) and/or Narrow Angle Camera (NAC) images (http://target.lroc.asu.edu/^{3}/)) to ensure the investigated areas are fresh and undisturbed. The application of these selection criteria was to assure that the examined central peaks are capable of representing deep materials from the lunar crust or upper mantle. The selected 166 craters range between ~35.1 km and ~199.5 km in diameter (d), and the excavation depth (D) ranges from ~5.05 km to ~33.21 km based on $D=0.109*d^{1.08}$ [Cintala and Grieve, 1998]. In order to investigate relative originated position of the central peak materials within the crust, the ratio of origin depth of central peak (D) to the average crustal thickness of the central peak region (T) extracted from Gravity Recovery and Interior Laboratory (GRAIL) crustal thickness map [Wieczorek et al., 2013] was used to describe the vertical distribution of Mg-spinel.

2.2. Datasets and image preprocessing

The Moon Mineralogy Mapper (M^3) is a state-of-the-art imaging spectrometer which is used to investigate the mineral and rock composition of the Moon [Pieters et al., 2009]. The global model of M^3 provides the lunar hyperspectral images (spectral range: 430-3000nm), which for the first time covers more than 90% of the lunar surface. [Green et al., 2011]. Seven optical periods (OPs) in the global model are distinguished based on varied coverage, phase angle, altitude, and spatial resolution. OP1A, OP1B, OP2A, OP2B observed the Moon at 140 m/pixel with high phase angles. In contrast, OP2C1, OP2C2, and OP2C3 have a resolution of 280 m/pixel with lower phase angles. A detailed summary of the OPs is given in [Besse et al., 2013].

The latest reflectance data (level 2) of M^3 in global mode, corrected for thermal [Clark et al., 2011] and photometric effects [Besse et al., 2013] and released on Dec. 8, 2011 by NASA, were used in this study. M^3 L2 images covering 166 craters were downloaded from the NASA PDS website. These images were geometrically corrected and smoothed for noise reduction. For geometric correction, the original reflectance images were warped based on latitude and longitude values of each pixel recorded together with image spectra. In the noise reduction process, pixels with a negative digital number were eliminated, and the moving average was used to smooth the image spectra (Figure 2-2). After spectral smoothing, continuum removal was applied to each image spectrum to isolate mineral diagnostic absorption features from the spectral continuum for mineral detection.

In addition to M^3, several other auxiliary datasets have been used in this study. The Clementine global mosaic image, created by the U.S. Geological Survey (USGS), is used as a global background image for analysis of mineral distribution. This data was acquired by Clementine mission, which was launched in 1994, and the range of wavelength is from 415 to 2000nm with 9 bands, and the spatial resolution of 1000m. Lunar Reconnaissance Orbiter (LRO) high spatial resolution images are used to characterize the geological character of investigated central peaks. LRO was launched on June 18th, 2009 [Robinson et al., 2010], and is currently in an extensional period. A global mosaic LRO Wide Angle Camera (WAC) and Narrow Angle Camera (NAC) images acquired from QuickMap website were used for each investigated central peak, the spatial resolution is at most 0.5 m/pixel. In addition, the lunar elevation map derived from the Lunar Orbiter Laser Altimeter (LOLA) on LRO spacecraft at 128 samples per degree spacing [Smith et al., 2010] approximately 250 m/pixel in latitude, was used to identified the topography of central peaks. Moreover, the global crustal thickness map (0.25 degree/pixel) obtained from the Gravity Recovery and Interior Laboratory (GRAIL) was downloaded from Wieczorek's website to combine with origin depth of central peaks for the description of vertical variations [Wieczorek et al., 2013].

2.3. Criteria for Mg-spinel detection

According to diagnostic properties of Mg-spinel summarized in Pieters et al. [2014] and practical experience for mineral detection, the detection of Mg-spinel with M^3 images relied on the following criteria. (1) 72 bands from 540 nm to 2537 nm were retained for spectral analysis (Figure 2-2) to eliminate the impact of imperfect thermal correction in long wavelength and maintain the wavelength range which is the most sensitive to mineral diagnostic absorption. (2) The deepest absorption band of each spectrum was required to be located in the wavelength range from 1738 nm (52nd band) to 2537 nm (72nd band) for qualifying the diagnostic absorption feature of Mg-spinel. (3) The absorption depth (AD) of the deepest absorption band should be larger than 0.05 to minimize the influences of thermal correction residue and inherent noise. The threshold of 0.05 for AD was determined based on the spectral features of typical Mg-spinel identified along the inner ring of Moscoviense Basin [Pieters et al., 2011]. The spectra of Mg-spinel were obtained from preprocessed 'M3G20090125T172601_V01_RFL.IMG' for locations 1 and 3 where Mg-spinel was detected in Pieters et al. [2011] (Figure 2-3). The integrated band depth (IBD) image exhibits the clear red color at two Mg-spinel-bearing locations as a result of strong absorption around 2 μm (Figure 2-3). Finally, 45 and 18 Mg-spinel spectra were extracted from locations 1 and 3 respectively. The average of these 63 Mg-spinel spectra is shown in Figure 2-4, where the deepest absorption depth around 2 μm is close to 0.05. (4) AD around 1 μm was set to be 0.02 or less to indicate the absence of mafic minerals (olivine and pyroxene). The criteria listed in (1), (2), (3) and (4) were implemented in Interactive Data Language (IDL) for initially automatic detection of Mg-spinel. (5) Manual evaluation for each potential Mg-spinel bearing pixel was conducted to verify the automatic detection results. The broad absorption shape, continuum inflection started around 1500 nm and no absorption feature in the short wavelength should be observed during manual detection to determine the presence of Mg-spinel. (6) Multi-temporal images, if available, were processed for each investigated central peak, and Mg-spinel detection was carried out using these images. The use of multi-temporal images helped eliminate the influence of imperfect thermal removal and photometric correction, as well as illumination differences due to local topography and achieve optimal detection. If Mg-spinel was observed more than once for the same central peak with multi-temporal images, it implies a reliable detection of Mg-spinel for this central peak. (7) The minimum number of identified Mg-spinel bearing pixels (MNP) among multi-temporal images was used as a conservative estimate to represent the likelihood of presence for Mg-spinel at each central peak. Taking Golitsyn crater (25.2S, 254.8E) as an example (Figure 2-5), six pixels were identified for the presence of Mg-spinel with 'M3G20090422T232600_V01_RFL.IMG' in Golitsyn's crater central peak (Figure 2-5-1A) and 53 Mg-spinel bearing pixels were detected with 'M3G20090520T065048_V01_RFL.IMG' (Figure 2-5-2A). Based on criterion (7), the MNP for Golitsyn's central peak (Figure 2-5B) is 6 rather than 53. For further verification, spectra (Figure 2-5C) were extracted for the highlighted pixels in Figure 2-5B and both spectra undoubtedly confirm the presence of Mg-spinel based on the significant absorption feature around 2 (AD>0.05) but insignificant absorption around 1 (AD<0.02). (8) The sum of MNP for Mg-spinel was normalized by the number of investigated crater central peaks (NCI) in each terrane or each layer. For example, the total MNP in SPAT is 14, and the number of investigated craters is 34 in SPAT. The MNP/NCI equals to 0.41 which is used to describe the likelihood of presence for Mg-spinel in SPAT.

2.4. Spectral features of other lunar common minerals

The presence of other lunar common minerals was also investigated in Mg-spinel bearing central peaks to infer the relation between Mg-spinel and other minerals. The examined minerals include olivine (Ol), crystalline plagioclase (Pl), orthopyroxene (Opx) and clinopyroxene (Cpx). The visible and near-infrared reflectance properties of returned lunar samples were analyzed [e.g., Adams, 1974; Adams and Goullaud, 1978; McCord et al., 1981, Pieters and Taylor, 1989] and revealed the unique spectral feature of each mineral. Laboratory spectral reflectance measurements of common lunar mineral separates are shown in Figure 2-6. Diagnostic absorption features of lunar minerals occur in reflected light from 400 to 2500 nm. Olivine shows a broad multiple absorption band near 1050 nm but no features at longer wavelengths. Sometimes, olivine exhibits a weak absorption near 2000 nm that might be caused by spinel inclusions [Cloutis et al., 2004; Isaacson and Pieters, 2010]. Crystalline plagioclase exhibits a weak absorption centered near 1250 nm due to 0.1% Fe^{2+} [Adams and Goullaud, 1978; Pieters, 1986]. This absorption band is usually only a minor contribution to a mineral mixture spectrum even though plagioclase may be a major mineral component [Adams and McCord, 1972]. Pyroxene displays two diagnostic absorption bands near 1000 and 2000 nm produced by Fe^{2+}. Low-Ca orthopyroxene, which is the dominant mafic mineral in almost all lunar highland rocks, displays two absorption bands near 900 and 1900 nm. With increasing Ca content, the absorption band centers shift to longer wavelengths [Adams, 1974]. Therefore, the high-Ca clinopyroxenes typically have diagnostic absorption bands near 980 and 2150 nm [Pieters, 1986].

3. Results

According to the criteria in section 2.3, Mg-spinel has been identified in 38 investigated crater central peaks (Figure 2-1). The information regarding 38 Mg-spinel bearing central peaks were tabulated in Table 2-1 including central coordinate, crater diameter (d), origin depth of central peak (D), average crustal thickness (T), D/T, MNP for Mg-spinel, coexisting minerals and available M^3 L2 images. A typical normalized reflectance spectrum and continuum removed reflectance spectrum of Mg-spinel from each crater central peak are shown in Figure 2-7 and Figure 2-8, respectively. All the spectra meet the criteria described in section 2.3 and exhibit significantly strong absorption near 2 µm but undetectable absorption around 1 µm. The maximal AD around 2 µm is more than 0.05

(Figure 2-9), suggesting the presence of Mg-spinel.

3.1. Distribution of Mg-spinel in the lunar crust

Laterally, among 38 Mg-spinel bearing central peaks identified on the Moon (Figure 2-1), 11 of them are in Feldspathic Highland Terrane (FHT), 25 in Procellarum KREEP Terrane (PKT) and only two in SPAT. The values of MNP/NCI for each terrane shown in Table 2-2A and plotted in Figure 2-10. Compared with SPAT (MNP/NCI=0.41), both PKT and FHT exhibit a high likelihood of presence for Mg-spinel. More Mg-spinel pixels were identified in PKT (MNP/NCI=4.87) than in FHT (MNP/NCI=4.05).

Vertically, Mg-spinel bearing lithologies are present at depths from ~5.14 km to ~28.44 km within the lunar crust. The D/T range 0.11-0.99 implies that the Mg-spinel can exist across the entire crust in the vertical direction. MNP versus D/T for each central peak was shown in Figure 2-11. Mg-spinel appears to be concentrated within the middle part of the lunar crust (D/T= 0.3-0.6). The MNP/NCI values are shown in Table 2-2B and delineated in Figure 2-12. Mg-spinel is most likely to be present in the middle crust (MNP/NCI=6.22). Based on this distribution of Mg-spinel, the crust could be tentatively subdivided into three layers using 0.3 and 0.6 as the thresholds.

Considering the vertical distribution of Mg-spinel in the three terranes separately, all the Mg-spinel bearing central peaks originated from upper crust (D/T<0.5) except for crater Compton (D/T= 0.97) in FHT (Table 2-1), and Mg-spinel could exist in the entire PKT crust from shallow to deep (D/T= 0.16-0.99). Two Mg-spinel bearing central peaks in SPAT originated from the location with D/T being 0.17 and 0.65 respectively.

The above observations indicate that Mg-spinel is widespread in both vertical and lateral dimensions of the lunar crust. The presence of Mg-spinel is more common than we expected, and Mg-spinel is most likely to represent a new prominent member of the lunar crust.

3.2. Co-existence of Mg-spinel with other minerals

Other common lunar minerals including olivine, crystalline plagioclase, orthopyroxene, and clinopyroxene have also been identified in the Mg-spinel bearing central peaks as shown in Table 2-1. Six Mg-spinel bearing central peaks have been determined to contain the olivine bearing materials. The amount of Mg-spinel is not proportional to olivine. For instance in the Copernicus central peaks (Figure 2-13), a large amount of olivine (MNP=1502) is present but a very small amount of Mg-spinel (MNP=7) has been identified. Olivine exists in all the peaks of Copernicus, but Mg-spinel was only found in one north small peak. Additionally, only Kovalevskaya central peak has been detected the co-occurrence of Mg-spinel and olivine in FHT. The other five Mg-spinel bearing central peaks with olivine were found in PKT, which possess relatively thin crust. The origin depth of the central peak identified the presence of both Mg-spinel and olivine ranges from ~5-18 km (D/T=0.16-0.61) which belongs to the upper crust. Moreover, 28 Mg-spinel bearing central peaks have been identified the presence of pyroxene (23 orthopyroxene bearing, and 23 clinopyroxene bearing). Olivine and pyroxene have been observed indicating that most of these Mg-spinel locations are probably associated with mafic materials.

Additionally, the presence of crystalline plagioclase has been detected in five Mg-spinel bearing central peaks (Table 2-1). The amount of Mg-spinel seems to be proportional to crystalline plagioclase. For example, Theophilus central peak (Figure 2-14) contains the largest amounts of both Mg-spinel and crystalline plagioclase in these five central peaks. Three of these five central peaks also contain olivine, and the remaining two were only detected for the presence of Mg-spinel and crystalline plagioclase. The origin depth for the five central peaks containing both Mg-spinel and crystalline plagioclase ranges from ~8 to 23 km (D/T 0.18-0.68).

Moreover, seven central peaks contain Mg-spinel and spectral featureless plagioclase. One example is Goodacre (-32.67 º, 14.08 º) (Figure 2-14), which is a crater located in the southern highlands on the near side and being ~44.09 km in diameter 6.5 km in origin depth. Only Mg-spinel and spectral featureless plagioclase were identified in this central peak. The D/T range of these seven central peaks is 0.19-0.96, which indicates that Mg-spinel could exist in the entire lunar crust and is not necessarily concurrent with olivine.

4. Petrogenesis of Mg-spinel

Understanding the petrogenesis of Mg-spinel offers a significant opportunity to refine the LMO and post-LMO processes. Even though there is no consensus on the origin of Mg-spinel currently, the Mg-spinel origin has been related to impact projectiles [Yue et al., 2013], impact melts [e.g. Treiman et al., 2010; Gross et al., 2014] or magmatic processes [e.g. Pieters et al., 2011; Vaughan et al., 2013; Prissel et al., 2014b].

4.1. Projectile remnants

Yue et al. [2013] suggested that Mg-spinel and olivine in crater central peaks could be the projectile remnants. This scenario is plausible because Mg-spinel has been observed in meteorites [e.g., Pieters and McFadden, 1994, Gross and Treiman, 2011] and airless bodies (e.g. Moon) that provide an opportunity for projectiles to be retained after being fragmented, vaporized, and dispersed during the impact event [Schultz and Gault, 1985]. However, the projectile remnants always contain high concentrations of siderophile elements (e.g. Fe, Ni), which is one of the important criteria to distinguish the impact origin materials from primitive igneous rocks [e.g. Warren, 1985]. The Mg-spinel only contains <5% FeO that means the presence of Mg-spinel in the projectile remnants should be under very special circumstances and is not a common event.

On the basis of the impact simulation results in Yue et al. [2013], most of the impact projectiles could be retained when the impact velocity is relatively low (less than 12 km/s). Bottke et al., [1996] and Minton and Malhotra, [2009] suggested ~25% of lunar impacts occur at velocities below 12 km/s. If the above statements are correct, it is reasonable to believe that at least a quarter of central peaks are expected to retain Mg-spinel and the likelihood of presence for Mg-spinel should be greater when the crater is larger. However, only 38 Mg-spinel bearing central peaks have been identified out of 317 central peaks (166 investigated and 151 uninvestigated spectral featureless) indicating that less than ~12% central peaks could be detected the appearance of Mg-spinel. Figure 2-16 shows the crater diameter versus MNP of Mg-spinel for each central peak. It can be seen that Mg-spinel in the central peaks of the larger craters is not necessarily abundant, and the medium size crater contains more Mg-spinel than small and large size craters. Furthermore, the impact projectile of the impact simulation in Yue et al. [2013] is a 7 km diameter dunite, and there is no direct evidence to demonstrate Mg-spinel could survive. Therefore, even if Mg-spinel could represent remnants from projectiles during impact processes, this should be rare, implying very few Mg-spinel central peaks could result from this scenario.

4.2. Impact melts

Another hypothesis is that Mg-spinel formed from olivine-plagioclase melts produced in impact cratering processes [e.g. Treiman et al., 2010; Gross et al. 2014]. The composition of impact melts and their differentiation products should depend on what portions of the moon were melted [Gross et al. 2014]. Note that here only impact melts on or near the surface are taken into account; impact melts produced from deep-seated materials (lower crust and mantle) will be discussed in section 4.3. The reason is that the composition of the deep-seated melts triggered by impacts is produced from the lunar interior and is not different from magmatic melts in composition.

Gross et al. [2014] conducted 1-bar crystallization experiments to produce spinel using rocks enriched in olivine and plagioclase which would be equivalent to impact-melting. A maximum of ~8 wt. % spinel was produced from the crystallization experiments on the composition similar to the returned sample Apollo 65785, and is much less than the value of the new Mg-spinel lithologies (20–30% spinel [Dhingra et al., 2011a]) detected by M^3. Meanwhile, the reflectance spectra of the experimental spinel were compared with Mg-spinel spectra derived from M^3. Although the experimental spinel has a broad 2 μm absorption feature which is similar to that found by M^3, the experimental spinel also shows an absorption feature around 1 μm probably caused by mafic glass which is in disagreement with the observation of Mg-spinel in M^3. Moreover, impact melts are usually mixed with the composition of the projectile itself containing highly siderophile elements [Hiesinger et al., 2006], which is not in line with the very low iron feature of Mg-spinel. In summary, although the impact melt origin of Mg-spinel cannot be ruled out entirely, it is not favored because most of Mg-spinel bearing locations observed with M^3 are old and undisturbed (inner ring, wall, central peak) which represents the Mg-spinel originated from deep-seated materials rather than surface impact melts [e.g. Pieters et al., 2011; Gross and Treiman et al., 2011] in the undisturbed central peak, it is unlikely for impact melts to occur. Hence, the 'impact melts' scenario is probably not suitable for explaining the origin of Mg-spinel in the central peaks observed with M^3.

4.3. Magmatic origins

The current hypothesis with respect to the magmatic origins of Mg-spinel has two main scenarios. One is that Mg-spinel origin appears to be linked to melting of deep-seated materials produced by plutonism [e.g. Pieters et al., 2011] or impact melts [e.g. Vaughan et al., 2013; Yamamoto et al., 2013a]. The other is that Mg-spinel is the product of assimilation between anorthositic crust and basaltic magma [e.g. Gross and Treiman, 2011; Prissel et al., 2014b]

4.3.1. Deep-seated crystallization

Pieters et al., [2011] suggested that Mg-spinel lacking mafic materials is a differentiation product of plutonic events, where melted Mg-suite highland rocks were incorporated with various amounts of magma ocean products such as ferroan anorthosites into a plutonic system, and Mg-spinel was generated by fractional crystallization during slow cooling of magma intrusions in the lower lunar crust or the interface between lunar crust and mantle. This plutonic scenario has been supported by many studies [e.g. Dhingra et al., 2011b; Bhattacharya et al., 2012; Kaur et al., 2012]. Pieters et al. [2014] reviewed current observations of Mg-spinel and suggested most Mg-spinels are associated with the thin crust area. They proposed that Mg-spinel should form during the interaction between ancient high Mg' magma with the anorthositic crust which is complementary to the scenario presented in Pieters et al. [2011]. In addition, Vaughan et al. [2013] proposed that Mg-spinel could be produced from impact melt mixtures of the anorthositic crust and mantle materials (an exogenic equivalent to plutons) during basin formation process. Yamamoto et al. [2013a] modified this scenario based on observations with SELENE SP data. They suggested that the formation of lunar impact basins caused melting of olivine-rich materials in the upper mantle and pure anorthosites in the crust, producing the Mg-spinel materials.

The deep-seated crystallization scenario in Vaughan et al. [2013] (impact melts) is weakened by the fact that mixing melts of ferroan anorthositic crust and mantle materials would likely produce ferroan-spinel rather than Mg-spinel [Vaughan et al., 2013; Vaughan and Head, 2014]. However, the validity of the Yamamoto et al. [2013a] is based on the observation that most basins with Mg-spinel possess the pure anorthosite and olivine. Indeed, three central peaks observed in this study exhibit the co-presence of Mg-spinel, plagioclase, and olivine. However, olivine cannot coexist with plagioclase at high pressures [Gross et al., 2014], which means those minerals cannot be produced simultaneously at deep locations and be excavated at the same time. Mg-spinel should be emplaced into the anorthositic crust by post crustal formation processes. Furthermore, the deep-seated crystallization scenario (impact melts) is also inconsistent with the observations in SPAT (Figure 2-17). SPA is the largest impact basin on the Moon, and it is most likely to produce a massive impact melt sheet which contains melted anorthositic crust and mafic mantle materials which could then differentiate and crystallize to form Mg-spinel. The thickness of SPA impact melts has been estimated to be ~50 km [Vaughan and Head, 2014]. If this is the case, more Mg-spinel is expected to be observed in the vicinity of SPA. However, only 2 Mg-spinel bearing central peaks (McKellar and Hausen) have been identified in SPAT (Figure 2-17). Both craters are located in the outer SPAT with the crater McKellar being in the north of SPAT and far away from the crater Hausen in the east of SPAT. The origin depth of these two crater central peaks is distinctively different with the Mckeller central peak stemming from 7.5 km (D/T=0.17) while Hausen from 26.7 km (D/T=0.65).

The long distance and different origin depths between Mckellar and Hausen, and the paucity of Mg-spinel in SPAT indicate that Mg-spinel in these two crater central peaks did not form from one large-scale impact event (SPA impact melts).

In contrast, the plutonism between anorthosite and high Mg' magma (probably Mg-suite parent magma) [e.g. Pieters et al., 2011] is a reasonable scenario to explain Mg-spinel formation. However, most Mg-spinel bearing central peaks contain a limited amount of Mg-spinel and MNP for Mg-spinel is less than 10 in 23 out of 38 Mg-spinel bearing central peaks. Moreover, not all Mg-spinel bearing lithologies are associated with large impact basins or thin crust areas. A comparison between MNP for Mg-spinel and crustal thickness of each central peak is shown in Figure 2-18. The trend of Mg-spinel associated with the regions of the thin crust [Pieters et al., 2014] cannot be observed. Mg-spinel is widespread in all locations of thin or thick crust areas. Furthermore, Mg-spinel is not necessarily concurrent with the appearance of olivine or pyroxene, nine Mg-spinel crater central peaks were determined to lack detectable mafic materials in this study. If mafic materials identified in the central peaks originate from Mg-suite magmatism, parts of Mg-spinel may have a source different from Mg-suite magma or an origin scenario different from Mg-suite plutonism. Nevertheless, local scale plutonic events should be a feasible scenario to explain the formation of Mg-spinel.

4.3.2. Assimilation (melt wall-rock reaction)

The origin of Mg-spinel has been proposed to be associated with the assimilation of high Mg, low Fe magma with wall-rock (anorthositic crust). Gross and Treiman [2011] suggested that Mg-spinel formed from a picritic magma that assimilated crustal anorthosite on its margin based on analysis of a fragment of the lunar meteorite ALHA 81005.

However, due to its relatively high-Fe, ALHA 81005 probably cannot exactly represent Mg-spinel observed with M^3. Well-designed and in-depth experimental studies put a constraint on the petrogenesis of Mg-spinel [Jackson et al., 2012; 2014; Prissel et al., 2012; 2013; 2014a; 2014b]. These experiments suggest that Mg-spinel is an assimilation product of Mg-suite parental magmas and anorthositic crust. The experimental results described in Prissel et al. [2013] indicate that lower Mg' (>75) spinel anorthosite lithologies may exist within the lunar crust, but are likely constrained to deep crustal origins (>10 km); high Mg' (>90) pink spinel anorthosite could present in the crust extensively without exact depth constraints. This experiment demonstrates the possibility of the presence of Mg-spinel in the relatively shallow layer (less than 10 km). Taylor and Pieters [2013] further suggested that the Very-High-Potassium (VHK) basaltic magma is a potential source intruding into an anorthosite crust to produce such high Mg' spinel.

Our observations are in good agreement with the assimilation scenario. First, Mg-spinel is widespread in both vertical and lateral dimensions of the lunar crust. The assimilation scenario allows Mg-spinel to form in both shallow and deep layers. Second, Mg-spinel shows a relatively low likelihood of presence in most of the investigated central peaks. The assimilation should occur at the edge of a magma chamber or the magma upwelling pipe (Figure 2-19) and the assimilation scale should be much smaller than plutonism. The little amount of Mg-spinel in central peak is most likely to represent the production of assimilation rather than plutonism. Third, only Mg-spinel and plagioclase (crystalline or noncrystalline) were identified in nine central peaks. Common mafic materials that are probably related to Mg-suite plutonism are not detected together with Mg-spinel, indicating that Mg-spinel is not generated from Mg-suite plutonism. Finally, the Mg-spinel anorthosite stability boundary could be as shallow as ~5 km on the basis of observations in this study. Therefore, the anorthositic crust assimilated by high Mg' magma (possible Mg-suite parent magma) is the reasonable scenario to explain the origin of Mg-spinel. The plutonism process cannot be ruled out because of the massive presence of Mg-spinel in some regions (e.g. Theophilus).

4.4. A new member of Mg-suite

Mg-spinel most likely represents a new member of Mg-suite in terms of its distribution, the most plausible petrogenesis as well as extremely high Mg'. The detection of Mg-spinel in this study clearly shows that the presence of Mg-spinel is by no means limited to a few areas; rather it is more common in the lunar crust than expected. Our observations indicate that Mg-spinel occurs in both vertical and lateral directions of the entire crust. If the detection area includes crater wall, crater ring, or ejecta, rather than just crater central peaks, the distribution of Mg-spinel could be dramatically different.

The origin of Mg-spinel is likely related to the Mg-suite magmatism being either plutonism or assimilation (Figure 2-19). Mg-suite plutonism is likely responsible for the origin of Mg-spinel in PKT. Mg-spinel is significantly concentrated in PKT and nearly all Mg-spinel bearing central peaks with olivine were identified in PKT. The crust underneath PKT has been permanently thinned and fractured by large impact basins (e.g. Procellarum and Insularum). Post-LMO magma is most likely to intrude into the crust and form plutons which would be excavated and emplaced to the lunar surface by later impacts. According to the distribution of Mg-spinel and occurrence of olivine, the plutonism for Mg-spine possibly occurred in the middle part of the lunar crust rather than the lower crust. On the other hand, the origin of Mg-spinel can be better characterized by assimilation between

Mg-suite magma with anorthositic crust. 15 central peaks originating from a depth less than 10 km have been identified for the presence of Mg-spinel without the appearance of olivine. Almost all of the Mg-spinel in FHT stems from the upper crust without olivine, which may indicate that the crust underneath FHT is too thick to permit magma intrusion to form plutons. These observations provide important evidence for using assimilation to explain the origin of Mg-spinel. Apparently, the petrogenesis of Mg-spinel in the lunar crust can be explained by both plutonism and assimilation associated with Mg-suite magmatism.

According to the high Mg', distribution and petrogenesis of Mg-spinel, we suggest that Mg-spinel is a new member of Mg-suite rocks. The origin of Mg-spinel leads to an improved understanding of Mg-suite magmatism and provides critical constraints on the compositional diversity of lunar crust and formation process.

5. Conclusions

38 Mg-spinel bearing central peaks were identified out of 166 craters investigated. The results indicate Mg-spinel could exist in the entire crust and appears to be concentrated within the middle layer underneath the PKT. Our observations combined with previous studies show that Mg-suite plutonism and assimilation between high Mg' magma with anorthositic crust (Figure 2-19) are possibly responsible for the origin of Mg-spinel. Both the distribution and petrogenesis of Mg-spinel lead to a novel conclusion that Mg-spinel is a new member of Mg-suite rocks. In order to put constraints on the origin of Mg-spinel related to Mg-suite magmatism, other regions (e.g. crater wall, basin inner ring) need to be analyzed with M^3 data. Meanwhile, the experimental constraints on Mg-spinel are necessary to be required.

Acknowledgements

I gratefully acknowledge the scientific suggestion of Carle M. Pieters and Tabb Prissel, and the assistance and support of Shuai Li, Kaishan Song, Linhai Li, and Zuchuang Li.

Table captions

Table 2-1. Information for 38 Mg-spinel bearing central peaks. 1: crater diameter. 2: origin depth of central peak on D=0.109*d1.08 [Cintala and Grieve, 1998]. 3: average crustal thickness of central peak region derived from GRAIL crustal thickness map [Wieczorek et al., 2013]. 4. Minimum number of pixels detected the presence of Mg-spinel (Sp), or olivine (Ol), or crystalline plagioclase (Pl) among multi-temporal images. 5. Star marker represents the presence of pyroxene (Opx: orthopyroxene; Cpx: clinopyroxene). 6. The classification of three crustal terranes cite from Jolliff et al., [2000]. 7. The average absorption depth of deepest absorption around 2 µm for each central peak.

Table 2-2. The lateral and vertical variation of Mg-spinel in the lunar crust and plotted in Figure 2-9 (A) and Figure 2-11 (B).

Tables

Table 2-1.

Crater name	Center Latitude	Center Longitude	d^1 (km)	D^2 (km)	T^3 (km)	D/T	MNP$_{Sp}$^{4}	MNP$_{Ol}$^{4}	MNP$_{Pl}$^{4}	Opx^5	Cpx^5	Terrane^6	AD^7	M^3 L2 Image
Golitsyn	-25.2	254.8	35.47	5.14	46.26	0.11	6			*	*	FHT	0.06	M3G20090422T232600
														M3G20090520T065048
Bianchini	48.78	325.63	37.59	5.48	34.63	0.16	13	8		*	*	PKT	0.07	M3G20090208T100012
														M3G20090611T043527
Pease	12.51	253.7	40.84	5.99	36.83	0.16	1				*	FHT	0.06	M3G20090213T180532
														M3G20090423T012445
														M3G20090520T065048
Leuschner	1.67	250.95	50.14	7.48	44.70	0.17	5				*	FHT	0.07	M3G20090214T000903
														M3G20090423T052045
Stiborius	-34.49	31.99	43.76	6.45	37.79	0.17	15			*		PKT	0.08	M3G20090203T061431
														M3G20090606T053022
McKellar	-15.72	189.14	50.16	7.48	43.29	0.17	9			*	*	SPAT	0.06	M3G20090815T074952
Lindenau	-32.35	24.77	53.08	7.95	43.41	0.18	1		2			PKT	0.06	M3G20090203T182711
Ball	-35.92	351.61	40.31	5.91	31.39	0.19	7			*		PKT	0.06	M3G20090206T065053
Goodacre	-32.67	14.08	44.09	6.51	34.34	0.19	25					PKT	0.20	M3G20090204T134332
														M3G20090607T153144
Lowell	-12.97	256.58	62.65	9.51	47.03	0.20	21			*	*	FHT	0.09	M3G20090213T115953
														M3G20090422T193000
Ohm	18.32	246.22	61.75	9.36	41.16	0.23	26				*	FHT	0.09	M3G20090214T074247
Morse	21.9	184.71	72.77	11.18	39.87	0.28	8					FHT	0.07	M3G20090815T162202
Zucchius	-61.38	309.35	63.18	9.60	32.36	0.30	1			*	*	PKT	0.07	M3G20090418T190900
Dalton	17.07	275.55	60.69	9.19	29.85	0.31	12					PKT	0.08	M3G20090115T174705
														M3G20090212T024412
Franklin	38.73	47.64	55.92	8.41	26.60	0.32	8			*	*	PKT	0.06	M3G20090202T003211
														M3G20090202T024131
Eudoxus	44.27	16.23	70.16	10.74	31.67	0.34	1			*	*	PKT	0.06	M3G20090204T113444
														M3G20090607T073505
Berkner	25.13	254.76	87.62	13.66	39.67	0.34	13					FHT	0.07	M3G20090213T155552
Robertson	21.84	254.63	89.85	14.04	38.39	0.37	6			*	*	FHT	0.07	M3G20090213T155552
														M3G20090422T235626
Miller	-39.37	0.78	61.37	9.30	25.27	0.37	14			*	*	PKT	0.06	M3G20090205T133443
Kovalevskaya	30.86	230.56	113.71	18.10	47.64	0.38	82	4	16	*	*	FHT	0.06	M3G20090424T191252
														M3G20090424T205837

Table 2-1. Continue

Crater name	Center Latitude	Center Longitude	d[1] (km)	D[2] (km)	T[3] (km)	D/T	MNP_{Sp}[4]	MNP_{Ol}[4]	MNP_{Pl}[4]	Opx[5]	Cpx[5]	Terrane[6]	AD[7]	M^3 L2 Image
Tycho	-43.3	348.78	85.29	13.27	31.97	0.41	2			*	*	PKT	0.07	M3G20090206T105850
														M3G20090415T202222
														M3G20090609T095022
Hayn	64.56	83.87	86.21	13.42	32.28	0.42	40			*	*	PKT	0.08	M3G20090602T082937
														M3G20090602T124100
Poynting	17.5	226.62	127.55	20.49	48.24	0.42	2			*	*	FHT	0.07	M3G20090425T030840
														M3G20090812T111903
Arzachel	-18.26	358.07	96.99	15.24	34.46	0.44	21			*	*	PKT	0.06	M3G20090205T193313
Geminus	34.42	56.66	81.98	12.71	27.46	0.46	1			*	*	PKT	0.05	M3G20090201T085853
														M3G20090604T064302
														M3G20090729T022657
Atlas	46.74	44.38	88.12	13.74	29.19	0.47	20	7		*	*	PKT	0.06	M3G20090202T083314
														M3G20090729T233354
Copernicus	9.62	339.92	96.07	15.09	31.93	0.47	7	1502		*		PKT	0.08	M3G20090207T044515
														M3G20090416T122951
														M3G20090513T191408
Moretus	-70.63	354.05	114.45	18.23	35.12	0.52	2			*		PKT	0.07	M3G20090205T214723
														M3G20090206T010833
Gassendi	-17.55	320.04	111.39	17.70	31.11	0.57	9	10	3	*		PKT	0.06	M3G20090208T160125
Albategnius	-11.24	4.01	130.84	21.06	35.96	0.59	6					PKT	0.09	M3G20090109T022525
														M3G20090205T092400
														M3G20090608T083142
Theophilus	-11.45	26.28	98.59	15.52	25.39	0.61	177	105	98			PKT	0.24	M3G20090203T160452
														M3G20090203T175131
														M3G20090731T045352
Hausen	-65.11	271.51	163.24	26.75	40.88	0.65	5			*	*	SPAT	0.07	M3G20090212T104932
Pythagoras	63.68	297.02	144.55	23.46	34.25	0.68	8		3			PKT	0.07	M3G20090419T171612
Sklodowska	-18.04	96.15	125.55	20.14	28.33	0.71	2				*	PKT	0.05	M3G20090601T062753
Walther	-33.25	0.62	134.23	21.65	28.69	0.75	28					PKT	0.16	M3G20090205T133443
														M3G20090608T125102
Neper	8.76	84.58	144.32	23.42	24.33	0.96	10					PKT	0.14	M3G20090602T074711
Compton	55.86	104.05	164.63	26.99	27.67	0.98	4			*	*	FHT	0.06	M3G20090531T172712
Joliot	25.79	93.39	172.79	28.44	28.76	0.99	3				*	PKT	0.05	M3G20090601T145212

Table 2-2.

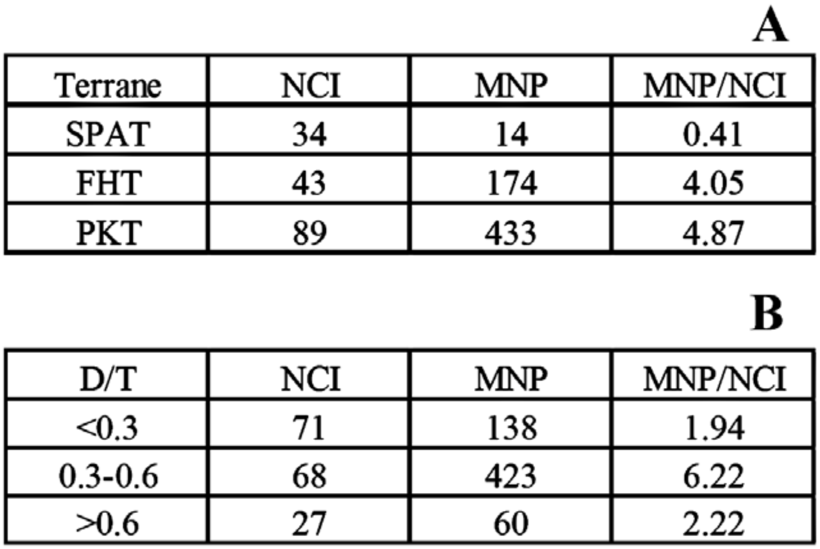

A

Terrane	NCI	MNP	MNP/NCI
SPAT	34	14	0.41
FHT	43	174	4.05
PKT	89	433	4.87

B

D/T	NCI	MNP	MNP/NCI
<0.3	71	138	1.94
0.3-0.6	68	423	6.22
>0.6	27	60	2.22

Figure captions

Figure 2-1. Distribution of Mg-spinel bearing crater central peaks overlaid on a LOLA DEM image of the Moon. Red solid circles represent 166 investigated central peaks, and yellow circles represent the results obtained in this study.

Figure 2-2. Typical Mg-spinel spectrum extracted from M^3 images in the Theophilus central peak. A: original M^3 reflectance spectrum. B: smoothed reflectance spectrum.

Figure 2-3. Color composite IBD image (R: IBD2000; G: IBD1000; B: reflectance at 1508 nm) for western Moscoviense Basin. The presence of Mg-spinel was identified at Location 1 and 3 in Pieters et al. [2011]. The spectra were extracted in the white circle areas and were calculated for the average spectrum in Figure 2-4.

Figure 2-4. Average spectrum of Mg-spinel in the inner ring of Moscoviense basin. This spectral obtained from 'M3G20090125T172601_V01_RFL.IMG' after spectral smoothing. The IBD images (see Figure 2-3) were used to determine which pixel represents Mg-spinel (the same as the method used in Pieters et al. [2011]) Finally, 45 and 18 Mg-spinel spectra were extracted in location 1 and location 3 (the same location as in Pieters et al. [2011]) respectively. The spectrum shown in this Figure represents the average spectrum of Mg-spinel in the location 1 and 3 along innermost ring of Moscoviense basin.

Figure 2-5. Multi-temporal images for Golitsyn crater (-25.2 ^{o}, 254.8 ^{o}).

1: M3G20090422T232600_V01_RFL.IMG; 2:M3G20090520T065048_V01_RFL.IMG. A: the M^3 L2 image for Golitsyn at 750 nm. B: Zoom in central peak region (the red box in A). C: the reflectance spectrum after continuum removal was extracted from the same location.

Figure 2-6. Laboratory spectral reflectance of common lunar minerals. *Spectrum of Mg-spinel is measured from terrestrial samples, currently Mg-spinel has not been found in any lunar samples.

Figure 2-7. Relative reflectance and continuum removed reflectance of typical Mg-spinel extracted from each crater central peak (excavation depth less than 10 km). These spectra are normalized to 1508 nm reflectance to emphasize the shape and strength of Mg-spinel absorption. The crater names are ordered by increasing origin depth of the central peak from top to bottom.

Figure 2-8. Typical Mg-spinel spectra extracted from each crater central peak (excavation depth larger than 10 km). These spectra are also normalized to 1508 nm reflectance that as same as the Figure 2-6.

Figure 2-9. Absorption depth around 2000 nm of typical Mg-spinel spectrum for each Mg-spinel bearing crater central peak identified in this study. The vertical axis represents crater names sorted by excavation depth (shown in Table 2-1). The horizontal axis shows the range of absorption depth around 2000nm from 0.04 to 0.1 to enhance the difference between each other. Four absorption depths are larger than 0.1 and marked by value. The crater names are ordered by increasing origin depth of the central peak from top to bottom.

Figure 2-10. Lateral variations of Mg-spinel in three terranes and the data is tabulated in Table 2-2A.

Figure 2-11. Vertical distribution and the likelihood of the presence of Mg-spinel bearing lithologies. The relative depth of each central peak (D/T) is shown in the vertical axis. The minimum number of pixels (MNP) for detected Mg-spinel in each central peak is shown in the horizontal axis.

Figure 2-12. Vertical variation of Mg-spinel in the lunar crust and the data in the Table 2-

2B.

Figure 2-13. Detailed information for Copernicus crater central peak. A: IBD (integrated band depth) image (Red: IBD2000, Blue: IBD1000, Green: M^3 reflectance at 1508 nm) on the M^3 reflectance image at 750 nm; B: LRO WAC mosaic image for Copernicus crater; C: the identified Mg-spinel bearing pixels (orange) and olivine bearing pixels (green) on M^3 reflectance image at 750 nm, the size is the same as the IBD image in A; D: LRO WAC mosaic image of Copernicus crater central peak in 3D perspective using LOLA data. Vertical exaggeration is ×2. Red circle highlight the Mg-spinel rich peak shown in E. E: LRO NAC image for the Mg-spinel rich area as be marked as a red circle in D.

Figure 2-14. Detailed information for Theophilus crater central peak. A: IBD (integrated band depth) image (Red: IBD2000, Blue: IBD1000, Green: M^3 reflectance at 1508 nm) on the M^3 reflectance image at 750 nm; B: LRO WAC mosaic image for Theophilus crater; C: the identified Mg-spinel (orange), olivine (green) and crystalline plagioclase (red) bearing pixels on M^3 reflectance image at 750 nm, the size is the same as the IBD image in A; D: LRO WAC mosaic image of Theophilus crater central peak in 3D perspective using LOLA data. Vertical exaggeration is ×2. Yellow circle highlight the Mg-spinel rich area is shown in E. E: LRO NAC image for the Mg-spinel rich area as be marked as a yellow circle in D.

Figure 2-15. Detailed information for Goodacre crater central peak. A: Mg-spinel bearing pixels (orange) are shown in M^3 reflectance image at 750 nm of Goodacre crater. B: IBD (integrated band depth) image at 2000. C: Mosaic M^3 reflectance image at 750 nm on the central peak of the Goodacre crater in 3D perspective using LOLA data. Vertical exaggeration is ×5. Orange color pixels represent Mg-spinel. D: LRO NAC image for the

Mg-spinel rich area.

Figure 2-16. Comparison between MNP (horizontal axis) and crater diameter (vertical axis)

Figure 2-17. The distribution of investigated crater central peaks within SPAT. The Mg-spinel bearing central peaks show in orange color.

Figure 2-18. Mineral detection results relative to crustal thickness and data shown in Table 2-1.

Figure 2-19. Schematic cross section of the lunar crust illustrates possible petrogenesis of Mg-spinel bearing lithology revised from Pieters et al. [2011] and Prissel et al. [2012]. The lunar crust is dominantly anorthosite overlain by a layer of megaregolith about 2~3 km. More mafic materials are present in the middle part of the lunar crust. The results of this study indicate that the Mg-spinel could exist in the nearly entire lunar crust in the vertical direction. The origin of Mg-spinel could be explained through assimilation (A) and plutonism (P) processes. According to results from this paper, the Mg-spinel and anorthosite stability boundary could be revised to ~5km.

Figures

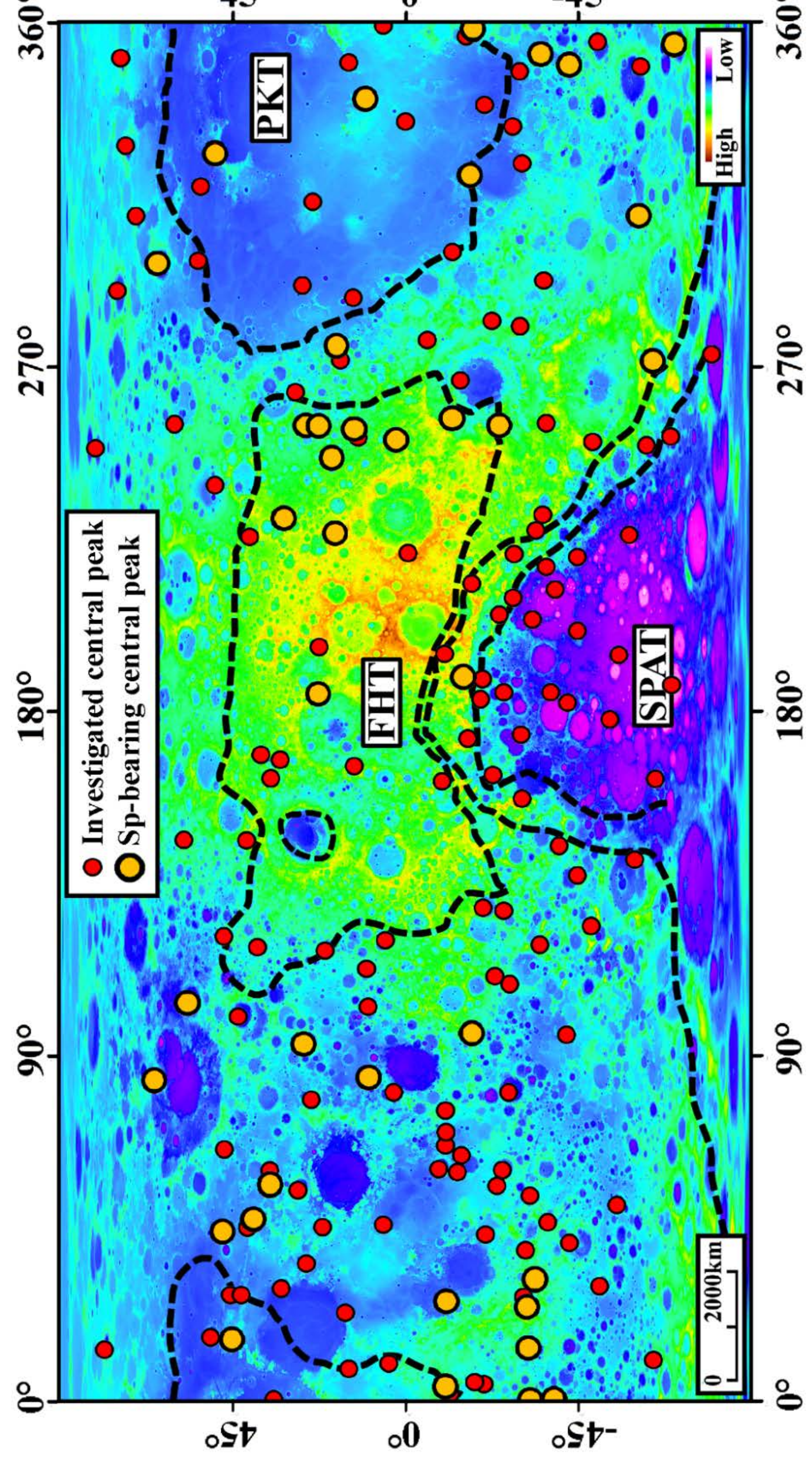

Figure 2-1.

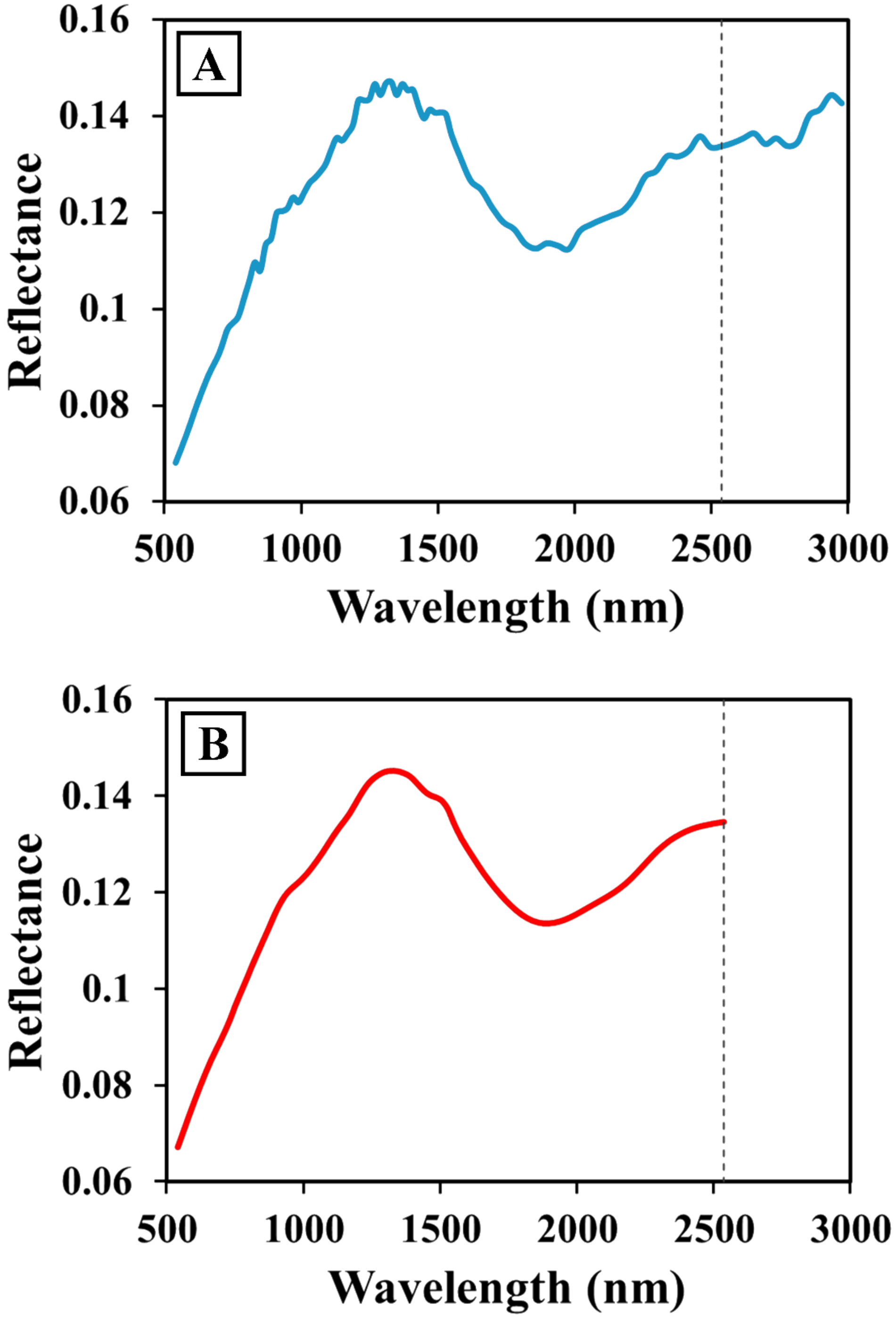
A
0.16
0.14
0.12
0.1
0.08
0.06
Reflectance
500
1000
1500
2000
2500
3000
Wavelength (nm)
B
0.16
0.14
0.12
0.1
0.08
0.06
Reflectance
500
1000
1500
2000
2500
3000
Wavelength (nm)

Figure 2-2.

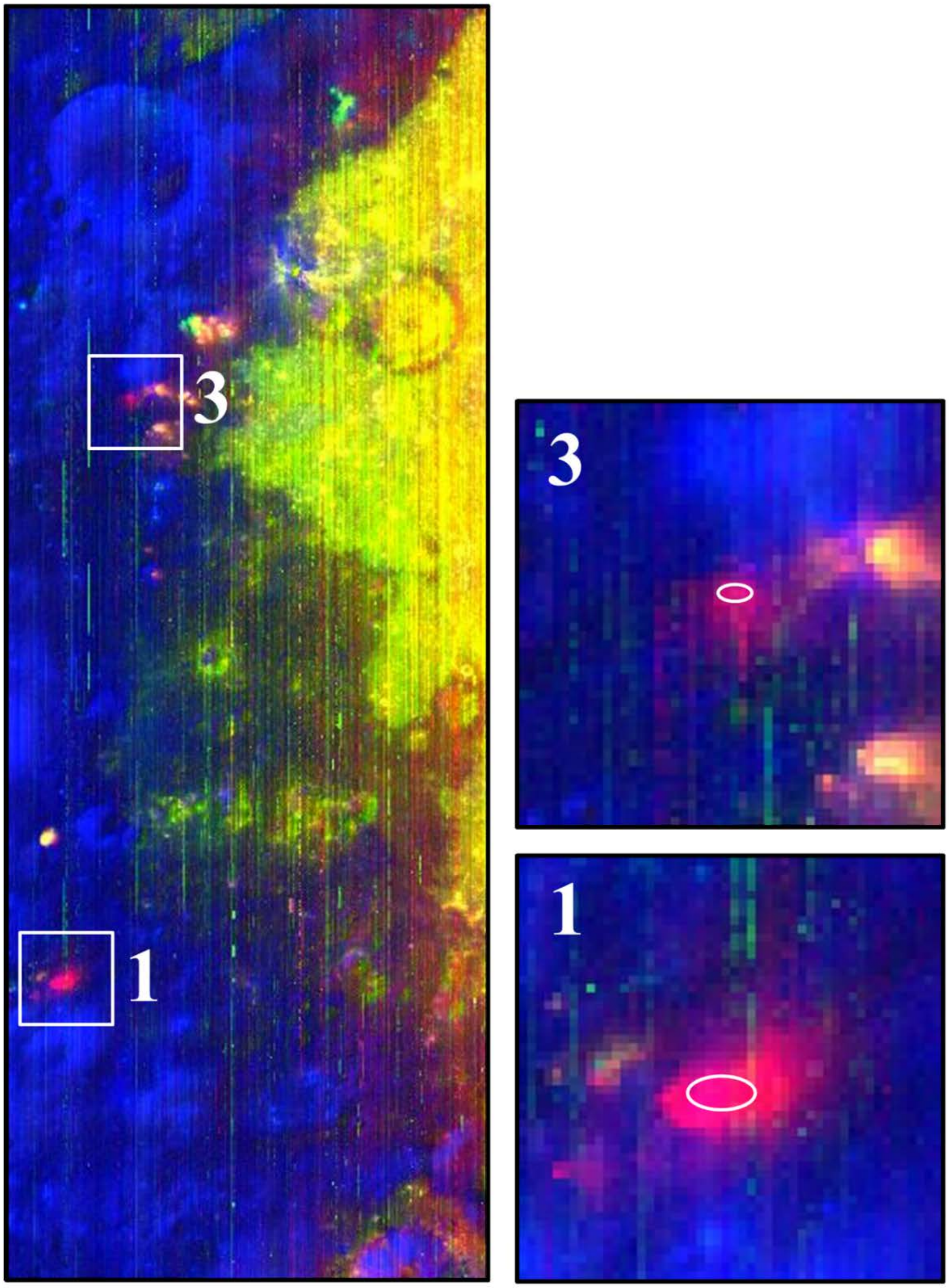

Figure 2-3.

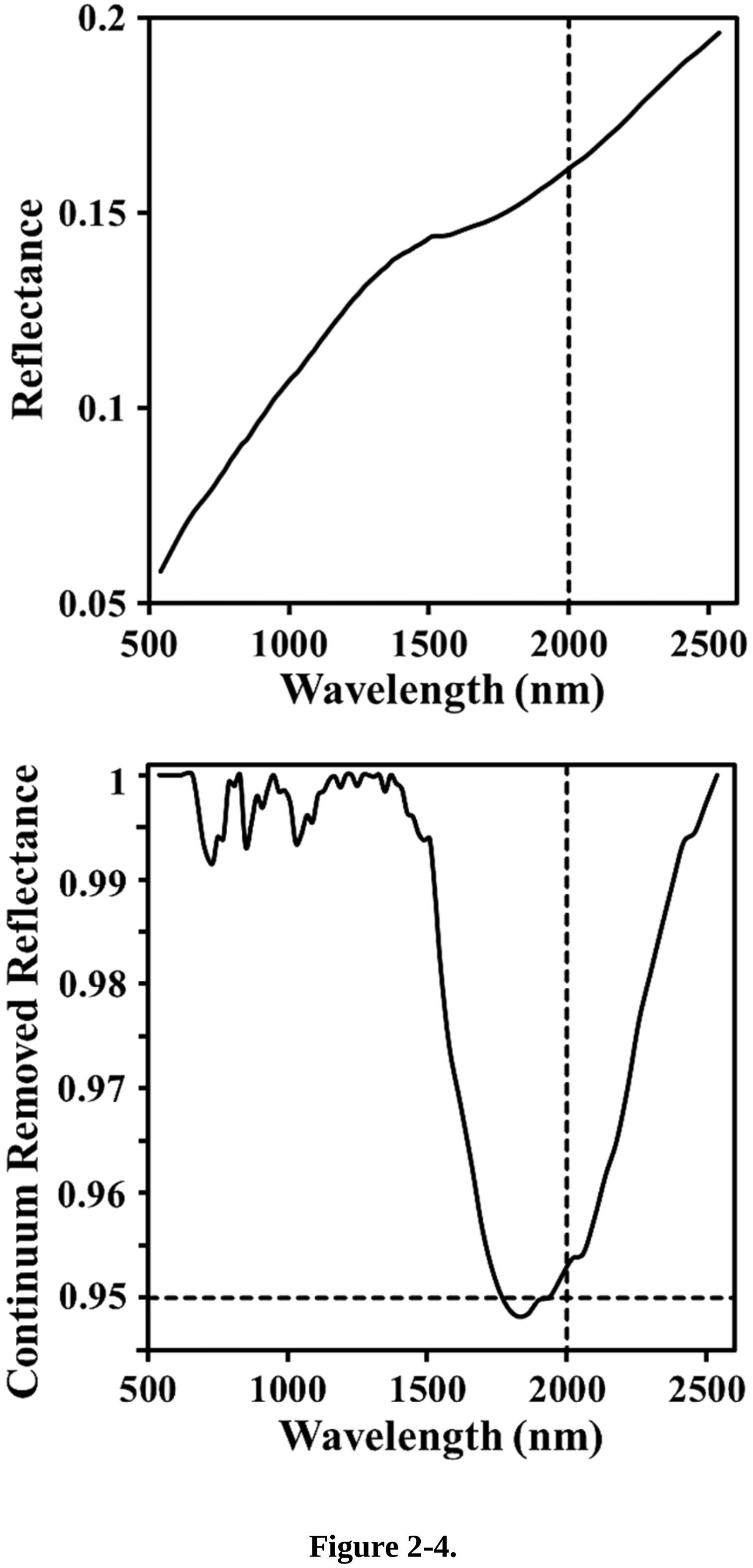
0.2
0.15
0.1
0.05
Reflectance
500
1000
1500
2000
2500
Wavelength (nm)
1
0.99
0.98
0.97
0.96
0.95
Continuum Removed Reflectance
500
1000
1500
2000
2500
Wavelength (nm)

Figure 2-4.

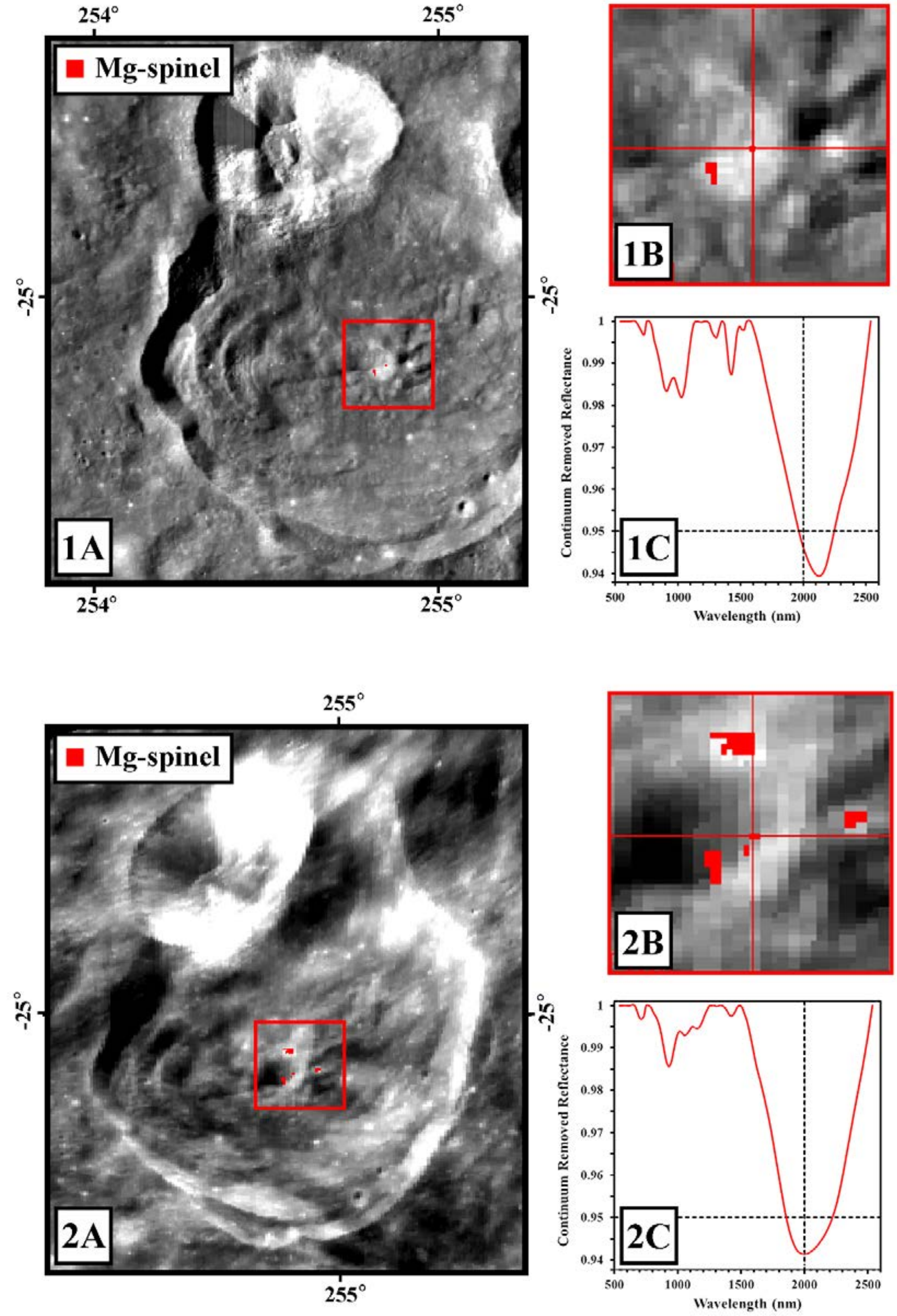
254°
255°
Mg-spinel
-25°
-25°
1A
254°
255°
1B
1C
Continuum Removed Reflectance
1
0.99
0.98
0.97
0.96
0.95
0.94
500
1000
1500
2000
2500
Wavelength (nm)
255°
Mg-spinel
-25°
-25°
2A
255°
2B
2C
Continuum Removed Reflectance
1
0.99
0.98
0.97
0.96
0.95
0.94
500
1000
1500
2000
2500
Wavelength (nm)

Figure 2-5.

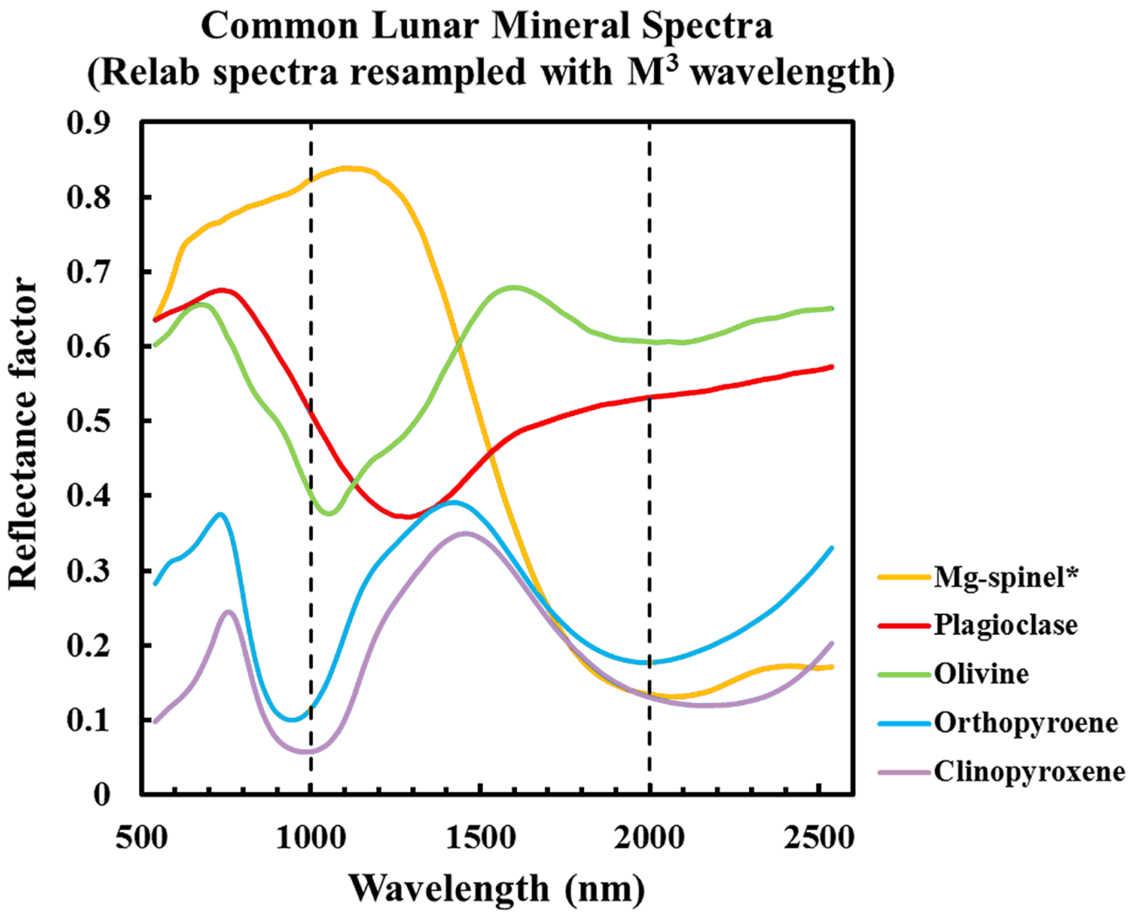
Common Lunar Mineral Spectra
(Relab spectra resampled with M3 wavelength)
0.9
0.8
0.7
0.6
0.5
0.4
0.3
0.2
0.1
0
Reflectance factor
500
1000
1500
2000
2500
Wavelength (nm)
Mg-spinel*
Plagioclase
Olivine
Orthopyroene
Clinopyroxene

Figure 2-6.

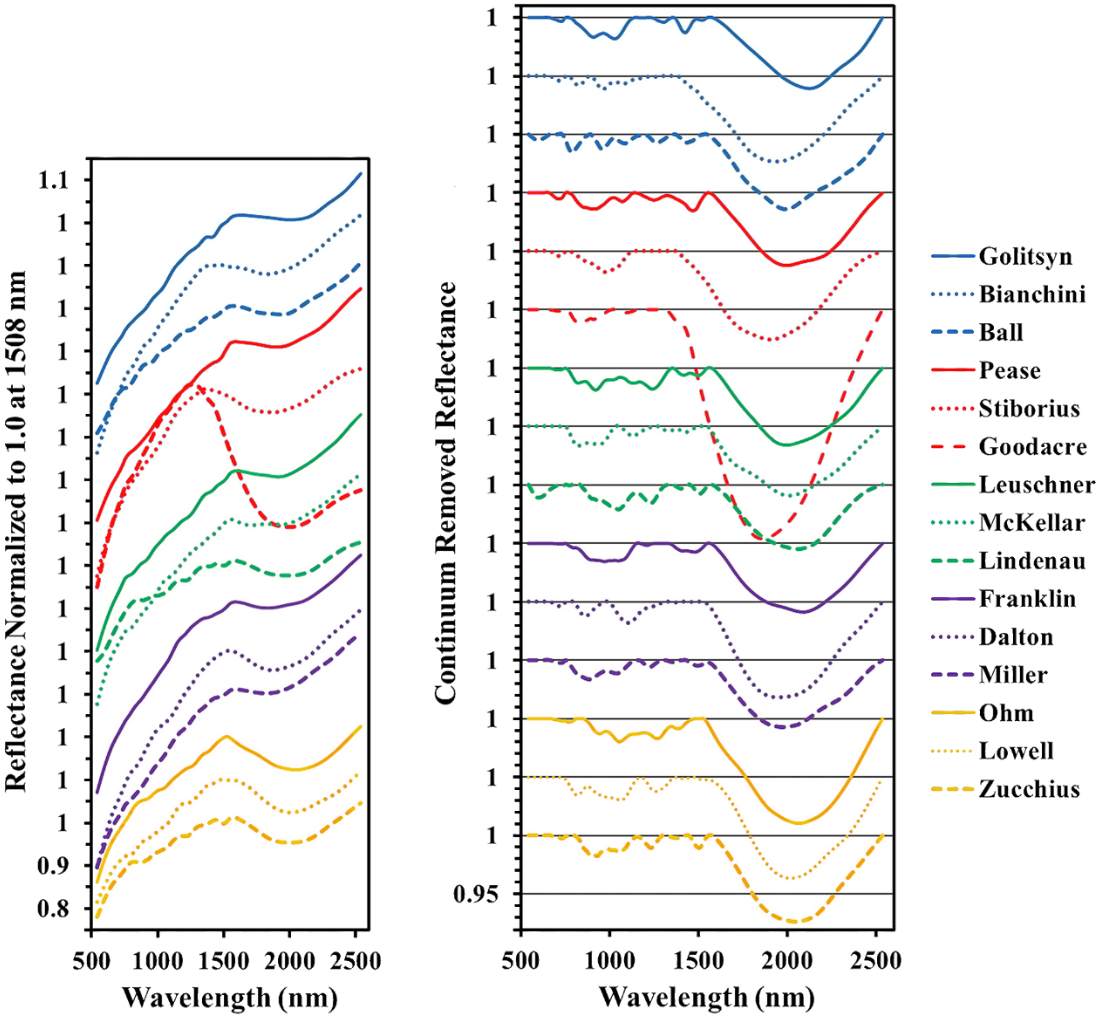

Reflectance Normalized to 1.0 at 1508 nm
1.1
1
1
1
1
1
1
1
1
1
1
1
1
1
1
0.9
0.8
500
1000
1500
2000
2500
Wavelength (nm)
Continuum Removed Reflectance
1
1
1
1
1
1
1
1
1
1
1
1
1
1
1
0.95
500
1000
1500
2000
2500
Wavelength (nm)
Golitsyn
Bianchini
Ball
Pease
Stiborius
Goodacre
Leuschner
McKellar
Lindenau
Franklin
Dalton
Miller
Ohm
Lowell
Zucchius

Figure 2-7.

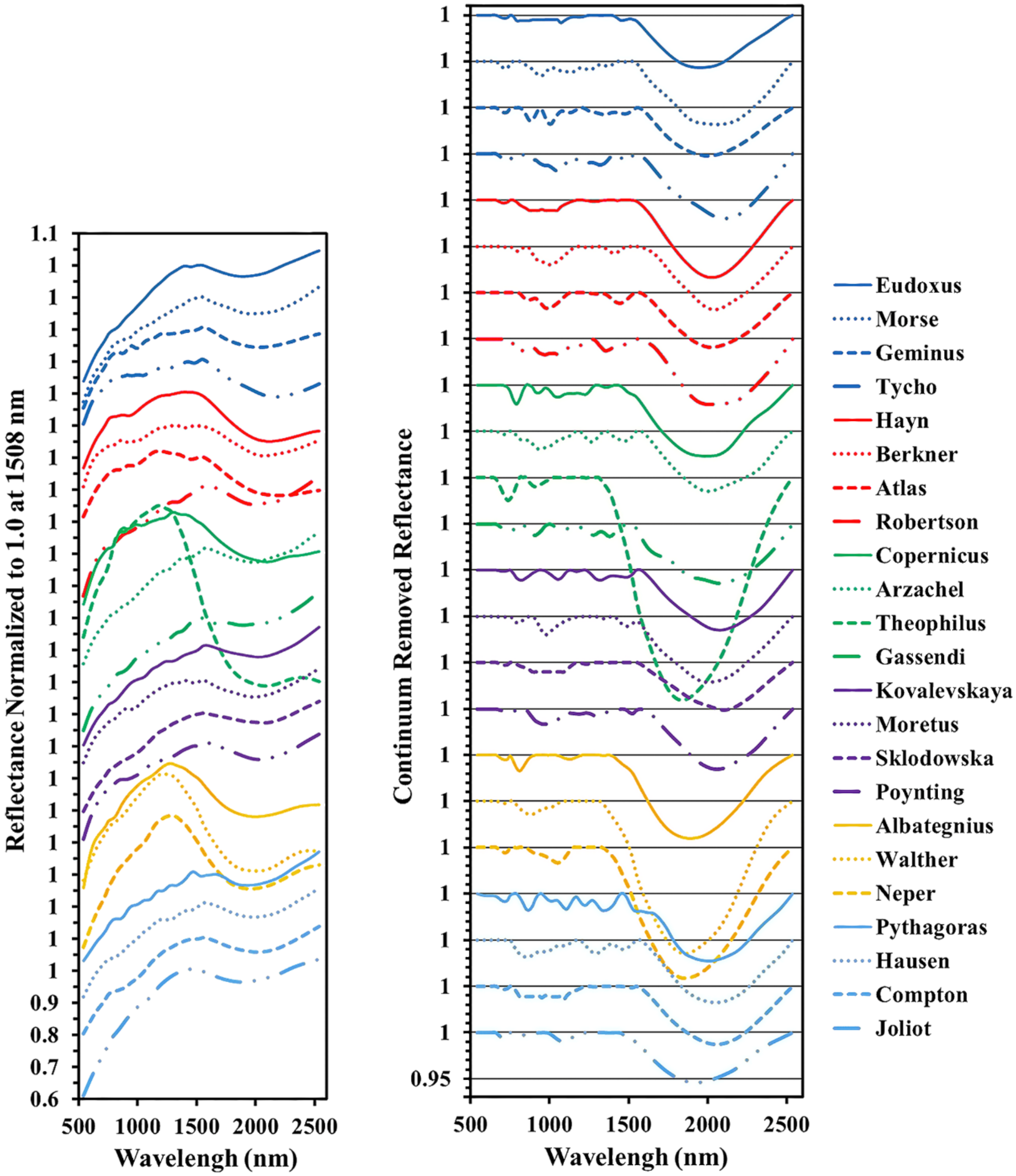
Reflectance Normalized to 1.0 at 1508 nm
1.1
1
0.9
0.8
0.7
0.6
500
1000
1500
2000
2500
Wavelengh (nm)
Continuum Removed Reflectance
1
0.95
500
1000
1500
2000
2500
Wavelengh (nm)
Eudoxus
Morse
Geminus
Tycho
Hayn
Berkner
Atlas
Robertson
Copernicus
Arzachel
Theophilus
Gassendi
Kovalevskaya
Moretus
Sklodowska
Poynting
Albategnius
Walther
Neper
Pythagoras
Hausen
Compton
Joliot

Figure 2-8.

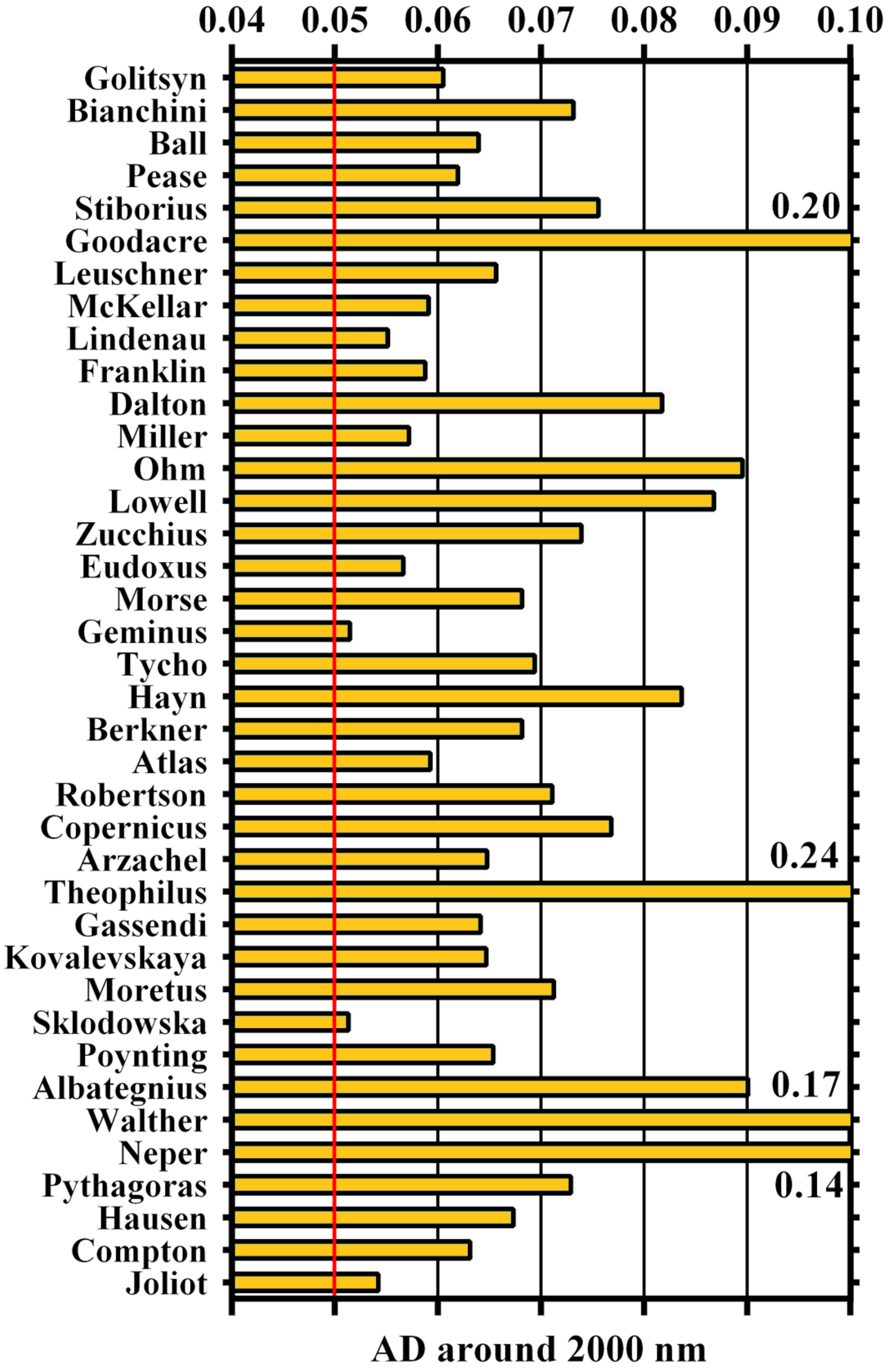
0.04
0.05
0.06
0.07
0.08
0.09
0.10
Golitsyn
Bianchini
Ball
Pease
Stiborius
Goodacre
Leuschner
McKellar
Lindenau
Franklin
Dalton
Miller
Ohm
Lowell
Zucchius
Eudoxus
Morse
Geminus
Tycho
Hayn
Berkner
Atlas
Robertson
Copernicus
Arzachel
Theophilus
Gassendi
Kovalevskaya
Moretus
Sklodowska
Poynting
Albategnius
Walther
Neper
Pythagoras
Hausen
Compton
Joliot
0.20
0.24
0.17
0.14
AD around 2000 nm

Figure 2-9.

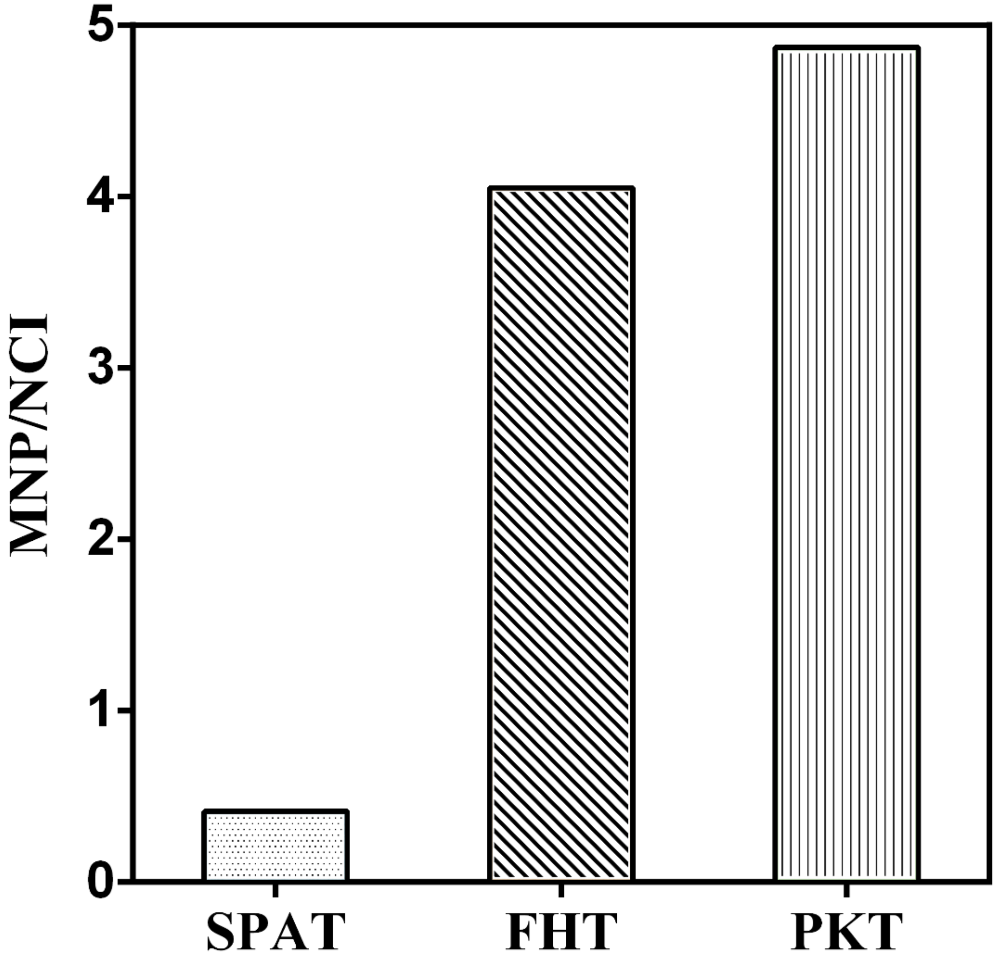

Figure 2-10.

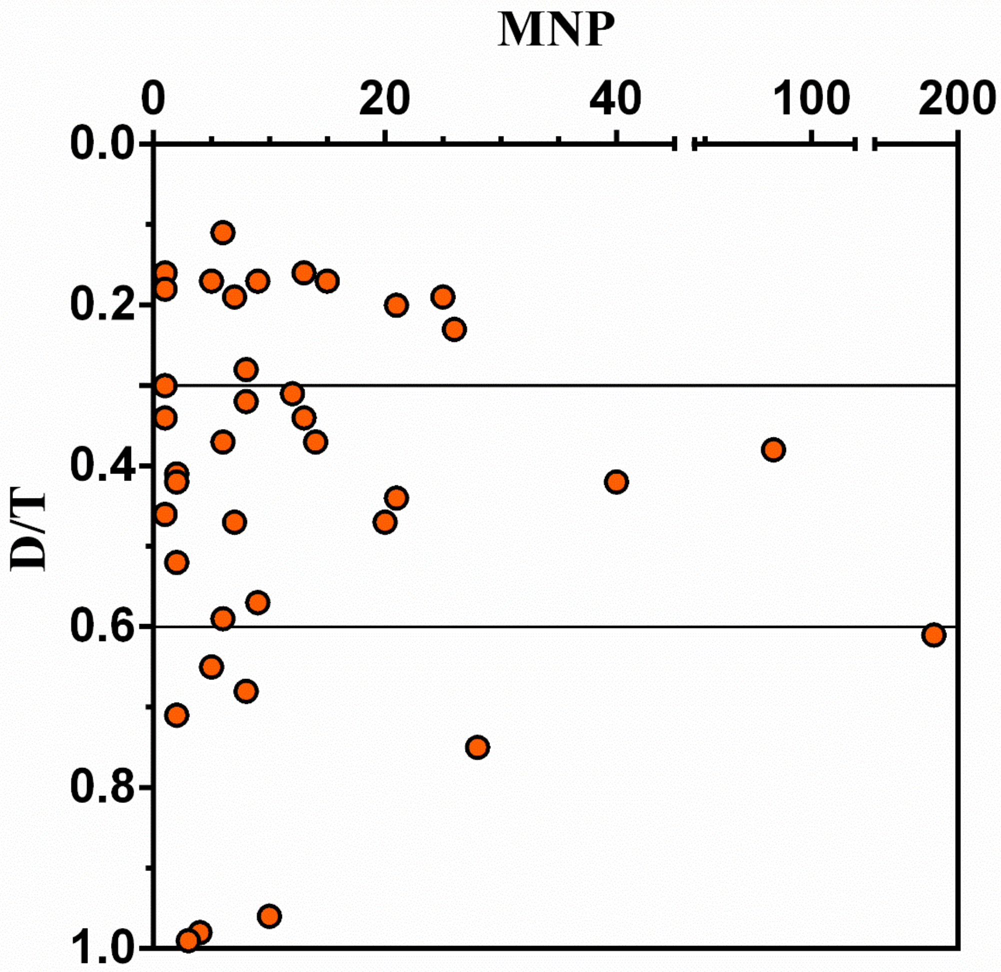

Figure 2-11.

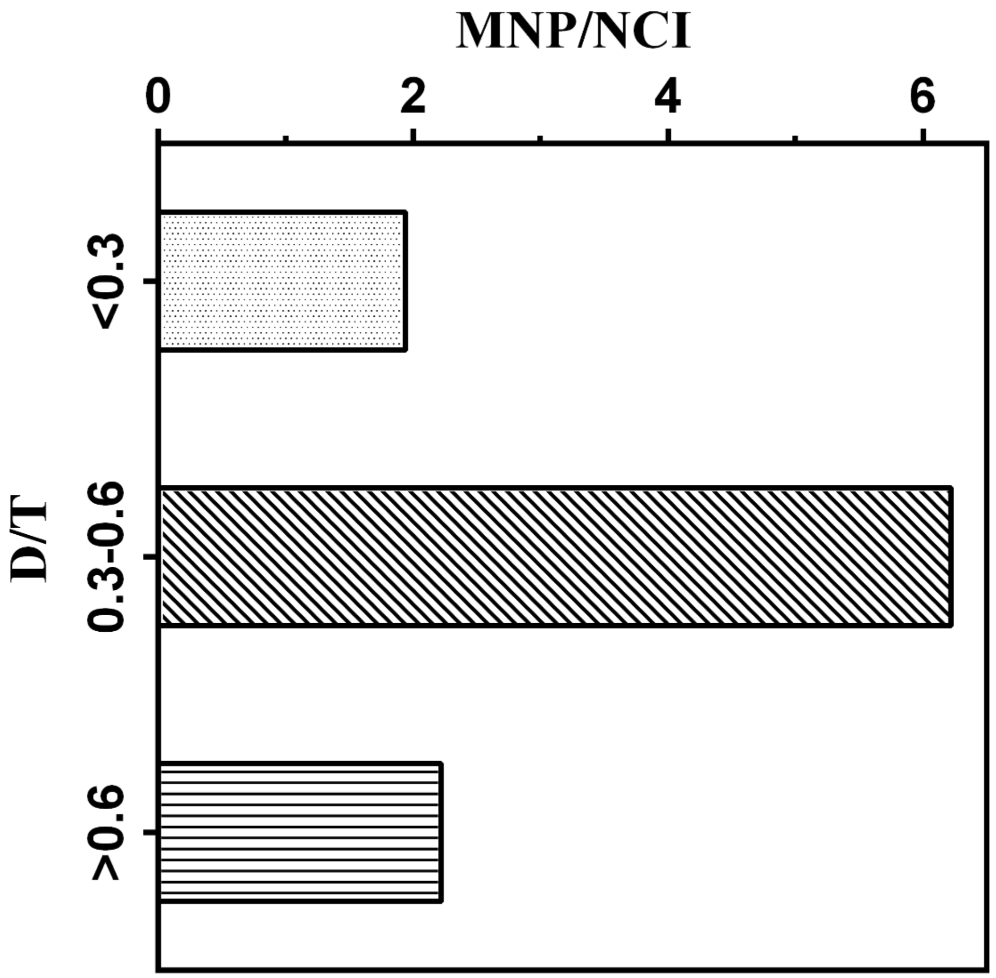

Figure 2-12.

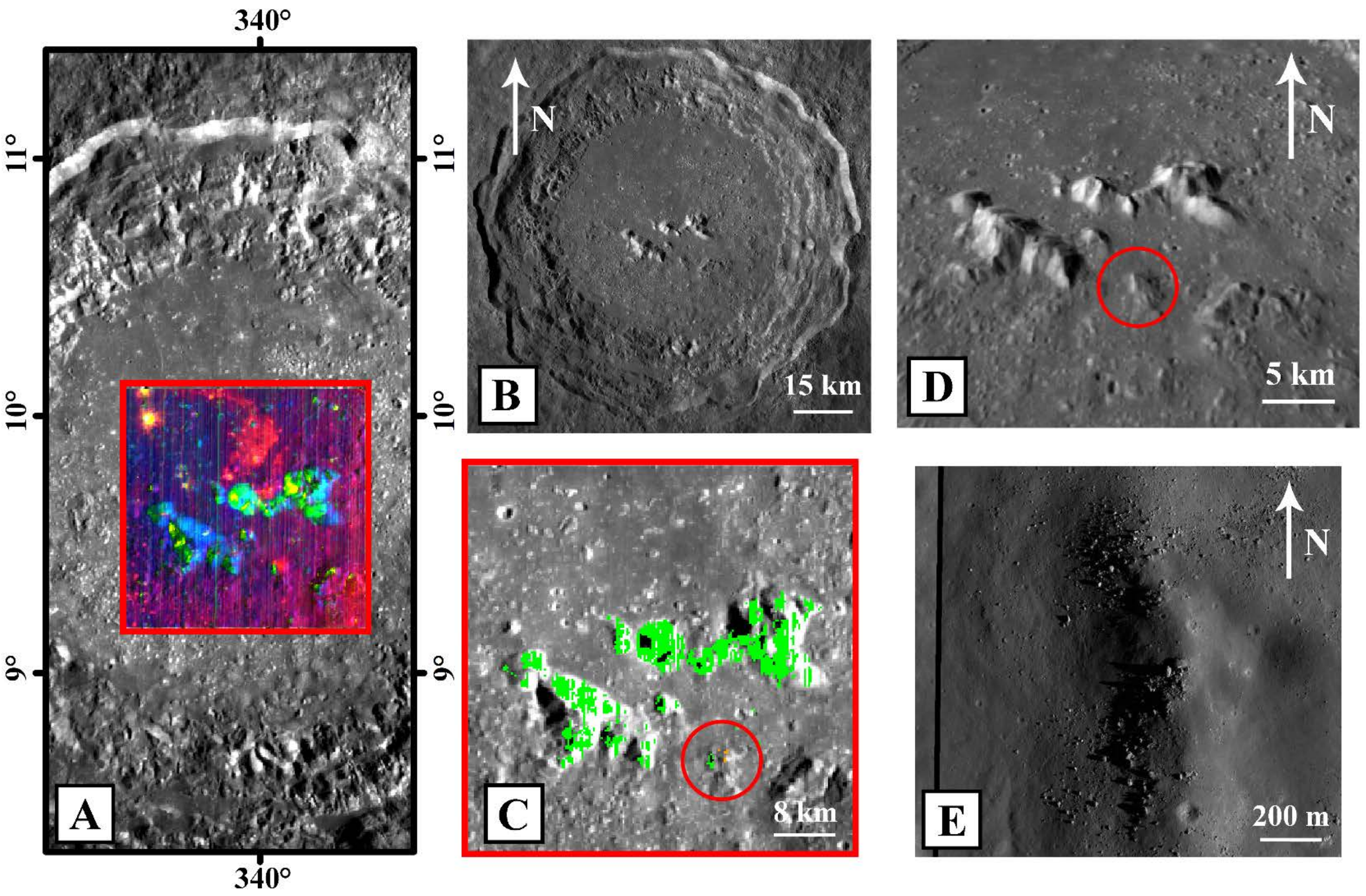

Figure 2-13.

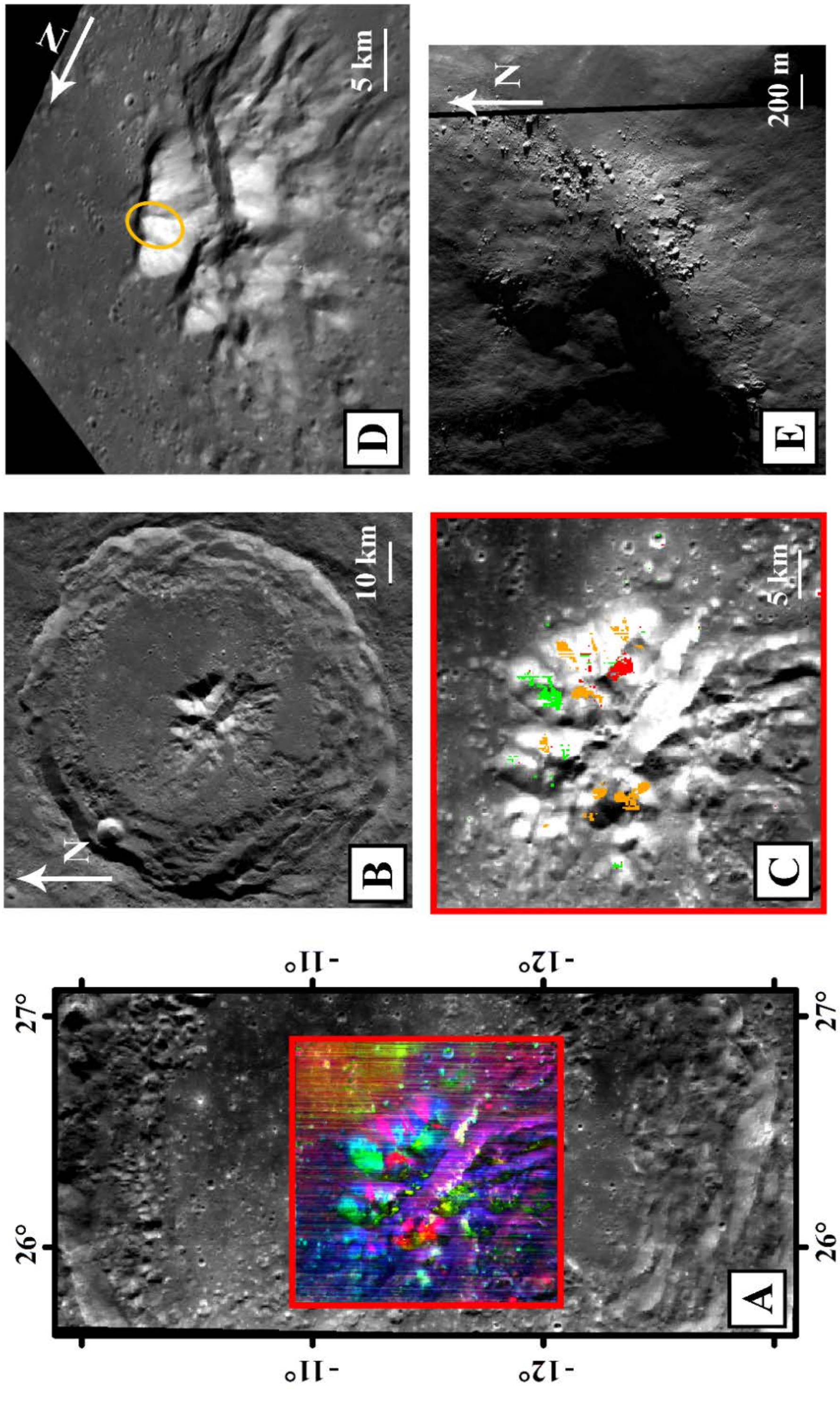

Figure 2.14.

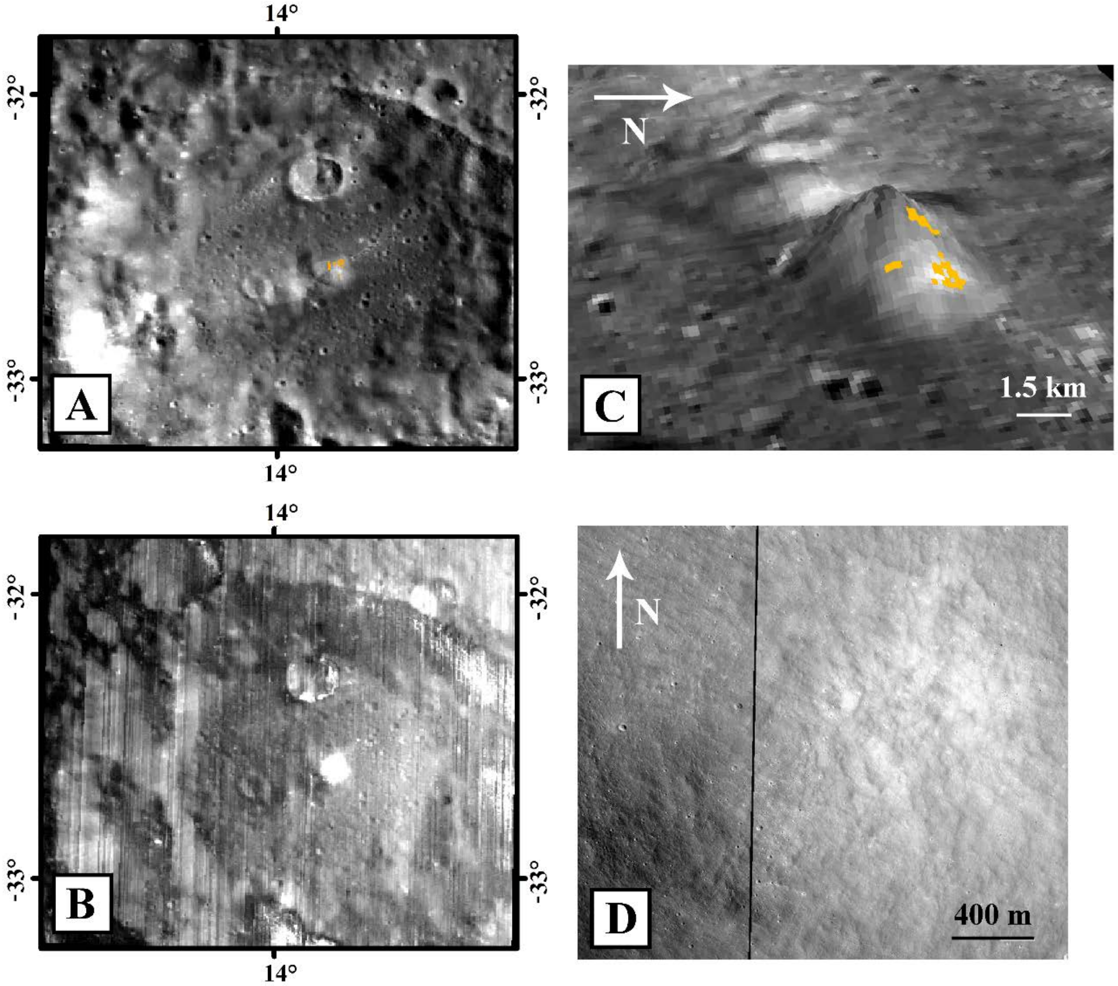

Figure 2-15.

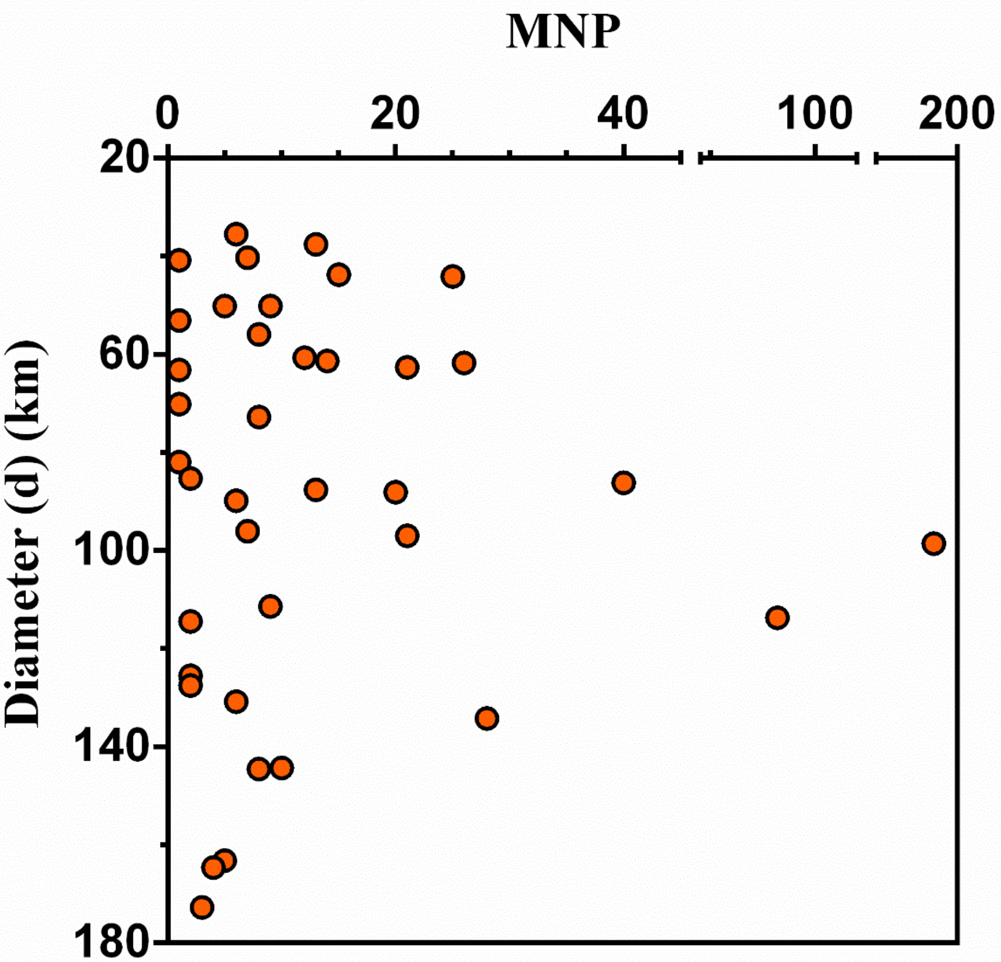

Figure 2-16.

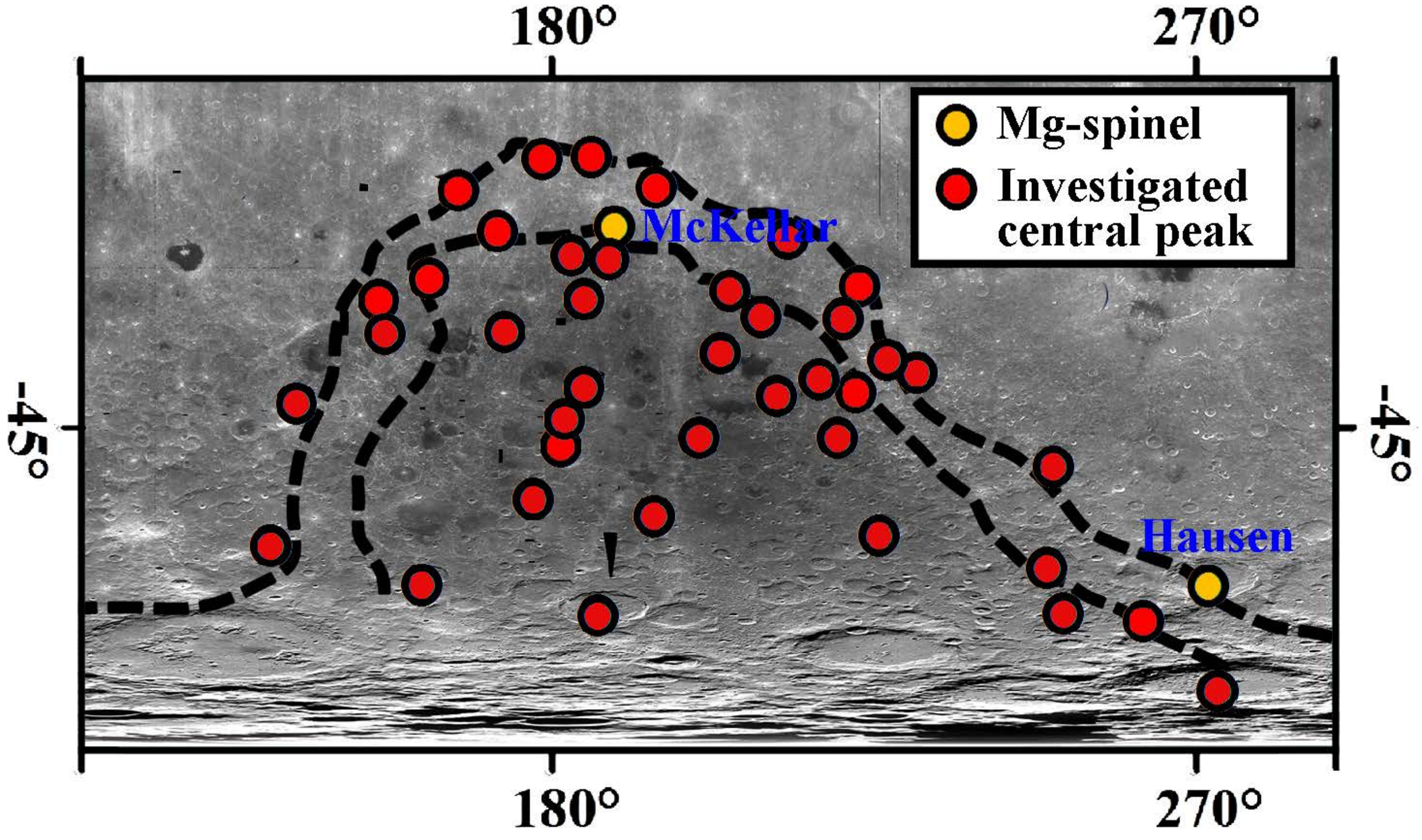
180°
270°
-45°
-45°
180°
270°
● Mg-spinel
● Investigated central peak
McKellar
Hausen

Figure 2-17.

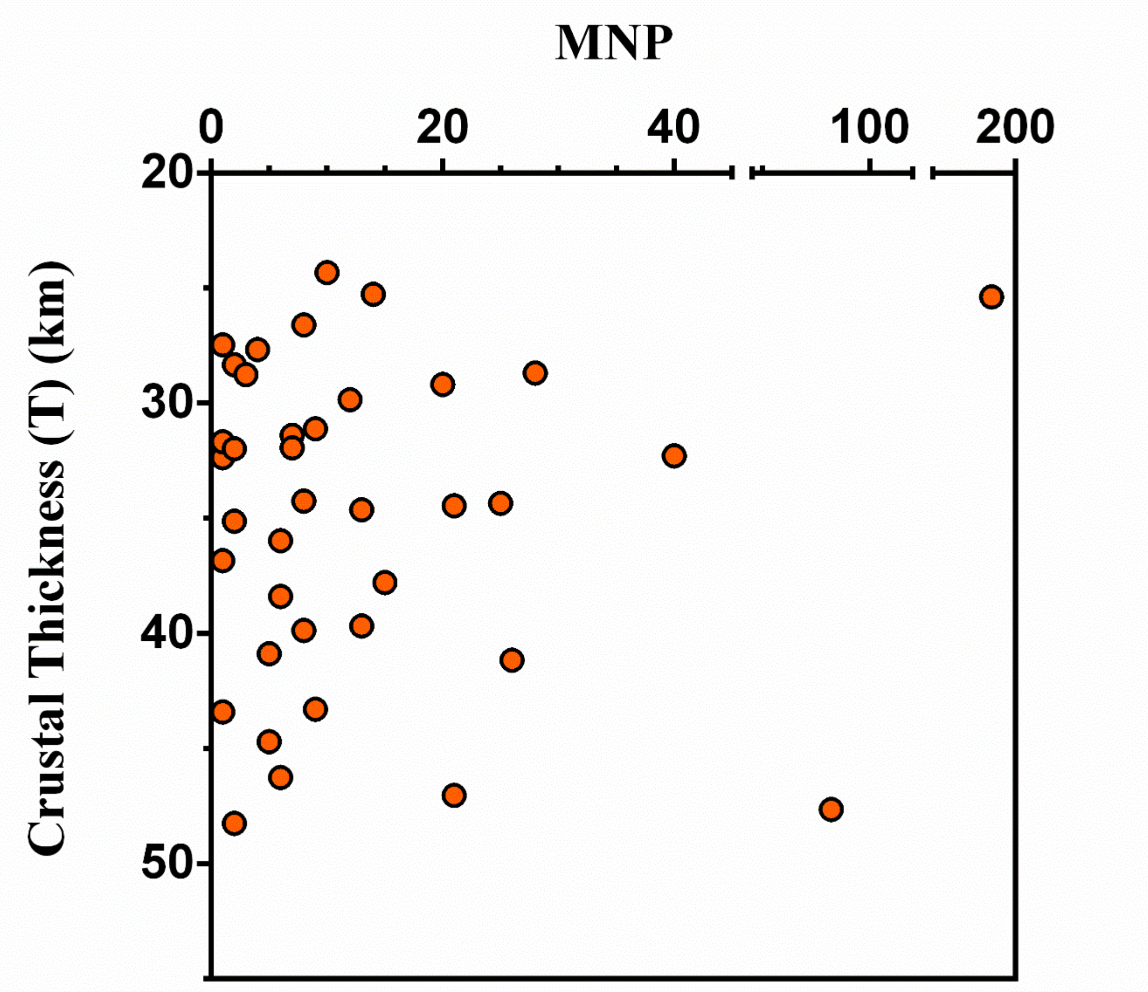

Figure 2-18.

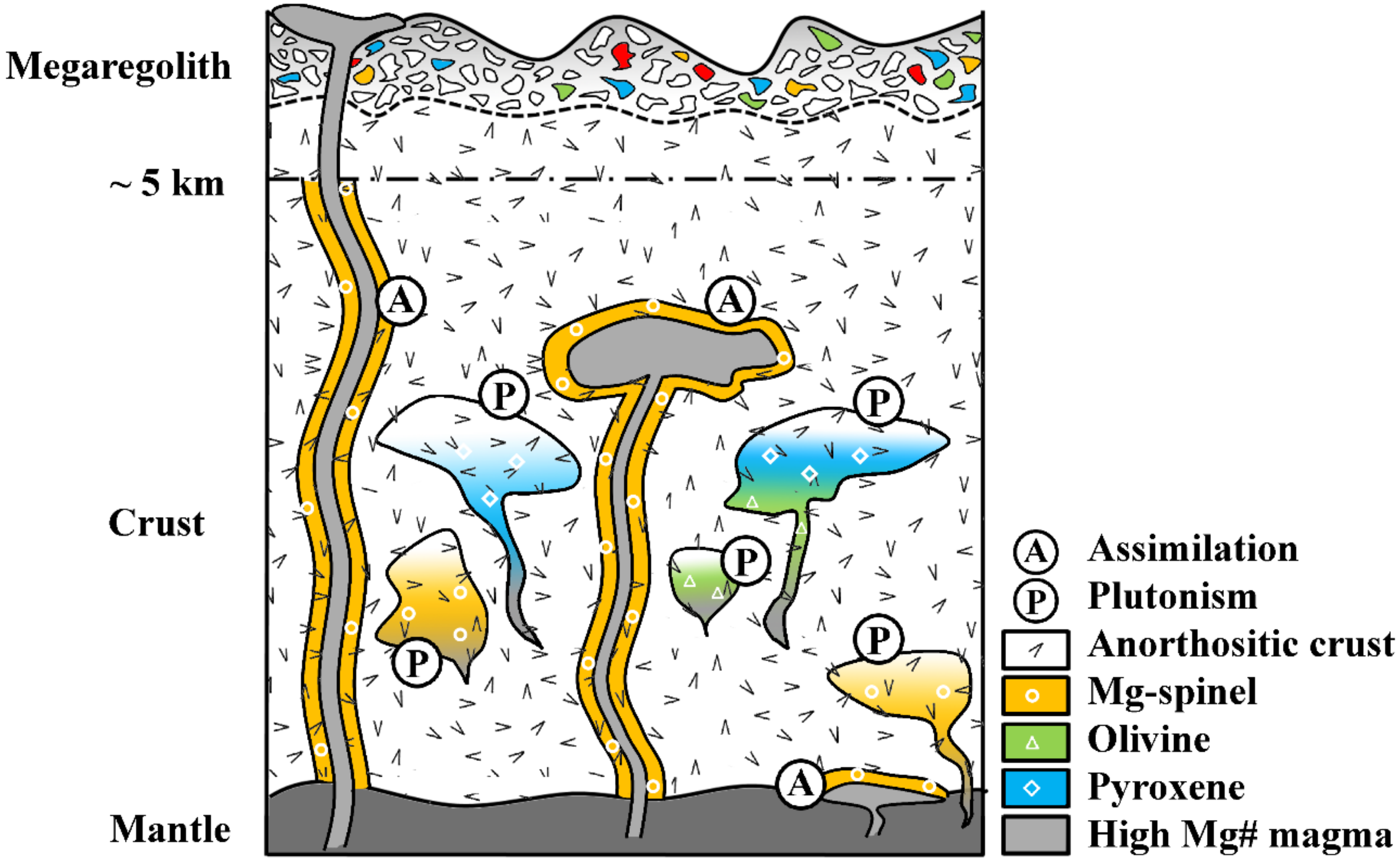
Megaregolith
~ 5 km
Crust
Mantle
A
P
A
Assimilation
P
Plutonism
Anorthositic crust
Mg-spinel
Olivine
Pyroxene
High Mg# magma

Figure 2-19.

References

Besse, S. et al., (2013). A visible and near-infrared photometric correction for Moon Mineralogy Mapper (M^3), *Icarus* 222(1), 229-242

Burns, R. G., (1993). Mineralogical Applications of Crystal Field Theory, 2nd ed., 551 pp., Cambridge Univ. Press, New York, doi:10.1017/CBO9780511524899.

Bhattacharya, S., et al., (2012). Mg-spinel-rich lithology at crater Endymion in the lunar nearside. In *39th COSPAR Scientific Assembly* (Vol. 39, p. 173).

Clark, R. N., et al., (2011). Thermal removal from near-infrared imaging spectroscopy data of the Moon, *Journal of Geophysical Research*, 116(E6) (2011).

Cintala, M. J., and Grieve, R. A. F., (1998). Scaling impact melting and crater dimensions: Implications for the lunar cratering record, *Meteoritics and Planetary Science*, 33(4), 889–912. doi:10.1111/j.1945-5100.1998.tb01695.x.

Cloutis, E. A., et al., (2004). Spectral reflectance-compositional properties of spinels and chromites: Implications for planetary remote sensing and geothermometry. *Meteoritics and Planetary Science,* 39(4), 545-565.

Dhingra, D., and Pieters, C. M., (2011). Mg-spinel rich lithology at crater Copernicus. *LPI Contributions*, 1646, 9.

Dhingra, D., et al., (2011a). Non-linear spectral un-mixing using Hapke Modeling: Application to remotely acquired M^3 spectra of spinel bearing lithologies on the moon. In *Lunar and Planetary Science Conference* (Vol. 42, p. 2431).

Dhingra, D., et al., (2011b). Compositional diversity at Theophilus Crater: Understanding the geological context of Mg-spinel bearing central peaks. *Geophysical Research Letters*, 38(11).

Gross, J., and Treiman, A. H. (2011). Unique spinel-rich lithology in lunar meteorite ALHA 81005: Origin and possible connection to M^3 observations of the farside highlands. *Journal of Geophysical Research: Planets* (1991–2012), 116(E10).

Gross, J., et al., (2014). Spinel-rich lithologies in the lunar highland crust: Linking lunar samples with crystallization experiments and remote sensing. *American Mineralogist*, 99(10), 1849-1859.

Hawke, B., et al., (2003). Hansteen Alpha: A volcanic construct in the lunar highlands. *Journal of Geophysical Research: Planets* (1991–2012), 108(E7).

Hiesinger, H., and Head, J. W., (2006). New views of lunar geoscience: An introduction and overview. *Reviews in mineralogy and geochemistry*, 60(1), 1-81.

Isaacson, P. J., and Pieters, C. M., (2010). Deconvolution of lunar olivine reflectance spectra: Implications for remote compositional assessment, *Icarus*, 210(1), 8–13, doi:10.1016/j.icarus.2010.06.004.

Jackson, C. R. M., et al., (2012). Compositional constraints on lunar spinel anorthosite: Synthesis of spinel with variable iron content. In *Lunar and Planetary Science Conference* (Vol. 43, p. 2335).

Jackson, C. R. M., et al., (2014). Visible-infrared spectral properties of iron-bearing aluminate spinel under lunar-like redox conditions†. *American Mineralogist*, 99(10), 1821-1833.

Jolliff, B.L., et al., (2000). Major lunar crustal terranes: Surface expressions and crust-mantle origins. Journal of Geophysical Research, 105:4197-4216

Kaur, P., et al., (2012). Compositional Diversity at Tycho Crater: Mg-Spinel Exposures Detected from Moon Mineralogical Mapper (M^ 3) Data. In *Lunar and Planetary Science Conference* (Vol. 43, p. 1434).

Kaur, P., and Chauhan, P., (2013a). Detection of Mg-Spinel Exposures from the Anorthositic Terrain Surrounding Mare Ingenii on the Far Side of the Moon. In *Lunar and Planetary Science Conference* (Vol. 44, p. 1547).

Kaur, P., and Chauhan, P., (2013b). Exposures of Mg-spinel on an evolved silicic lithology Hansteen Alpha on the Moon. In *Lunar and Planetary Science Conference* (Vol. 44, p. 1348).

Kaur, P., and Chauhan, P., (2014). Detection of spinel exposures from some near side locations of the Moon. In *Lunar and Planetary Science Conference* (Vol. 45, p. 2059).

Lal, D., et al., (2011). Identification of spinel group of minerals on central peak of crater Theophilus. In *Lunar and Planetary Science Conference* (Vol. 42, p. 1339).

Lal, D., et al., (2012). Detection of Mg spinel lithologies on central peak of crater Theophilus using Moon Mineralogy Mapper (M^3) data from Chandrayaan-1. *Journal of earth system science*, 121(3), 847-853.

Pieters, C. M., and McFadden L. A., (1994). Meteorite and asteroid reflectance spectroscopy: Clues to early solar system processes, *Annual Review of Earth and Planetary Sciences*, 22, 457–497, doi:10.1146/annurev.ea.22.050194.002325.

Pieters, C. M., et al., (2009). The Moon Mineralogy Mapper (M^3) on Chandrayaan-1. *Current Science*. 96, 500-505.

Pieters, C. M., et al., (2010). Identification of a new spinel-rich lunar rock type by the Moon Mineralogy Mapper (M^3). In *Lunar and Planetary Science Conference* (Vol. 41, p. 1854).

Pieters, C. M., et al., (2011). Mg-spinel lithology: A new rock type on the lunar farside. *Journal of Geophysical Research: Planets* (1991–2012), 116(E6).

Pieters, C. M., et al., (2013). Compositional evolution of the early lunar crust: observed diverse mineralogy of the upper and lower crust. In *Lunar and Planetary Science Conference* (Vol. 44, p. 2545).

Pieters, C. M., et al., (2014). The Second Conference on the Lunar Highlands Crust and New Directions. The distribution of Mg-spinel across the Moon and constraints on crustal origin. *American Mineralogist*, 99(10), 1893-1910.

Prissel, T. C., et al., (2012). Melt-wallrock reactions on the Moon: Experimental constraints on the formation of newly discovered Mg-spinel anorthosites. In *Lunar and Planetary Science Conference* (Vol. 43, p. 2743).

Prissel, T. C., et al., (2013). An “uncollected” member of the Mg-suite: Mg-Al pink spinel anorthosites and their place on the Moon. In *Lunar and Planetary Science Conference* (Vol. 44, p. 3066).

Prissel, T. C., et al., (2014a). Petrogenesis of the Lunar Highlands Mg-suite as told by Spinel. In *Lunar and Planetary Science Conference* (Vol. 45, p. 2514).

Prissel, T. C., et al., (2014b). Pink Moon: The petrogenesis of pink spinel anorthosites and implications concerning Mg-suite magmatism. *Earth and Planetary Science Letters*, 403, 144-156.

Schultz, P. H., and Gault, D. E., (1985), Clustered impacts: Experiments and implications, *Journal of Geophysical Research*, 90, 3701–3732, doi:10.1029/JB090iB05p03701.

Shearer, C. K., and Papike, J. J., (1999). Magmatic evolution of the Moon. *American Mineralogist*, 84, 1469-1494

Shirley, D. N. (1983). A partially molten magma ocean model. *Journal of Geophysical Research: Solid Earth* (1978–2012), 88(S02), A519-A527.

Srivastava, N., and Gupta, R. P. (2012). Compositional diversity inside Lowell Crater, Orientale Basin: Evidences for extensive spinel rich deposits. *LPI Contributions*, 1677, 55-56.

Srivastava, N., and Gupta, R. P. (2013). Spatial distribution of spinel in the Orientale Basin: New insight from M^3. In *Lunar Planetary Science Conference* (Vol. 44, p.1509).

Sunshine, J. M., et al., (2010). Hidden in plain sight: Spinel-rich deposits on the nearside of the Moon as revealed by Moon Mineralogy Mapper (M^3). In *Lunar and Planetary Science Conference* (Vol. 41, p. 1508).

Sun, Y., et al., (2013). Detection of Mg-Spinel Bearing Central Peaks Using M^3 Images. In *Lunar and Planetary Science Conference* (Vol. 44, p. 1393).

Taylor, L. A., and Pieters, C. M. (2013). Pink-spinel anorthosite formation: Considerations for a feasible petrogenesis. *In Lunar and Planetary Science Conference* (Vol. 44, p. 2785).

Treiman, A.H., et al., (2010). Magnesian anorthositic granulites in lunar meteorites in lunar meteorites Allan Hills 81005 and Dhofar 309: Geochemistry and global significance. *Meteoritics and Planetary Science*, 45, 163–180.

Treiman, A. H., et al., (2015). Lunar Rocks Rich in Mg-Al Spinel: Enthalpy Constraints Suggest Origins by Impact Melting. In *Lunar and Planetary Science Conference* (Vol. 46, p. 2518).

Vaughan, W. M., et al., (2013). Geology and petrology of enormous volumes of impact melt on the Moon: A case study of the Orientale basin impact melt sea. *Icarus*, 223(2), 749-765.

Vaughan, W. M., and Head, J. W., (2014). Impact melt differentiation in the South Pole-Aitken basin: Some observations and speculations. *Planetary and Space Science*, 91, 101-106.

Warren, P. H. (1985). The magma ocean concept and lunar evolution. *Annual Review of Earth and Planetary Sciences*, 13, 201-240.

Wieczorek, M. A., et al., (2013). The crust of the Moon as seen by GRAIL. *Science* 6120, 671–675. (doi:10.1126/science.1231530)

Yamamoto, S., et al., (2013a). Global distribution of Mg-spinel on the Moon revealed by SELENE spectral profiler. In *Lunar and Planetary Science Conference* (Vol. 44, p. 1768).

Yamamoto, S., et al., (2013b). A new type of pyroclastic deposit on the Moon containing Fe-spinel and chromite. *Geophysical Research Letters*, 40(17), 4549-4554.

Yue, Z., et al., (2013). Projectile remnants in central peaks of lunar impact craters. *Nature Geoscience*, 6(6), 435-437

CHAPTER 3

DISTRIBUTION AND ORIGIN OF OLIVINE ON THE MOON: NEW INSIGHTS FROM M^3 IMAGES OF CRATER CENTRAL PEAKS

Abstract

A systematic survey of olivine bearing crater central peaks on the global scale has been conducted with the Moon Mineralogy Mapper (M^3) images. The outcomes of this study show that ~5% of investigated central peaks contain olivine (Ol), and the olivine-rich areas are concentrated in the middle layer of the lunar crust underneath the Procellarum KREEP Terrane (PKT). Most of the Ol-bearing central peaks also contain crystalline plagioclase (Pl). Mg-spinel (Sp) and pyroxene (Px) have been detected in some Ol-bearing central peaks. Based on the observations in this study, three possible scenarios for the origin of olivine are thoroughly discussed including impact origin, mantle uplift, and magmatic origin. The scenarios of impact origin and mantle uplift cannot fully explain the observations of Ol-bearing central peaks. Therefore, we prefer the magmatic origin scenario and propose a hybrid magmatic scenario to unravel the petrogenesis of olivine in the central peaks. Procellarum basin and Insularum basin permanently thinned and fractured the crust in the PKT, which leads to a potential magma upwelling into the lunar crust. Either plutonic events or magmatic transportation could emplace the olivine-rich materials to relative shallow layers of the crust. Ultimately the olivine-rich materials were excavated by impact craters and rebounded to the central peaks. Further investigations of olivine are necessary to be conducted and could provide fundamental constraints on the petrogenesis of olivine on the Moon.

1. Introduction

Olivine is one of the most common minerals in rocks of the lunar crust and mantle. It is typically the earliest mineral to crystallize from a mafic magma and provides significant records of the chemistry of its parent magma as well as early geological evolution of the Moon due to differentiation, melting and impact modification.

The presence of olivine was first identified in lunar soils, mare basalts, Mg-suite rocks, anorthosites, breccias and glasses [Heiken et al., 1991]. It was found in fine-grained lunar basalts where it amounts to 7% of the Apollo 11 rocks, and is as much as 55% of some Apollo 12 rocks [Levinson et al., 1971].

Olivine exhibits a wide and strong absorption feature at 1000 nm, which is the spectroscopic basis for detection of olivine using the visible and near infrared spectroscopy. Early examples for spectroscopic detection of olivine are the Earth-based telescopic observations in Aristarchus crater [Hawke et al., 1983; Lucey et al., 1986] and Copernicus crater [Pieters, 1982; Pieters and Wilhelms, 1985; Smrekars and Pieters, 1985; Pinet et al., 1993]. In contrast to low spatial resolutions of telescopic observations, Clementine multispectral images provide high-resolution spacecraft data to determine the distribution of olivine on the lunar surface, and were used for detection of olivine in Copernicus crater in several investigations [e.g., Pieters et al., 1994; Mouelic and Langevin, 2001] as well as in the Aristarchus area [Mouelic et al., 1999]. Tompkins and Pieters [1999] identified other possible olivine-bearing areas including Theophilus, Langrenus, Tsiolkovsky, Keeler, and Crookes with Clementine UVVIS data. Using Clementine UV-VIS and near infrared (NIR) images, Lucey (2004) derived a global mineral map from Clementine UVVIS-NIR images revealing olivine-rich areas within the western regional mare basalts (WRMB).

Nevertheless, low spectral resolutions of multispectral images could lead to a potential erroneous inference regarding the identification of olivine. Hyperspectral data permit a relatively accurate assessment of olivine distribution. Results from analyzing the Selenological and Engineering Explorer (SELENE) Spectral Profiler (SP) data indicate the central peaks of Tsiolkovsky crater are mixtures of plagioclase and pyroxene [Matsunaga et al., 2008] rather than olivine-rich rocks [Pieters and Tompkins, 1999]. The first global detection of olivine-rich locations with SP data was conducted by Yamamoto et al. [2010], and provided new clues to the distribution of olivine on the lunar surface. Yamamoto et al. [2010] suggested that most of the identified olivine-rich sites are concentrated on the lunar nearside and primarily associated with impact basins. Other recent studies with the Moon Mineralogy Mapper (M^3) images have validated previous results for the detection of olivine, and shown new locations for the presence of olivine. For example, the presence of olivine in Aristarchus was definitized with M^3 images [Mustard et al., 2011; Wiseman et al., 2012], and four other olivine-rich regions (a small crater near Mare Moscoviense, the Copernicus central peaks, Aristarchus, and the crater Marius in the Marius Hills) were identified and analyzed with images of the same type [Isaacson et al., 2011]. Using M^3 images, similar work was conducted at the rim of Crisium basin [Powell at al., 2012]. All these studies of using M^3 data to detect olivine are limited to local scales, a global investigation has not been conducted through such an investigation could provide critical constraints on the origin of olivine on the Moon.

The origin for remotely detected olivine has been a debated issue for decades. Pieters [1982] suggested three possible sources of olivine in the Copernicus region including early lunar differentiation cumulates in the mantle, magma chamber in the crust, or either of above relocated by an earlier event. These possibilities were refined by Pieters and Wilhelms [1985] who proposed the origin of olivine at the Copernicus crater is ascribed to regional crust thinning as a result of the formation of the Procellarum and Insularum impact basins, and the excavation of the Copernicus impact to the olivine-rich materials which originated from a pluton or other intrusions in the lunar crust. Pinet et al. [1993] supported this interpretation but suggested a large diameter pluton underneath the Copernicus should be required. On the other hand, most of the current studies consider the lunar mantle as the sources of olivine [e.g. Yamamoto et al., 2010]. Yamamoto et al. [2010] observed that olivine-rich areas are mostly associated with large impact basins or thin crust and lack of plagioclase surrounding the olivine exposures and suggested the identified olivine-bearing materials be dunite. Therefore, Yamamoto et al. [2010] favored a mantle origin of olivine and proposed olivine-rich materials were excavated from the lunar mantle by basin formation impacts. Moreover, Yue et al. [2013] suggested the olivine observed in the central peaks could be projectile remnants based on numerical simulation of impact cratering processes.

In order to help resolve the uncertainty surrounding the origin of the lunar olivine, a global survey of lunar crater central peaks is conducted with M^3 images. The objectives of this study are 1) to investigate the lateral and vertical distributions of olivine in the lunar crust, 2) to examine the olivine distribution in the framework of each of above mentioned hypotheses and determine their validity, and 3) to propose the most possible petrogenesis of olivine on the basis of the observations in this study.

2. Approach

The data and methods used in this study have been described in detailed in Sun et al.

[2015], a brief description is given below. Lunar crater central peaks commonly rebounded from deep-seated layers (the lunar crust and the upper mantle) of the Moon, and they provide a practical approach to investigation of the compositional variation in the lateral and vertical dimensions of the lunar interior. 166 lunar crater central peaks (Figure 3-1) out of 1559 craters in the USGS crater database were selected based on crater diameter (larger than 35 km), the presence of obvious peak topography on the basis of Lunar Orbiter Laser Altimeter (LOLA) elevation data, the availability of M^3 L2 (level 2) reflectance images and the presence of significant spectral absorption features. Each central peak was observed with high spatial resolution images at most 0.5 meters per pixel (Lunar Reconnaissance Orbiter (LRO) Wide Angle Camera (WAC) and/or Narrow Angle Camera (NAC) images (http://target.lroc.asu.edu/q3/)) to make sure the investigated areas are fresh and undisturbed and represent deep pristine materials from the lunar crust or the upper mantle. The selected 166 craters are from ~35.1 km to ~199.5 km in diameter (d), and the origin depth (D) of central peak ranges from ~5.05 km to ~33.21 km based on $D=0.109*d^{1.08}$[Cintala and Grieve, 1998]. M^3 L2 multi-temporal images for 166 craters were geometrically corrected and smoothed for noise reduction. Pixels with negative reflectance values or within shadow were eliminated. The spectra were smoothed with a moving window average and retained 72 bands from 540 nm to 2537 nm which is sensitive to spectrally diagnostic absorptions of minerals for further analysis.

Continuum removal was applied to each image spectrum to isolate mineral diagnostic absorption features from the spectral continuum for olivine detection. Olivine typically has a broad multiple absorption feature near 1050 nm which is caused by crystal field transitions of Fe^{2+} ions located in two distorted octahedral crystallographic sites (the M1 and M2 sites) [Burns, 1993]. In order to reduce the influence of the inherent noise and residue of imperfect thermal and photometric correction in M^3 data, thresholds of absorption depth and multi-temporal images have been applied in this study. When the detected pixel exhibited the spectral feature with the absorption depth larger than 0.05 around 1050 nm and less than 0.02 around 2000 nm, this pixel was determined as the potential Ol-bearing pixel. These criteria have been implemented in Interactive Data Language (IDL) for automatic detection of olivine with a large volume of M^3 images. The spectral shape and reflectance magnitude cannot be taken into account in automatic detection with IDL. Thus, manual verification for each potential olivine-bearing pixel is necessary to obtain reliable results. During the manual verification, the pixels that showed both high albedo and a broad absorption feature around 1050 nm were determined for multi-temporal images of each crater and were retained for further comparison. Detections for each central peak with multi-temporal M^3 images could result in different numbers of olivine-bearing pixels. When this occurred, the minimum value of manually retained pixels (MNP) for each crater central peak was used to represent the likelihood of the presence for olivine. The final identified Ol-bearing pixels were expected to represent relatively pure olivine because spectra for mixtures of olivine and pyroxene are disproportionately dominated by pyroxene. The lack of a detectable absorption feature around 2000 nm indicate that the pyroxene is likely less than 5% [Pieters, 1982]. Meanwhile, the identified high albedo pixels eliminates the spectra which may represent Fe-Ti glass rather than olivine. However, the presence of plagioclase is hard to be isolated when plagioclase forms mixtures with olivine because the spectral absorption of the former is more easily masked by the latter [e.g. Cheek and Pieters, 2014]. Therefore, the identified olivine-bearing pixels are most likely to represent pure olivine with an uncertain portion of plagioclase, at least without a significant amount of other mafic materials.

The presence of crystalline plagioclase (Pl), Mg-spinel (Sp), orthopyroxene (Opx) and clinopyroxene (Cpx) in Ol-bearing central peaks were also determined by use of the method described in Sun et al. [2015]. The Pl represents the composition of the primitive lunar crust, and pyroxene (Px) exhibits the high likelihood of presence in Mg-suite rocks which are related to the post-LMO magmatism. The new mineral, Mg-spinel, represents a new member of Mg-suite rocks based on its distribution and Mg-suite related petrogenesis (Chapter 2). Therefore, the relations of these minerals to olivine could provide important arguments for supporting or rejecting an olivine origin hypothesis.

Additionally, integrated band depth (IBD) images were derived and used as an auxiliary indicator for mineral detection. IBD1000 was derived from 27 channels within the 750 - 1309 nm region of M^3 data and IBD2000 within the 1528 - 2537 nm region. IBD is the summation of the band depth for every spectral channel. False color composite images were created to illustrate major mineral absorptions (red: IBD1000; green: IBD2000; blue: reflectance at 1508 nm). In this composite, olivine and crystalline plagioclase appear largely red, Mg-spinel are bright green, and pyroxene is shown in various colors such as yellow, light green, and cyan (e.g. Figure 3-5A).

In order to determine the vertical distribution of olivine in the lunar crust, the ratio D (origin depths of central peaks) to T (average crustal thickness of crater central peaks derived from Gravity Recovery and Interior Laboratory (GRAIL) data) was used to describe relative position of olivine existence in the lunar crust [Sun et al., 2015].

3. Results

14 olivine-bearing central peaks have been identified out of 166 investigated craters in this study shown in Figure 3-1. A typical continuum removed M^3 spectrum for each olivine-bearing crater central peak shows a broad absorption band near 1050 nm but weak absorption around 2000 nm (Figure 3-2). The information about 14 olivine-bearing central peak is tabulated in Table 3-1 including coordinates, crater diameter (d), origin depth of central peak (D), crustal thickness (T), co-existence minerals, probably associated basin, and excavation depth of associated basin. The results are presented in the following four sections. First, an example crater central peak (Theophilus) is given to illustrate the result of olivine identification. Second, the lateral and vertical variations of olivine in the crust are described in two sections respectively. The final section depicts the co-existence of olivine with other minerals.

3.1. Example crater: Theophilus

The Theophilus crater has a diameter of ~98 km and is located in the northwest of the Nectaris basin, which overlaps the north rim of crater Cyrillus (Figure 3-3). The petrological diversity of the Theophilus central peaks was observed with remote sensing techniques. Tompkins and Pieters [1999] suggest the central peaks of Theophilus are mostly composed of anorthosite with small amounts of troctolite. 25.3% of olivine in the Theophilus central peaks was determined based on radiative transfer modeling with Clementine images [Cahill et al., 2009]. Later, the presence of olivine in the Theophilus central peaks was identified using SELENE SP data in a global olivine survey [Yamamoto et al. 2010]. Recently the central peak of Theophilus attracted much attention because of the discovery of Mg-spinel using M^3 images [Dhingra et al., 2011; Sun et al., 2013; Pieters et al., 2014].

Shown in Figure 3-4 are the olivine detection results for the central peak of Theophilus using two M^3 reflectance images (M3G20090203T160452_V01_RFL.IMG, M3G20090731T045352_V01_RFL.IMG). 237 Ol-bearing pixels were identified with the first image and 105 Ol-bearing pixels with the second image, then based on the MNP principle the likelihood of present for olivine in Theophilus central peak is 105 rather than 237. The detailed images for Theophilus central peak are shown in Figure 3-5. The IBD image overlays the M^3 reflectance image at 750 nm (Figure 3-5A) to demonstrate the compositional diversity of Theophilus central peaks where Ol-bearing materials are abundant. Figure 3-5C shows our olivine detection results which are in agreement with hints of IBD image but are more accurate than IBD. Ol is mainly concentrated on one north peak and co-existing with Sp. The 3D view and high spatial resolution LRO NAC image of Theophilus central peaks are displayed in Figure 3-5D and 5E. The significantly uplifted topography and the clear outcrops indicate this central peak is undisturbed and could represent the deep-seated materials excavated by Theophilus crater.

Pl has been identified in the peak on the east where is marked as a red circle in Fig 5C. The co-existence of Ol with Pl could be interpreted as a plutonic layer intruded into anorthositic crust and then both Ol and Pl were excavated by Theophilus crater to the surface and emplaced in the central peaks. However, the Theophilus region (Figure 3-3) experienced multiple excavation events (Nectaris basin, Cryillus crater and then Theophilus crater). The Cryillus (98.09 in diameter) has a similar crater diameter to Theophilus and could excavate similar materials from the same depth. However, only spectral featureless materials were detected with M^3 in the Cryillus central peak. The peak compositional difference between Theophilus and Cryillus central peaks could be due to 1) the sub-Theophilus plutonic intrusion is too small to be excavated by Cryillus, or 2) the Cryillus central peak was disturbed by resurfacing processes such that olivine and other materials cannot be detected spectrally. Furthermore, the availability of M^3 data could lead to a potential inaccurate detection because the Cryillus central peak is not entirely covered by M^3 data.

3.2. Lateral variations

For lateral variations, Ol-bearing crater central peaks are sparsely distributed on the Moon (Figure 3-1). Most of the Ol-bearing central peaks are concentrated within Procellarum KREEP Terrane (PKT), and seven of them located surrounding impact basins. The presence of olivine has been identified in the central peaks of three craters within Feldspathic Highlands Terrane (FHT). However, olivine-bearing central peaks are not observed in South-Pole Aitken Terrane (SPAT), which is in line with the global olivine map derived with Clementine data (Lucey, 2004).

3.2.1. Olivine in PKT

Consistent with observations in Lucey [2004] and Staid and Pieters [2001], our results clearly demonstrate that Ol-bearing locations are concentrated on the WRMB area (Figure 3-1). This result is also in agreement with Yamamoto et al. [2010] who suggested most of the olivine-rich sites are associated with impact basins on the nearside of the Moon. Based on our olivine detection results, the central peaks of Copernicus, Eratosthenes and Theophilus show an extremely high likelihood of presence for Ol. Copernicus and Eratosthenes are close to the Imbrium basin (Figure 3-6), and Theophilus is around Nectaris basin (Figure 3-3). Theophilus has been described in 3.1; the description below is focused on the results for Copernicus and Eratosthenes.

Copernicus (~96 km in diameter) is a young complex crater located in the south of the Imbrium basin (Figure 3-6). The presence of olivine has been identified in Copernicus region with numerous studies using telescopic [e.g., Pieters, 1982; Pieters and Wilhelms, 1985] and spacecraft observations [e.g., Pieters et al., 1994; Le Mouélic and Langevin, 2001; Cahill et al., 2009; Bugiolacchi et al., 2011]. Ol-bearing lithology in the Copernicus central peaks was discovered using Earth-based telescopic data [Pieters, 1982]. Later, this finding was confirmed with multispectral images including Clementine data [e.g., Pieters et al., 1994; Cahill et al., 2009] and SELENE MI data [Arai et al., 2011]. Recently, the studies with hyperspectral data also demonstrate that the olivine-rich central peaks exist in crater Copernicus [e.g., Yamamoto et al., 2010; Dhingra et al., 2014; Sun and Li, 2014]. The detection results from this study are consistent with previous findings. A large number of olivine-bearing pixels have been identified in the Copernicus central peaks (Figure 3-7). Almost all the central peak areas show red color in the IBD image (Figure 3-7A) indicating the presence of strong absorption around 1 μm but weak or no absorption around 2 μm. The LRO WAC mosaic image of the crater Copernicus is shown in Figure 3-7B. Figure 3-7C displays our olivine detection results in green color which imply an extremely high likelihood for olivine presence in Copernicus central peaks. Nearly all central peak areas are covered by Ol-bearing materials including peaks and hillsides which exhibit obviously uplifted topography and the undisturbed feature (Figure 3-7D and Figure 3-7E). In addition to Ol, a small amount of Sp-bearing materials has been detected which provides critical clues to the petrological diversity of Copernicus central peaks. This finding is in agreement with previous studies [Dhingra and Pieters, 2011, Sun et al., 2013].

Eratosthenes is a ~59 km crater that lies on the boundary between Mare Imbrium and Mare Sinus Aestuum. Eratosthenes is overlain by the rays from crater Copernicus to the southwest. The central peak of Eratosthenes has been observed with telescopic data and was likely to dominate by pyroxene [Pieters, 1982]. Tompkins and Pieters [1999] re-examined the composition of the Eratosthenes central peaks with Clementine images and pointed out the possibility of presence for olivine. A recent study about mineral detection using Diviner data revealed the olivine-rich composition in the central peaks in addition to a small proportion of pyroxene or plagioclase [Song et al., 2013]. The high likelihood for the Ol presence has been determined in the central peaks with M^3 images in this study (Figure 3-8). The Ol-bearing materials are present in the east peak and along the ridge of the west peak mountain (Figure 3-8A and Figure 3-8C). Taking the eastern peak as an illustration, the high spatial resolution image (LRO NAC) (Figure 3-8E) reflects high albedo and fresh outcrop which indicate the materials in this peak definitely originate from deep layers. Very limited amounts of Pl (only 2 pixels) and Cpx are detected in the Eratosthenes central peaks. The crater Eratosthenes is close to Copernicus and both of them show high possibility for Ol presence in the central peaks, which indicates the Ol in the central peaks of these two craters may share the same source as the Ol in sub-Copernicus layer.

Apart from central peaks in Copernicus, Eratosthenes and Theophilus, other identified Ol-bearing materials in the central peaks of Bianchini, Gassendi, Humboldt, Macrobius, Petavius, Philolaus, Schluter within PKT are determined to have a low likelihood for olivine presence (even less than 10 pixels) as shown in Table 3-1.

3.2.2. Olivine in FHT

Three Ol-bearing central peaks have been discovered in crater Jackson (3 pixels), Kovalevskaya (4 pixels) and Keeler (4 pixels) within FHT in this study. This is in disagreement with the observations of global olivine detection using SELENE SP data [Yamamoto et al., 2010] which is probably due to low spatial resolution (~1.7 km footprints at the equator) of SP data.

Jackson is a ~71 km diameter impact crater that is located in the northern hemisphere on the far side of the Moon (Figure 3-9). The crater central peak of Jackson was interpreted to contain 80-90% plagioclase with pyroxene and olivine with Clementine images [Tompkins and Pieters, 1999]. Cahill et al. [2009] suggested the Jackson crater central peak contains 10.5% olivine based on a quantitative analysis with Clementine images. In this study, 3 olivine-bearing pixels have been identified in one peak on the north as shown in bright red in Figure 3-9A and green in Figure 3-9C. The presence of Pl was also detected in the same peak which is in line with the observations of SELENE SP data [Matsunaga et al., 2008].

Kovalevskaya is a complex crater located on the lunar farside and ~109 km in diameter (Figure 3-10B). The outer rim is generally well-formed, and the inner walls are composed of terraces and slumped shelves. There is a set of obvious peaks at the center of Kovalevskaya crater. Spectral analysis of 109 central peaks with Clementine multispectral data revealed that the Kovalevskaya crater central peaks are dominated by anorthosite and gabbroic-noritic-troctolitic anorthosite with 80-90% plagioclase [Tompkins and Pieters, 1999]. In this study, the presence of olivine has been identified in one small peak in the northwest of the Kovalevskaya central peaks (Figure 3-10C). This small olivine-bearing peak can also be observed as rock outcrops using the LRO NAC image (Figure 3-10E). Meanwhile, the presence of Pl was found on the west side of the south end peak and marked as the red circle in Figure 3-10C. Mg-spinel has been detected in all peaks of this area [Sun et al., 2013] along with Opx and Cpx. All of the above observations indicate the compositional diversity of Kovalevskaya central peaks.

Keeler is a large lunar crater of ~158 in diameter and located on the lunar farside. The presence of olivine in Keeler central peak was first suggested by a global petrology survey of central peaks using Clementine data [Tompkins and Pieters, 1999]. The model abundance of olivine was estimated as 13% by Cahill et al. [2009]. However, Yamamoto et al. [2010] argued against the presence of olivine in Keeler central peaks with SELENE SP observation. In contrast, our results demonstrate Ol indeed exists in the northwest hillside of Keeler central peaks in spite of low likelihood for the presence (4 pixels) (Figure 3-11). This paradox is probably caused by the different spatial resolution of SP and M^3. The average interval between SP footprints is ~1.7 km at the equator, but the spatial resolution of M^3 is at least 280 m. Apparently, M^3 data could lead to more accurate assessment than SP. In addition, a large number of Pl bearing pixels have been identified in the central peak of Keeler, which may represent the primitive composition of the lunar crust.

All three olivine bearing central peaks in FHT possess a kind of commonality which is the presence of a considerable amount of Pl and a small amount of Ol. This is in accord with the geochemical signature of FHT (high Al_2O_3 but low FeO) [Jolliff et al., 2001].

3.2.3. Olivine in SPAT

Our results indicate that no Ol-bearing central peak was identified in SPAT. Figure 3-

12 shows all the investigated crater central peaks in SPAT. The investigated craters are distributed all over the SPAT, meaning that the detection result in this study is representative. Materials within SPAT are supposed to represent the deep-seated composition from the lower crust or upper mantle. A thorough discussion has been performed regarding the vertical compositional trend of the lunar crust and upper mantle in Sun et al. [2015]. Sun et al. [2015] suggest a global primitive anorthosite layer present in the lower crust and the composition of the upper mantle is most likely to be orthopyroxene rather than olivine. All Opx-bearing central peaks identified in Sun et al. [2015] are shown in Figure 3-12 suggesting the primary composition in SPAT is Opx. Results from this study support the same conclusion that the upper mantle is primarily Opx rather than Ol as in Sun et al. [2015]. Alternatively, the materials in SPAT likely represent impact melts rather than the original composition of the Moon or the mixture of upper mantle and impact melts.

3.3. Vertical variations

Results from this study indicate Ol exists in the lunar crust from ~5.48 km to ~33.21 km. Comparison the MNP of Ol for each central peak with the D/T ratio is shown in Figure 3-13 and reveals most of the Ol-bearing central peaks originated from roughly 10 to 20 km depths (D/T: 0.3~0.6), three Ol-bearing central peaks are from shallow layers (D/T<0.3) and four from deep layers (D/T>0.6). Among 14 Ol-bearing craters, 12 excavated a depth above the crust-mantle interface based on the estimation of crustal thickness derived from GRAIL data with the exceptions of Petavius and Humboldt.

Crater Petavius is ~184 km in diameter and located to the southeast of the Mare Fecunditatis. Previous investigations suggested that the Petavius central peak consist of anorthosite [Pieters, 1986; Hawke et al., 1995]. Song et al. [2013] also demonstrated the Petavius central peak mainly contained anorthosite using the CF value derived from Diviner data. In this study, 7 olivine bearing pixels were identified in a north peak of this crater (Figure 3-14). Quite a few Pl bearing pixels were found simultaneously and were distributed on every peak, which is consistent with previous studies.

Humboldt is a large lunar crater with ~200 km in diameter and is close to Mare Australe. Multiple central peaks form a range in the north and a group of central peaks in the south (Figure 3-15D). CF values for Diviner data indicate the composition of Humboldt central peaks shows little evidence for mafic materials and is more anorthositic [Song et al., 2013]. The detection results from this study are apparently in accord with the results from the analysis of the Diviner data. The Ol-bearing materials are concentrated on a small peak of the north peak range (Figure 3-15). A large amount of Pl is determined for both the south peaks (red circle in Figure 3-15C) and along the ridge of the north peak range.

The central peaks of both Petavius and Humboldt were not been detected for a large number of Ol-bearing materials, which is not unexpected, but Pl was identified to be abundant. It is highly plausible that the materials excavated by the craters Petavius and Humboldt may not come from the lunar mantle composition due to the estimated local crustal thicknesses for them were smaller than the actual values. Alternately, if the craters Petavius and Humboldt indeed penetrated to the upper mantle, the detected composition for the central peaks of these two crater indicates that the upper mantle lacks olivine, which is in line with the speculation based on the observation made for SPAT (3.2.3).

3.4. Co-existence of olivine with other minerals

Regarding the coexistence of Ol with other minerals (Pl, Sp, and Px), nine olivine-bearing central peaks contain Pl, and three of them show the occurrence of Ol and Pl without Px. The Humboldt central peaks exhibit the highest likelihood of presence for Pl. All nine central peaks bearing both Ol and Pl originated from relatively deep layers larger than ~10 km (the minimum value of D/T is 0.28).

Among 14 Ol-bearing central peaks, 10 were detected to show the presence of Px. In addition, six of the Ol-bearing crater central peaks are identified to contain Sp, indicating that Sp and Ol don't have to coexist and the abundances of these two mineral do not have to be proportional [Sun et al., 2013].

4. Petrogenesis of olivine

Currently three scenarios have been proposed to explain the petrogenesis of olivine on the Moon, which include the impact origin [Yue et al. 2013], mantle uplifting [e.g. Pieters and Wilhelms, 1985; Yamamoto et al., 2010] and the magmatic origin [e.g. Pieters and Wilhelms, 1985]. The following discussion is focused on determining which scenario is most plausible.

4.1. Scenario A: impact origin (projectile remnants)

Yue et al. [2013] proposed that the source of olivine in the central peaks could be the projectile remnants. Based on their impact simulation model, a dunite projectile is almost vaporized and little can survive from an impact if the projectile speed is above 14 km/s. In contrast, most of the projectile could survive if the impact velocity is less than 12 km/s, the projectile remnant can be highly fractured but not vaporized. Meanwhile, the numerical simulations of asteroid orbital evolution revealed that approximate 25% of lunar impacts occur at speeds below 12 km/s. [Bottke et al., 1996; Minton and Malhotra, 2009]. Thus, a prominent portion of impactor materials could remain in the crater central peaks. Therefore, Yue et al. [2013] concluded that the olivine observed in the crater central peaks may not originate from the Moon and could be exogenic.

If we assume the impact origin scenario is correct, a large number of olivine-bearing central peaks should be observed. However, only 14 olivine-bearing central peaks are identified out of 317 crater central peaks (166 investigated in this study, 151 non-investigated spectral featureless), implying only ~5% of Ol-bearing central peaks on the Moon. This value is significantly lower than the expected for the impact origin scenario, but in line with the global map of olivine derived from radiative transfer modeling of Clementine UVVIS spectra [Lucey, 2004] which revealed that olivine is present at low abundances (~ 5 wt. %) on the Moon. Additionally, if the impact origin scenario is responsible for the olivine origin, the abundance of remained olivine is expected to increase with the projectile size because large impactors have higher possibility to survive than small impactors at the same impact velocity. This also implies that large craters should have more remained olivine in the central peak than a small crater. Correlation of crater diameter with MNP of Ol for the central peaks is shown in Figure 3-16. It can be seen that the MNP trend does not increase with crater diameter, and the correlation is inconsistent with the impact origin scenario. Most of the Ol-bearing central peaks only contain limited amounts of olivine except for Copernicus, Eratosthenes, and Theophilus. Therefore, the impact origin scenario may not be a primary agent responsible for the origin of olivine observed in the central peaks.

4.2. Scenario B: mantle uplift (one excavation, multiple excavations)

Pieters and Wilhelms [1985] describe a possible mantle uplift scenario for the origin of olivine in the Copernicus central peaks. They suggested the sub-Copernicus crust (<10 km) was permanently thinned as a result of the Procellarum and Insularum impacts. The mantle is uniquely more accessible at Copernicus. The Copernicus impact penetrated to the uplifted mantle and excavated the mantle material to form the central peaks. Alternately, Yamamoto et al. [2010] proposed another mantle uplift scenario in which large basins (e.g. Crisium basin) could excavate mantle materials in thin crust regions and emplace the mantle materials into shallow enough to be penetrated by later craters. The multiple excavations by basins and impacts ultimately result in the mantle materials on the lunar surface. For the convenience of the discussion below, we call the first hypothesis one excavation scenario and the second hypothesis multiple excavation scenario. The schematic diagrams show in Figure 3-21.

4.2.1. One excavation scenario

The observations in this study appear to be in disagreement with one excavation scenario. The sub-Copernicus crust is about 30.38 km thick based on GRAIL estimations while the origin depth of Copernicus central peaks is roughly 15.09 km. The Copernicus impact is not possible to penetrate the mantle with only one excavation. According to D/T, all identified Ol-bearing central peaks originated from the lunar crust rather than the mantle except for Petavius and Humboldt. The D/T for the Petavius central peak is ~1.0, implying the crater Petavius can access to the interface of crust and mantle. The sub-Humboldt crust is extremely thin; the D/T for Humboldt central peak is larger than 1.5, indicating the crater Humboldt is highly possible to excavate mantle materials. However, the central peaks of both Petavius and Humbolt contain a large amount of crystalline plagioclase. Olivine typically crystallizes first from LMO, whereas the plagioclase crystallization occurred after 70-80% crystallization of LMO [Snyder et al. 1992]. It is commonly believed that plagioclase floated to form the primitive lunar crust and the mafic cumulates (including olivine) made up the lunar mantle [e.g. Shearer and Papike, 1999]. The crystalline plagioclase (nearly pure anorthosite) commonly represents the composition of the ancient lunar crust on the basis of previous studies [e.g. Ohtake et al., 2009; Yamamoto et al., 2012; Donaldson Hanna., 2014]. If the detected olivine has the mantle origin and represents the early stage crystallization product of the lunar magma ocean, then it is not possible that the mantle origin olivine and crystalline plagioclase could form contemporaneously from magma ocean crystallization, indicating that it is impossible for these two minerals to be located in the same layer. Furthermore, the mantle origin olivine and crystalline plagioclase cannot be excavated by the impact cater simultaneously. Therefore, olivine excavated by the craters Petavius and Humbolt is most unlikely to represent mantle materials. The erroneous indication of D/T for these two craters may be caused by the estimation of local crustal thickness.

Moreover, other seven central peaks bearing both Ol and Pl also provide substantial evidence to refuse the one excavation hypothesis. In other words, olivine and crystalline plagioclase cannot be exposed in the central peak simultaneously unless the mantle olivine has already been emplaced in relatively shallow layers and mingled with crystalline plagioclase in the lunar crust before the excavation of an impact.

4.2.2. Multiple excavation scenario

The craters owning Ol-bearing central peaks and being close to impact basins are shown in Figure 3-3 (Imbrium basin), Figure 3-17 (Orientale basin), Figure 3-18 (Crisium basin), and Figure 3-19 (Humorum basin). These impact basins are discussed to demonstrate whether the multiple excavation scenario is feasible to explain the origin of olivine.

Empirically, the maximum excavation depth of an impact basin is thought to be approximately one-tenth of the excavation cavity diameter [Croft, 1981; Spudis, 1993] and the excavation cavity diameter is estimated to be one-half to two-thirds of the basin diameter [Croft, 1981; Grieve et al., 1981]. Taking Imbrium Basin of 1160 km in diameter as an example, the excavation cavity is ~580-773 km in diameter and the maximum excavation depth of Imbrium is about ~58-77 km. The excavation depth for five associated impact basins is tabulated in Table 3-1. Compared with crustal thickness, all five basins are expected to excavate the lunar mantle materials except for Humorum basin. The deep-seated materials excavated by impact basins would be emplaced on the wall, ring, and ejecta of the basins. The basin-associated craters with Ol-bearing materials are all located surrounding the impact basin and superimposed on the basin ejecta (Figure 3-3, Figure 3-17 to Figure 3-19).

As shown in the method section, the origin depth of the central peak has been calculated based on $D=0.109*d^{1.08}$ [Cintala and Grieve, 1998] and shown in Table 3-1. Although it is very difficult to determine the thickness of basin ejecta [Pike, 1974], the thickness of the Imbrium ejecta at Copernicus was estimated to range from 0.4 to 3.0 km [Pieters and Wilhelms, 1985]. Apparently, the crater Copernicus (origin depth of the central peak is ~15 km) penetrated to the sub-ejecta layers and excavated the crustal materials to emplace in the central peak. In contrast, the thickness of the Orientale ejecta was measured to be ~0.2 to 2.9 km [Fassett et al., 2011], therefore the origin depth of the Ol-bearing central peaks of the crater Schluter (Figure 3-20) which is close to Orientale Basin is ~13.65 km. The Schluter central peak must be predominantly derived from the sub-Orientale layer. Given smaller sizes of the basins Nectaris, Crisium and Humorum than the basins Imbrium and Oriental, it is reasonable to assume that the basin ejecta other than from the basins Imbrium and Oriental would be thinner, and that the investigated central peaks must have originated from beneath of basin ejecta. Even for the smallest crater Bianchini, the origin depth of its central peak should be larger than 5 km. Therefore, the craters which are detected to have Ol-bearing central peaks should mainly excavate the lunar crust material rather than basin ejecta.

The compositional examination for the crater central peaks in the vicinity of the large basins reveals the impossibility of the mantle origin olivine to appear in the central peak via the multiple excavation processes. Taking Imbrium basin as an example (Figure 3-6), five craters near Imbrium Basin have been investigated in this study including Bianchini, Aristarchus, Kepler, Copernicus and Eratosthenes which are located in the maria. The average mare thickness on the nearside is generally less than 400 m and the maximum thickness of mare is up to 4 km. [Head and Wilson, 1992; Wieczorek et al., 2006]. Compared with the origin depth of the five crater central peaks surrounding the Imbrium basin, all five craters were definitely penetrated to the layers (probably basin ejecta layer) underneath the mare basalts. As aforementioned, mantle materials were excavated by Imbrium basin and emplaced as basin ejecta on the lunar surface. We assume that the basin ejecta is dominated by olivine, and later impact craters with central peaks only excavated the materials in this ejecta layer. Therefore, all the crater central peaks surrounding the Imbrium basin are expected to exhibit the presence of olivine. However, our observations are inconsistent with this assumption. The central peaks of the crater Bianchini, Copernicus and Eratosthenes have been identified the presence of olivine and no olivine has been found in the central peaks of Aristarchus and Kepler. Moreover, the small craters (such as Aristarchus and Kepler) are supposed to have more chance to excavate ejecta olivine than large craters because small peak craters are most likely to access the basin ejecta while large peak craters (such as Copernicus) can easily penetrate into deep layers underneath the ejecta. Both Aristarchus and Kepler central peaks are only identified to contain plagioclase and pyroxene without olivine, this implies that the ejecta materials are not olivine dominated. The olivine identified in Copernicus and Eratosthenes central peaks may originate from sub-Imbrium ejecta layer because these two large craters have high possibility to penetrate the ejecta layer. The Aristarchus and Kepler impact was not large enough to excavate the possible underlying olivine-rich unit, or the olivine-rich unit is only located underneath the Copernicus-Eratosthenes region. The small amount of olivine in the Bianchini central peak is possible to be generated by small plutonic event underneath Bianchini.

In summary, the multiple excavation scenario is not suitable to explain the petrogenesis of olivine in the central peaks.

4.3. Scenario C: magmatic origin (pluton, magmatic transport)

One magmatic origin scenario for observed Ol-bearing crater central peaks on the Moon was first proposed by Pieters and Wilhelms [1985], which states that the olivine of the Copernicus central peaks was excavated from the lunar crust, and more exactly from a olivine-rich layered pluton intruding the lunar crust. This layered pluton or intrusion is considered to have a large diameter based on the amount of olivine present in the Copernicus central peak [Pinet et al., 1993]. The other magmatic origin scenario was suggested by Powell et al. [2012] and claims that mantle cumulates or xenoliths containing olivine could be transported and emplaced to the shallow layer or surface through intrusive magmatism into the crust. The cartoons regarding the pluton and magmatic transport scenarios show in Figure 3-22.

Results from this study are mostly consistent with the magmatic scenarios. The reasons are the following: (1) Olivine has relatively low likelihood of presence in the most of central peaks and an asymmetric distribution, which are in disagreement with Scenario A. (2) Scenario B fails to explain the coexistence of olivine and crystalline plagioclase. (3) According to the discussion in section 4.2, the investigated craters cannot access to mantle materials through either one excavation scenario or multiple excavation scenario. (4) Much evidence indicates that PKT has a thinner crust than FHT, which enables magma to intrude easily into the crust underneath PKT. This is in line with the olivine detection results in the central peaks (olivine is concentrated within the crust underneath the PKT) indicate that the magmatic scenario can better explain the asymmetric distribution of olivine in the crust. (5) Both petrologic analysis and remote sensed observation provide important clues to the existence of olivine in shallow layers. Previous petrologic experiments suggested the formation of olivine in relatively shallow crust layers, and olivine can form through fractional crystallization at both high and low pressures [Ford et al., 1983] and from partial melting at low pressure [Hess, 1994]. Specifically, dunite clasts in Apollo 17 breccias had been initially speculated to represent a lithology from the lunar mantle [Bell et al., 1975] but they were later considered to be Mg-suite lithologies and formed through near-surface olivine accumulation [Ryder, 1992]. Dunite xenoliths in lunar basalt 74275 were also determined to form at relatively shallow depths [Shearer et al. 2015]. All of these petrological observations indicate the identified olivine-rich materials could generate from magmatic activities in relatively shallow layers. Along with Mg-Spinel, olivine has been determined to originate from relatively shallow layers [Sun et al., 2013; Sun and Li, 2014] with M^3 images.

It is necessary to point out that determining which magmatic scenario (pluton or magmatic transport) is the major process for the origin of olivine is difficult just based on the current observations. Transportation of solid cumulates or xenoliths seems difficult to explain a large-scale occurrence of olivine in some regions (e.g. Copernicus). Some olivine-bearing central peaks originate from relatively shallow layers (e.g. origin depth of Bianchini is ~5.5 km) or contain a limited amount of olivine (only a few pixels), which cannot be well explained using plutonic intrusions. Typically, a pluton represents a body of intrusive igneous rock slowly crystallized from a magma and several kilometers in dimension. MNP for olivine in six central peaks is less than 8 which means olivine exposure is less than 1 km. This observation is not in line with the common recognition of pluton. Additionally, for instance, the MNP for olivine in Copernicus is 1502 which means the olivine exposure is more than 200 km. It means at least 200 km olivine-rich unit exist in the sub-Copernicus layers. Such large area of the olivine-rich unit is impossible to represent the unmelted cumulates or xenoliths. Neither plutonic intrusion nor magmatic transport alone can accommodate the observations made in this study. Building upon the above mentioned reasons, a hybrid magmatic scenario is proposed here for the origin of olivine identified in the central peak. Large impact basins (e.g. Procellarum and Insularum) permanently thinned and fractured the crust in the PKT, resulted in a potential magma upwelling with/without a small portion of unmelt mafic cumulates or xenoliths to settle the relatively shallow layers, and/or generated magma chambers which could crystallize to produce olivine-rich materials. Ultimately the olivine-rich materials were excavated by impact craters and emplaced in the central peak. The plutonic event is most likely responsible for the source of olivine in Copernicus, Eratosthenes, and Theophilus because of a large amount of identified olivine. According to the origin depth of Copernicus and Eratosthenes central peaks, the sub-Copernicus pluton is at least 6 km thick ($D_{Copernicus}$ (15.09 km)-$D_{Eratosthenes}$(8.87 km)). The crater Eratosthenes may overlay the boundary of this olivine-rich pluton and the lunar crust because of the presence of crystalline plagioclase. In the case of other identified olivine - bearing central peaks, the pluton is probably in a limited area underneath the crust, or only a small amount of cumulates or xenoliths exist in the sub-crater crust. However, the possibility for the impact origin to contribute to the origin of olivine in some central peaks cannot be ruled out. Moreover, the olivine-rich materials in the wall, ring, and ejecta of the basin rather than crater central peak may be explained by the mantle uplift scenarios.

5. Conclusions

14 olivine-bearing central peaks have been determined in this study out of 166 investigated craters. The results indicate that the olivine-rich areas are concentrated within the middle layer of the lunar crust (D/T: 0.3-0.6) underneath the PKT. Most of olivine bearing central peaks are also identified in association with crystalline plagioclase. Impact origin scenario and mantle uplift scenario fails to explain the observations in this study, so the magmatic origin is most likely to unravel the origin of olivine in the central peak. A hybrid magmatic origin scenario has been proposed. The large number of olivine-rich materials identified in the central peaks of Copernicus, Eratosthenes and Theophilus could be generated by a large area of pluton underneath the craters. The occurrence of the small

amount of olivine-bearing materials may originate from the small pluton or olivine-rich materials (cumulates and xenoliths) transported by magma. However, the impact origin and mantle uplift scenario cannot be entirely excluded on the basis of current observations. In order to place more accurate constraints on the origin of olivine, other regions (e.g. crater wall) need to be analyzed.

Acknowledgements

We would like to thank Yunzhao Wu and Dawei Liu for the thoughtful and thorough suggestion, which improved this manuscript.

Table caption

Table 3-1. All the information of olivine-bearing central peaks. 1: Origin depth of central peak is calculated based on D=0.109*d1.08 [Cintala and Grieve, 1998]; 2: Average crustal thickness of each central peak is derived from GRAIL data [Wieczorek et al., 2013]; 3: the number in the ‘Sp’ ‘Ol’ and ‘Pl’ column represents the MNP for each mineral, and the ‘*’ represent the presence of pyroxene. 4: The crustal terranes were classified in Jolliff et al. [2000], PKT: Procellarum KREEP Terrane, FHT: Feldspathic Highlands Terrane; 5: possible associated basin. 6: the excavation depth of the associated basin. 7: the last column lists the available M3 images for each central peak.

Table

Table 3-1.

Crater name	Center Latitude	Center Longitude	Diameter (d) (km)	Origin Depth (D)[1] (km)	Crustal Thickness (T)[2] (km)	D/T	Sp	Ol	Pl	Opx	Cpx	Terrane[4]	Basin[5]	Excavation depth of basin[6]	M^3 L2 image
Bianchini	48.78	325.63	37.59	5.48	34.93	0.16	13	8		*	*	PKT	Imbrium	~58.00-77.33	M3G20090208T100012
															M3G20090611T043527
Jackson	22.05	196.68	71.38	10.95	39.75	0.28		3	14	*	*	FHT			M3G20090621T025007
															M3G20090718T101402
Eratosthenes	14.47	348.68	58.77	8.87	30.88	0.29		211	2		*	PKT	Imbrium	~58.00-77.33	M3G20090206T124510
															M3G20090415T202222
															M3G20090609T101951
Macrobius	21.26	45.97	62.79	9.53	30.73	0.31		10		*	*	PKT	Crisium	~37.00-49.33	M3G20090105T194305
															M3G20090202T042831
															M3G20090605T040250
															M3G20090729T185951
Philolaus	72.22	327.12	71.44	10.96	32.09	0.34		8		*	*	PKT			M3G20090611T043527
Kovalevskaya	30.86	230.56	113.71	18.10	47.93	0.38	82	4	16	*	*	FHT			M3G20090424T191252
															M3G20090424T205837
Gassendi	-17.55	320.04	111.39	17.70	46.79	0.38	9	10	3	*		PKT	Humorum	~21.25-28.33	M3G20090208T160125
															M3G20090208T175211
Schluter	-5.93	276.61	87.55	13.65	32.48	0.42		3	6			PKT	Orientale	~46.50-62.00	M3G20090212T003453
															M3G20090421T082045
															M3G20090712T050712
															M3G20090712T093119
Copernicus	9.62	339.92	96.07	15.09	30.38	0.50	7	1502		*		PKT	Imbrium	~58.00-77.33	M3G20090207T044515
															M3G20090416T122951
															M3G20090513T191408
															M3G20090610T030313
Atlas	46.74	44.38	88.12	13.74	27.00	0.51	20	7		*	*	PKT			M3G20090202T063731
															M3G20090202T083314
															M3G20090605T081431
Theophilus	-11.45	26.28	98.59	15.52	25.39	0.61	177	105	98			PKT	Nectaris	~43.00-57.33	M3G20090203T160452
															M3G20090731T045352
Keeler	-9.78	161.78	158.07	25.83	38.29	0.67		4	115			FHT			M3G20090623T182551
Petavius	-25.39	60.78	184.06	30.45	30.55	1.00		7	83		*	PKT			M3G20090104T161446
															M3G20090728T171132
Humboldt	-27.02	80.96	199.46	33.21	21.13	1.57		27	286			PKT			M3G20090602T121452

Figure captions

Figure 3-1. Distribution of 166 investigated crater central peaks (red dots) on LOLA DEM of the Moon. 14 The ol-bearing central peak identified in this study have been shown in green dots. Black dash lines describe three distinct lunar terranes. PKT: Procellarum KREEP Terrane; FHT: Feldspathic Highlands Terrane; SPAT: South-Pole Aitken Terrane.

Figure 3-2. Typical continuum removed reflectance spectra of olivine extracted from each crater central peak. The crater names are ordered by increasing origin depth of the central peak from top to bottom.

Figure 3-3. Theophilus is located near Mare Nectaris and overlays the crater Cyrillus. The background image is resized from LRO WAC global mosaic image. The solid star represents relative depth (D/T) and filling fringe colors show identified minerals in this study. (Sp: Mg-spinel; Ol: olivine; Pl: crystalline plagioclase; Cpx: Clinopyroxene; Opx: orthopyroxene)

Figure 3-4. Multi-temporal images for Theophilus crater central peak. The below images are resized from 'M3G20090203T160452_V01_RFL.IMG' and 'M3G20090731T045352_V01_RFL.IMG' respectively after data preprocessing. A: the M^3 L2 image for Theophilus crater central peak at 750 nm from 'M3G20090203T160452_V01_RFL.IMG', and the identified olivine-bearing pixels (237) show in green color. B: The location is as the same as A for Theophilus central peak, but from 'M3G20090731T045352_V01_RFL.IMG', and olivine-bearing pixels (105) in green color.

Figure 3-5. Detailed information for Theophilus crater central peak. A: IBD (integrated band depth) image (Red: IBD1000, Blue: IBD2000, Green: M^3 reflectance at 1508 nm) on the M^3 reflectance image at 750 nm; B: LRO WAC mosaic image for Theophilus crater; C: the identified olivine-bearing pixels (green color) on M^3 reflectance image at 750 nm, the size is the same as the IBD image in A; D: LRO WAC mosaic image of Theophilus crater central peak in 3D perspective using LOLA data. Vertical exaggeration is ×2. Yellow circle highlight the olivine-rich area is shown in E. E: LRO NAC image for the olivine-rich area as be marked as a yellow circle in D.

Figure 3-6. The craters surrounding the Mare Imbrium. The background image is resized from LRO WAC global mosaic image. The solid star represents relative depth (D/T) and filling fringe colors show identified minerals in this study. (Sp: Mg-spinel; Ol: olivine; Pl: crystalline plagioclase; Cpx: Clinopyroxene; Opx: orthopyroxene). The presence of Ol has been identified in the central peaks of Bianchini, Copernicus, and Eratosthenes, but not in Aristarchus and Kepler (The Kepler does not belong to the investigated crater in this study because the diameter of Kepler is less than 35 km).

Figure 3-7. Detailed information for Copernicus crater central peak. A: IBD (integrated band depth) image (Red: IBD1000, Blue: IBD2000, Green: M^3 reflectance at 1508 nm) on the M^3 reflectance image at 750 nm; B: LRO WAC mosaic image for Copernicus crater; C: the identified olivine-bearing pixels (green color) on M^3 reflectance image at 750 nm, the size is the same as the IBD image in A; D: LRO WAC mosaic image of Copernicus crater central peak in 3D perspective using LOLA data. Vertical exaggeration is ×2. Yellow circle highlight the one example olivine-rich peak shown in E. E: LRO NAC image for the olivine-rich area as be marked as a yellow circle in D.

Figure 3-8. Detailed information for Eratosthenes crater central peak. The captions for A-E are the same as the information for Copernicus in Figure 3-7.

Figure 3-9. Detailed information for Jackson crater central peak. The captions for A-E are the same as in Figure 3-5.

Figure 3-10. Detailed information for Kovalevskaya crater central peak. The captions for A-E are the same as in Figure 3-5. The red circle in C represent the area identified crystalline plagioclase.

Figure 3-11. Detailed information for Keeler crater central peak. The captions for A-E are the same as in Figure 3-5.

Figure 3-12. The distribution of investigated crater central peaks within SPAT. The Opx-bearing central peaks show in blue color.

Figure 3-13. Vertical distribution and the likelihood of the presence of olivine bearing lithology. The relative depth of each central peak shown on the vertical axis is calculated by D/T. The minimum number of pixels (MNP) for detected olivine in each central peak is shown in the horizontal axis.

Figure 3-14. Detailed information for Petavius crater central peak. The captions for A-E are the same as in Figure 3-5.

Figure 3-15. Detailed information for Humboldt crater central peak. The captions for A-E are the same as in Figure 3-5.

Figure 3-16. Comparison between MNP (horizontal axis) and crater diameter (vertical axis).

Figure 3-17. The craters are surrounding the Orientale basin. The background image is resized from LRO WAC global mosaic image. The solid star represents relative depth (D/T) and filling fringe colors show identified minerals in this study. (Sp: Mg-spinel; Ol: olivine; Pl: crystalline plagioclase; Cpx: Clinopyroxene; Opx: orthopyroxene). The presence of Ol only has been identified in the central peaks of Schluter.

Figure 3-18. The craters are surrounding the Mare Crisium. The background image is resized from LRO WAC global mosaic image. The solid star represents relative depth (D/T) and filling fringe colors show identified minerals in this study. (Sp: Mg-spinel; Ol: olivine; Pl: crystalline plagioclase; Cpx: Clinopyroxene; Opx: orthopyroxene). The presence of Ol has been identified in the central peaks of Macrobius.

Figure 3-19. The craters are surrounding the Mare Humorum. The background image is resized from LRO WAC global mosaic image. The solid star represents relative depth (D/T) and filling fringe colors show identified minerals in this study. (Sp: Mg-spinel; Ol: olivine; Pl: crystalline plagioclase; Cpx: Clinopyroxene; Opx: orthopyroxene). The presence of Ol has been identified in the central peaks of Gassendi.

Figure 3-20. Detailed information for Schluter crater central peak. The captions for A-E are the same as in Figure 3-5.

Figure 3-21. Schematic diagrams for mantle uplift scenarios

Figure 3-22. Schematic diagrams for magmatic origin scenarios

Figures

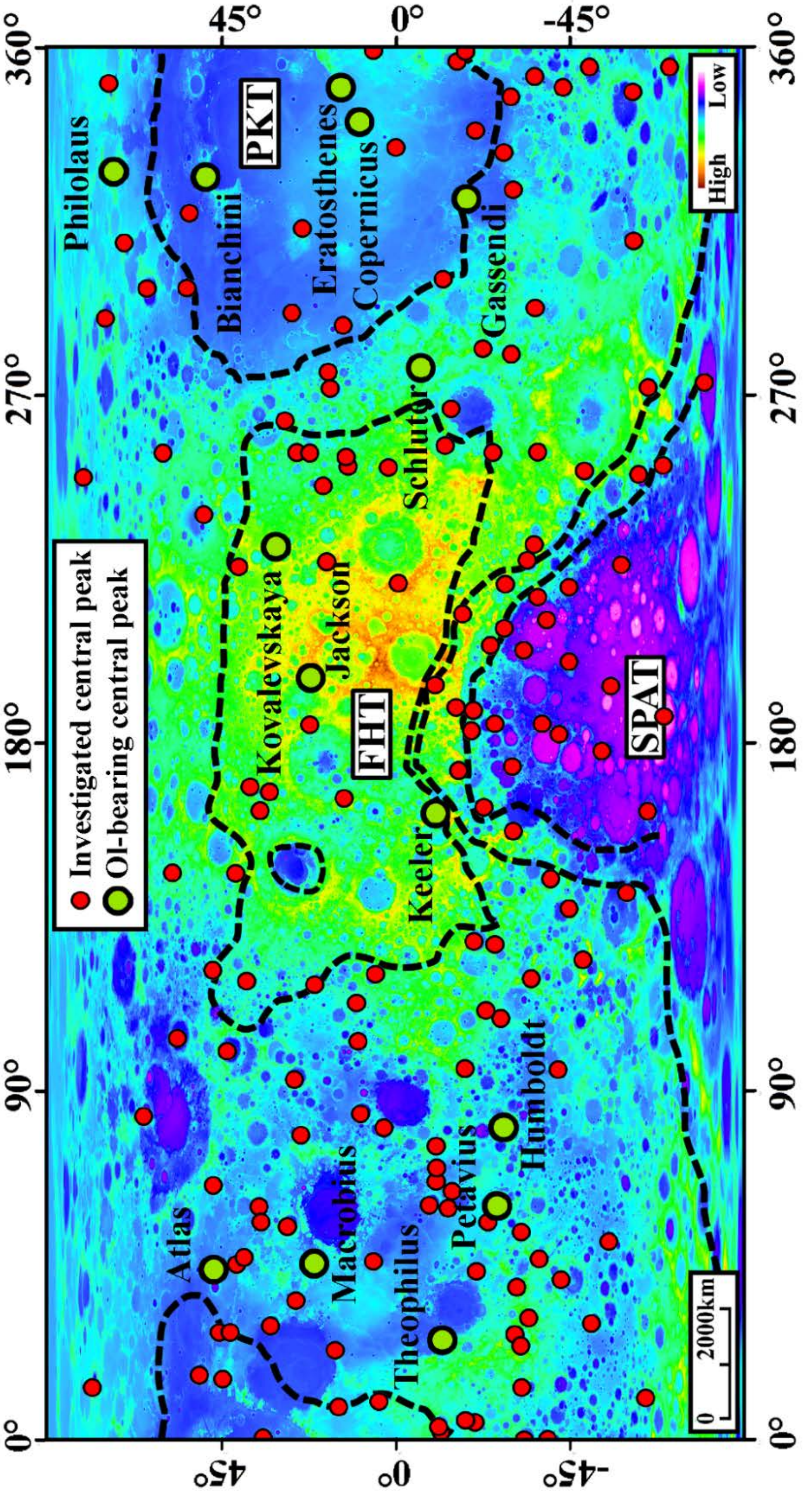

Figure 3-1.

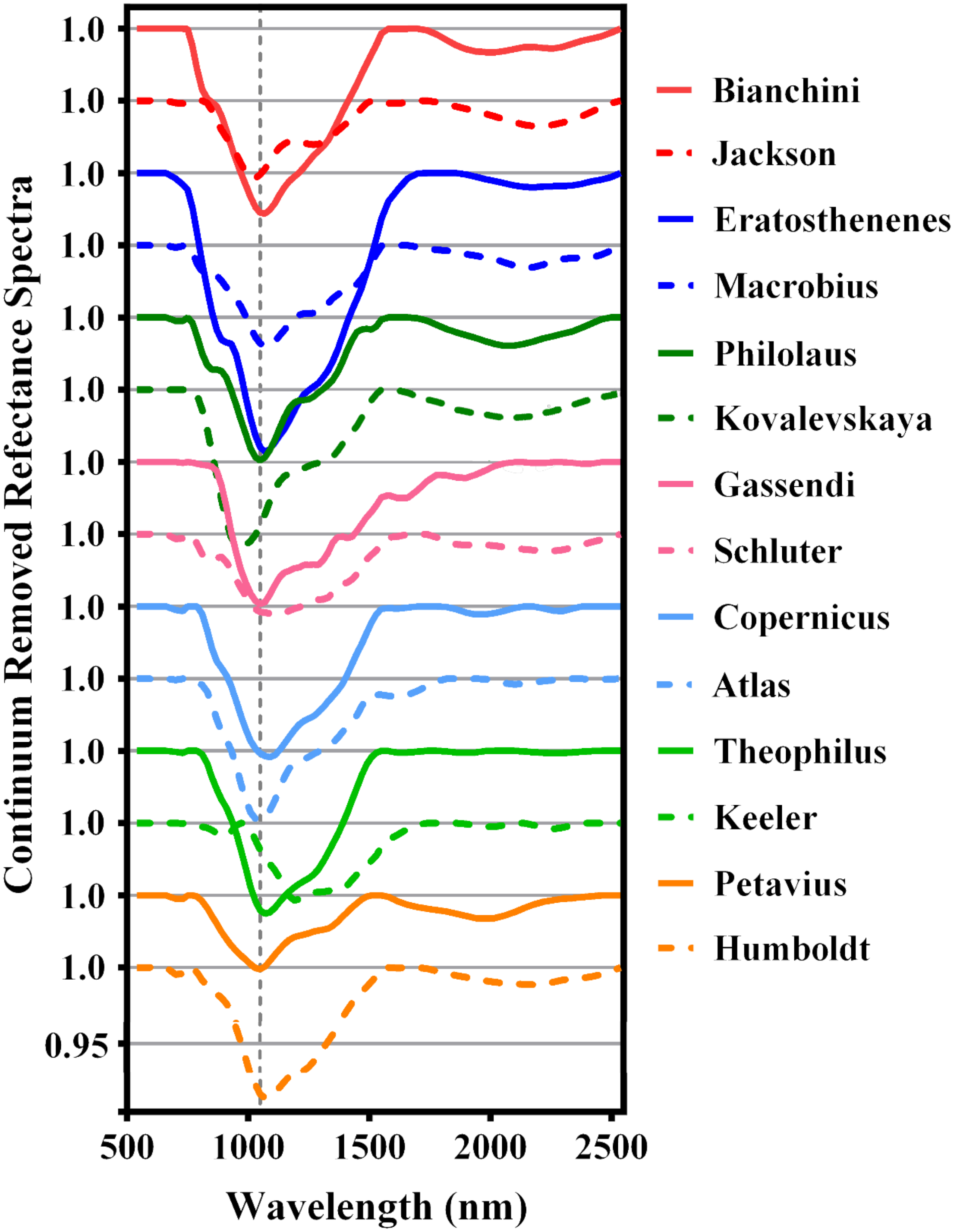
Continuum Removed Refectance Spectra
1.0
1.0
1.0
1.0
1.0
1.0
1.0
1.0
1.0
1.0
1.0
1.0
1.0
1.0
1.0
0.95
500
1000
1500
2000
2500
Wavelength (nm)
Bianchini
Jackson
Eratosthenenes
Macrobius
Philolaus
Kovalevskaya
Gassendi
Schluter
Copernicus
Atlas
Theophilus
Keeler
Petavius
Humboldt

Figure 3-2.

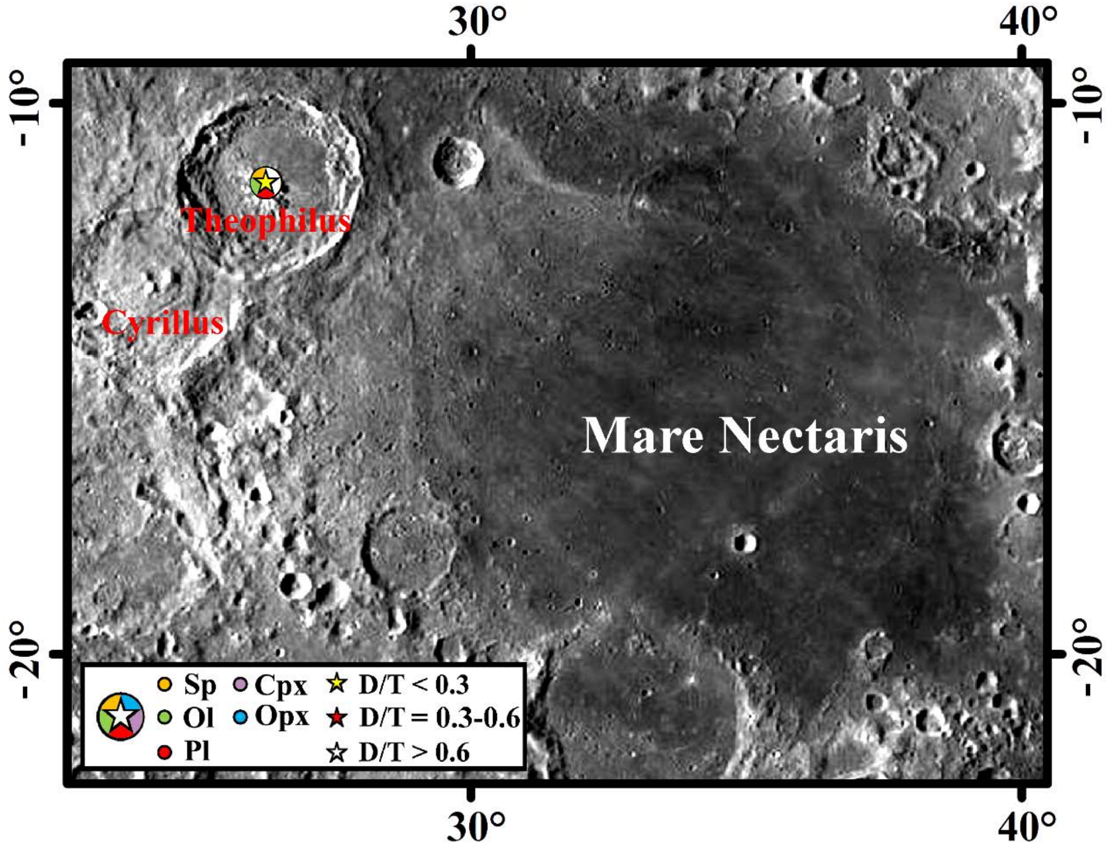
30°
40°
-10°
-20°
Theophilus
Cyrillus
Mare Nectaris
Sp
Ol
Pl
Cpx
Opx
D/T < 0.3
D/T = 0.3-0.6
D/T > 0.6

Figure 3-3.

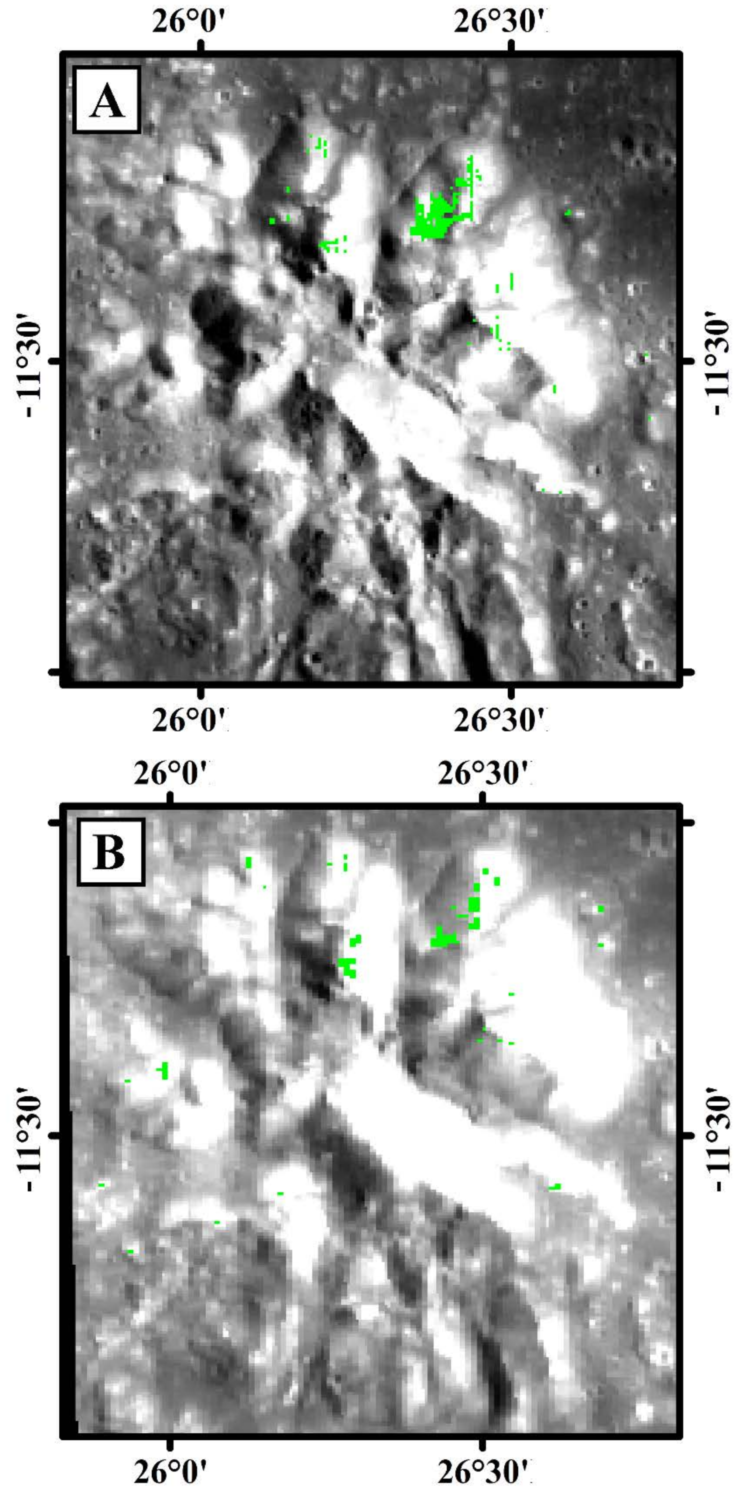

Figure 3-4.

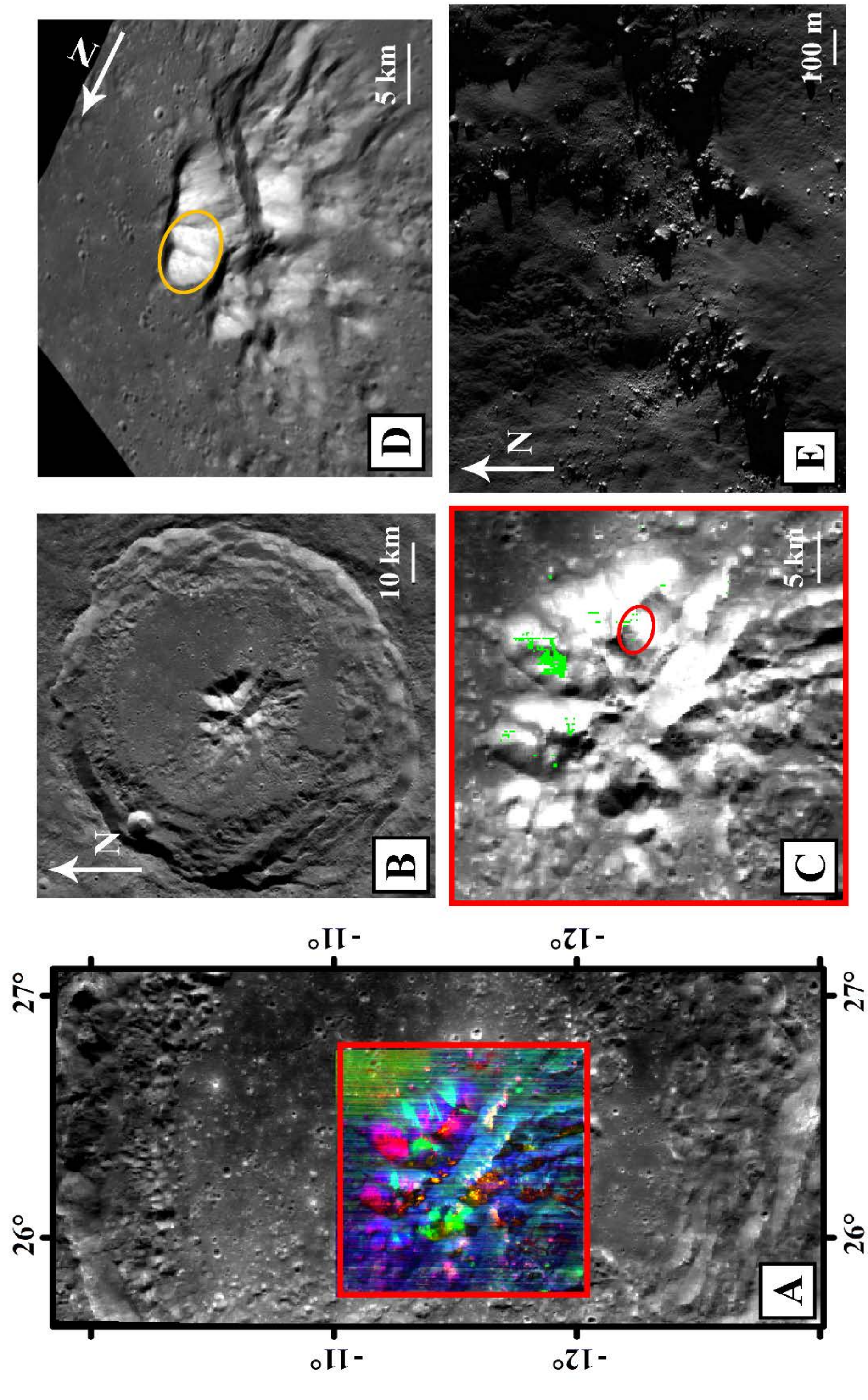

Figure 3-5.

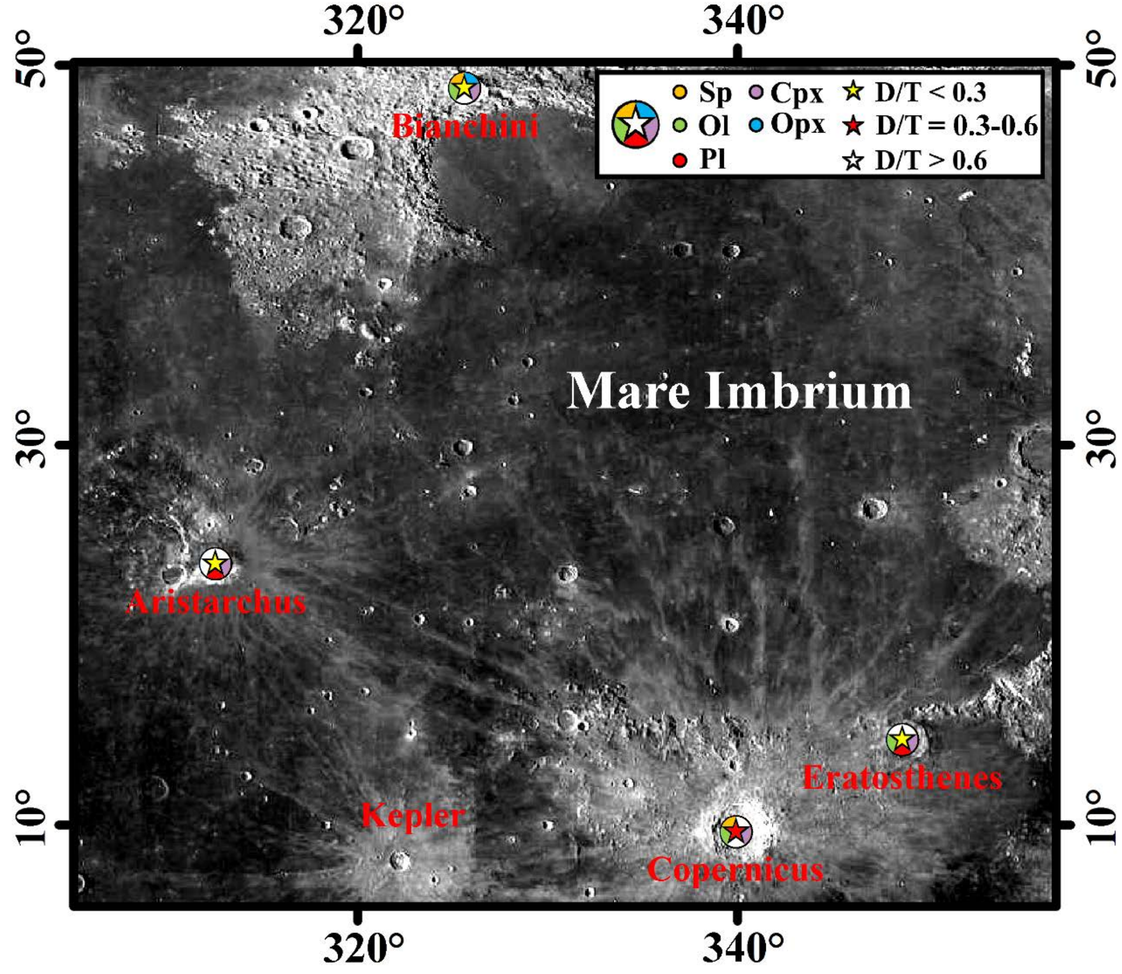
320°
340°
50°
30°
10°
Sp
Ol
Pl
Cpx
Opx
D/T < 0.3
D/T = 0.3-0.6
D/T > 0.6
Bianchini
Mare Imbrium
Aristarchus
Eratosthenes
Kepler
Copernicus

Figure 3-6.

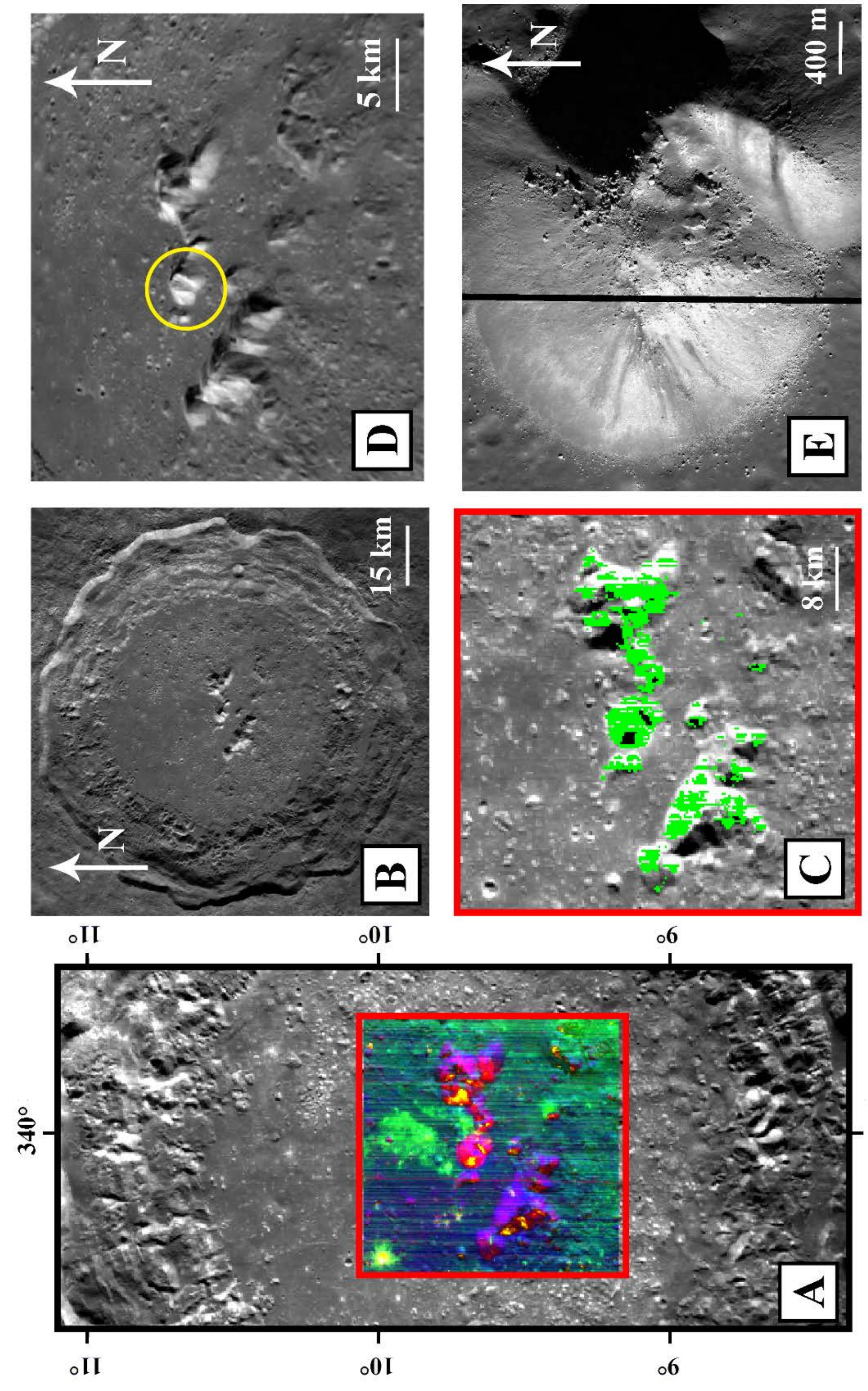

Figure 3-7.

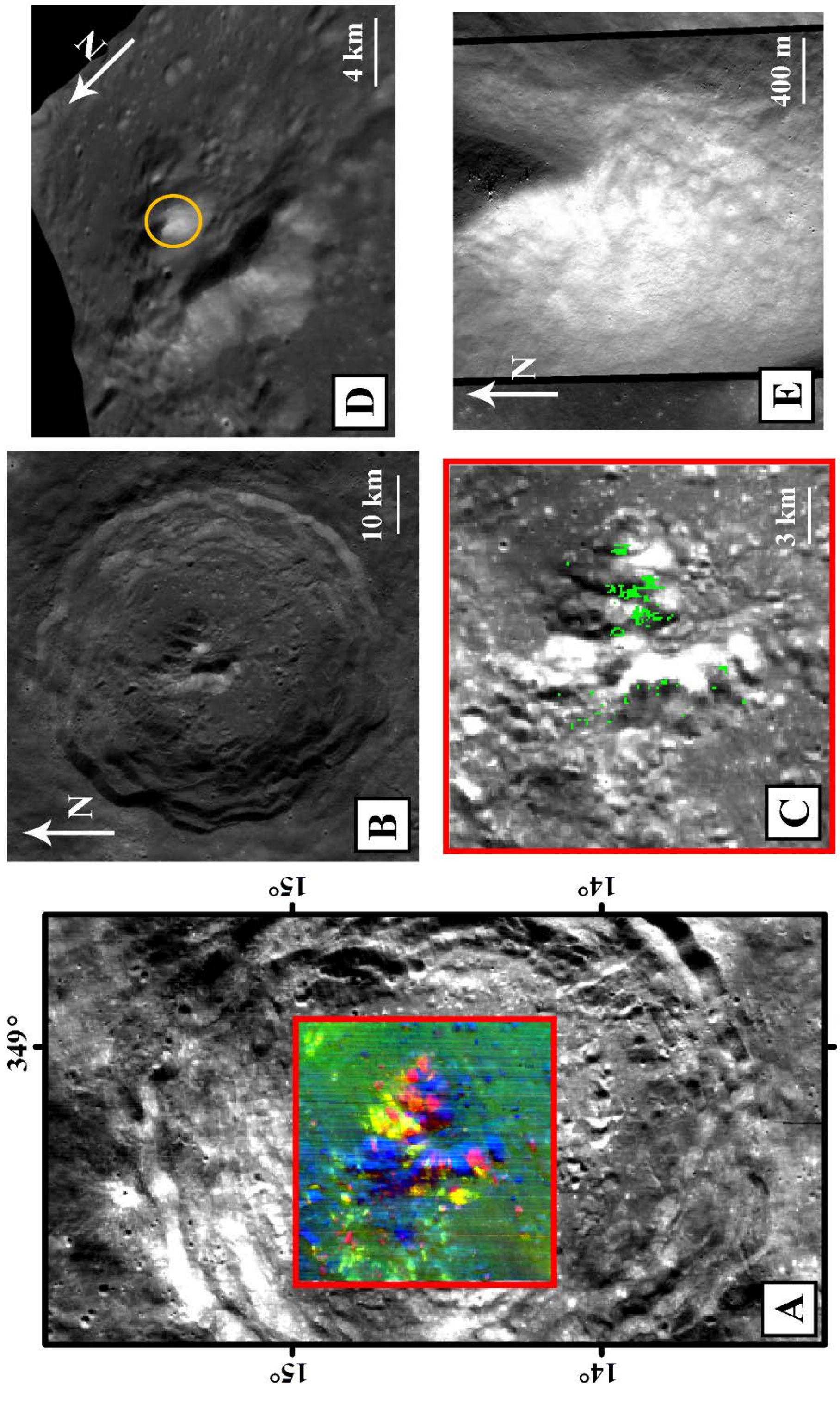

Figure 3-8.

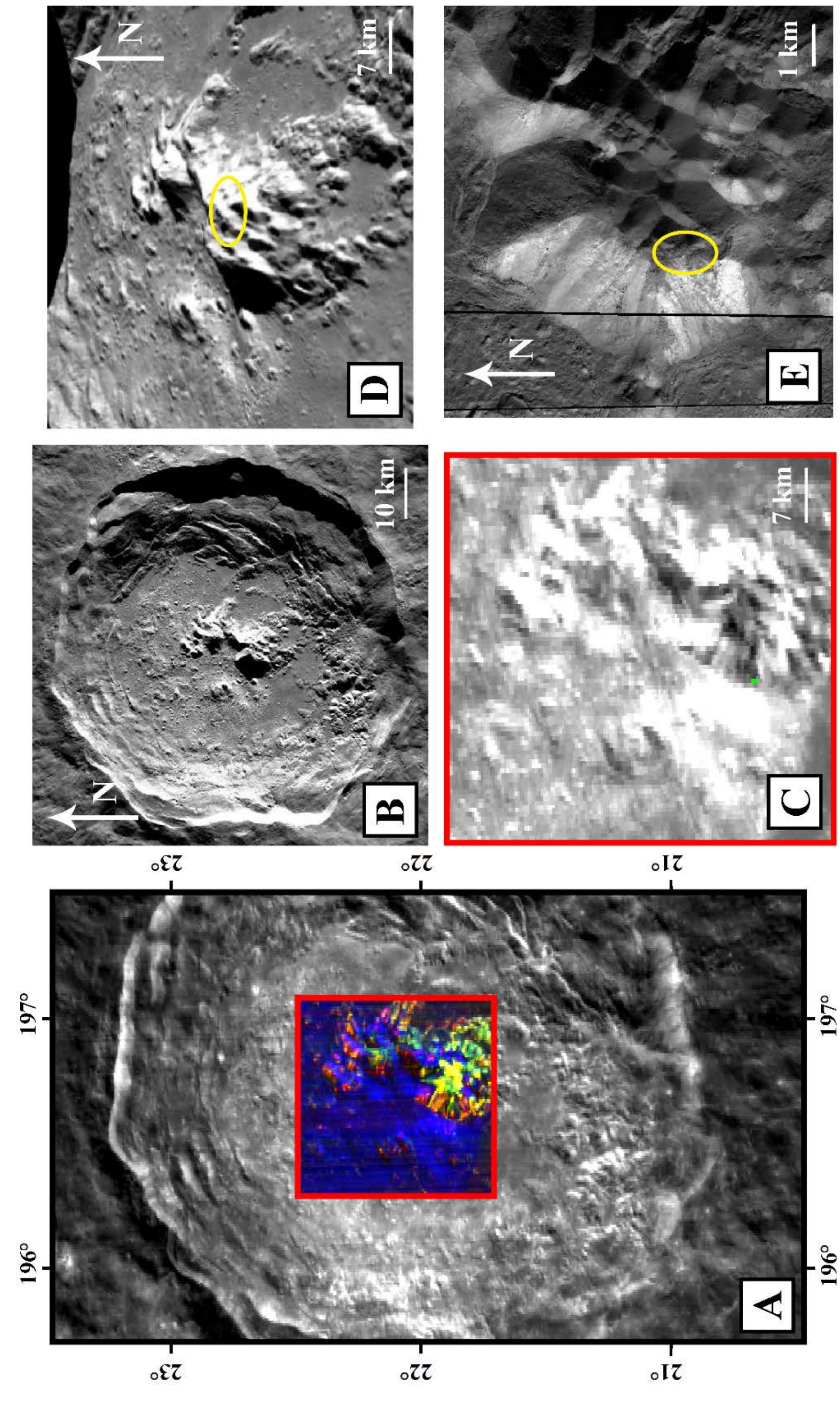

Figure 3-9.

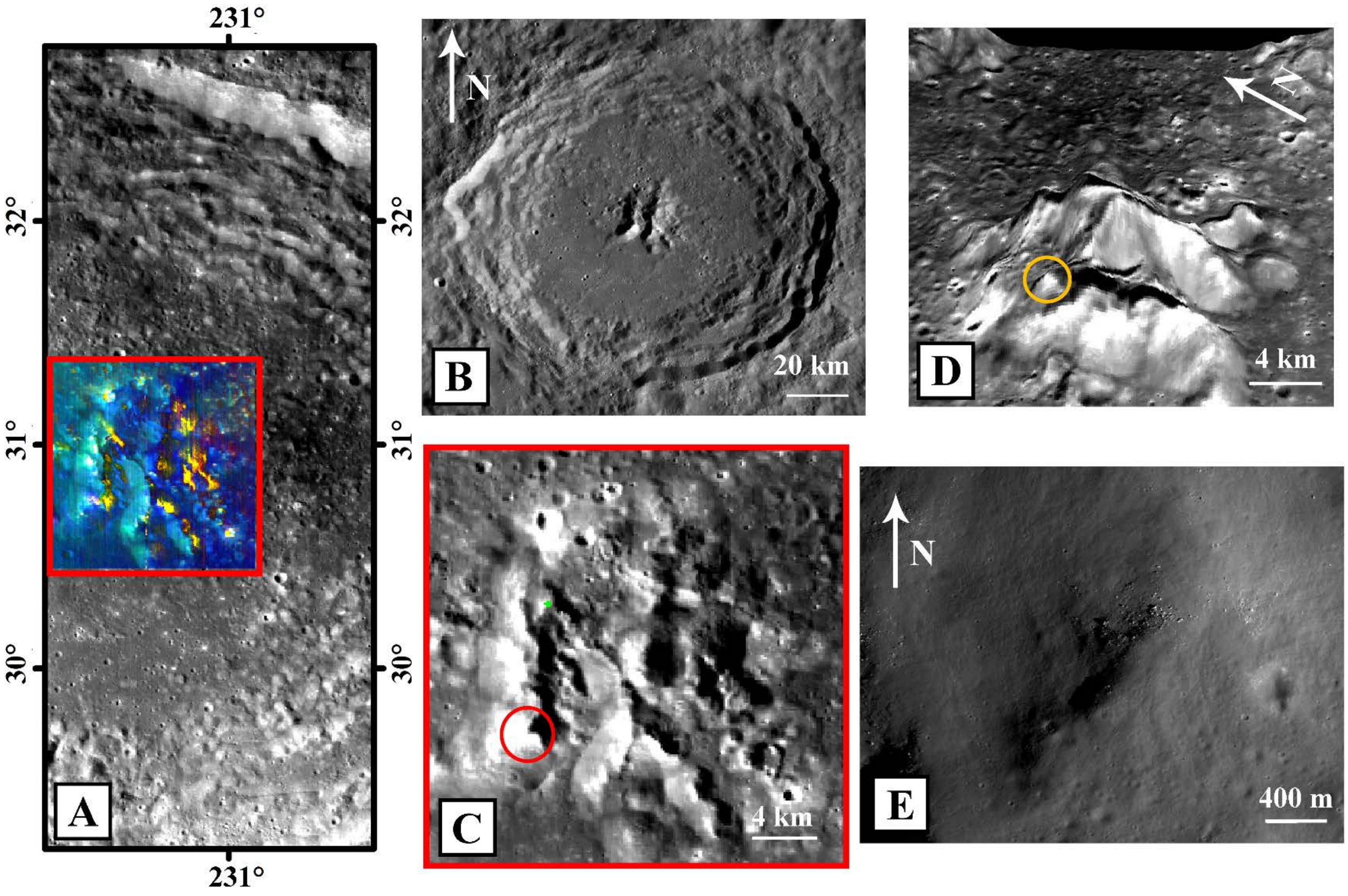

Figure 3-10.

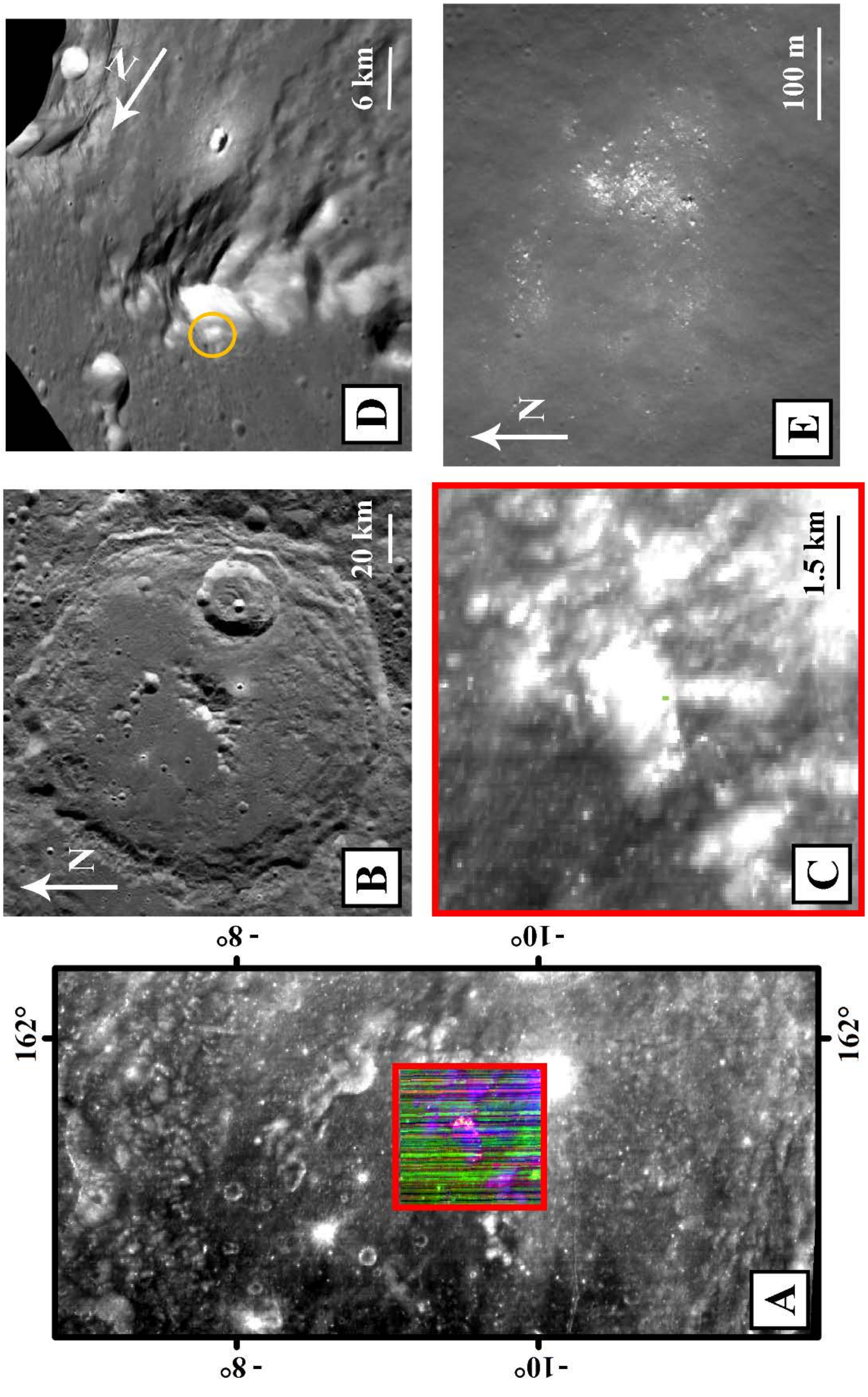

Figure 3-11.

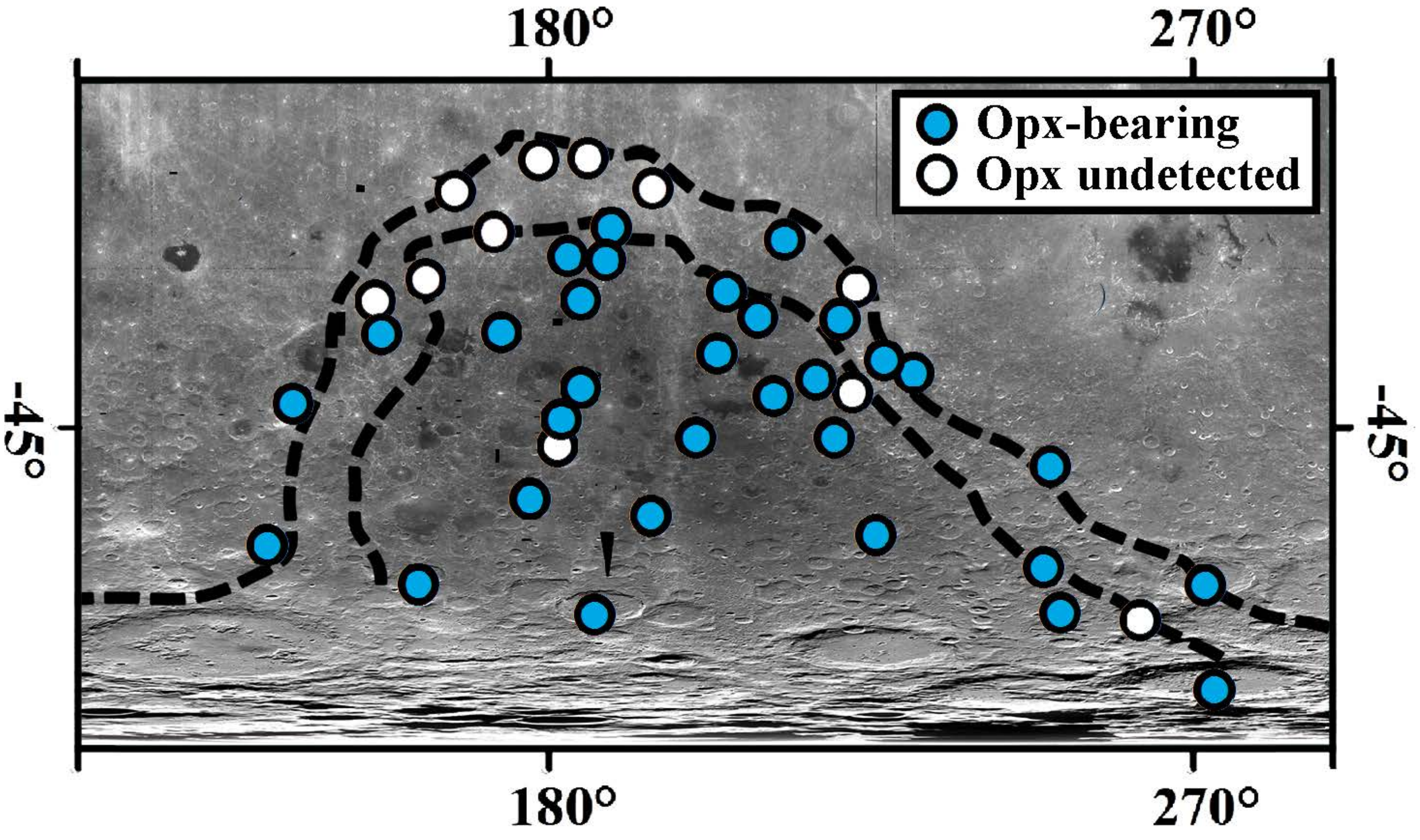

Figure 3-12.

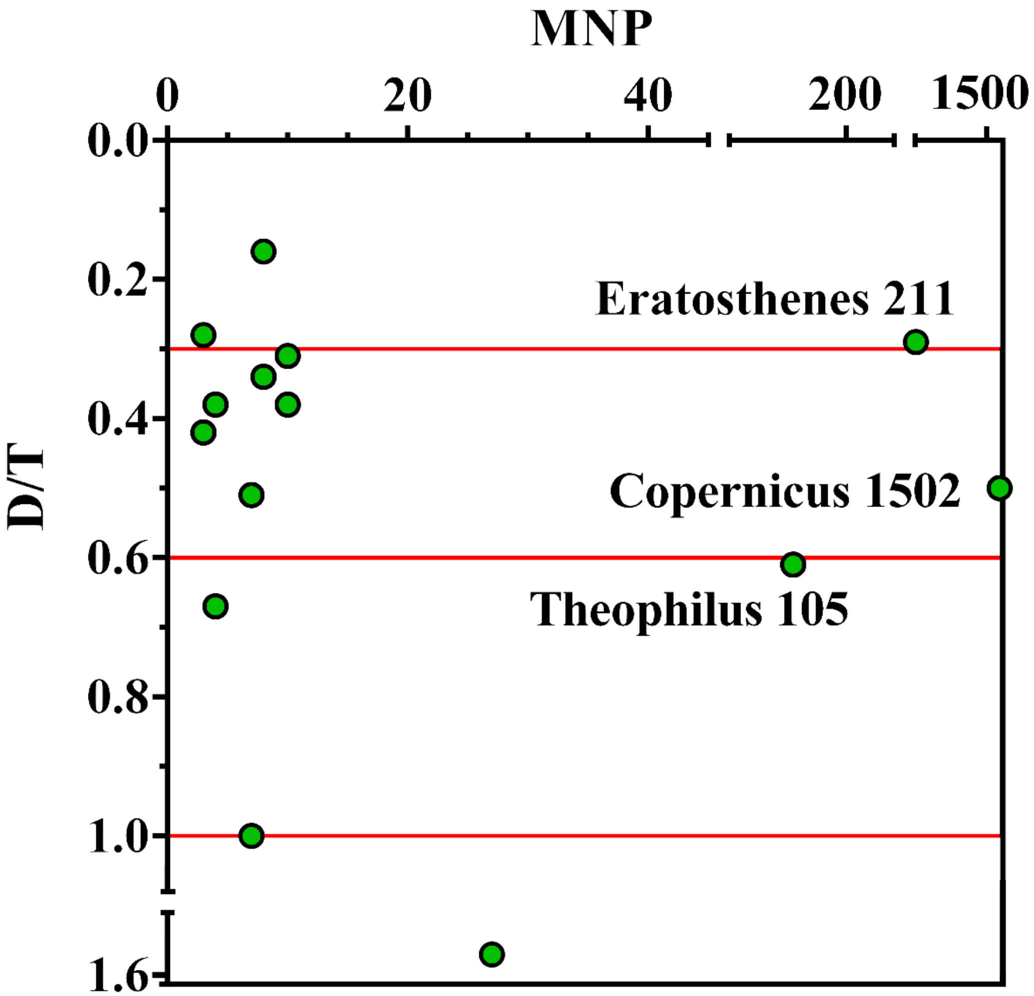
MNP
0
20
40
200
1500
D/T
0.0
0.2
0.4
0.6
0.8
1.0
1.6
Eratosthenes 211
Copernicus 1502
Theophilus 105

Figure 3-13.

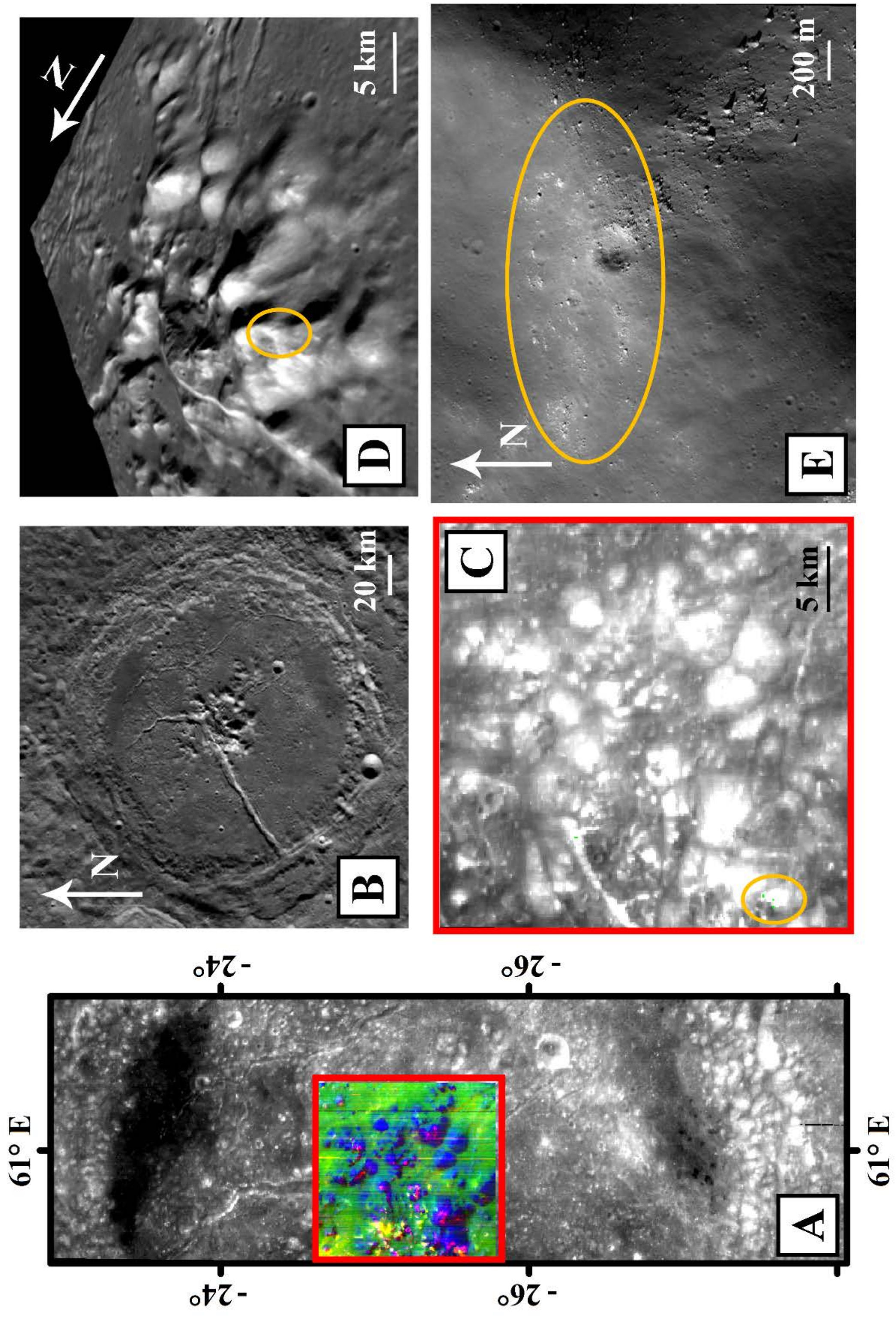

Figure 3-14.

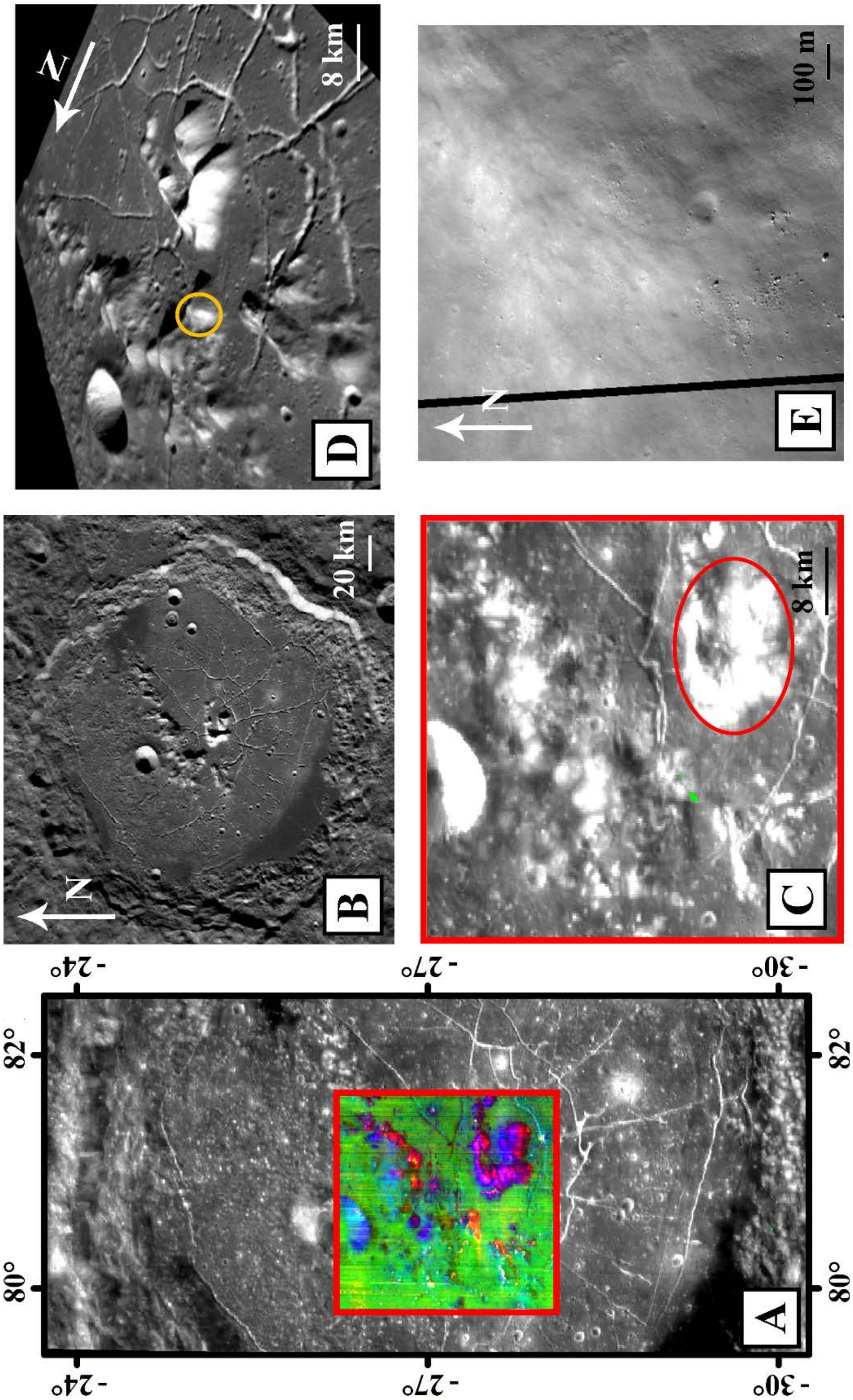

Figure 3-15.

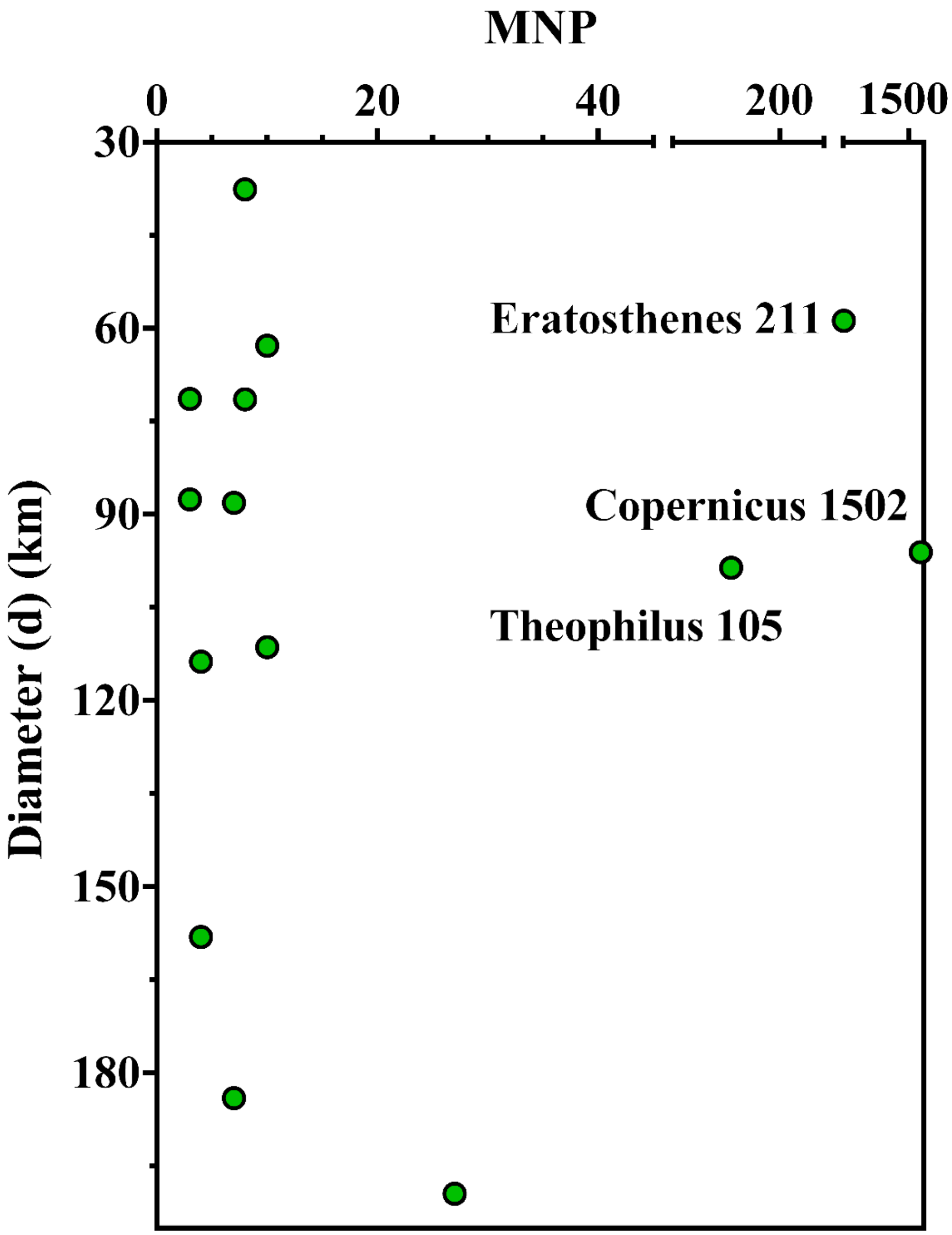
MNP
0
20
40
200
1500
30
60
90
120
150
180
Diameter (d) (km)
Eratosthenes 211
Copernicus 1502
Theophilus 105

Figure 3-16.

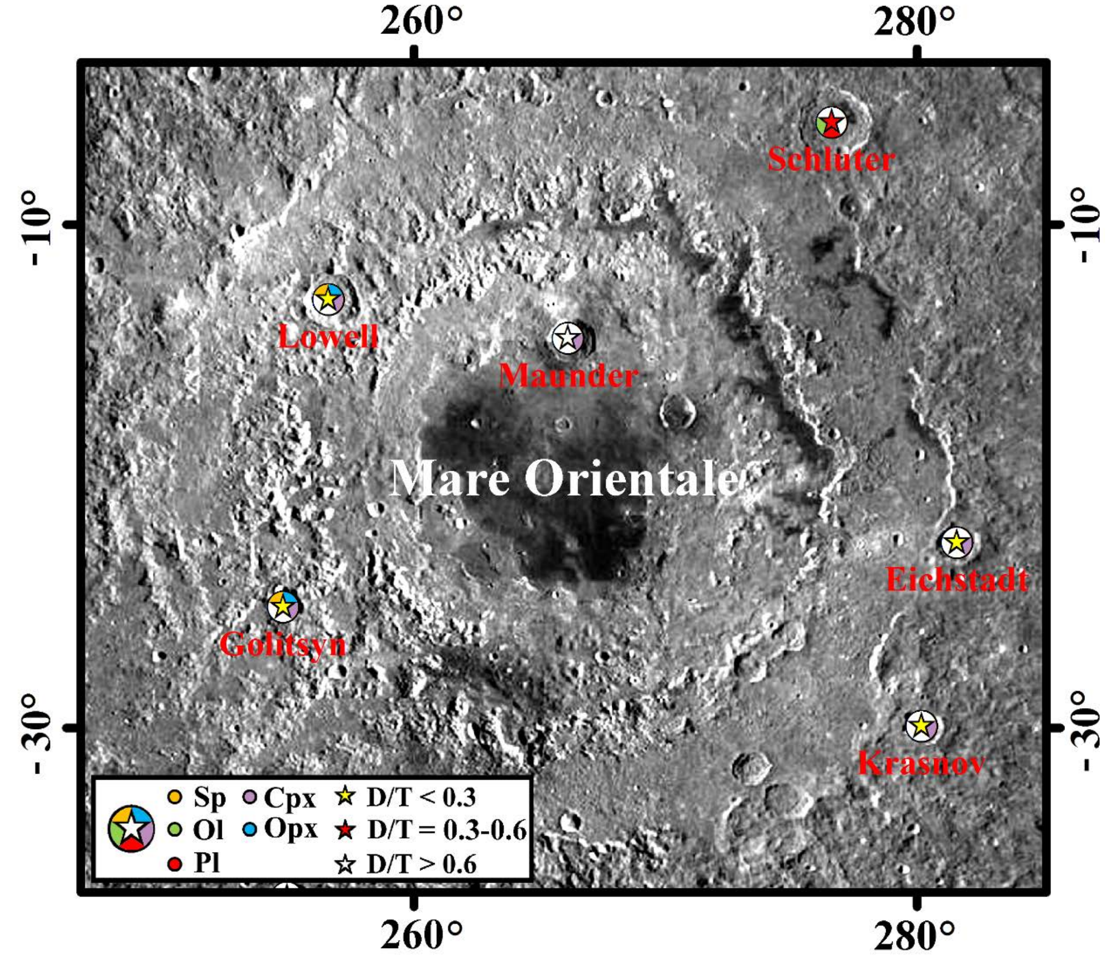
260°
280°
-10°
-30°
Schluter
Lowell
Maunder
Mare Orientale
Eichstadt
Golitsyn
Krasnov
● Sp
● Ol
● Pl
● Cpx
● Opx
★ D/T < 0.3
★ D/T = 0.3-0.6
☆ D/T > 0.6

Figure 3-17.

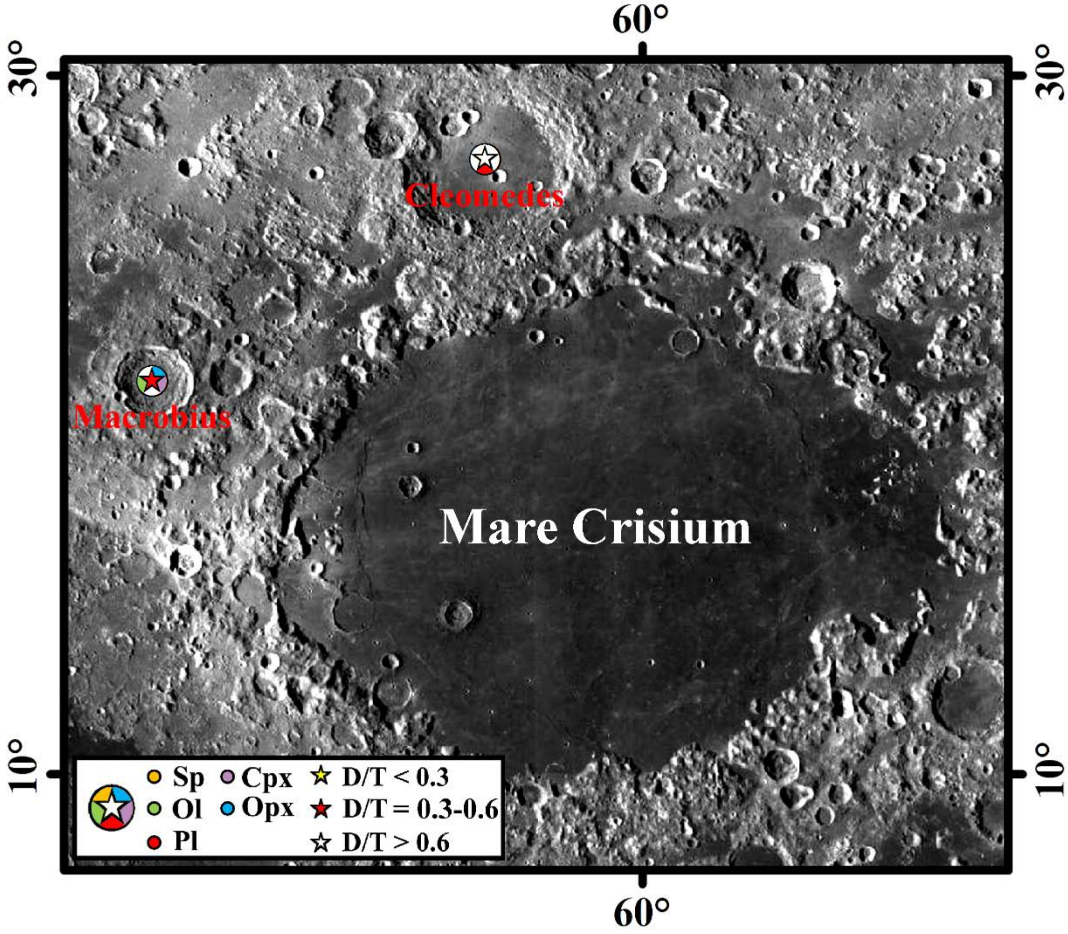
60°
30°
30°
Cleomedes
Macrobius
Mare Crisium
10°
10°
Sp
Cpx
D/T < 0.3
Ol
Opx
D/T = 0.3-0.6
Pl
D/T > 0.6
60°

Figure 3-18.

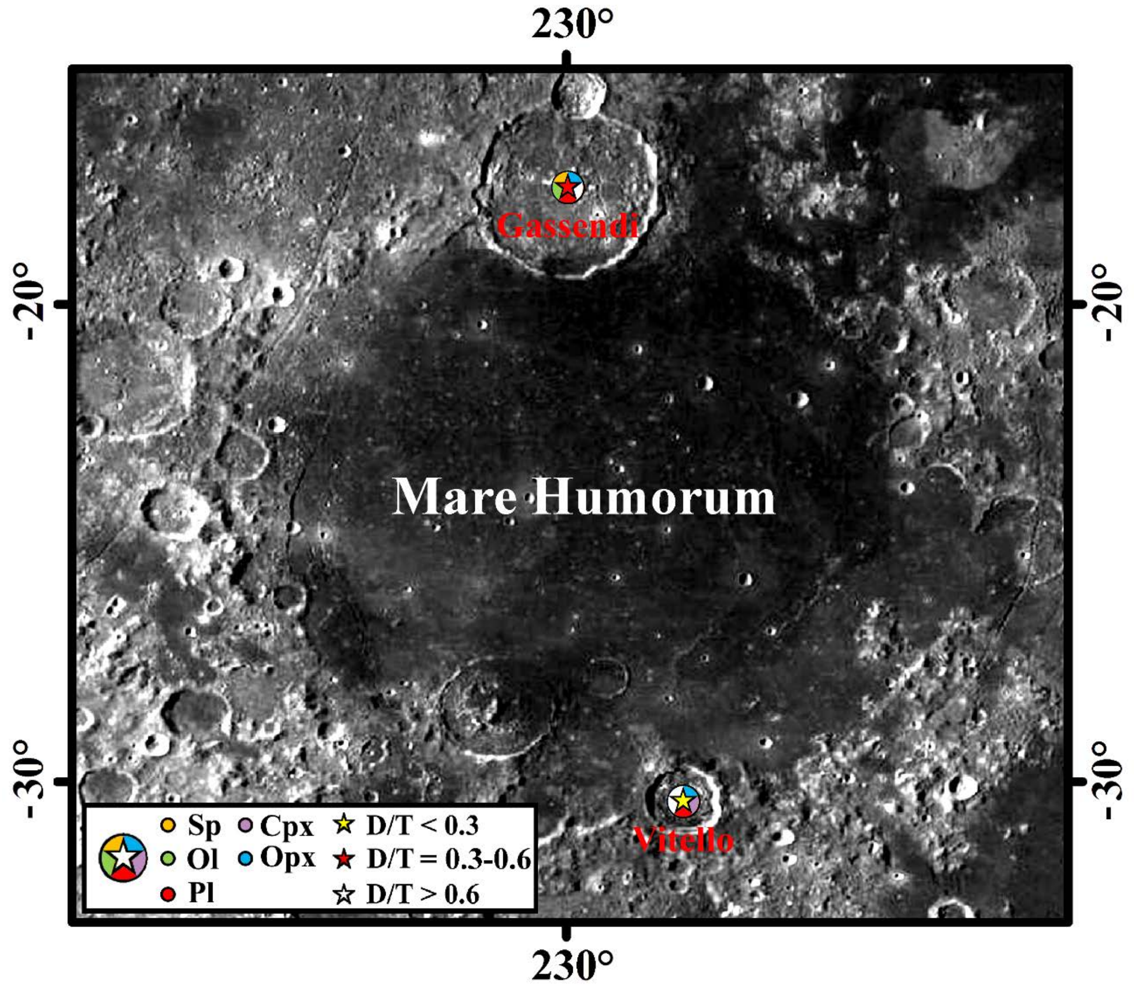
230°
-20°
-30°
Gassendi
Mare Humorum
Vitello
Sp
Ol
Pl
Cpx
Opx
D/T < 0.3
D/T = 0.3-0.6
D/T > 0.6

Figure 3-19.

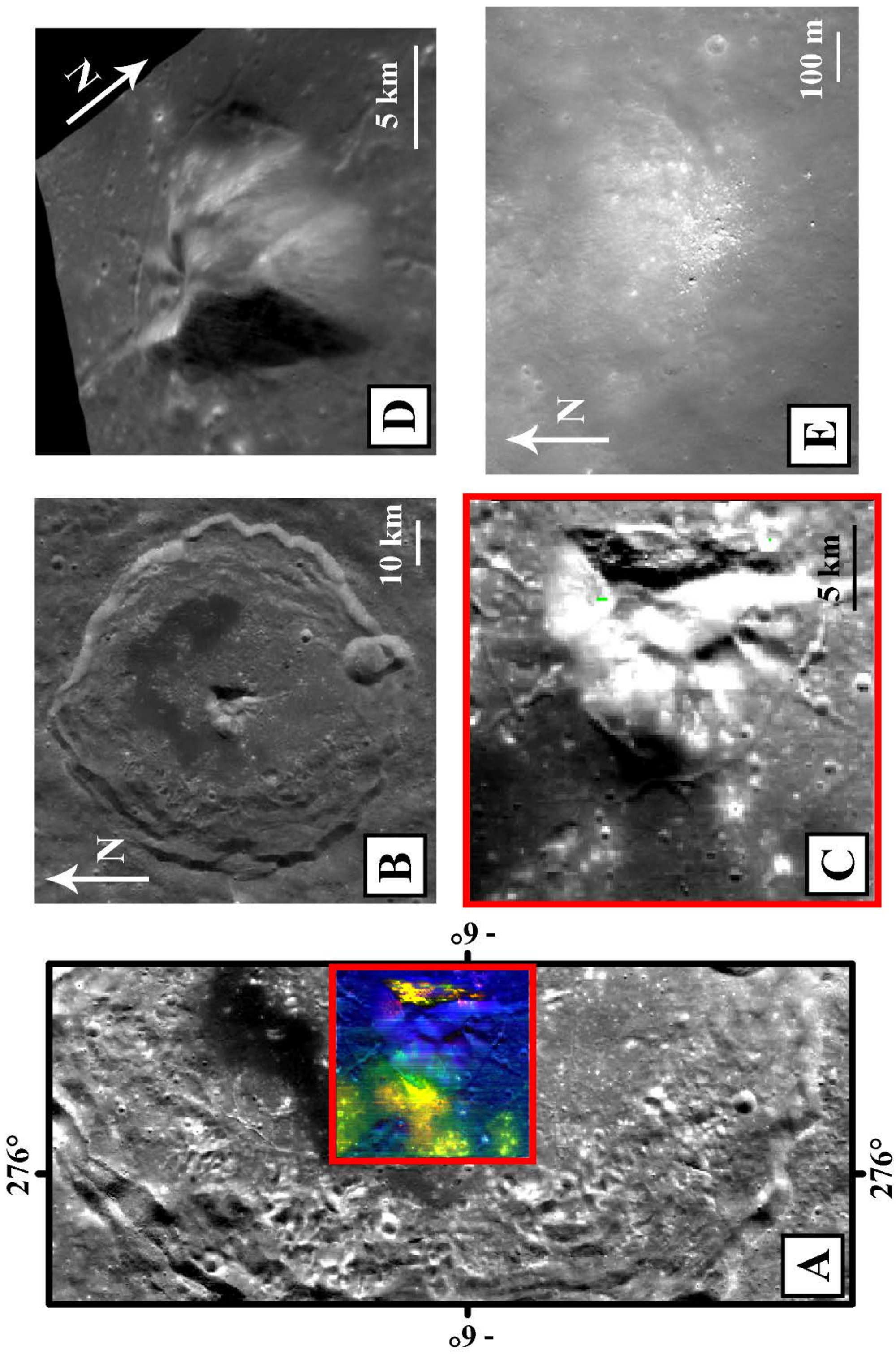

Figure 3-20.

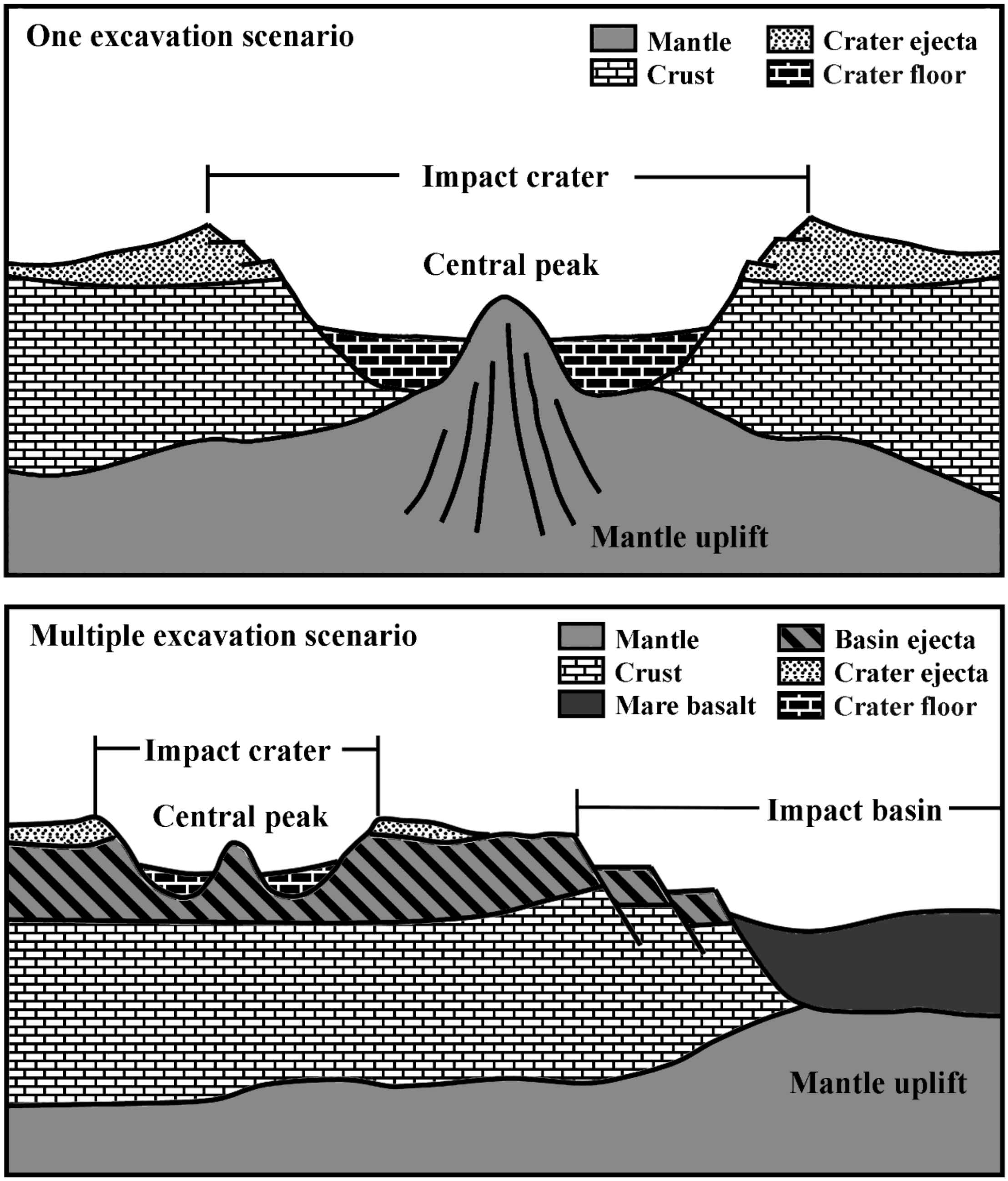
One excavation scenario
Mantle
Crust
Crater ejecta
Crater floor
Impact crater
Central peak
Mantle uplift
Multiple excavation scenario
Mantle
Crust
Mare basalt
Basin ejecta
Crater ejecta
Crater floor
Impact crater
Central peak
Impact basin
Mantle uplift

Figure 3-21.

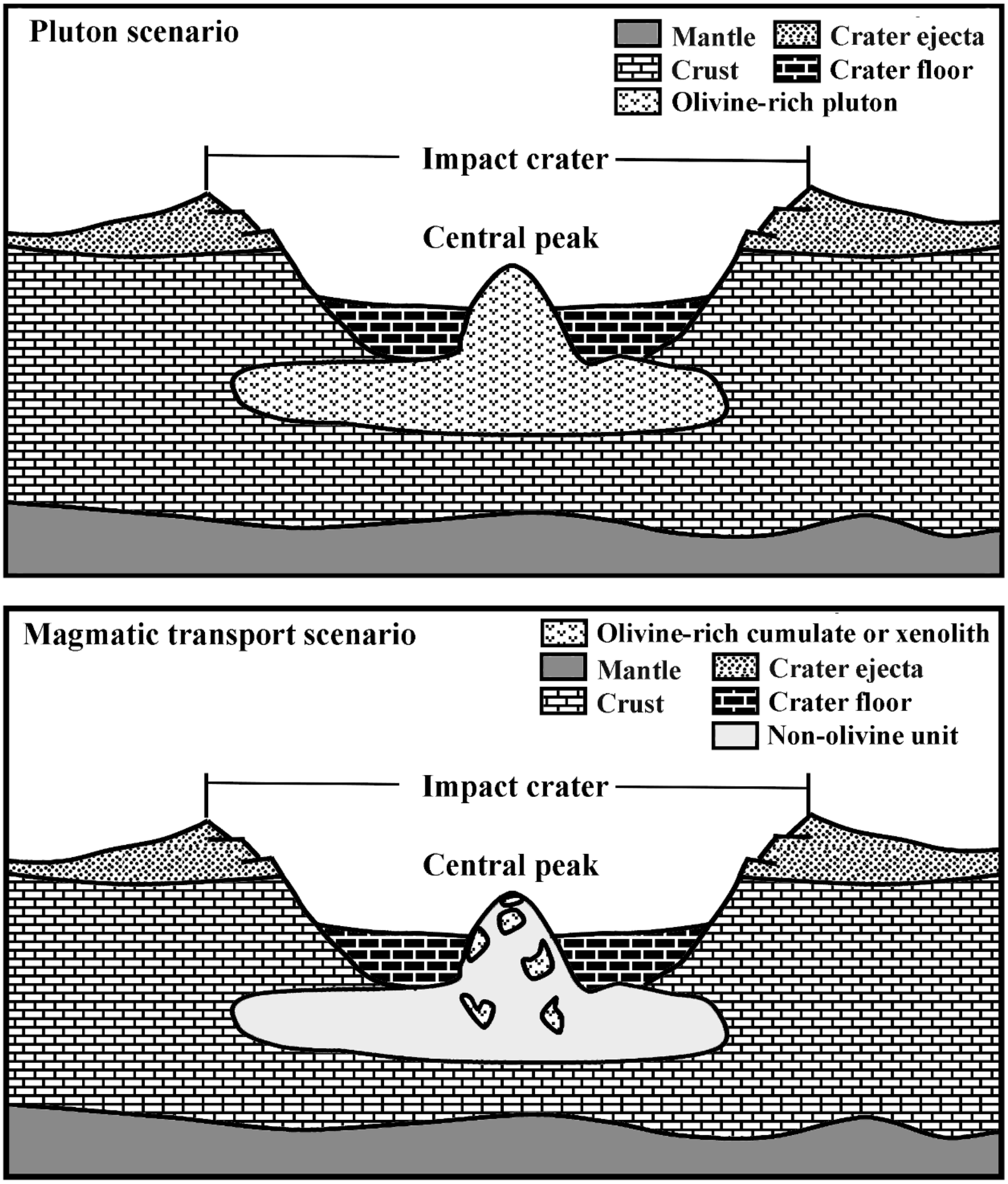
Pluton scenario
Mantle
Crater ejecta
Crust
Crater floor
Olivine-rich pluton
Impact crater
Central peak
Magmatic transport scenario
Olivine-rich cumulate or xenolith
Mantle
Crater ejecta
Crust
Crater floor
Non-olivine unit
Impact crater
Central peak

Figure 3-22.

References

Arai, T., et al., (2011). Possible Crustal Boundary Exposed at Lunar Copernicus Crater. *In Lunar and Planetary Science Conference* (Vol. 42, p. 2139).

Bell, P. M., et al., (1975). The problem of the origin of symplectites in olivine-bearing lunar rocks. *In Lunar and Planetary Science Conference* (Vol. 6, p. 231-248).

Bugiolacchi, R., et al. (2011). An in-depth look at the lunar crater Copernicus: Exposed mineralogy by high resolution near-infrared spectroscopy, *Icarus*, 213, 43–63.

Burns, R. G., (1993). Mineralogical Applications of Crystal Field Theory, 2nd ed., 551 pp., Cambridge Univ. Press, New York, doi:10.1017/CBO9780511524899.

Cahill, J. T. S., et al., (2009). Compositional variations of the lunar crust: Results from radiative transfer modeling of central peak spectra, *Journal of Geophysical Research*, 114(E9), 1–17. doi:10.1029/2008JE003282.

Cheek, L. C., and Pieters, C. M., (2014). The Second Conference on the Lunar Highlands Crust and New Directions. Reflectance spectroscopy of plagioclase-dominated mineral mixtures: Implications for characterizing lunar anorthosites remotely. *American Mineralogist*, 99(10), 1871-1892.

Cintala, M. J., and Grieve, R. A. F., (1998). Scaling impact melting and crater dimensions: Implications for the lunar cratering record, *Meteorit. Planet. Sci.*, 33(4), 889–912. doi:10.1111/j.1945-5100.1998.tb01695.x.

Croft, S. K., (1981). The excavation stage of basin formation-A qualitative model. *In Multi-ring basins: Formation and Evolution* (Vol. 1, pp. 207-225).

Dhingra, D., et al., (2011). Non-linear spectral un-mixing using Hapke Modeling: Application to remotely acquired M^3 spectra of spinel bearing lithologies on the moon. *In Lunar and Planetary Science Conference* (Vol. 42, p. 2431).

Dhingra, D., and Pieters, C. M., (2011). Mg-spinel rich lithology at crater Copernicus. *LPI Contributions,* 1646, 9.

Dhingra, D., et al., (2014). Nature and distribution of olivine at Copernicus crater: new insights about origin from integrated high resolution mineralogy and imaging. *In Lunar and Planetary Institute Science Conference* (Vol. 45, p. 1117).

Fassett, C. I., et al., (2011). Thickness of proximal ejecta from the Orientale Basin from Lunar Orbiter Laser Altimeter (LOLA) data: Implications for multi-ring basin formation. *Geophysical Research Letters,* 38(17).

Ford, C. E., et al., (1983). Olivine-liquid equilibria: temperature, pressure and composition dependence of the crystal/liquid cation partition coefficients for Mg, Fe^{2+}, Ca and Mn. *Journal of Petrology*, 24(3), 256-266.

Grieve, R. A. F., et al., (1981). Constraints on the formation of ring impact structures, based on terrestrial data. *In Multi-ring basins: Formation and evolution* (Vol. 1, pp. 37-57).

Hawke, B. R., et al., (1983). Spectral studies of the Aristarchus region: Implications for the composition of the lunar crust. *In Lunar and Planetary Science Conference* (Vol. 14, pp. 289-290).

Hawke, B. R., et al., (1995) Remote sensing studies of lunar anorthosite deposits. *In Lunar and Planetary Science Conference* (Vol. 26, p. 563).

Heiken, G., et al., (1991). Lunar sourcebook: A user's guide to the Moon. CUP Archive.

Hess, P. C., (1994). Petrogenesis of lunar troctolites. *Journal of Geophysical Research*, 99:19,083-19,093

Holsapple, K. A., (1993). The scaling of impact processes in planetary sciences. *Annual Review of Earth and Planetary Sciences*, 21, 333-373.

Isaacson, P. J., et al., (2011). Remote compositional analysis of lunar olivine-rich lithologies with Moon Mineralogy Mapper (M^3) spectra, *Journal of Geophysical Research*, 116, E00G11, doi: 10.1029/2010JE003731.

Jolliff, B.L., et al., (2000). Major lunar crustal terranes: Surface expressions and crust-mantle origins. *Journal of Geophysical Research*, 105:4197-4216

Le Mouélic, S., et al., (1999). The distribution of olivine in the crater Aristarchus inferred from Clementine NIR data. *Geophysical Research Letters*, 26(9), 1195-1198.

Le Mouélic, S., and Langevin, Y., (2001). The olivine at the lunar crater Copernicus as seen by Clementine NIR data. *Planetary and Space Science*, 49(1), 65-70.

Levinson, A. A., and Taylor, S. R., (1971). Moon rocks and minerals: scientific results of the study of the Apollo 11 lunar samples with preliminary data on Apollo 12 samples. *Elsevier*.

Lucey, P. G., et al., (1986). A compositional study of the Aristarchus region of the Moon using near-infrared reflectance spectroscopy. *Journal of Geophysical Research: Solid Earth* (1978–2012), 91(B4), 344-354.

Lucey, P. G., (2004). Mineral maps of the Moon. *Geophysical Research Letters,* 31(8).

Matsunaga, T., et al., (2008). Discoveries on the lithology of lunar crater central peaks by SELENE Spectral Profiler. *Geophysical Research Letters*, 35(23).

Mustard, J. F., et al., (2011). Compositional diversity and geologic insights of the Aristarchus crater from Moon Mineralogy Mapper data. *Journal of Geophysical Research: Planets* (1991–2012), 116(E6).

Pike, R. J., (1974). Ejecta from large craters on the Moon: Comments on the geometric model of McGetchin et al. *Earth and Planetary Science Letters,* 23(3), 265-271.

Pieters, C. M., (1982). Copernicus crater central peak: Lunar mountain of unique composition. *Science*, 215(4528), 59-61

Pieters, C. M., and Wilhelms, D. E., (1985). Origin of olivine at Copernicus. *Journal of Geophysical Research: Solid Earth* (1978–2012), 90(S02), C415-C420.

Pieters, C. M., (1986). Composition of the lunar highland crust from near-infrared spectroscopy. *Reviews of Geophysics*, 24(3), 557-578.

Pieters, C. M., et al., (1994). A sharper view of impact craters from Clementine data. *Science*, 266(5192), 1844-1848.

Pieters, C. M., et al., (2011). Mg-spinel lithology: A new rock type on the lunar farside. *Journal of Geophysical Research: Planets* (1991–2012), 116(E6).

Pieters, C. M., et al., (2014). The Second Conference on the Lunar Highlands Crust and New Directions. The distribution of Mg-spinel across the Moon and constraints on crustal origin. *American Mineralogist*, 99(10), 1893-1910.

Pinet, P. C., et al., (1993). Copernicus: A regional probe of the lunar interior. *Science*, 260(5109), 797-801.

Powell, K. E., et al., (2012). Olivine detections at the rim of Crisium basin with Moon Mineralogy Mapper. *In Lunar and Planetary Science Conference* (Vol. 43, p. 1689).

Prissel, T. C., et al., (2014). Pink Moon: The petrogenesis of pink spinel anorthosites and implications concerning Mg-suite magmatism. *Earth and Planetary Science Letters*, 403, 144-156.

Ryder, G., (1992). Chemical variation and zoning of olivine in lunar dunite 72415-Near-surface accumulation. *In Lunar and Planetary Science Conference* (Vol. 22, pp. 373-380).

Shearer, C. K., and Papike, J. J., (1999). Magmatic evolution of the Moon. *American Mineralogist,* 84, 1469-1494.

Shearer, C. K., et al., (2015). Exploring the Moon's Surface for Remnants of the Lunar Mantle 1. Dunite Xenoliths in Mare Basalts. A Crustal or Mantle Origin?. *In Lunar and Planetary Science Conference* (Vol. 46, p. 1426).

Smrekar, S., and Pieters, C. M., (1985). Near-infrared spectroscopy of probable impact melt from three large lunar highland craters. *Icarus*, 63(3), 442-452.

Snyder, G. A., et al., (1992). A chemical model for generating the sources of mare basalts: Combined equilibrium and fractional crystallization of the lunar magmasphere. *Geochim Cosmochim Acta* 56:3809-3823

Spudis, P. D., (1993). Geology Multi-ring Basins, 263 pp., Cambridge Univ. Press, New York.

Staid, M. I., and Pieters, C. M., (2001). Mineralogy of the last lunar basalts: Results from Clementine. *Journal of Geophysical Research: Planets* (1991–2012), 106(E11), 27887-27900.

Song, E., et al., (2013). Bulk mineralogy of lunar crater central peaks via thermal infrared spectra from the Diviner Lunar Radiometer: A study of the Moon's crustal composition at depth. *Journal of Geophysical Research: Planets*, 118(4), 689-707.

Sun, Y., et al., (2013). Detection of Mg-Spinel Bearing Central Peaks Using M^ 3 Images. *In Lunar and Planetary Science Conference* (Vol. 44, p. 1393).

Sun, Y., and Li, L., (2014). Global Investigation of Olivine Bearing Crater Central Peaks with M^3 Images. *In Lunar and Planetary Science Conference* (Vol. 45, p. 1653).

Sun, Y., et al., (2015). Characterization of lunar crust mineralogy with the Moon Mineralogy Mapper images: a new crustal compositional model. To be submitted.

Tompkins, S., and Pieters, C. M., (1999). Mineralogy of the lunar crust: Results from Clementine. *Meteoritics and Planetary Science*, 34(1), 25-41.

Wiseman, S. M., et al., (2012). Origin of Aristarchus Olivine Based on M^ 3 and Diviner Analyses. *In Lunar and Planetary Science Conference* (Vol. 43, p. 2515).

Wieczorek, M. A., et al., (2013). The crust of the Moon as seen by GRAIL. *Science* 6120, 671–675. (doi:10.1126/science.1231530)

Yamamoto, S., et al., (2010). Possible mantle origin of olivine around lunar impact basins detected by SELENE. *Nature Geoscience*, 3(8), 533-536.

Yue, Z., et al., (2013). Projectile remnants in central peaks of lunar impact craters. *Nature Geoscience*, 6(6), 435-437.

CHAPTER 4

CHARACTERIZATION OF LUNAR CRUST MINERALOGY WITH MOON MINERALOGY MAPPER IMAGES:

A NEW CRUSTAL COMPOSITIONAL MODEL

Abstract

We propose a new three-layer model for the lunar crust through a global mineralogy survey of 166 impact crater central peaks using the Moon Mineralogy Mapper (M^3) images. The ratio D (origin depth of the central peak) to T (average crustal thickness) is used to describe the vertical variations of the lunar crust. The uppermost layer ($D/T < 0.3$) is anorthositic or noritic megaregolith that has been heavily modified by the impact cratering. The middle layer ($D/T = 0.3\text{-}0.6$) contains Mg-suite rock equivalent (mafic materials and Mg-spinel anorthosite), which indicates the post-Lunar Magma Ocean magmatism frequently occurred within this layer. For the lowermost layer ($D/T > 0.6$), we speculate a global pure anorthositic layer exist which might represent the primitive crustal composition produced by Lunar Magma Ocean (LMO). In addition, no olivine bearing materials were identified within the South-Pole Aitken Terrane (SPAT) which might imply the composition of the lunar upper mantle is orthopyroxene rather than olivine. All the mafic materials and Mg-spinel are concentrated within Procellarum KREEP Terrane (PKT) that reveals the secondary magmatism have often occurred underneath PKT. Feldspathic Highlands Terrane (FHT) is suggested Ca-rich because more clinopyroxene (Cpx) has been identified than the orthopyroxene (Opx). In order to validate the new three-layer model, accurate estimation of pyroxene (Px), additional regions (e.g. basins, crater wall and ejecta) and datasets (e.g. LRO, Diviner) need to be taken into account in the future.

1. Introduction

Analysis of the lunar samples returned by the Apollo and Luna missions (1969-1976) as well as lunar meteorites provide first-hand information about lunar crustal rock types. It revealed the compositional heterogeneity of the lunar crust [Heiken et al., 1991] and grouped the lunar highland rock into two primary categories: ferroan anorthosite and Mg-suite rocks. Ferroan anorthosite is primarily composed of the Ca-rich plagioclase (An content generally >94) with much fewer, low Mg/(Mg+FeO) mafic silicates (pyroxene and olivine). The Mg-suite contains norite, gabbro, troctolite, and dunite, which all are made up of plagioclase and relatively high Mg/(Mg+FeO) mafic silicates. The use of remote sensing data also leads to an improved understanding of the compositional diversity of the lunar crust. Jolliff et al. [2000] conducted a new geochemical investigation of the lunar surface using the distribution and concentrations of Fe and Th derived from Lunar Prospector and Clementine spacecraft images, and classified the lunar crust into three distinct provinces: Feldspathic Highlands Terrane (FHT), Procellarum KREEP Terrane (PKT), and South Pole-Aitken Terrane (SPAT). FHT is characterized by high albedo, extensive cratering, elevated topography, and highly anorthositic compositions. PKT is delineated primarily on the basis of its high Th concentration and the presence of KREEP. Most of the crust within PKT has a composition similar to KREEP basalt or its differentiated equivalent (possible Mg-suite). SPAT is a compositional anomaly area with high Fe but lacking KREEP, indicating its major rock type norite.

The compositional variation of the lunar crust is fundamentally ascribed to crystallization and differentiation of a lunar magma ocean (LMO). The LMO hypothesis has been widely used to explain the formation of the lunar crust and mantle [e.g., Smith et al., 1970; Wood et al., 1970; Warren and Wasson, 1977, 1979; Warren, 1985], which basically states that mafic cumulates first crystallized from the magma ocean to from the mantle, and anorthositic cumulates floated up to form the crust [Smith et al., 1970; Wood et al., 1970]. Post-LMO activities due to melting of the mafic cumulates gave rise to the additional compositional complexity of the lunar crust as indicated by other igneous assemblages (e.g. Mg-suite) [Shearer et al., 2006]. Moreover, the lunar crust was subject to unceasing impact bombardment, which is responsible for the formation of thin regolith and thick megaregolith and fractured crustal rocks [Toksöz et al., 1974; Hartmann, 1973]. While this simplified scenario appears to be reasonable for explaining the diversity of the lunar crust to the first order, a number of details with respect to the formation and evolution of the lunar crust are still unclear. For example, is the ferroan anorthosite ubiquitous in both lateral and vertical directions of the lunar crust? What is the spatial scale of the Mg-suite magmatism in the lunar crust? These unsolved questions have stimulated numerous studies of lunar crust rock types and mineral compositions.

Previous studies have come up with different models to characterize petrology and mineralogy of the lunar crust, as well as their variation with depth. Ryder and Wood [1977] analyzed melt-rock deposit samples (15445, 15455) and proposed the lunar crust could be composed of two (anorthositic gabbro above Low-K Fra Mauro (LKFM) basalts) or three compositional layers (anorthositic gabbro, LKFM basalts and mafic ANT including troctolites, spinel-troctolites, dunite and norite), in which mafic minerals increase with depth. A different two-layer lunar crust model was also proposed by Spudis et al. [1984] and Spudis and Davis [1986] based on their studies of lunar samples, orbital geochemical data and impact cratering processes on the Moon. This model stated that the Moon had a ferroan anorthositic upper layer (Al_2O_3 ~26-28 wt. %) overlaying a mafic noritic lower layer (Al_2O_3 ~20 wt. %). Meantime, Spudis and Davis [1986] estimated the thickness of the anorthositic upper layer to range from ~10 km to ~35 km. Through examining near-infrared reflectance spectra of lunar highlands, Pieters [1986] investigated the petrological composition of the lunar nearside crust and demonstrated the diversity of the lunar crust in the vertical direction. An expansion of this study was undertaken later by Tompkins and Pieters [1999] who analyzed ultraviolet and visible multispectral Clementine images of 109 crater central peaks. Tompkins and Pieters [1999] suggested the lunar crust is extremely anorthositic (An ~82%) in the upper layer (~5-30 km) and less mafic (An ~75%) than previously assumed in the lower crust (~25-55 km). Combining a quantitative geophysical model with the compositional results from Tompkins and Pieters [1999], Wieczorek and Zuber [2001] identified distinct compositional complexity between the upper and lower crust and emphasized the upper crust is more extremely anorthositic (An ~88%).

Some researchers pointed out three-layer models are more suitable for describing the structure of the lunar crust. The earliest three layer model was proposed by Ryder and Wood [1977] arguing for three compositional layers for the lunar crust (anorthositic gabbro, LKFM basalts and mafic ANT). Based on the orbital geochemical information associated with analysis of large impact basins, Spudis et al. [1999] and Bussey and Spudis [2000] proposed another three-layer crustal model asserting that the lunar crust has a noritic upper layer (FeO ~4-6 wt. %, Al_2O_3 ~26 wt. %) down to depths of ~15-20 km, pure anorthositic middle layer (FeO <2 wt. %, Al_2O_3 >33 wt. %) at depths between ~15 and ~35 km and more mafic lower layer (FeO ~9-12 wt. %, Al_2O_3 ~18-20 wt. %) at depth of ~ 35 to 65 km.

The three-layer model has been supported by a global detection of lunar anorthosite with multispectral images [Hawke et al., 2003]. Recently, Taylor and Wieczorek [2014] have redefined the lunar bulk chemical composition for three-layer lunar crust models.

In contrast to the two- and three-layer models, two studies on central peak mineral composition with Clementine images [Cahill et al., 2009] and Diviner data [Song et al., 2013] did not find systematic compositional heterogeneity in the vertical direction of the lunar crust. Cahill et al. [2009] also suggested the lunar crust composition is independent of lunar terranes, and the major crustal composition is similar to Mg-suite rocks found lunar samples. They also found that while mafic materials seemed to increase with depth in PKT and SPAT, but show otherwise for the FHT crust.

Although the lunar crustal structure and evolution have been investigated for decades, the previous crustal models built upon the limited returned lunar samples and low quality of remote sensing data cannot accommodate new observations made by recent lunar missions, and may not be valid. For instance, the average crustal thickness has been revised to 34-43 km derived from Gravity Recovery and Interior Laboratory (GRAIL) data [Wieczorek et al., 2013], which is much thinner than previously estimated (60-70 km). The new lunar crustal thickness implies the previous crustal models probably misclassified part of the lunar mantle as the lunar crust. Hence, it is necessary to conduct a new investigation of the lunar crustal composition and structure with recent data in order to improve our understanding of lunar thermal history and magmatic evolution. Recently acquired global, high-spatial resolution hyperspectral Moon Mineralogy Mapper (M^3) images provide us such an opportunity to examine compositional trends across the entire lunar crust. In this study, a systematic screening of lunar crater central peaks using the M^3 images was conducted to examining the mineral composition of the lunar crust. Combining the origin depth of the central peak with new measurements of lunar crustal thickness, the vertical variation of the lunar crust is refined and a new crustal model is proposed.

2. Methodology

2.1. Lunar crater central peak

The study of the impact crater central peaks offers a practical approach for identifying the composition of the lunar crust. Commonly, the materials in the crater central peaks could reflect the composition of deep layers (crust or mantle), because the lunar impact craters larger than 35 km in diameter have uplifted the central peaks as a result of deep-seated materials rebounding to the surface during impact cratering process. Previous studies of central peaks indicate that the depth from which the peak material originates is a function of final crater diameters [Cintala and Grieve, 1994; 1998; Melosh, 1989; Roddy, 1977]. Roddy [1977] and Melosh [1989] advocated that the pre-impact depth of central peak material is roughly 0.1 or 0.2 times of the crater diameter. Cintala and Grieve [1998] considered both the excavation of crustal materials and the extent of the impact melting to predict the maximum origin depth of central peaks (D) which is a function of final impact crater diameter (d): $D=0.109*d^{1.08}$. As in Cahill et al. [2009], this equation was used in this study.

Investigated lunar crater central peaks were selected from 1559 lunar craters listed in the USGS crater database. The selection of these lunar crater peaks was based on the following criteria: 1) Craters are larger than 35 km in diameter; 2) craters exhibit obvious peak topography based on M^3 images and Lunar Orbiter Laser Altimeter (LOLA) elevation data; 3) central peaks are entirely covered by M^3 L2 reflectance images. Based on these criteria, 317 craters are determined to have central peaks (Figure 4-1). However, only 166 of them were selected for further analysis because they show significantly strong spectral absorption features and likely represent exposed deep pristine materials from the lunar crust or upper mantle. The selected 166 craters ranges from 35.1 to 199.5 km in diameter (d), and from 5.05 km to 33.21 km in depth based on $D=0.109*d^{1.08}$[Cintala and Grieve, 1998].

2.2. Spectral analysis

The Moon Mineralogy Mapper (M^3) is designed to characterize and map lunar minerals and rock composition in the context of their geologic evolution [Pieters et al., 2009]. As the first hyperspectral sensor (spectral range: 430-3000 nm) imaging the lunar surface, M^3 was operated in global and target modes [Green et al., 2011]. In the global mode, the observations of M^3 were made at spectral resolutions of 20-40 nm and divided into seven optical periods (Ops) on the basis of varied coverage, phase angle, altitude, and spatial resolution. Among those OPs, OP1A, OP1B, OP2A, OP2B have a spatial resolution of 140 m/pixel and are mainly located on the near side of the Moon at high phase angles. In contrast, OP2C1, OP2C2, and OP2C3 have a resolution of 280 m/pixel at lower phase angles. A detailed summary of the OPs is given in Besse et al. [2013]. Images from the global mode cover more than 90% of entire lunar surface, while those in the target mode represent a limited number of images at 10 nm spectral resolution and 70 m/pixel spatial resolution [Boardman et al., 2011]. Primary data used in this study are M^3 L2 (level 2) reflectance images in the globe mode, which were released on Dec. 8, 2011. M^3 L2 data were derived from M^3 L1B (level 1B) radiance data and calibrated for statistical polishing, thermal removal [Clark et al., 2011] and photometric correction [Besse et al., 2013]. Data analysis for this investigation was concentrated on M^3 images at 140 m resolution. 280 m resolution M^3 images were analyzed when higher resolution images were not available or at low quality.

M^3 images of 166 craters were downloaded from the NASA PDS website. These images were geometrically corrected and smoothed for noise reduction. For the geometric correction, the original reflectance images were warped based on latitude and longitude values of each pixel. For the noise reduction, pixels with negative reflectance values or within shadow were eliminated, and the spectra were smoothed using a moving window average method. After spectral smoothing, 72 bands from 540 nm to 2537 nm in which spectrally diagnostic absorptions for minerals are present were retained for further analysis.

Continuum removal was applied to each image spectrum to isolate mineral diagnostic absorption features from the spectral continuum. Based on the diagnostic absorption feature of common lunar minerals (Mg-spinel [Sp] ~ 2 μm, Olivine [Ol] ~ 1.05 μm, Crystalline plagioclase [Pl] ~ 1.25 μm, Orthopyroxene [Opx] < 0.95 μm, ~2 μm, Clinopyroxene [Cpx] > 0.95 μm, ~ 2 μm), we created a set of criteria for determining the presence of these minerals (Table 1). The absorption depth (AD) of 0.05 was used to determine the presence of diagnostic absorption feature and 0.02 to represent the absence of absorption. In order to reduce uncertainties induced by imperfect thermal removal, as well as illumination differences due to local topography, multi-temporal M^3 images were processed and analyzed for each crater to ensure the reliability of the mineral detection.

Each pixel detected for the presence of individual minerals can represent a mineral mixture rather than a single pure mineral, so it is critical to understand the spectral feature of mineral mixtures. On the basis of previous mineral spectral mixing experiments [e.g.

Crown and Pieters, 1987; Cloutis et al., 1986; Ohtake et al., 2009; Serventi et al., 2013], pyroxene (Px) is a spectrally dominating mineral in mineral mixtures and delectable even at 10%, but other minerals must have relatively high abundance to be detectable . Therefore, pixels showing detectable minerals (Sp, Ol, Pl) are expected to be relatively pure except for Px. Px-bearing pixels most likely represent mixtures of Px and other minerals.

In order to investigate the compositional variation of the lunar crust, a semi-quantitative analysis was conducted to assess the likelihood for the presence of each mineral in the investigated central peaks. The minimum number of pixels (MNP) at which a mineral had been detected was used to quantify the presence of relatively pure materials (Sp, Ol, and Pl). Note that the MNP is a conservative and relative estimate for the presence of a mineral considering possible detection inconsistency among multi-temporal images. The number of craters (NC) which have Px-bearing central peaks was used to quantify the presence of Cpx and Opx, and comparing the importance of Cpx relative to Opx. However, NC cannot be used for comparison between a Px and other minerals. For the purpose of comparison among different terranes or different layers and elimination of the influence on unevenly distribution of examined crater, we used NCI (the number of craters investigated within a certain terrane or layer) to normalize the MNP and NC, which is different from the method used in Sun and Li [2015]. The ratio of MNP to NCI is used to represent the likelihood for the presence of Sp, Ol and Pl in the individually investigated area and NC/NCI is used for Px. For instance, MNP for Sp in SPAT is 14 and NCI of SPAT is 34. The MNP/NCI (0.41) is used to exhibit the likelihood of presence for Sp in SPAT. The results for one example crater (Jackson) will be present in 3.1 to illustrate how to use this semi-quantitative analysis.

2.3. Lunar crustal thickness

Lunar crustal thickness is fundamentally important for describing the vertical structure of the lunar crust. The crustal thickness has been revised several times. The initial analysis of the Apollo seismic data indicated that the crust was about 55–60 km thick [Toksöz et al., 1974; Nakamura, 1983; Goins et al., 1981]. Laser altimeter data were collected showing the farside crust would be thicker than that of the nearside [Kaula et al., 1974]. The Clementine and Lunar Prospector missions obtained the first global topographic maps of the Moon [Smith et al., 1997] and allowed for the first construction of global crustal thickness models. After that, many studies suggested that the lunar crust was thinner than previously thought [e.g., Wieczorek and Phillips, 1997; Khan et al., 2000; Khan and Mosegaard, 2002; Lognonné et al., 2003; Wieczorek et al., 2006]. Most recent estimation on the basis of GRAIL gravity data indicated that the thinnest crust was located beneath the Crisium and Moscoviense impact basins and a new estimate for the average crustal thickness is 34 km in light of Model 1 in Wieczorek et al. [2013]. The crustal thickness map (Model 1) of the Moon used in this study has a spatial resolution of 0.25 degree per pixel and was downloaded from Mark Wieczorek's website (http://www.ipgp.jussieu.fr/~wieczor/GRAILCrustalThicknessArchive/GRAILCrustalThicknessArchive.html). According to this thickness map, all the investigated crater central peaks were determined to originate within the lunar crust except for Petavius and Humboldt that may have excavated the lunar upper mantle. In order to figure out where the peak materials originated within the crust relative to the crust-mantle interface, the ratio of origin depth (D) to average crustal thickness (T) of the central peak was used to describe the vertical variation of mineralogy in the lunar crust. A D/T value less than 1 indicates the original position of central peaks is within the crust; the smaller D/T is, the shallower original position should be. Alternatively, D/T values larger than 1 mean the mantle origin of the materials in those peaks, and equal to 1 the crust-mantle origin.

3. Results

A central peak example (Jackson) is presented to illustrate how spectral analysis is used to characterize the compositional diversity and the origin of the central peak relative to the crust-mantle boundary. The rest of results from this study are presented in terms of the compositional complexity among three major terranes without considering the origin depth of the central peaks, and the vertical heterogeneity of the lunar crust relative to the ratio D/T.

3.1. Analysis of Jackson central peak

Jackson is a prominent large impact crater (~71 km in diameter) that is located on the far side of the Moon. Tompkins and Pieters, [1999] investigated the central peak of Jackson with Clementine images and suggested the materials in Jackson central peak are 80-90% plagioclase with pyroxene and olivine. Later, quantitative analysis of Jackson central peak mineralogy exhibit the major lithology is anorthositic gabbro consist of 10.5 vol % olivine, 6.4 vol % orthopyroxene, 18.4 vol % clinopyroxene, and 64.7 vol % plagioclase [Cahill et al. 2009]. Matsunaga et al. [2008] identified the presence of crystalline plagioclase in Jackson central peak with the observations of Selenological and Engineering Explorer (SENELE) Spectral Profiler (SP) data. The detection results for Jackson central peak in this study are in line with the previous studies.

Jackson central peak can be entirely covered by two M^3 images including 'M3G20090621T025007_V01_RFL.IMG' and 'M3G20090718T101402_V01_RFL.IMG'. Figure 4-2 shows the detection results for Pl-bearing pixels (red color) as an example with these two images respectively. 260 pixels were identified the presence of Pl in the Jackson central peak with ‘M3G20090621T025007_V01_RFL.IMG’, and 14 pixels were detected the presence of Pl with ‘M3G20090718T101402_V01_RFL.IMG’. ‘14’ was used as MNP_{Pl} to represent the likelihood of presence for Pl in Jackson central peak rather than ‘260’ as a conservative estimation among multi-temporal images. Using the same two images, the MNP_{Ol} was determined as 3 to represent the likelihood of presence for Ol in Jackson central peak. No Sp-bearing pixel was found in either image. The presence of Opx and Cpx were both identified in Jackson central peak. However, the amount of Opx and Cpx cannot be determined with certainty because the Px-bearing pixel probably represents a mixture rather than pure Px on the basis of spectroscopy knowledge discussed in 2.2. Even though more Cpx-bearing pixels were detected than Opx-bearing pixels, it does not necessarily represent more Cpx content in Jackson central peak than Opx. Therefore, we only use NC to represent the presence of Px. NC_{Opx} for Jackson central peak was marked as 1 and NC_{Cpx} is also 1.

The origin depth (D) of Jackson central peak is 10.95 km based on $D=0.109*d^{1.08}$ (d: crater diameter of Jackson=71.38 km) [Cintala and Grieve, 1998]. The average crustal thickness (T) of Jackson central peak is 51.94 km based on the GRAIL crustal thickness map [Wieczorek et al., 2013]. So D/T is calculated and equals to 0.21 which imply the materials in Jackson central peak stemming from the upper crust. All the results of Jackson central peak were tabulated in Table 4-2 as well as other investigated crater central peaks.

3.2. Mineral variations of the lunar crust among three distinct terranes

Among 166 investigated craters, 38 central peaks were identified to be Sp-bearing [Sun et al., 2013], 14 Ol-bearing [Sun and Li, 2014], 21 Pl-bearing, and 151 Px-bearing with 122 of them being Opx-bearing and 100 Cpx-bearing (Figure 4-3). The presence of Cpx is more common than expected which is consistent with the result from an analysis of SENELE SP data [Ogawa et al., 2011]. Features of each investigated central peak were tabulated in Table 4-2 including center coordinate, diameter (d), origin depth of central peak (D), average crustal thickness (T), D/T, MNP (Sp, Ol, Pl), and NP (Opx, Cpx).

The compositional variability within the three different terranes without considering the origin depth of the central peaks is shown in Figure 4-4, and summarized in Table 4-3A. Table 4-3A1 presents for each terrane the number of investigated crater central peaks (NCI), MNP for relatively pure materials (Sp, Ol, Pl), NC for Opx and Cpx. The normalized MNP and NP by NCI are shown in Table 4-3A2, which were used to generate Figure 4-4.

For the PKT, the terrane with high abundances of incompatible elements and iron content [Jolliff et al., 2000], shows the relatively high likelihood for the presence of each mineral considered in this study. Specifically, Ol-bearing materials are found to concentrate within PKT, which is consistent with the global olivine map presented by Lucey et al. [2004]. The MNP/NCI is grossly high for Ol in PKT (21.33) relative to FHT (0.26) and SPAT (0.00). Opx was detected more in PKT than FHT but has the least Cpx among three terranes. PKT is also identified to have the highest likelihood for the presence of Sp (MNP/NCI=4.87). Relatively high amounts of Ol, Opx and Sp in PKT may indicate the highly frequent post-LMO magmatism underneath this area, which has been confirmed by the analysis of Th and other incompatible elements on the lunar surface [Lawrence et al., 1998]. Moreover, PKT is determined to have a relatively high amount of Pl, which is disagreement with the results derived from SELENE SP data that no pure anorthosite has been identified in PKT [Yamamoto et al., 2012]. This inconsistency may result from different spatial resolutions between SP (~1.7 km at the equator) and M^3 (140 m or 280 m).

FHT is highly feldspathic, and probably represents the primary magma ocean flotation crust of the Moon [Wieczorek et al., 2006]. The observations in this study show that FHT has the highest likelihood for the presence of Pl- (MNP/NCI=7.23) and Cpx- (NC/NCI=0.74) bearing materials among the three terranes, indicating the extremely anorthositic nature of FHT [e.g., Nyquist and Shih 1992] and the enrichment of FHT in Calcium. Usually, high-Ca composition crystallizes preferentially on the basis of Bowen's reaction series [Bowen, 1922]. Hence, the most abundant Ca content in FHT is consistent with the ancient age of this terrane. The observations to both Pl and Cpx provide critical evidence for the generation of the primordial FHT crust from LMO. Additionally, FHT was detected to have a considerable amount of Sp-bearing and very few Ol- bearing pixels, suggesting the post-LMO magmatism in FHT is not as extensive as PKT.

SPAT is characterized by its geochemical anomalies (high FeO, poor KREEP) and the largest basin on the Moon. This study shows the Opx is the only dominant mineral determined in SPAT and in terms of the presence likelihood, and all other minerals considered show the lowest value for MNP/NCI (Sp, Ol, Pl) and NC/NCI (Cpx) across the three terranes. This result implies that the deep-seated materials that were excavated by SPA are dominated by Opx instead of Ol. This conclusion is in good agreement with the results from cratering simulation [Melosh, 2014] and seismic studies of the lunar upper mantle [Khan et al. 2006].

3.3. Crustal mineralogy and stratigraphy

All five investigated minerals could exist at various depths of the lunar crust shown in

Figure 4-5. Correlations between MNP of Sp, Ol, and Pl with D/T reflect that Sp and Ol are concentrated within the middle part of the crust (D/T=0.3-0.6) and Pl appears to increase with D/T culminating in the deep layer of the crust (D/T>0.6). Based on the detected vertical distribution of minerals in the entire lunar crust, three compositionally distinct layers are evident: the uppermost layer (D/T < 0.3), middle layer (D/T=0.3-0.6), and lowermost layer (D/T>0.6), as shown in Figure 4-6A, and summarized in Table 4-3B. With the exception of Pl, all the investigated minerals show the highest normalized MNP and NC within the middle layer. The compositional trend for mafic minerals shown in previous studies was not observed in our results. The amount of Pl is concentrated in the lowermost layer and increases from the uppermost to the lowermost layer. The compositional variation of the three terranes for each layer is shown in Figure 4-7 and summarized in Table 4-4.

In the uppermost layer (D/T < 0.3), shown in the first column of Figure 4-7, all the identified minerals show the low likelihood for their presence. FHT has the highest likelihood for the presence of Sp, Pl, and Cpx, but a small amount of Ol and the lowest likelihood for the presence of Opx. PKT contains a considerable amount of Sp, Opx and Cpx, and shows the highest value of MNP/NCI for Ol (Table 4-4). SPAT has the highest likelihood for the presence of Opx, but Ol and Pl bearing materials was not identified within this layer. Compared with two lower layers (Figure 4-6A), the uppermost layer shows a relatively lower content of spectrally detectable materials that may be related to heavy impact cratering on the top layer of the lunar crust.

The middle layer (D/T=0.3~0.6) is rich in the most of the common minerals except for Pl (Figure 4-6A). Within this layer (the middle column in Figure 4-7), PKT exhibits the highest likelihood for the presence of Ol, Sp and Pl, and a considerable amount of Px. In contrast, FHT shows a lower possibility for the presence of Ol and Sp but a larger amount of Cpx than PKT. SPAT does not display the presence of Ol and Sp but shows the highest likelihood for the presence for Opx. Within the middle layer, Opx was detected more than Cpx in all the three terranes. The extremely high value of MNP/NCI for Ol (27.35 in Table 4-3B2) and the presence of large amount of Opx and Sp indicate that the post-LMO magmatism frequently occurred within this layer.

The lowermost layer (D/T>0.6) has been detected to have the largest amount of Pl (nearly pure ferroan anorthosite). All the investigated minerals show the relatively low likelihood for the presence except for the Pl (Figure 4-6A). Within this layer (the left column in Figure 4-7), Pl has been identified in both FHT and PKT but not in SPA. PKT contains the most Ol and Sp; FHT has the largest amount of Pl but very little other minerals; SPAT is identified for the presence of Sp and Px and contains more Opx than Cpx which is not the case for PKT and FHT. In PKT and FHT, the likelihood for the presence of Px is apparently less than the two upper layers. Very high values of MNP/NCI for Pl in PKT (35.27) and FHT (40.83) shown in Table 4-4 indicate that the primitive crustal materials are possibly retained within the lowermost layer.

4. Discussion

4.1. Anorthositic crust

The presence and distribution of anorthosite in the lunar crust provide important constraints on the nature of LMO. Numerous previous studies pay attention to the crustal anorthosite. Ferroan anorthosite, the major composition of the lunar crust is commonly determined on the basis of mineralogical and geochemical analysis of lunar samples returned by Apollo missions [e.g., Taylor, 1991]. Investigations of telescopic near-infrared reflectance spectra exhibited the presence of anorthosite covering tens of square kilometers on the lunar nearside. All those anorthosites are mainly located on the inner rings of impact basins such as the inner Rook Mountains of the Orientale basin and the Grimaldi basin [Spudis et al., 1984; Hawke et al., 1991; 1993; 2003]. Other exposures of anorthosite were identified near the outer rings of basins and also were found in the central peaks and walls of impact craters. [e.g., Hawke et al., 1993; Pieters, 1986; Coombs et al., 1990]. Global detection of anorthosite has been conducted with Clementine UVVIS spectra. Hawke et al. [2003] suggested the anorthosite existed in the inner rings of basins using the estimation of FeO abundance from Clementine images (FeO abundance is less than 4 wt. % which probably represents the abundance of plagioclase is more than 90%). A great number of anorthositic central peaks which were likely originated from depths ranging from 5 to 20 km were further identified by Tompkins and Pieters [1999] using Clementine data. While Cahill et al. [2009] proposed that 70 vol % plagioclase do exist at the depth of 30–50 km through quantitative spectral analysis of central peaks. Due to the limitation of spatial and spectral resolutions, the numerous studies about the anorthosite detection with newest remote sensing data acquired from SELENE and M^3 missions have been conducted. Ohtake et al. [2009] report the global distribution of pure anorthosite with SELENE Multiband Imager (MI) data. This study has been revised by Yamamoto et al. [2012] with SELENE Spectral Profiler (SP) data. More details have been proposed by Donaldson Hanna et al. [2014] using M^3 images and Diviner data. All these studies demonstrate the anorthosite is distributed extensively and provide the persuasive evidence for the presence of buoyant anorthositic cumulates that comprised the primary lunar crust and were formed during the differentiation of LMO.

Our results provide direct and indirect evidence to verify the major component of the lunar crust be anorthositic materials. First, 21 Pl-bearing crater central peaks with 840 pixels (Table 4-3) have been identified out of 166 investigated craters. The Pl-bearing materials are distributed in both lateral and vertical dimensions of the lunar crust. Pl has been detected in all three terranes while only FHT contains Pl in all three layers (Figure 4-8). FHT probably retain the relatively intact part of the ancient crust on the Moon. Second, an enormous amount of spectral featureless materials have been identified in both 166 investigated crater central peaks and 151 non-investigated crater central peaks (Figure 4-1). The number of spectral featureless pixels is at least four to five times than the number of pixels with diagnostic absorption feature. The materials in the central peaks are supposed to be fresh (high albedo) and could represent the deep-seated materials rebounded from the lunar crust. These spectral featureless and high-albedo materials were believed to be consistent with shocked or non-crystalline plagioclase [e.g., Spudis et al., 1984; Pieters, 1986; Hawke et al., 1991; 2003; Peterson et al., 1995]. The presence of a large amount of spectral featureless plagioclase indicates an anorthositic rich crust. Third, the relatively high likelihood for the presence of Sp and Px has been identified in the entire lunar crust. The detectable Sp-bearing materials represent Mg-spinel anorthosite [e.g. Pieters et al., 2011] with at least 70% plagioclase which derived from the estimation using nonlinear spectral unmixing with Hapke's radiative transfer model [Dhingra et al., 2011]. The materials with Px spectral feature most likely represent the mixture of more plagioclase but less Px. Both the presence of Sp and Px substantially infer that the lunar crust contains a lot of anorthositic materials. Therefore, all above evidence indicates the lunar crust is mainly made up of the extensively anorthositic materials and represents the flotation cumulates differentiated from the lunar magma ocean. This is the prerequisite for all the following discussions and provides critical evidence for the existence of LMO.

4.2. The SPAT might be not a crustal terrane

The South Pole–Aitken (SPA) basin is generally recognized as the oldest and largest impact basin (diameter: 2050-2400 km) on the Moon [Garrick-Bethell and Zuber, 2009]. According to the excavation depth calculated with the model by Cintala and Grieve [1998], the entire lunar crust should have been completely removed by basin formation processes. However, whether the upper mantle materials have been excavated in SPAT is still uncertain. Some studies based on multispectral images demonstrated no definite exposure of the lunar mantle in SPAT [Lucey et al., 1998; Pieters et al., 1997; 2001; Wieczorek et al., 2008; Cahill et al., 2009]. Considering the transient cavity radius of SPA (840 to 1400 km) [Spudis, 1993; Petro and Pieters, 2002; Potter et al., 2012] and the observation that the maximum excavation depth during an impact can be ~10% of the transient cavity diameter [Melosh, 1989], it is reasonable to believe that SPA has swept out most of the lunar crust and excavated into the mantle. This prediction is consistent with the result from cratering simulation [Melosh et al., 2014], implying the exposure of the upper mantle cumulates by SPAT.

Based on the LMO hypothesis, the structure of the early, pre-SPA on the Moon was an outer plagioclase-rich crust overlying a mantle of pyroxene and olivine cumulates differentiated from LMO [Hurwitz and Kring, 2014]. The early-crystallizing phases such as Mg-rich olivine and orthopyroxene sink to the bottom, while denser, late-crystallizing phases such as clinopyroxene, ilmenite, and other incompatible-rich phases settle in the shallow mantle. The amounts of olivine and orthopyroxene are expected to increase with depth. This structure represents the Moon at the end of LMO crystallization [Wood et al., 1970; Hess and Parmentier, 1995; Elkins-Tanton et al., 2011]. This gravitationally unstable structure is supposed to undergo gravitational overturn. During the overturn event, the deep cumulates mixed with shallow cumulate or relocated the lighter Mg-rich olivine and orthopyroxene to the upper mantle [Hess and Parmentier, 1995; Elkins-Tanton et al., 2011]. If the SPA impact occurred before overturn, the primary composition of SPA should be observed as clinopyroxene; otherwise, the presence of large amounts of orthopyroxenes would indicate post-overturn SPA.

Previous remote sensing observations suggest SPAT shows distinct geochemical signature. SPAT is characterized by anomalously high concentrations of FeO, TiO_2 [Lucey et al., 1998], and Th [Lawrence et al., 2000] compared to the surrounding highlands (~2–3 ppm vs. <1 ppm). The dominant mafic materials in SPAT were determined as low-Ca pyroxene (Opx) [Pieters et al., 1997; 2001]. The investigations of central peaks within SPAT show a limited compositional range [Tompkins and Pieters, 1999; Nakamura et al., 2009; Moriarty et al., 2013], indicating a nearly homogeneous Opx-rich layer underneath SPAT. Our results (Figure 4-4) also show the major composition of SPAT is Opx-bearing materials. Compared with PKT and FHT, all investigated minerals show a relatively low likelihood of the presence in SPAT except for Opx. The Pl trend observed in PKT and FHT (Pl clustered in the lowermost layer) is not present in SPAT (Figure 4-8). No Ol-bearing central peaks have been detected in SPAT. If SPAT was considered to represent the exposure of lower crustal rocks of FHT [Wieczorek et al., 2006], SPAT should contain a large amount of Pl similar to PKT and FHT. However, the significant difference between

SPAT and other terranes, particularly there is no a considerable amount of Pl, indicates the materials of SPAT may represent the composition of the upper mantle rather than the lower crust. The limit amount of spectrally detectable materials suggests SPA were strong blended by the overturn event or impact cratering. The dominance of Opx and the absence of Ol may imply the SPA impact occurred after or during the gravitational overturn. The composition of the upper mantle could be Opx-dominant rather than Ol. This conclusion is also obtained by Lucey et al. [2014] through a global survey of small craters with the SP data. Overall, SPAT reveals the feature of the upper mantle rather than the lunar crust, so SPAT as a lunar crustal terrane may not be appropriate.

4.3. A new three-layer crustal model

When the origin depth of crater central peak and the crustal thickness are factored into the analysis of mineral composition in the lunar crust, the global mineralogy investigation reported here suggests a new three-layer model for the lunar crust (Figure 4-9). The entire crust is highly anorthositic and relatively homogeneous. The so-called ‘layer’ in this new model represents the compositional changes in vertical direction which most likely occur on the local scale and do not necessarily occur in the entire layer. Although the lunar crust is probably relatively homogeneous in composition, the new three-layer model is proposed on the basis of the investigations in this study which indicate the distributions of investigated minerals are significantly associated with depth. The new three-layer model will help us better understand the evolution of the lunar crust, especially for the post-LMO magmatism. In addition, SPAT is more likely to represent the upper mantle, so the discussion below is only focused on PKT and FHT (Figure 4-6B).

The uppermost layer ($D/T<0.3$) is anorthositic or noritic within the depth range of roughly 5-10 km in PKT and ~5-15 km in FHT. The lunar crustal materials have been fractured, brecciated, mixed and redistributed by impacts since 4.5 billion years ago to generate a few kilometers highly fragmented layer (megaregolith) underlying a roughly 5-15 m fine-grain surface soil layer (regolith) [Heiken et al., 1991]. Even the detailed properties of the megaregolith are essentially unknown; the uppermost layer in this new three-layer model is regarded as the megaregolith layer based on the following evidence. First, detected Sp Ol and Pl show low likelihood for the presence while Px has relatively high probability for the presence (Figure 4-6B), which probably caused by heavily mixing by impact cratering in the uppermost layer. Second, early studies suggested the thickness of the megaregolith is roughly 2~3km [Hartmann, 1973; Head, 1976; Warren and Rasmussen, 1987] based on the results from modeling cratering processes or analysis of early geologic and seismic data. However, Spudis et al. [1999] and Bussey and Spudis et al. [2000] proposed the megaregolith is typically 10-20 km on the basis of orbital geochemical data. The most recent result for this depth range is 5-10 km [Blanchette-cuertin et al., 2011; Taylor and Wieczorek, 2014]. Meanwhile, it was suggested the megaregolith on the farside should be thicker than the nearside [Blanchette-cuertin et al. 2011]. All these observations agree with the depth range that this study has estimated for the uppermost crustal layer. Therefore, the uppermost layer in this new model is described as mageregolith with highly fractured, and mixed signature at depth from 5~10km in PKT and 5~15 km in FHT.

The middle layer (D/T 0.3 - 0.6) ranging from 10 km to 20 km is rich in all investigated minerals except for Pl. Relatively high amounts of Ol and Px are consistent with the signature of Mg-suite rocks in the lunar samples that content higher mafic materials compared to ferroan anorthosites. Although Sp (Mg-spinel anorthosite) has not been found in any returned lunar samples, it has been suggested to be a new member of Mg-suite rocks by a study addressing Mg-spinel petrogenesis using petrological experiments [Prissel et al. 2014]. Considering the presence of Ol, Px and Sp within PKT, the composition of this layer could be called the Mg-suite (relatively magnesium-rich plutonic rocks) which has high values of Mg/Fe and elevated incompatible elements compared to ferroan anorthosite.

While the detailed mechanism for the Mg-suite formation is not very clear, Mg-suite rocks have been considered as intrusions into preexisting LMO derived ferroan anorthositic crust. This means that the Mg-suite magmatism should follow the generation of the ferroan anorthositic lunar crust (LMO). Hess [1994] was ascribed the formation of Mg-suite as well as high Mg' and high incompatible elements of Mg-suite to melting early LMO cumulates to form Mg-suite parent magmas and incorporating a KREEP component. Results from this study suggest that this post-LMO magmatism should frequently occur in the middle layer underneath the PKT.

McCallum and Schwartz [2001] suggested that Mg-suite plutons were emplaced at depths of ~20-50 km in the lunar crust through recalculating the pressures and temperatures of equilibration of troctolite sample 76535 and three spinel cataclasites from 15445, 77517, and 73263. However, Sp and Ol in the relatively shallow layer (less than 20 km) have been observed using M^3 data on the global scale [Sun et al., 2013; Sun and Li, 2014]. Petrologic experiments have also confirmed this possibility. Hess [1994] proposed high Mg' olivine could be generated by partial melting Mg-rich cumulates at a low pressure. Studies about dunite xenoliths in lunar basalt 74275 also demonstrate olivine could form at relatively shallow depths in addition to deep crust or upper mantle [Shearer et al., 2015].

Alternatively, Mg-spinel could be produced through the assimilation of anorthositic crust by high Mg, low Fe magma in a wide pressure range that corresponds to the originated depth even less than 10 km [Prissel et al., 2014]. Furthermore, the 20 km seismic discontinuity was determined for the Apollo 12 and 14 sites based on the Apollo-era crustal velocity models [Khan et al., 2000, Khan and Mosegaard, 2002]. This discontinuity has been attributed to fractures and compositional change [Wieczorek and Phillips 1997], which supports the observations made in this study, i.e. this discontinuity might be the boundary between the middle layer and lowermost layer in this new three-layer model. Higher fracture density in the middle layer than the lowermost layer facilitates magma intrusion from the deep location. This may explain why mineral detection results for this middle layer are different among the three terranes. Our results also show significant asymmetry of compositional distribution within the middle layer. Ol, Opx and Sp (Mg-suite equivalents) all are concentrated within PKT (Figure 4-7 and Table 4-4), which is not the case for another two terranes. Presumably, this asymmetry should be caused by post-LMO magmatism that are probably associated with a thin crust and large basins (such as Imbrium, Oceanus Procellarum) in PKT. In contrast, the crust is much thicker in FHT, thus more resistant to magma intrusion than PKT. Comparison between the mineral detection results and lunar crustal thickness is shown in Figure 4-10, indicating the trends of increasing plagioclase and decreasing mafic materials with crustal thickness [Cahill et al., 2009] do not exist in the results of this study. Results from this study indicate that all investigated minerals appear to concentrate within 30 km thick crust. This depth range is in good agreement estimated crust thickness with the most recently acquired GRAIL data for the Apollo 12 and Apollo 14 landing sites, and both of which are located within PKT

[Wieczorek et al., 2013]. The distribution of mafic and Sp bearing materials within the middle layer may indicate the lunar crust has asymmetric thermal evolution as suggested by Laneuville et al. [2013]. Therefore, the post-LMO magmatism for the formation of Mg-suite may frequently occur underneath PKT, and the origin depth of Mg-suite could be limited to roughly 10-20 km based on the results presented here.

The lowermost layer (D/T>0.6) including lower crust and a part of the crust-mantle interface, is enriched in Pl (pure ferroan anorthosite). Both PKT and FHT show extremely a high amount of pure ferroan anorthosite in this layer. Ferroan anorthosite (An_{94-98}) was first identified in the lunar samples returned by Apollo missions [e.g., Wood et al., 1970]. Ferroan anorthosite was also found to be widespread in the inner ring of basins and the crater central peaks with telescopic observations and multispectral images [e.g. Pieters, 1986]. However, most early studies on remotely identifying anorthosite were based on high albedo, very low FeO and TiO_2 abundance and the absence of mafic mineral diagnostic absorption, rather than the diagnostic absorption band at 1.25 μm for Fe-bearing crystalline plagioclase because this absorption was difficult to confirm. Fortunately, the newest high-quality datasets such as SELENE MI, SP, and M^3 have allowed for identifying pure ferroan anorthosites with high confidence. The extensive presence of the purest anorthosite (approaching 100 vol%) on the Moon has been confirmed with SELENE MI data [Ohtake et al., 2009] and SP data [Yamamoto et al., 2012a]. Yamamoto et al. [2012a] proposed the existence of a 50 km thick pure anorthosite layer. Recent studies by Donaldson Hanna [2014] using M^3 and Diviner data have suggested that spectrally pure anorthosite is distributed widely across the lunar surface and associated with a thick crust. They also stated that the presence of a primary anorthositic layer within the 30 km depth could be evidence for a single differentiation event like LMO. In this study, Pl has been identified in all three layers within the depth range 7.95-33.21 km. The fact that Pl is concentrated within the lowermost layer leads to the speculation that a global pure anorthositic layer exists in the lower crust, and could represent the primordial composition of the lunar crust. The thickness of this primary anorthositic layer is at least 10 to 15 km.

4.4. Comparison between the new three-layer crustal model and previous crustal models

The new three-layer compositional model for the lunar crust suggests that the lunar crust consists of the uppermost megaregolith layer, the middle layer that contains Mg-suite rocks as a result of post-LMO magmatism and the lowermost global primitive anorthositic layer. The new three-layer model constraints Mg-suite rocks to the middle layer of the lunar crust and the pure anorthosite to the lowermost layer, which is not consistent with the scenario suggested by previous crustal models [e.g. Pieters, 1986; Tompkins and Pieters, 1999] stating that Mg-suite rocks exist in the lower crust covered by the pure anorthositic layer. This paradox might be caused by inaccurate estimation and low resolution of the remote sensing data used in previous studies [e.g. Pieters, 1986; Tompkins and Pieters, 1999]. Early estimated the crustal thickness is much thicker than the currently accepted value, and an overestimated crust thickness could lead to an inaccurate determination of the interface between the upper mantle to the lunar crust. For instance, Tompkins and Pieters [1999] suggested the anorthositic upper crust is about 5-30 km and the mafic lower crust about 25-55 km. It is evident that the upper mantle was misclassified as the lower crust and the upper crust in this classification should represent the whole lunar crust. However, it is difficult to distinguish different minerals with the multispectral images (very low spectral resolution). As an example, olivine is nearly impossible to be distinguishable from pyroxene or mixtures of olivine and pyroxene using the Clementine UVVIS images [Tompkins and Pieters, 1999]. Mg-spinel is not detectable using Clementine UVVIS images without 2 µm band. Low spectral resolution images cannot be used to reliably detect various minerals in the lunar crust. In addition, the lower crust was defined as mafic materials mainly based on the observations in SPAT [e.g. Pieters et al., 1997]. However, the materials in SPAT most likely represent the upper mantle or the mixture of impact melts with upper mantle composition rather than the lower crust on the basis of the most recent studies [e.g., Melosh et al., 2014]. This study shows that unlike PKT and FHT, an obvious vertical compositional trend does not exist beneath the SPAT. According to the new three-layer model, if SPAT could represent the lower crust, the composition of SPAT should have pure anorthosite similar to the lower layer of PKT and FHT. Because only a tiny amount of pure anorthosite was detected in SPAT, SPAT should be classified as upper mantle rather than the lower crust.

The new three-layer model is opposite to the previous three-layer crustal model [Spudis et al., 1999; Bussey and Spudis, 2000] based on the geochemical information. To address this inconsistency, FeO concentration has been calculated for all 317 crater central peaks with Clementine UVVIS images using the algorithm in Le Mouélic et al. [2002]. The vertical trend of FeO concentration and its correlation with D/T ratio are shown in Figure 4-11 and Table 4-6. Crater central peaks which are not imaged by the Clementine or show the negative FeO centration are excluded. The 151 uninvestigated central peaks (spectral featureless) show relatively lower FeO than the 166 investigated central peaks (Figure 4-11A), implying the spectral featureless materials may represent the pure anorthosite. FHT

(Figure 4-11C) shows the lowest average FeO concentration (3.91 wt. %) while SPAT (Figure 4-11B) shows the highest average FeO concentration (5.84 wt. %) among the three terrains, indicating that FHT may represent the primitive lunar crustal composition but SPAT is more mafic underneath lunar crust. Vertically, no matter considering SPAT or not, FeO wt. % does not increase with depth as shown in Table 4-6C (three terrenes) and 6D (without considering SPAT). Without considering SPAT (Table 4-6D), it seems that FeO concentration decreases with depth, which is consistent with the fact that pure anorthosite increases with depth. However, there is no large difference among three layers in total. The FeO concentration for all three layers is ~4-5 wt. % (Table 4-6C), indicating the lunar crust is homogenously anorthositic which strongly support the presence of LMO. Nevertheless, the original three-layer model [Spudis et al., 1999; Bussey and Spudis, 2000] may misclassify part of the lunar mantle into the crust. Our results are more reliable than previous studies because they are built upon more accurate determination with M^3 images and new crustal thickness gained from GRAIL data. The new three-layer model provides very strong arguments for the presence of primitive anorthositic flotation cumulates, thus supports the LMO hypothesis.

5. Conclusions

The mineralogy investigations of 166 impact crater central peaks were conducted to show the lateral and vertical variations in the lunar crust. Here we report several new implications regarding lunar crustal composition and structure.

1) The lunar crust is anorthositic in total with the variations produced by post-LMO activities.
2) SPAT might be not a crustal terrane and could represent the upper mantle rather than

the lower crust. Opx is enriched within the SPAT, but no detectable Ol that may indicate the major composition of the lunar mantle is orthopyroxene instead of olivine.

3) The distribution of Mg-suite bearing materials (Ol, Sp, Px) implies the post-LMO magmatism have frequently occurred in the middle layer underneath the PKT.
4) A global pure anorthositic layer is detected in the lowermost part of the lunar crust, which provides powerful evidence for the presence of floating anorthositic culminates consistent with the lunar magma ocean hypothesis.
5) A new three-layer crustal model has been proposed based on our observations. The uppermost layer: anorthositic or noritic megaregolith and has been heavily modified by impact cratering; the middle layer: Mg-suite equivalent materials and has been heavily modified by post-LMO magmatism; the lowermost layer: pure ferroan anorthosite which might represent the primitive crustal composition generated by LMO.

6. Future work

In order to validate the new three-layer model for the lunar crust, future work will continue to the analysis of common lunar minerals in additional regions (e.g. basins, crater wall and ejecta) with M^3. Second to integrate other new dataset (Chang’e, SELENE, Lunar Reconnaissance Orbiter, and Diviner) for validating the results derived from M^3. In addition, the quantitative spectral analysis should be taken into account to accurate the compositional diversity of the lunar crust, especially for pyroxene detection. Additional assessments of lunar samples are also necessary to provide the efficient petrological constraints for the new three-layer model.

Acknowledgements

We gratefully acknowledge the suggestion and support of Yunzhao Wu. The first author also appreciates the discussion with Dawei Liu in the preparation of the manuscript.

Table captions

Table 4-1. Criteria for lunar common mineral detection with M^3 L2 images. AD: spectral absorption depth; λ: wavelength position of the deepest absorption.

Table 4-2. The information and detection results for all 166 investigated crater central peaks.

Table 4-3. The data for the comparison among three terranes (A) and among three layers (B). C show the data for three layers without considering SPAT. The data in Table 4-3 are plotted in Figure 4-4 and Figure 4-6.

Table 4-4. The data for comparison among three terranes in each layer shown in Figure 4-7.

Table 4-5. The data for comparison among three layers in each terrane shown in Figure 4-

8.

Table 4-6. FeO concentration. A: Total FeO concentration for investigated and uninvestigated central peaks. B: The variations of FeO concentration among three terranes. C: The variations of FeO concentration among three layers. D: The variations of FeO concentration among three layer without considering SPAT.

Tables

Table 4-1.

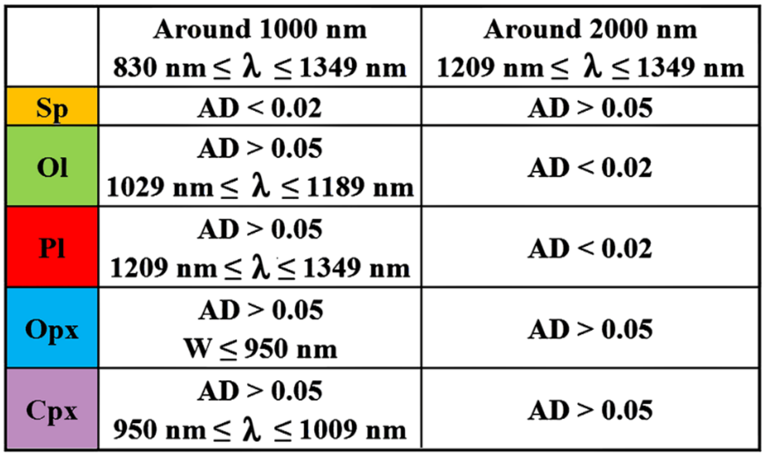

	Around 1000 nm $830\ \mathrm{nm} \leq \lambda \leq 1349\ \mathrm{nm}$	Around 2000 nm $1209\ \mathrm{nm} \leq \lambda \leq 1349\ \mathrm{nm}$
Sp	$\mathrm{AD} < 0.02$	$\mathrm{AD} > 0.05$
Ol	$\mathrm{AD} > 0.05$ $1029\ \mathrm{nm} \leq \lambda \leq 1189\ \mathrm{nm}$	$\mathrm{AD} < 0.02$
Pl	$\mathrm{AD} > 0.05$ $1209\ \mathrm{nm} \leq \lambda \leq 1349\ \mathrm{nm}$	$\mathrm{AD} < 0.02$
Opx	$\mathrm{AD} > 0.05$ $W \leq 950\ \mathrm{nm}$	$\mathrm{AD} > 0.05$
Cpx	$\mathrm{AD} > 0.05$ $950\ \mathrm{nm} \leq \lambda \leq 1009\ \mathrm{nm}$	$\mathrm{AD} > 0.05$

Table 4-2.

Crater name	Center Latitude	Center Longitude	Diameter (d) (km)	Origin Depth $(D)^1$ (km)	Crustal Thickness $(T)^2$ (km)	D/T	Sp	Ol	Pl	Opx	Cpx	FeO (wt. %)^3	Terrane
Agrippa	4.10	10.47	43.75	6.45	37.64	0.17				1		1.94	PKT
Airy	-18.14	5.61	38.90	5.68	32.11	0.18				1	1	4.78	PKT
Aitken	-16.44	172.96	129.69	20.86	40.39	0.52			17		1	3.27	SPAT
Albategnius	-11.24	4.01	130.84	21.06	35.96	0.59	6					3.77	PKT
Alden	-23.51	111.11	111.44	17.71	38.30	0.46				1	1	5.83	FHT
Alpetragius	-16.05	355.49	40.02	5.86	32.28	0.18				1		6.09	PKT
Anaxagoras	73.48	349.83	51.90	7.76	33.61	0.23				1	1		PKT
Antoniadi	-69.30	186.94	137.92	22.30	17.85	1.25				1		1.24	SPAT
Aristarchus	23.73	312.51	39.99	5.86	29.90	0.20			7		1	4.89	PKT
Aristillus	33.88	1.21	54.37	8.16	23.51	0.35				1		9.75	PKT
Aristoteles	50.24	17.32	87.57	13.65	24.26	0.56				1		1.81	PKT
Arzachel	-18.26	358.07	96.99	15.24	34.46	0.44	21			1	1	3.77	PKT
Atlas	46.74	44.38	88.12	13.74	29.19	0.47	20	7		1	1	7.60	PKT
Ball	-35.92	351.61	40.31	5.91	31.39	0.19	7			1		2.29	PKT
Barkla	-10.67	67.22	40.90	6.00	27.87	0.22				1		6.07	PKT
Barringer	-28.22	209.57	66.89	10.21	26.67	0.38				1		9.06	SPAT
Berkner	25.13	254.76	87.62	13.66	39.67	0.34	13					4.53	FHT
Bernoulli	34.93	60.61	47.30	7.02	25.37	0.28				1		5.28	PKT
Bhabha	-55.50	194.69	70.25	10.76	13.58	0.79				1	1	7.17	SPAT
Bianchini	48.78	325.63	37.59	5.48	34.63	0.16	13	8		1	1	5.46	PKT
Biela	-54.99	51.63	77.03	11.89	28.67	0.41				1		3.95	PKT
Birkeland	-30.17	174.01	81.64	12.66	22.80	0.55				1		7.57	SPAT
Bok	-20.26	188.42	43.03	6.34	31.40	0.20				1		8.32	SPAT
Borman	-39.06	211.75	50.72	7.57	12.66	0.60				1		9.81	SPAT
Boyle	-53.29	177.89	57.13	8.61	13.56	0.63				1	1	6.34	SPAT
Briggs	26.45	290.81	36.75	5.34	25.64	0.21				1		11.07	PKT
Bullialdus	-20.75	337.74	60.72	9.19	18.11	0.51				1	1	9.62	PKT
Burg	45.07	28.21	41.04	6.02	22.19	0.27				1	1	7.88	PKT
Butlerov	12.05	251.19	38.77	5.66	39.56	0.14					1		FHT
Campanus	-28.04	332.10	46.41	6.88	24.24	0.28				1	1	12.24	PKT
Cantor	38.04	118.69	75.72	11.67	30.59	0.38					1	3.42	FHT
Cardanus	13.27	287.50	49.57	7.38	22.69	0.33				1	1	8.56	PKT
Carpenter	69.52	308.77	59.06	8.92	29.76	0.30				1		3.43	PKT
Cepheus	40.68	45.78	39.43	5.77	27.83	0.21				1		4.52	PKT
Chebyshev	-34.01	227.12	179.05	29.56	38.59	0.77				1			SPAT
Cleomedes	27.60	55.50	130.77	21.05	30.40	0.69			8			4.52	PKT
Compton	55.86	104.05	164.63	26.99	27.67	0.98	4			1	1	3.99	FHT
Copernicus	9.62	339.92	96.07	15.09	31.93	0.47	7	1502		1		3.08	PKT
Crookes	-10.40	194.90	48.25	7.17	48.45	0.15					1	1.67	SPAT
Dalton	17.07	275.55	60.69	9.19	29.85	0.31	12					4.83	PKT
Davisson	-37.93	185.03	92.46	14.48	18.14	0.80				1	1	10.70	SPAT
De Vries	-19.68	183.22	57.51	8.67	39.08	0.22				1		8.54	SPAT
Doerfel	-68.97	251.47	68.63	10.49	31.53	0.33				1		4.62	SPAT
Donati	-20.69	5.10	35.84	5.20	29.51	0.18				1		4.62	PKT
Dryden	-33.21	203.85	54.45	8.17	25.90	0.32				1	1	7.24	SPAT
Drygalski	-79.57	272.82	162.49	26.61	34.34	0.77				1			SPAT
Eichstadt	-22.63	281.58	49.57	7.38	32.93	0.22					1	4.72	PKT
Einstein	16.60	271.35	181.47	29.99	30.47	0.98					1	1.52	FHT
Eratosthenes	14.47	348.68	58.77	8.87	27.36	0.32		211	2		1	6.79	PKT
Eudoxus	44.27	16.23	70.16	10.74	31.67	0.34	1			1	1	6.85	PKT
Fabricius	-42.75	41.84	78.90	12.20	30.19	0.40				1	1	1.49	PKT
Fabry	43.07	100.68	179.44	29.63	30.59	0.97			3				FHT
Finsen	-42.29	182.28	72.98	11.21	16.03	0.70				1	1	8.19	SPAT
Fizeau	-58.19	225.89	107.08	16.96	18.32	0.93				1		3.92	SPAT
Franklin	38.73	47.64	55.92	8.41	26.60	0.32	8			1	1	4.70	PKT
Froelich	80.00	248.37	56.73	8.54	31.55	0.27				1	1		FHT

Table 4-2. Continue

Crater name	Center Latitude	Center Longitude	Diameter (d) (km)	Origin Depth (D)[1] (km)	Crustal Thickness (T)[2] (km)	D/T	Sp	Ol	Pl	Opx	Cpx	FeO (wt. %)[3]	Terrane
Gassendi	-17.55	320.04	111.39	17.70	31.11	0.57	9	10	3	1		8.09	PKT
Geminus	34.42	56.66	81.98	12.71	27.46	0.46	1			1	1	3.09	PKT
Golitsyn	-25.20	254.80	35.47	5.14	46.26	0.11	6			1	1	3.24	FHT
Goodacre	-32.67	14.08	44.09	6.51	34.34	0.19	25					5.23	PKT
Harpalus	52.73	316.51	39.77	5.82	27.11	0.21				1		10.05	PKT
Hausen	-65.11	271.51	163.24	26.75	40.88	0.65	5			1	1		SPAT
Hayn	64.56	83.87	86.21	13.42	32.28	0.42	40			1	1	0.43	PKT
Humboldt	-27.02	80.96	199.46	33.21	21.93	1.51		27	286			2.56	PKT
Hutton	37.22	168.68	45.17	6.68	40.71	0.16				1		3.43	FHT
Jackson	22.05	196.68	71.38	10.95	51.94	0.21		3	14	1	1		FHT
Jenner	-42.01	95.98	73.66	11.32	30.72	0.37				1		11.80	PKT
Joliot	25.79	93.39	172.79	28.44	28.76	0.99	3				1	4.19	PKT
Kapteyn	-10.79	70.59	48.65	7.24	27.67	0.26				1		4.19	PKT
Keeler	-9.78	161.78	158.07	25.83	38.29	0.67		4	115			0.97	FHT
King	4.96	120.49	76.21	11.75	42.98	0.27				1	1		FHT
Klein	-11.99	2.53	43.47	6.41	35.21	0.18				1	1	6.14	PKT
Kovalevskaya	30.86	230.56	113.71	18.10	47.64	0.38	82	4	16	1	1	3.20	FHT
Krasnov	-29.93	280.18	41.17	6.04	34.02	0.18					1	3.79	PKT
La Perouse	-10.67	76.28	80.40	12.45	29.73	0.42				1		3.26	PKT
Lame	-14.76	64.56	84.28	13.10	30.38	0.43				1	1	5.60	PKT
Langmuir	-35.85	231.11	91.50	14.31	41.32	0.35				1	1	5.11	SPAT
Langrenus	-8.86	61.04	131.98	21.26	30.81	0.69			8	1	1		PKT
Lansberg	-0.31	333.37	38.75	5.66	30.38	0.19				1	1	10.60	PKT
Laue	28.29	262.95	89.17	13.92	37.36	0.37				1		5.55	FHT
Leavitt	-44.86	220.11	69.31	10.60	19.29	0.55				1		9.36	SPAT
Leuschner	1.67	250.95	50.14	7.48	44.70	0.17	5				1		FHT
Lindenau	-32.35	24.77	53.08	7.95	43.41	0.18	1		2			5.36	PKT
Lobachevskiy	9.76	113.07	87.26	13.60	34.50	0.39			3	1	1	2.66	FHT
Lodygin	-17.42	213.22	56.11	8.44	47.08	0.18				1	1	3.72	SPAT
Lohse	-13.76	60.31	43.34	6.39	31.08	0.21				1		5.12	PKT
Lovell	-36.74	217.53	35.10	5.09	30.50	0.17				1		6.23	SPAT
Lowell	-12.97	256.58	62.65	9.51	47.03	0.20	21			1	1		FHT
Lyman	-64.96	162.47	83.25	12.93	21.74	0.59				1		7.89	SPAT
Macrobius	21.26	45.97	62.79	9.53	30.71	0.31		10		1	1	5.19	PKT
Maginus	-50.03	354.02	155.58	25.39	31.13	0.82				1	1	0.53	PKT
Manilius	14.45	9.07	38.34	5.59	30.88	0.18					1	5.17	PKT
Mariotte	-28.46	220.94	70.27	10.76	39.35	0.27				1	1	3.13	SPAT
Markov	53.43	297.16	39.92	5.84	25.24	0.23				1	1	5.80	PKT
Maunder	-14.52	266.12	53.80	8.07	12.34	0.65					1	4.61	FHT
McKellar	-15.72	189.14	50.16	7.48	43.29	0.17	9			1	1	3.11	SPAT
Mendel	-48.83	250.14	139.65	22.60	35.42	0.64				1		3.97	SPAT
Mercurius	46.66	66.07	64.30	9.78	27.00	0.36			6	1	1	4.53	PKT
Miller	-39.37	0.78	61.37	9.30	25.27	0.37	14			1	1		PKT
Millikan	46.76	121.52	93.97	14.73	31.08	0.47					1	3.46	FHT
Moiseev	9.44	103.26	61.56	9.33	31.57	0.30				1	1	2.74	FHT
Moretus	-70.63	354.05	114.45	18.23	35.12	0.52	2			1			PKT
Morse	21.90	184.71	72.77	11.18	39.87	0.28	8					2.27	FHT
Neander	-31.35	39.88	49.22	7.33	36.04	0.20				1		3.07	PKT
Neper	8.76	84.58	144.32	23.42	24.33	0.96	10					3.70	PKT
Nusl	32.19	167.45	60.58	9.17	38.80	0.24				1	1	2.31	FHT
O Day	-30.42	157.29	70.41	10.79	36.49	0.30				1		3.87	SPAT
Ohm	18.32	246.22	61.75	9.36	41.16	0.23	26				1	4.63	FHT
Olcott	20.57	117.79	79.94	12.37	35.98	0.34			1	1	1	4.46	FHT
Orlov	-25.77	184.92	72.93	11.20	24.02	0.47				1	1	6.89	SPAT
Pallas	5.48	358.35	49.51	7.37	41.03	0.18				1	1	6.46	PKT
Paracelsus	-22.92	163.44	85.88	13.37	28.25	0.47					1	7.17	SPAT

Table 4-2. Continue

Crater name	Center Latitude	Center Longitude	Diameter (d) (km)	Origin Depth $(D)^1$ (km)	Crustal Thickness $(T)^2$ (km)	D/T	Sp	Ol	Pl	Opx	Cpx	FeO (wt. %)^3	Terrane
Pascal	74.36	289.37	108.20	17.16	33.53	0.51				1			PKT
Pauli	-44.76	137.35	95.28	14.95	30.19	0.50				1		8.72	FHT
Pease	12.51	253.70	40.84	5.99	36.83	0.16	1				1		FHT
Pentland	-64.57	11.34	56.45	8.50	31.70	0.27				1	1	0.86	PKT
Petavius	-25.39	60.78	184.06	30.45	30.96	0.98		7	83		1		PKT
Petzval	-62.73	249.17	93.47	14.65	30.45	0.48				1		7.87	SPAT
Philolaus	72.22	327.12	71.44	10.96	32.09	0.34		8		1	1		PKT
Piazzi	-36.16	291.99	102.57	16.19	32.79	0.49					1	5.12	PKT
Pikelner	-48.37	124.25	40.96	6.01	33.96	0.18				1	1	5.44	FHT
Pitatus	-29.88	346.47	100.63	15.86	28.27	0.56				1	1	8.85	PKT
Pitiscus	-50.61	30.57	79.85	12.36	32.79	0.38				1	1	3.82	PKT
Pizzetti	-35.06	119.29	53.47	8.01	32.22	0.25					1	4.16	FHT
Plana	42.25	28.22	42.97	6.33	30.65	0.21				1	1	5.53	PKT
Plinius	15.36	23.61	41.31	6.06	27.18	0.22				1	1	7.87	PKT
Plummer	-24.62	205.14	75.70	11.66	38.58	0.30				1		7.01	SPAT
Plutarch	24.18	79.05	69.59	10.65	30.17	0.35					1	3.94	PKT
Posidonius	31.88	29.99	95.06	14.92	22.97	0.65				1	1	6.20	PKT
Poynting	17.50	226.62	127.55	20.49	48.24	0.42	2			1	1	3.25	FHT
Prandtl	-59.62	141.54	87.53	13.64	29.38	0.46				1	1	3.73	SPAT
Pythagoras	63.68	297.02	144.55	23.46	34.25	0.68	8		3				PKT
Ramsay	-40.02	145.04	61.28	9.28	32.26	0.29				1		4.91	SPAT
Rheita	-37.10	47.17	70.81	10.85	30.70	0.35				1		2.79	PKT
Robertson	21.84	254.63	89.85	14.04	38.39	0.37	6			1	1	3.58	FHT
Romer	25.43	36.41	43.70	6.44	32.30	0.20				1	1	4.88	PKT
Rothmann	-30.81	27.70	41.67	6.12	36.66	0.17				1	1	5.49	PKT
Rutherfurd	-61.15	347.75	49.98	7.45	30.62	0.24				1	1	4.20	PKT
Santbech	-20.99	44.06	62.24	9.44	31.54	0.30				1	1	6.12	PKT
Sarton	49.12	238.86	71.33	10.94	19.57	0.56				1		7.09	FHT
Scaliger	-27.26	109.14	86.40	13.45	31.64	0.43					1	5.91	FHT
Schluter	-5.93	276.61	87.55	13.65	32.15	0.42		3	6			5.04	PKT
Schubert	2.78	81.01	51.94	7.77	31.73	0.24					1	4.81	PKT
Scoresby	77.73	14.13	54.93	8.25	27.92	0.30				1			PKT
Sirsalis	-12.49	299.49	44.17	6.52	39.16	0.17				1	1	3.39	PKT
Sklodowska	-18.04	96.15	125.55	20.14	28.33	0.71	2				1	0.84	PKT
Spencer Jones	13.06	165.84	88.19	13.76	36.34	0.38				1		2.35	FHT
Stearns	34.68	162.60	38.94	5.69	43.45	0.13					1	2.37	FHT
Steklov	-36.73	254.95	36.61	5.32	40.07	0.13				1	1	4.42	FHT
Stevinus	-32.49	54.14	71.54	10.97	28.55	0.38				1	1	5.07	PKT
Stiborius	-34.49	31.99	43.76	6.45	37.79	0.17	15			1		3.90	PKT
Stormer	57.14	146.65	68.62	10.49	34.40	0.30				1		4.24	FHT
Taruntius	5.50	46.54	57.32	8.64	19.28	0.45					1	13.10	PKT
Theophilus	-11.45	26.28	98.59	15.52	25.39	0.61	177	105	98			2.38	PKT
Thiel	40.17	225.44	35.67	5.18	45.79	0.11					1	3.70	FHT
Tsiolkovskiy	-20.38	128.97	184.39	30.51	39.15	0.78			127		1	6.23	FHT
Tycho	-43.30	348.78	85.29	13.27	31.97	0.41	2			1	1	6.45	PKT
Vavilov	-0.87	221.23	98.22	15.45	56.71	0.27			32	1	1	3.20	FHT
Vitello	-30.42	322.45	42.51	6.25	33.30	0.19				1	1	8.41	PKT
Walther	-33.25	0.62	134.23	21.65	28.69	0.75	28					5.62	PKT
Waterman	-25.70	128.18	74.91	11.53	33.99	0.34				1	1	4.17	FHT
White	-44.80	200.96	42.34	6.23	18.63	0.33				1		10.05	SPAT
Wiener	40.90	146.51	113.39	18.05	36.96	0.49					1	1.82	FHT
Wrottesley	-23.90	56.62	58.38	8.81	32.34	0.27				1	1	5.17	PKT
Zsigmondy	59.52	254.70	66.88	10.20	35.91	0.28				1		3.72	FHT
Zucchius	-61.38	309.35	63.18	9.60	32.36	0.30	1			1	1		PKT

Table 4-3.

A1		MNP			NC	
Terrane	NCI	Sp	Ol	Pl	Opx	Cpx
SPAT	34	14	0	17	31	15
FHT	43	174	11	311	25	32
PKT	89	433	1898	512	66	53
Total	166	621	1909	840	122	100

A2	MNP/NCI			NC/NCI	
Terrane	Sp	Ol	Pl	Opx	Cpx
SPAT	0.41	0.00	0.50	0.91	0.44
FHT	4.05	0.26	7.23	0.58	0.74
PKT	4.87	21.33	5.75	0.74	0.60

B1		MNP			NC	
D/T	NCI	Sp	Ol	Pl	Opx	Cpx
<0.3	71	138	11	55	55	46
0.3-0.6	68	423	1860	152	53	39
>0.6	27	60	38	633	14	15
Total	166	621	1909	840	122	100

B2	MNP/NCI			NC/NCI	
D/T	Sp	Ol	Pl	Opx	Cpx
<0.3	1.94	0.15	0.77	0.77	0.65
0.3-0.6	6.22	27.35	2.24	0.78	0.57
>0.6	2.22	1.41	23.44	0.52	0.56

C1		MNP			NC	
D/T	NCI	Sp	Ol	Pl	Opx	Cpx
<0.3	62	129	11	55	47	42
0.3-0.6	53	423	1860	135	40	33
>0.6	17	55	38	633	4	10
Total	132	607	1909	823	91	85

C2	MNP/NCI			NC/NCI	
D/T	Sp	Ol	Pl	Opx	Cpx
<0.3	2.08	0.18	0.89	0.76	0.68
0.3-0.6	7.98	35.09	2.55	0.75	0.62
>0.6	3.24	2.24	37.24	0.24	0.59

Table 4-4.

D/T < 0.3		MNP			NC	
Terrane	NCI	Sp	Ol	Pl	Opx	Cpx
SPAT	9	9	0	0	8	4
FHT	20	67	3	46	12	17
PKT	42	62	8	9	35	25

	MNP/NCI			NC/NCI	
Terrane	Sp	Ol	Pl	Opx	Cpx
SPAT	1.00	0.00	0.00	0.89	0.44
FHT	3.35	0.15	2.30	0.60	0.85
PKT	1.48	0.19	0.21	0.83	0.60

D/T = 0.3-0.6		MNP			NC	
Terrane	NCI	Sp	Ol	Pl	Opx	Cpx
SPAT	15	0	0	17	13	6
FHT	17	103	4	20	12	11
PKT	36	320	1856	115	28	22

	MNP/NCI			NC/NCI	
Terrane	Sp	Ol	Pl	Opx	Cpx
SPAT	0.00	0.00	1.13	0.87	0.40
FHT	6.06	0.24	1.18	0.71	0.65
PKT	8.89	51.56	3.19	0.78	0.61

D/T > 0.6		MNP			NC	
Terrane	NCI	Sp	Ol	Pl	Opx	Cpx
SPAT	10	5	0	0	10	5
FHT	6	4	4	245	1	4
PKT	11	51	34	388	3	6

	MNP/NCI			NC/NCI	
Terrane	Sp	Ol	Pl	Opx	Cpx
SPAT	0.50	0.00	0.00	1.00	0.50
FHT	0.67	0.67	40.83	0.17	0.67
PKT	4.64	3.09	35.27	0.27	0.55

Table 4-5.

SPAT		MNP			NC	
D/T	NCI	Sp	Ol	Pl	Opx	Cpx
<0.3	9	9	0	0	8	4
0.3-0.6	15	0	0	17	13	6
>0.6	10	5	0	0	10	5

	MNP/NCI			NC/NCI	
D/T	Sp	Ol	Pl	Opx	Cpx
<0.3	1.00	0.00	0.00	0.89	0.44
0.3-0.6	0.00	0.00	1.13	0.87	0.40
>0.6	0.50	0.00	0.00	1.00	0.50

FHT		MNP			NC	
D/T	NCI	Sp	Ol	Pl	Opx	Cpx
<0.3	20	67	3	46	12	17
0.3-0.6	17	103	4	20	12	11
>0.6	6	4	4	245	1	4

	MNP/NCI			NC/NCI	
D/T	Sp	Ol	Pl	Opx	Cpx
<0.3	3.35	0.15	2.30	0.60	0.85
0.3-0.6	6.06	0.24	1.18	0.71	0.65
>0.6	0.67	0.67	40.83	0.17	0.67

PKT		MNP			NC	
D/T	NCI	Sp	Ol	Pl	Opx	Cpx
<0.3	43	74	8	9	35	25
0.3-0.6	35	308	1856	115	28	22
>0.6	11	51	34	388	3	6

	MNP/NCI			NC/NCI	
D/T	Sp	Ol	Pl	Opx	Cpx
<0.3	1.72	0.19	0.21	0.81	0.58
0.3-0.6	8.80	53.03	3.29	0.80	0.63
>0.6	4.64	3.09	35.27	0.27	0.55

Table 4-6.

A

FeO (wt. %)	NCI	Mean
Investigated	145	5.17
Uninvestigated	138	3.99
Total	283	4.59

B

Lateral	Investigated		Uninvestigated		Total	
Terrane	NCI	Mean	NCI	Mean	NCI	Mean
SPAT	31	6.18	6	4.06	37	5.84
FHT	35	3.92	31	3.89	66	3.91
PKT	79	5.32	101	4.02	180	4.59

C

Vertical	Investigated		Uninvestigated		Total	
D/T	NCI	Mean	NCI	Mean	NCI	Mean
<0.3	61	5.02	84	4.16	145	4.52
0.3-0.6	64	5.56	47	3.67	111	4.76
>0.6	20	4.35	7	4.16	27	4.30

D

Vertical	Investigated		Uninvestigated		Total	
D/T	NCI	Mean	NCI	Mean	NCI	Mean
<0.3	52	5.05	82	4.15	134	4.50
0.3-0.6	49	5.09	45	3.70	94	4.42
>0.6	13	3.50	5	3.89	18	3.61

Figure captions

Figure 4-1. Distribution of 317 crater central peaks (dots) on Clementine 750nm band image. 166 investigated crater central peak shows in yellow dots. 151 uninvestigated crater central peaks shown in pink dots only have the spectral featureless materials.

Figure 4-2. Multi-temporal images for Jackson crater central peak. The below images are resized from 'M3G20090621T025007_V01_RFL.IMG' and 'M3G20090718T101402_V01_RFL.IMG' respectively after data preprocessing. A: the M^3 L2 image for Jackson crater central peak at 750 nm from 'M3G20090621T025007_V01_RFL.IMG', and the identified Pl-bearing pixels (260) show in red color. B: The location is as the same as A for Jackson central peak, but from 'M3G20090718T101402_V01_RFL.IMG', and Pl bearing pixels (14) in red color.

Figure 4-3. Location of examined central peaks overlaid on the LOLA DEM of the Moon. Solid stars represent relative depth (D/T) and filling fringe colors show identified minerals in this study. Black dash lines describe three distinct lunar terranes. D: the origin depth of the central peak. T: average crustal thickness of central peak derived from GRAIL. Sp: Mg-spinel. Ol: Olivine. Pl: crystalline plagioclase. Opx: orthopyroxene. Cpx: clinopyroxene.

Figure 4-4. Compositional variations among three distinct terranes without considering the origin depth of the central peak. The MNP/NCI and NC/NCI for all three terranes show in Table 4-3A.

Figure 4-5. Comparison between MNP and D/T for Mg-spinel (Sp), olivine (Ol) and crystalline plagioclase (Pl). The data show in Table 4-2.

Figure 4-6. Vertical variation of lunar crust including the uppermost layer (D/T<0.3), the middle layer (D/T=0.3-0.6) and the lowermost layer (D/T>0.6). A: all three terranes (SPAT, FHT, and PKT) are included. B: only FHT and PKT are considered. The MNP/NCI and NC/NCI for all three layers show in Table 4-3B and Table 4-3C.

Figure 4-7. Comparison among three distinct terranes in each layer and the data show in Table 4-4.

Figure 4-8. Comparison of three layers in each terrane and the data show in Table 4-5.

Figure 4-9. Schematic diagram for the new three-layer model of the lunar crust.

Figure 4-10. Mineral detection results relative to the crustal thickness and data show in Table 4-2.

Figure 4-11. The variations of FeO concentration with depth in the crust. A: FeO concentration for all 317 central peaks. B, C and D show the FeO concentration for three distinct terranes respectively. All FeO concentration is shown in Table 4-2 and Table 4-6.

Figures

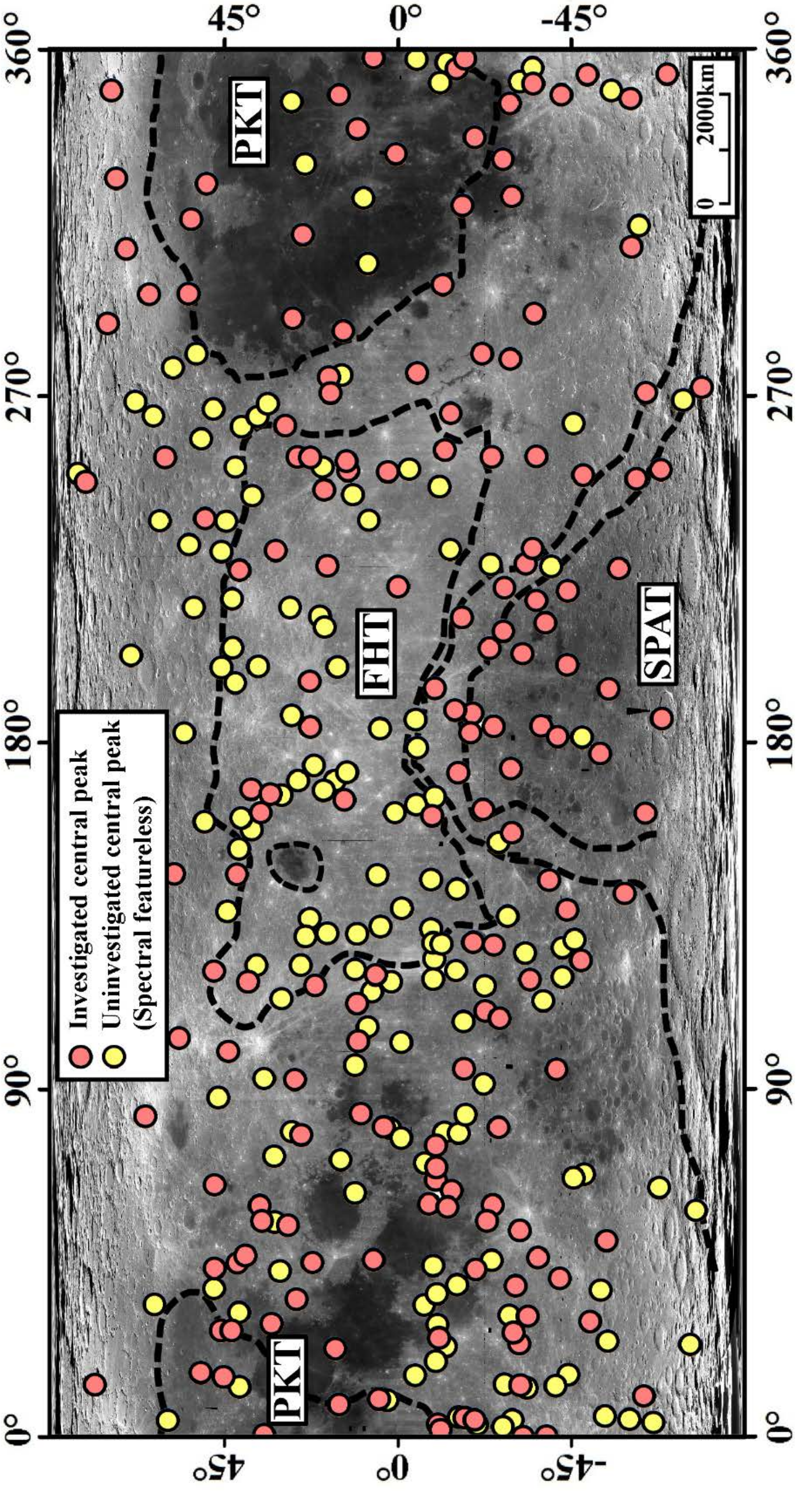

Figure 4-1.

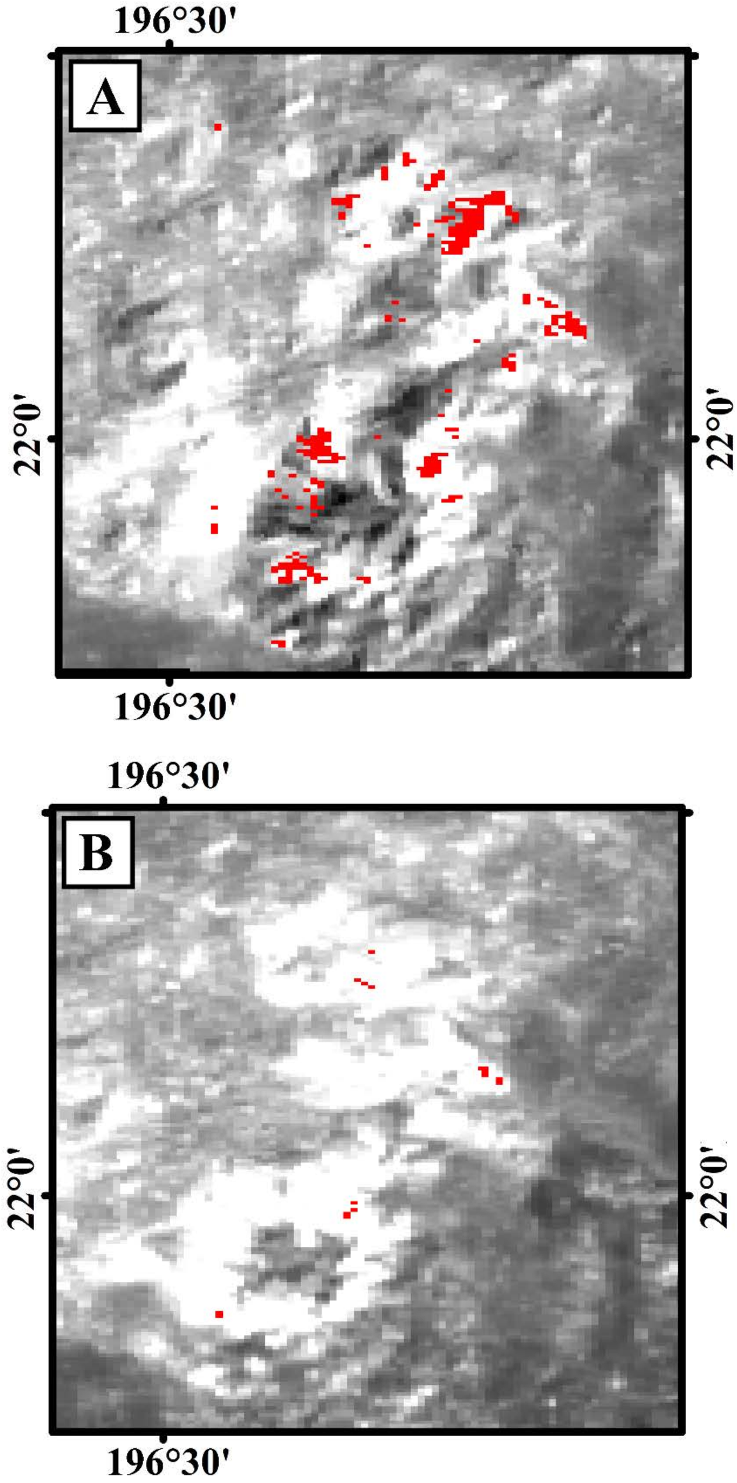

Figure 4-2.

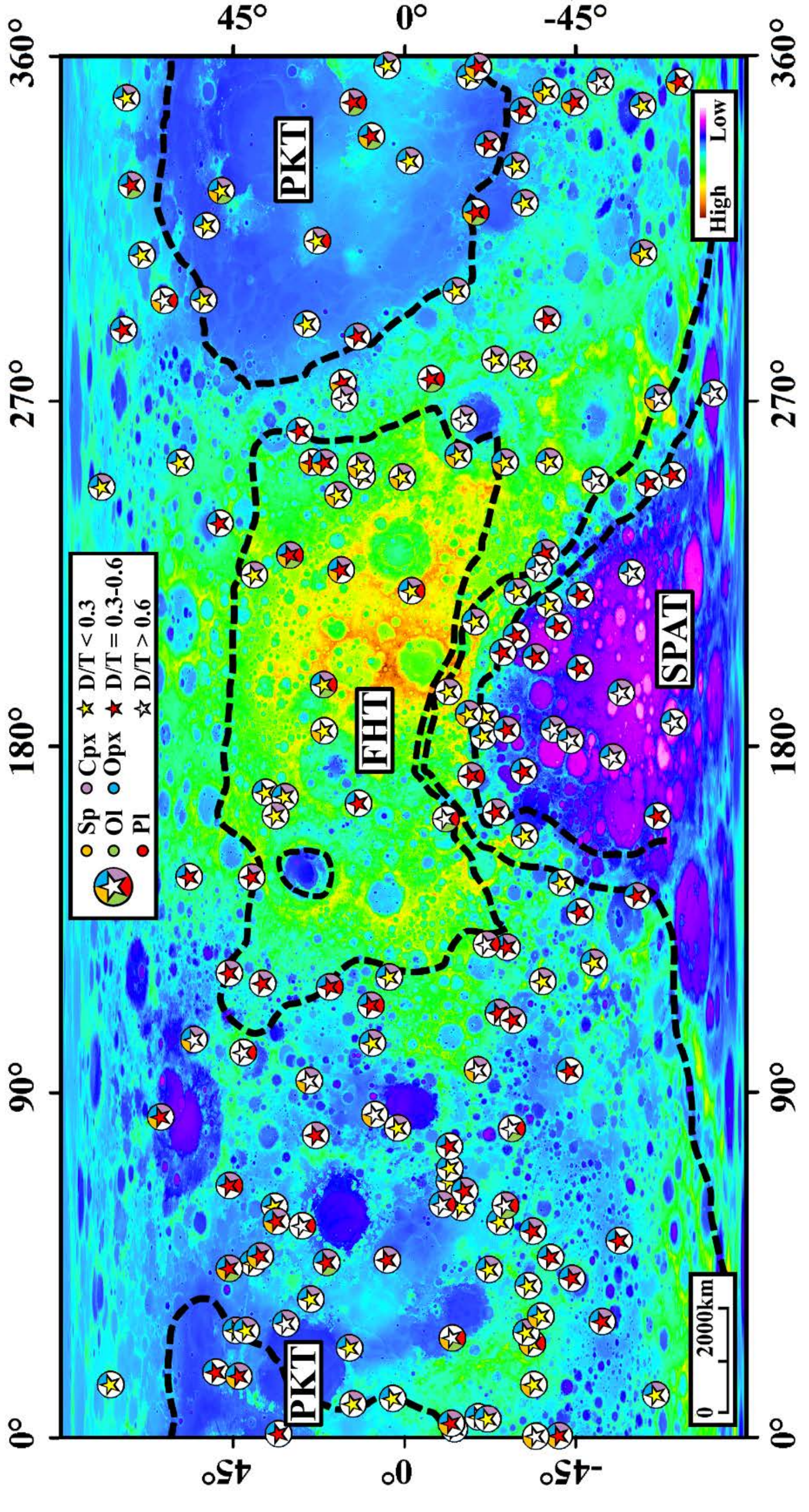
0°
90°
180°
270°
360°
45°
0°
-45°
PKT
PKT
FHT
SPAT
Sp
Cpx
D/T < 0.3
Ol
Opx
D/T = 0.3-0.6
Pl
D/T > 0.6
0
2000km
High
Low

Figure 4-3.

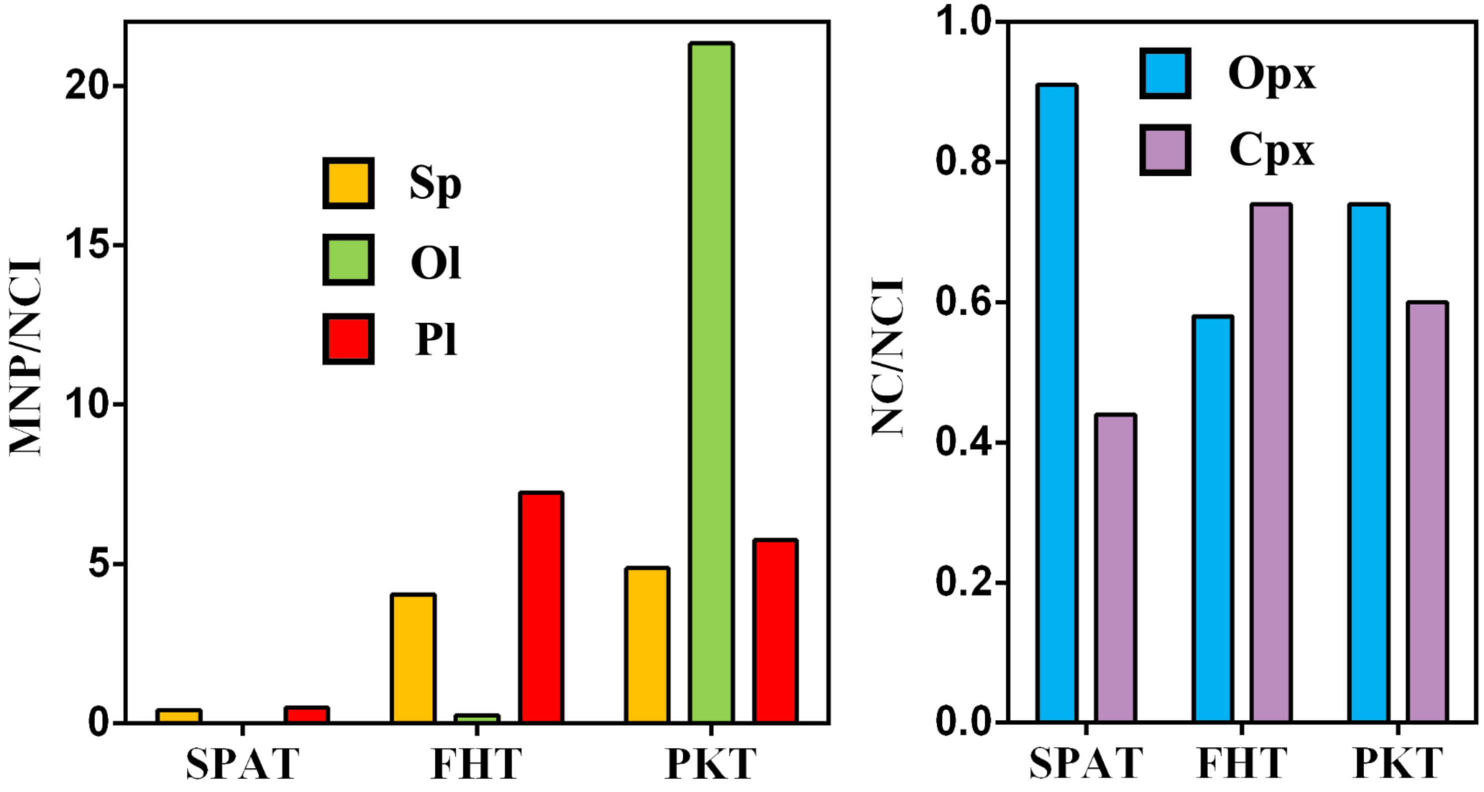
MNP/NCI
20
15
10
5
0
Sp
Ol
Pl
SPAT
FHT
PKT
NC/NCI
1.0
0.8
0.6
0.4
0.2
0.0
Opx
Cpx
SPAT
FHT
PKT

Figure 4-4.

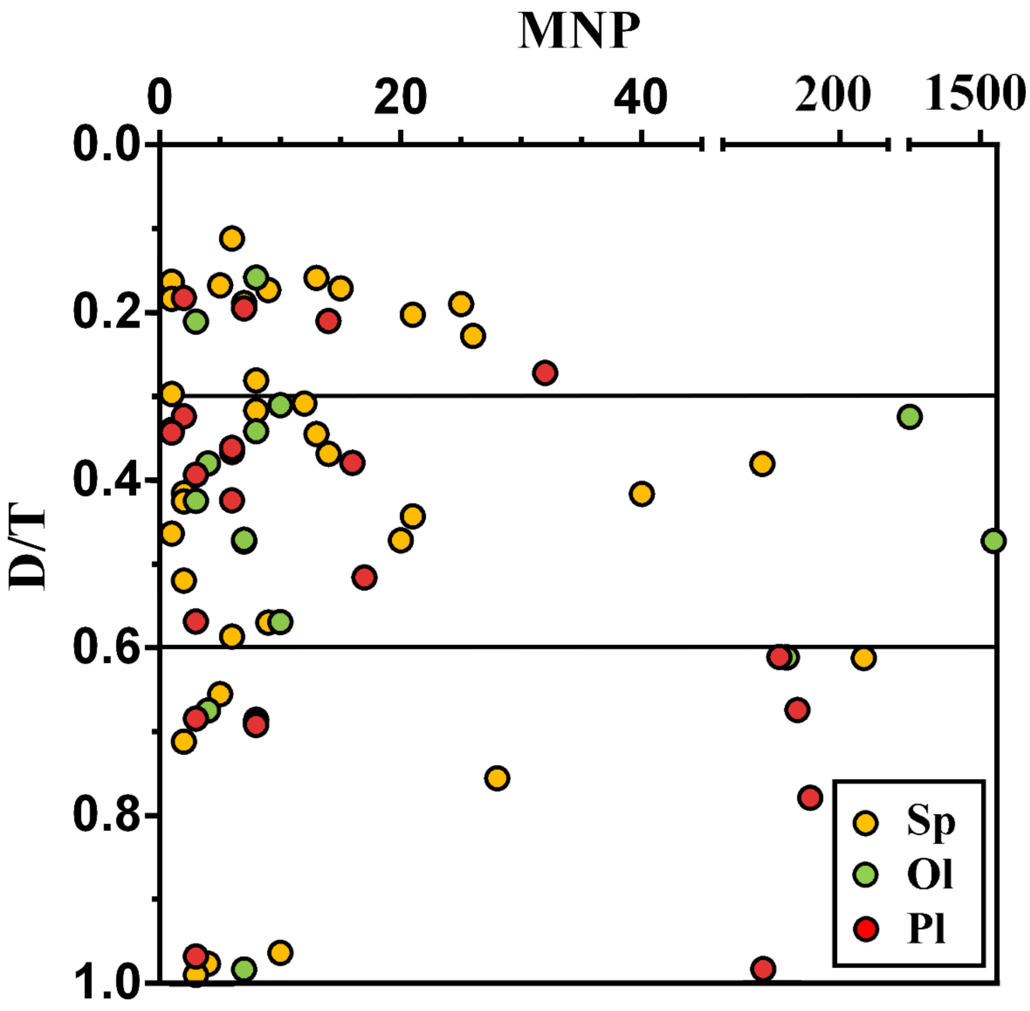

Figure 4-5.

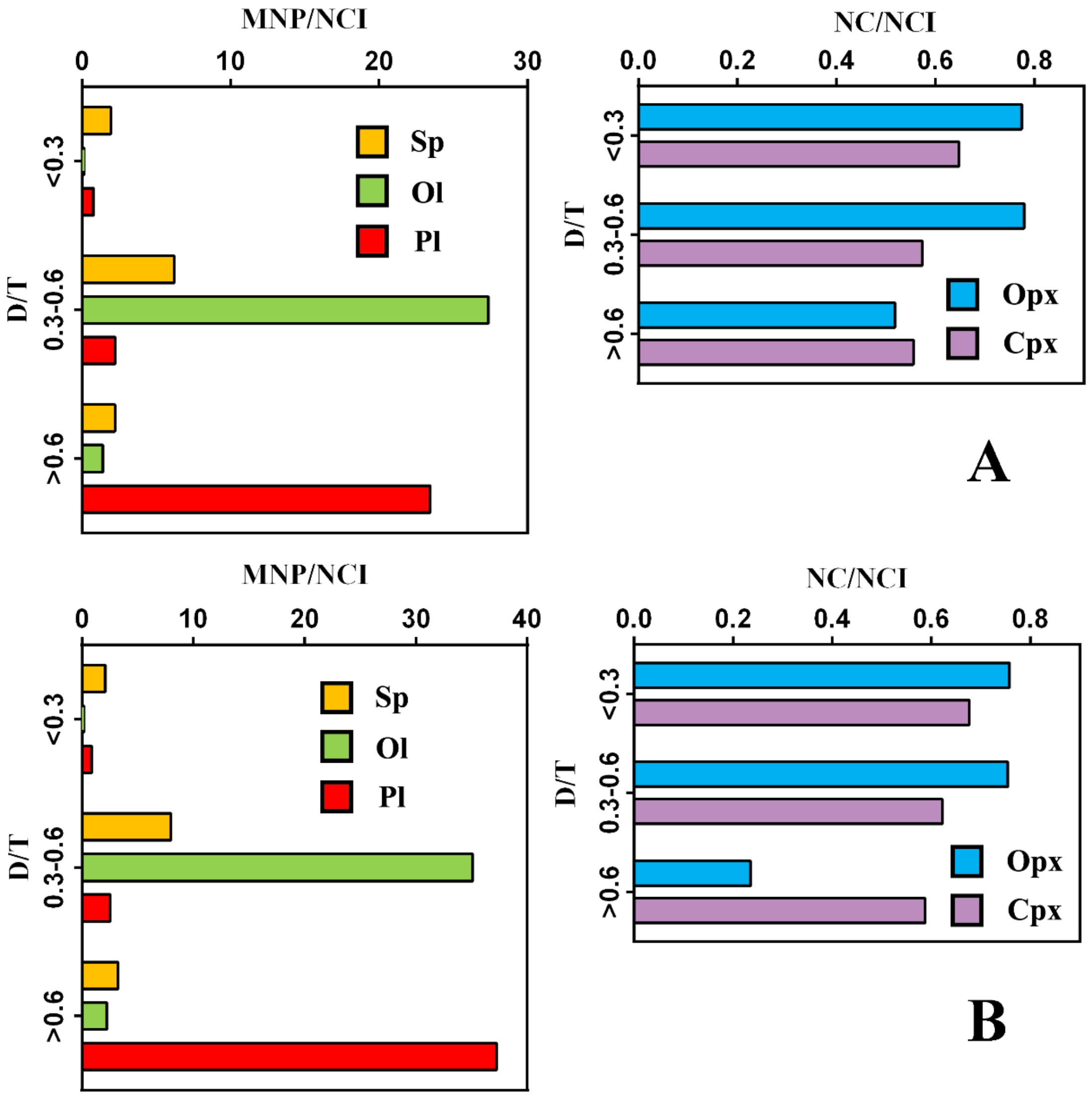
MNP/NCI
0
10
20
30
D/T
<0.3
0.3-0.6
>0.6
Sp
Ol
Pl
NC/NCI
0.0
0.2
0.4
0.6
0.8
Opx
Cpx
A
MNP/NCI
0
10
20
30
40
D/T
<0.3
0.3-0.6
>0.6
Sp
Ol
Pl
NC/NCI
0.0
0.2
0.4
0.6
0.8
Opx
Cpx
B

Figure 4-6.

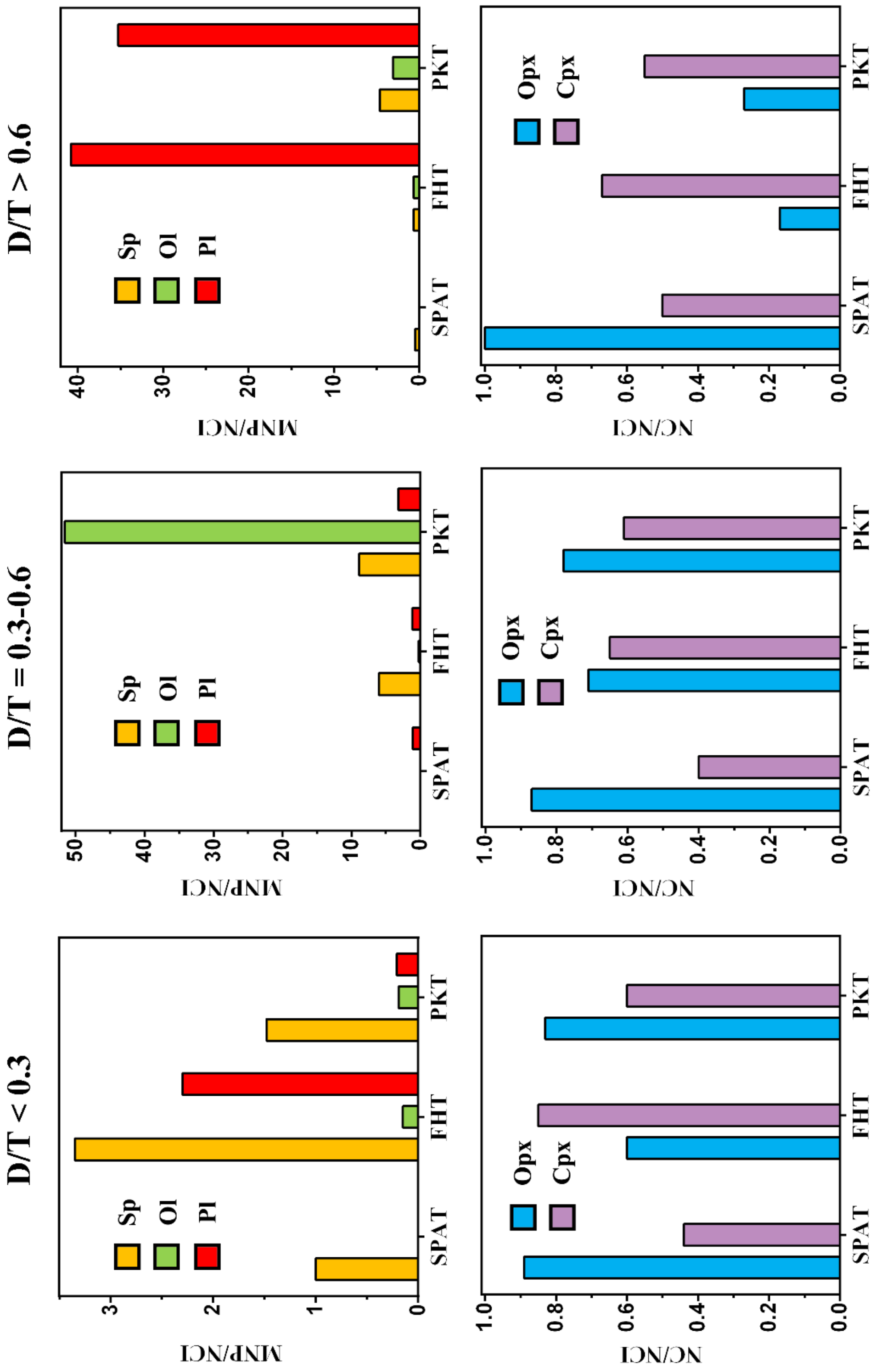
D/T < 0.3
D/T = 0.3-0.6
D/T > 0.6
MNP/NCI
NC/NCI
Sp
Ol
Pl
Opx
Cpx
SPAT
FHT
PKT
0
1
2
3
10
20
30
40
50
0.0
0.2
0.4
0.6
0.8
1.0

Figure 4-7.

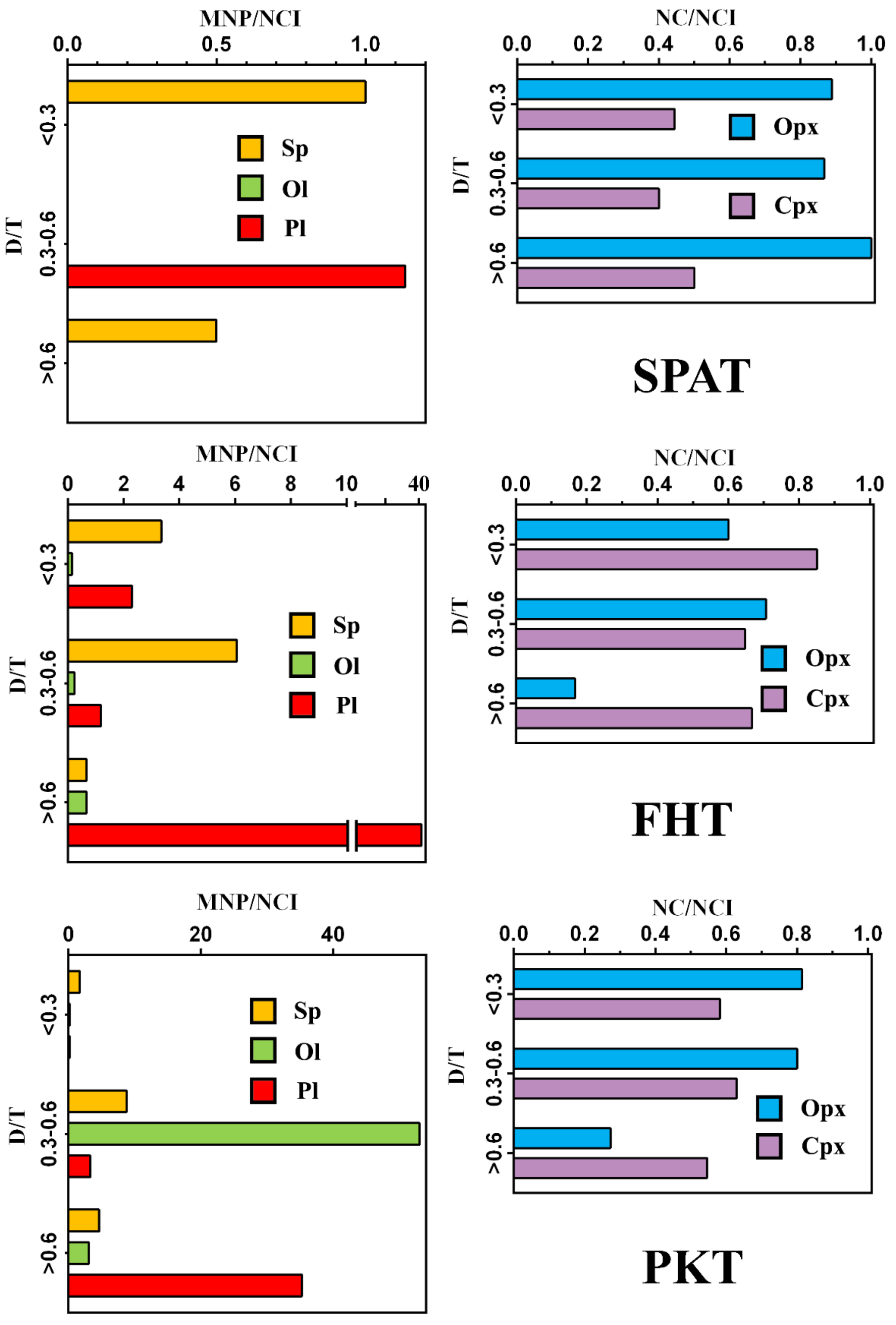
MNP/NCI
0.0
0.5
1.0
D/T
<0.3
0.3-0.6
>0.6
Sp
Ol
Pl
NC/NCI
0.0
0.2
0.4
0.6
0.8
1.0
D/T
<0.3
0.3-0.6
>0.6
Opx
Cpx
SPAT
MNP/NCI
0
2
4
6
8
10
40
D/T
<0.3
0.3-0.6
>0.6
Sp
Ol
Pl
NC/NCI
0.0
0.2
0.4
0.6
0.8
1.0
D/T
<0.3
0.3-0.6
>0.6
Opx
Cpx
FHT
MNP/NCI
0
20
40
D/T
<0.3
0.3-0.6
>0.6
Sp
Ol
Pl
NC/NCI
0.0
0.2
0.4
0.6
0.8
1.0
D/T
<0.3
0.3-0.6
>0.6
Opx
Cpx
PKT

Figure 4-8.

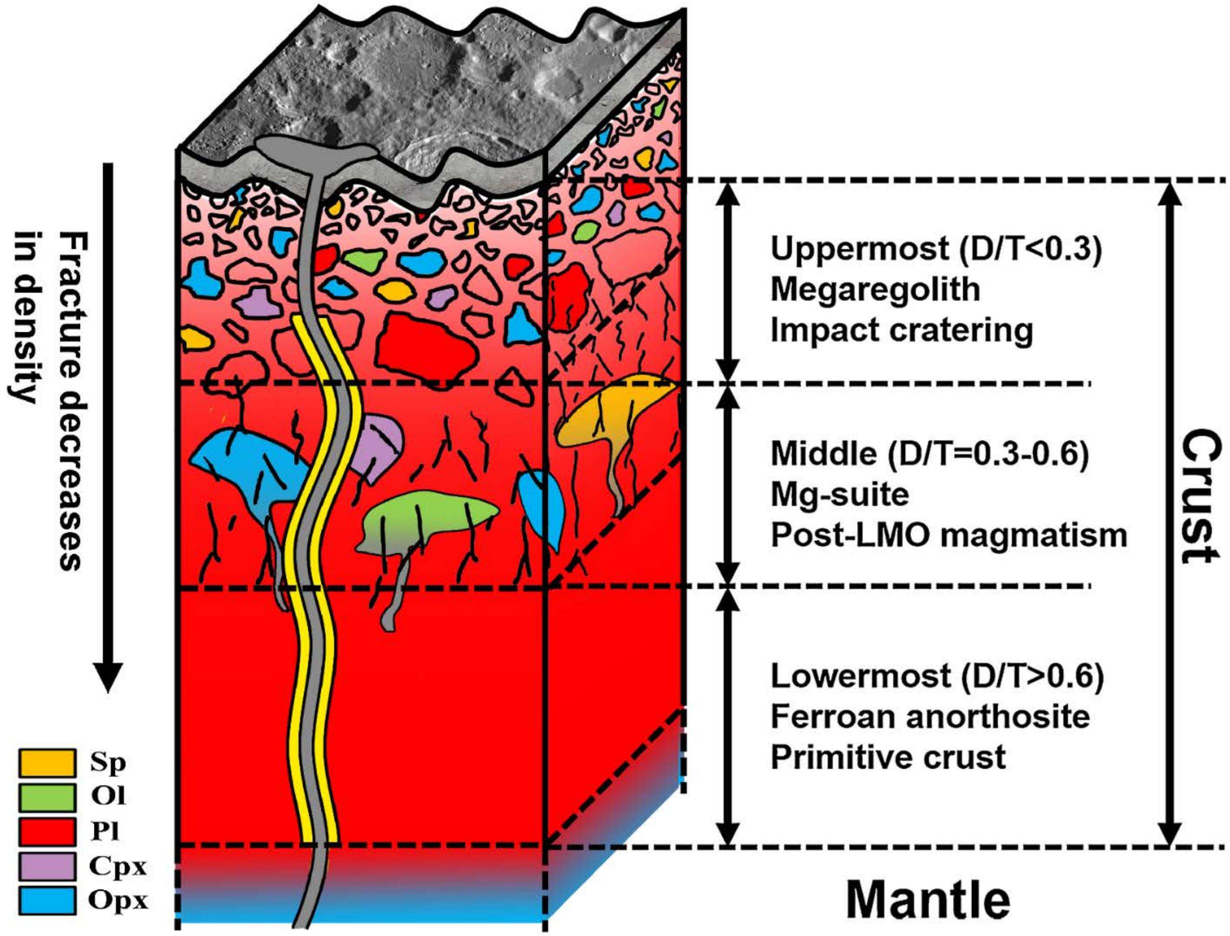
Crust
Uppermost (D/T<0.3)
Megaregolith
Impact cratering
Middle (D/T=0.3-0.6)
Mg-suite
Post-LMO magmatism
Lowermost (D/T>0.6)
Ferroan anorthosite
Primitive crust
Mantle
Fracture decreases in density
Sp
Ol
Pl
Cpx
Opx

Figure 4-9.

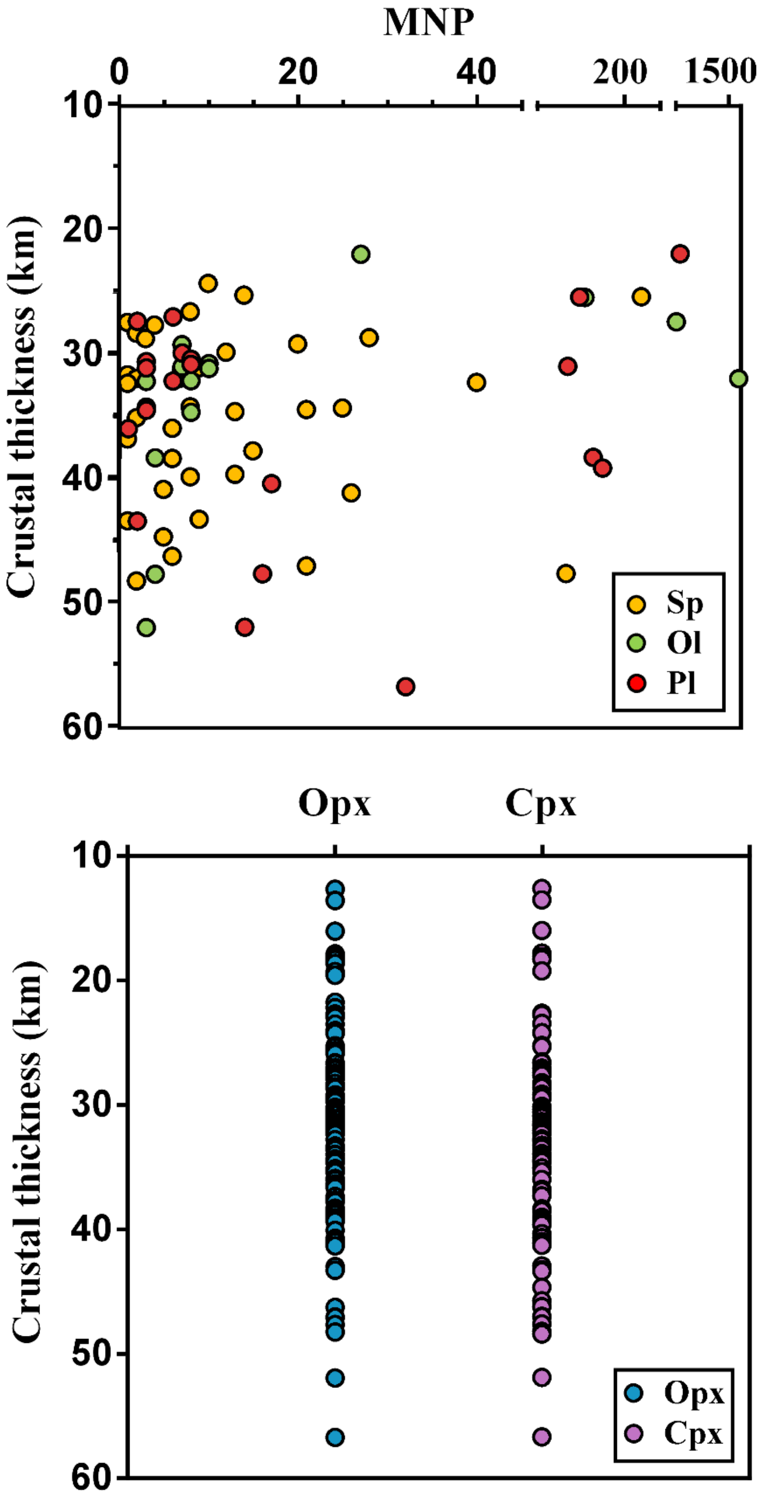
MNP
0
20
40
200
1500
Crustal thickness (km)
10
20
30
40
50
60
Sp
Ol
Pl
Opx
Cpx
Crustal thickness (km)
10
20
30
40
50
60
Opx
Cpx

Figure 4-10.

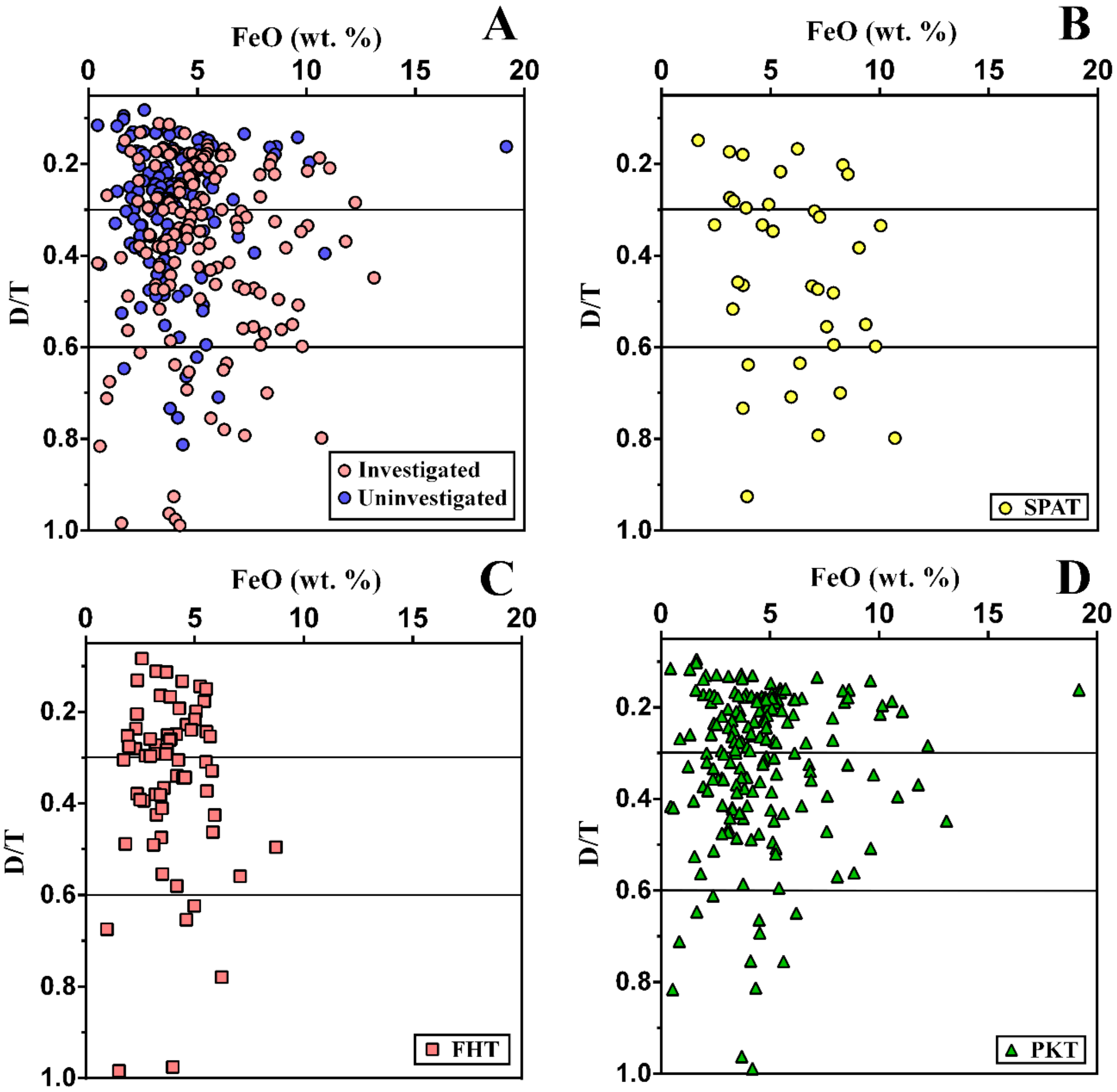
A
FeO (wt. %)
0
5
10
15
20
D/T
0.2
0.4
0.6
0.8
1.0
Investigated
Uninvestigated
B
SPAT
C
FHT
D
PKT

Figure 4-11.

References

Besse, S., et al., (2013). A visible and near-infrared photometric correction for Moon Mineralogy Mapper (M^3), *Icarus*, 222(1), 229-242.

Blanchette-Guertin, J. F., et al., (2011). Mission strategies for determining the vertical extent and structure of the lunar megaregolith. *In Lunar and Planetary Science Conference* (Vol. 42, p. 1405).

Bowen, N. L., (1922). The reaction principle in petrogenesis. *The Journal of Geology*, 177-198.

Boardman, J. W., et al., (2011). Measuring moonlight: An overview of the spatial properties, lunar coverage, selenolocation, and related Level 1B products of the Moon Mineralogy Mapper, *Journal of Geophysical Research: Planets* (1991–2012), 116(E6).

Bussey, D. B. J., and Spudis, P. D., (2000). Compositional studies of the Orientale, Humorum, Nectaris, and Crisium lunar basins. *Journal of Geophysical Research* 105:4235-4243

Cahill, J. T. S., et al., (2009). Compositional variations of the lunar crust: Results from radiative transfer modeling of central peak spectra, *Journal of Geophysical Research*, 114(E9), 1–17. doi:10.1029/2008JE003282.

Cintala, M. J., and Grieve, R. A. F., (1994). The effects of differential scaling of impact melt and crater dimensions on lunar and terrestrial craters: Some brief examples. *In Large Meteorite Impacts and Planetary Evolution*, pp. 51-59. GSA Spec. Paper 293, Geological Society of America, Boulder, Colorodo, USA.

Cintala, M. J., and Grieve, R. A. F., (1998). Scaling impact melting and crater dimensions: Implications for the lunar cratering record, *Meteorit. Planet. Sci.*, 33(4), 889–912. doi:10.1111/j.1945-5100.1998.tb01695.x.

Clark, R. N., et al., (2011). Thermal removal from near-infrared imaging spectroscopy data of the Moon, *Journal of Geophysical Research: Planets* (1991–2012), 116(E6).

Cloutis, E. A., et al., (1986). Calibrations of phase abundance, composition, and particle size distribution for olivine-orthopyroxene mixtures from reflectance spectra. *Journal of Geophysical Research: Solid Earth* (1978–2012), 91(B11), 11641-11653.

Crown, D. A., and Pieters, C. M., (1987). Spectral properties of plagioclase and pyroxene mixtures and the interpretation of lunar soil spectra. *Icarus*, 72(3), 492-506.

Coombs, C. R., et al., (1990). The Alphonsus region: A geologic and remote sensing persepective. *In Lunar and Planetary Science Conference* (Vol. 20, pp. 161-174)

Dhingra, D., et al., (2011). Non-linear spectral un-mixing using Hapke Modeling: Application to remotely acquired M^3 spectra of spinel bearing lithologies on the moon. *In Lunar and Planetary Science Conference* (Vol. 42, p. 2431).

Donaldson Hanna, K. L., et al., (2014). Global assessment of pure crystalline plagioclase across the Moon and implications for the evolution of the primary crust. *Journal of Geophysical Research: Planets*, 119(7), 1516-1545.

Elkins-Tanton, L. T., et al., (2011). The lunar magma ocean: Reconciling the solidification process with lunar petrology and geochronology, *Earth and Planetary Science Letters,* 304, 326–336, doi:10.1016/j. epsl.2011.02.004.

Garrick-Bethell, I., and Zuber, M. T., (2009). Elliptical structure of the lunar South Pole–Aitken basin, *Icarus,* 204, 399–408.

Green, R., et al., (2011). The Moon Mineralogy Mapper (M^3) imaging spectrometer for lunar science: Instrument description, calibration, on-orbit measurements, science data calibration and on-orbit validation, *Journal of Geophysical Research*, 116, E00G19.

Goins, N. R., et al., (1981). Structure of the lunar crust at highland site Apollo station 16. *Geophysical Research Letters,* 8, 29–32. (doi:10.1029/GL008i001p00029)

Hartmann, W. K., (1973). Ancient lunar megaregolith and subsurface structure: *Icarus*, v. 18, p. 634–639.

Hawke, B. R., et al., (1991). Remonte sensing studies of the Orientale region of the Moon: A pre-Galileo view. *Geophysical Research Letters*, 18:2141-2144

Hawke, B. R., et al., (1993). Remote sensing studies of the terrain northwest of the Humorum basin. *Geophysical Research Letters*, 20:419-422

Hawke, B. R., et al., (2003). Distribution and modes of occurrence of lunar anorthosite. *Journal of Geophysical Research*, 108:5050, doi:10.1029/2002JE001890

Head, J. W., (1976). The significance of substrate characteristics in determining morphology and morphometry of lunar craters. *In Lunar and Planetary Science Conference* (Vol. 7, pp. 2913-2929).

Heiken, G. H., et al., (1991). The Lunar Sourcebook: a user’s guide to the Moon. Cambridge Univ. Press

Hess, P. C., (1994). Petrogenesis of lunar troctolites. *Journal of Geophysical Research*, 99:19,083-19,093

Hess, P. C., and Parmentier, E. M., (1995). A model for the thermal and chemical evolution of the Moon’s interior: Implications for the onset of mare volcanism, *Earth and Planetary Science Letters*, 134, 501–514, doi:10.1016/0012- 821X(95)00138-3.

Hurwitz, D. M., and Kring, D. A., (2014). Differentiation of the South Pole–Aitken basin impact melt sheet: Implications for lunar exploration. *Journal of Geophysical Research: Planets*, 119(6), 1110-1133.

Jolliff, B. L., et al., (2000). Major lunar crustal terranes: Surface expressions and crust-mantle origins. *Journal of Geophysical Research: Planets* (1991–2012), 105(E2), 4197-4216.

Kaula, W. M., et al., (1974). Apollo laser altimetry and inferences as to lunar structure. *In Lunar and Planetary Science Conference* (Vol. 5, pp. 3049-3058).

Khan, A., et al., (2000). A new seismic velocity model for the Moon from a Monte Carlo inversion of the Apollo lunar seismic data. *Geophysical Research Letters,* 27(11), 1591-1594.

Khan, A., and Mosegaard, K., (2002). An inquiry into the lunar interior: A nonlinear inversion of the Apollo lunar seismic data. *Journal of Geophysical Research: Planets* (1991–2012), 107(E6), 3-1.

Khan, A., et al., (2006). Are the Earth and the Moon compositionally alike? Inferences on lunar composition and implications for lunar origin and evolution from geophysical modeling. *Journal of Geophysical Research: Planets* (1991–2012), 111(E5).

Laneuville, M., et al., (2013). Asymmetric thermal evolution of the Moon. *Journal of Geophysical Research: Planets*, 118(7), 1435-1452.

Lawrence, D. J., et al., (1998). Global elemental maps of the Moon: The Lunar Prospector gamma-ray spectrometer. *Science*, 281(5382), 1484-1489.

Lawrence, D. J., et al., (2000). Thorium abundances on the lunar surface. *Journal of Geophysical Research: Planets* (1991–2012), 105(E8), 20307-20331.

Le Mouélic, S., et al., (2002). Calculating iron contents of lunar highland materials surrounding Tycho crater from integrated Clementine UV-visible and near-infrared data. *Journal of Geophysical Research: Planets* (1991–2012), 107(E10), 4-1.

Lognonné, P., et al., (2003). A new seismic model of the Moon: implications for structure, thermal evolution and formation of the Moon. *Earth and Planetary Science Letters*, 211(1), 27-44.

Lucey, P. G., et al., (1998). FeO and TiO_2 concentrations in the South Pole-Aitken basin: Implications for mantle composition and basin formation. *Journal of Geophysical Research: Planets* (1991–2012), 103(E2), 3701-3708.

Lucey, P. G., (2004). Mineral maps of the Moon. *Geophysical Research Letters,* 31(8).

Lucey, P. G., et al., (2014) A large spectral survey of small lunar craters: Implications for the composition of the lunar mantle. *American Mineralogist*, 99(11-12), 2251-2257.

Matsunaga, T., et al., (2008). Discoveries on the lithology of lunar crater central peaks by SELENE Spectral Profiler. *Geophysical Research Letters*, 35(23).

McCallum, I. S., and Schwartz, J. M., (2001). Lunar Mg suite: thermobarometry and petrogenesis of parental magmas. *Journal of Geophysical Research: Planets* (1991–2012), 106(E11), 27969-27983.

Melosh, H. J., (1989). Impact Cratering: A Geologic Process, 245 pp., Oxford Univ. Press, New York.

Melosh, H. J., et al., (2014). The Moon's upper mantle: mostly OPX, not Olivine?. *In Lunar and Planetary Science Conference* (Vol. 45, p. 2505).

Moriarty, D. P., et al., (2013). Compositional heterogeneity of central peaks within the South Pole-Aitken Basin. *Journal of Geophysical Research: Planets*, 118(11), 2310-2322.

Nakamura, Y., (1983). Seismic velocity structure of the lunar mantle. *Journal of Geophysical Research: Solid Earth* (1978–2012), 88(B1), 677-686.

Nakamura, R., et al., (2009). Ultramafic impact melt sheet beneath the South Pole-Aitken basin on the Moon. *Geophysical Research Letters*, 36(22).

Nyquist, L. E., and Shih, C. Y., (1992). The isotopic record of lunar volcanism. *Geochimica et Cosmochimica Acta*, 56(6), 2213-2234.

Ogawa, Y., et al., (2011). The widespread occurrence of high-calcium pyroxene in bright-ray craters on the Moon and implications for lunar-crust composition. *Geophysical Research Letters*, 38(17).

Ohtake, M., et al., (2009). The global distribution of pure anorthosite on the Moon. *Nature*, 461(7261), 236-240.

Peterson, C. A., et al., (1995). Spacecraft remote sensing studies of lunar anorthosite deposits. *In Bulletin of the American Astronomical Society* (Vol. 27, p. 1109).

Petro, N. E., and Pieters, C. M., (2002). The size and location of the transient crater of the South Pole-Aitken Basin. *In Lunar and Planetary Science Conference* (Vol. 33, p. 1848).

Pieters, C. M., (1986). Composition of the lunar highland crust from near-infrared spectroscopy. *Reviews of Geophysics*, 24(3), 557-578.

Pieters, C. M., et al., (1997). Mineralogy of the Mafic Anomaly in the South Pole-Aitken Basin: Implications for excavation of the lunar mantle. *Geophysical Research Letters*, 24(15), 1903-1906.

Pieters, C. M., et al., (2001). Rock types of South Pole-Aitken basin and extent of basaltic volcanism. *Journal of Geophysical Research: Planets* (1991–2012), 106(E11), 28001-28022.

Pieters, C. M., et al., (2009). The Moon mineralogy mapper (M^3) on Chandrayaan-1. *Current Science*, 96(4), 500-505.

Pieters, C. M., et al., (2011). Mg-spinel lithology: A new rock type on the lunar farside. *Journal of Geophysical Research: Planets* (1991–2012), 116(E6).

Potter, R. W. K., et al., (2012). Constraining the size of the South Pole-Aitken basin impact, *Icarus*, 220, 730–743, doi:10.1016/j.icarus.2012.05.032.

Prissel, T. C., et al., (2014). Pink Moon: The petrogenesis of pink spinel anorthosites and implications concerning Mg-suite magmatism. *Earth and Planetary Science Letters*, 403, 144-156.

Roddy, D. J., (1977). Large-scale impact and explosion craters-Comparisons of morphological and structural analogs. *In Impact and explosion cratering: Planetary and terrestrial implications* (Vol. 1, pp. 185-246).

Ryder, G., and Wood, J. A., (1977). Serenitatis and Imbrium impact melts-Implications for large-scale layering in the lunar crust. *In Lunar and Planetary Science Conference* (Vol. 8, pp. 655-668).

Serventi, G., et al., (2013). Spectral variability of plagioclase–mafic mixtures (1): Effects of chemistry and modal abundance in reflectance spectra of rocks and mineral mixtures. *Icarus*, 226(1), 282-298.

Shearer, C. K., et al., (2006). Thermal and magmatic evolution of the Moon. *Reviews in Mineralogy and Geochemistry*, 60(1), 365-518.

Shearer, C. K., et al., (2015). Exploring the Moon's Surface for Remnants of the Lunar Mantle 1. Dunite Xenoliths in Mare Basalts. A Crustal or Mantle Origin?. *In Lunar and Planetary Science Conference* (Vol. 46, p. 1426).

Smith, J. V., et al., (1970). Petrologic history of the moon inferred from petrography, mineralogy and petrogenesis of Apollo 11 rocks. *Geochimica et Cosmochimica Acta* Supplement, 1, 897.

Smith, D. E., et al., (1997). Topography of the Moon from the Clementine LIDAR. *Journal of Geophysical Research: Planets* (1991–2012), 102(E1), 1591-1611.

Song, E., et al., (2013). Bulk mineralogy of lunar crater central peaks via thermal infrared spectra from the Diviner Lunar Radiometer: A study of the Moon's crustal composition at depth. *Journal of Geophysical Research: Planets*, 118(4), 689-707.

Spudis, P. D., et al., (1984). Composition of Orientale basin deposits and implications for the lunar basin-forming process. *Journal of Geophysical Research: Solid Earth* (1978-2012), 89(S01), C197-C210.

Spudis, P. D., and Davis, P. A., (1986). A chemical and petrological model of the lunar crust and implications for lunar crustal origin. *Journal of Geophysical Research: Solid Earth* (1978–2012), 91(B13), E84-E90.

Spudis, P. D., (1993). The Geology of Multiringed Basins, Cambridge Univ. Press, New York.

Spudis, P. D., et al., (1999). Structure and composition of the lunar crust. In *New Views of the Moon 2: Understanding the Moon through the Integration of Diverse Datasets* (Vol. 1, p. 61).

Sun, Y., et al., (2013). Detection of mg-spinel bearing central peaks using M^3 images. *In Lunar and Planetary Science Conference* (Vol. 44, p. 1393).

Sun, Y., and Li, L., (2014). Global investigation of olivine bearing crater central peaks with M^3 images. *In Lunar and Planetary Science Conference* (Vol. 45, p. 1653).

Sun, Y., and Li, L., (2015). Characterization of lunar crust mineralogy with M^3 data. In *Lunar and Planetary Science Conference* (Vol. 46, p. 2941).

Taylor, G. J., et al., (1991). Lunar rocks. *Lunar sourcebook*, 183-284.

Taylor, G. J., and Wieczorek, M. A., (2014). Lunar bulk chemical composition: a post-Gravity Recovery and Interior Laboratory reassessment. Philosophical Transactions of the Royal Society A: *Mathematical, Physical and Engineering Sciences*, 372(2024), 20130242.

Toksöz, M. N., et al., (1974). Structure of the Moon. *Reviews of Geophysics*, 12(4), 539-567.

Tompkins, S., and Pieters, C. M., (1999). Mineralogy of the lunar crust: Results from Clementine. *Meteoritics and Planetary Science*, 34(1), 25-41.

Wieczorek, M. A., and Phillips, R. J., (1997). The structure and compensation of the lunar highland crust. *Journal of Geophysical Research: Planets* (1991–2012), 102(E5), 10933-10943.

Wieczorek, M. A., and Zuber, M. T., (2001). The composition and origin of the lunar crust: Constraints from central peaks and crustal thickness modeling. *Geophysical Research Letters*, 28(21), 4023-4026.

Wieczorek, M. A., et al., (2006). The constitution and structure of the lunar interior. *Reviews in mineralogy and geochemistry*, 60(1), 221-364.

Wieczorek, M. A., et al., (2008). The Mantle of the Moon: Exposed and Sampled?. *In Lunar and Planetary Science Conference* (Vol. 39, p. 1271).

Wieczorek, M. A., et al., (2013). The crust of the Moon as seen by GRAIL. *Science*, 339(6120), 671-675.

Wood, J. A., et al., (1970). Lunar anorthosites and a geophysical model of the moon. *Geochimica et Cosmochimica Acta* Supplement, 1, 965.

Warren, P. H., and Wasson, J. T., (1977). Pristine nonmare rocks and the nature of the lunar crust. *In Lunar and Planetary Science Conference* (Vol. 8, pp. 2215-2235).

Warren, P. H., and Wasson, J. T., (1979). The origin of KREEP. *Reviews of Geophysics*, 17(1), 73-88.

Warren, P. H., (1985). The magma ocean concept and lunar evolution. *Annual Review of Earth and Planetary Sciences*, 13, 201-240.

Warren, P. H., and Rasmussen, K. L., (1987). Megaregolith insulation, internal temperatures, and bulk uranium content of the Moon. *Journal of Geophysical Research: Solid Earth* (1978–2012), 92(B5), 3453-3465.

Yamamoto, S., et al., (2012). Massive layer of pure anorthosite on the Moon. *Geophysical Research Letters*, 39(13).

CHAPTER 5

CONCLUSIONS AND FUTURE WORK

1. Conclusions

1) This study has demonstrated a new Mg-spinel bearing rock type extensively exists in the lunar crust. Mg-spinel has been found in 38 central peaks of 166 investigated craters and presents in all three terranes and in both shallow and deep layers. The likelihood for Mg-spinel seems to be relatively high in the middle layer of the lunar crust underneath the PKT. Mg-spinel is not required to co-occur with mafic minerals (olivine and pyroxene) because nine central peaks have been identified for the presence of only Mg-spinel and plagioclase. The extensive presence of Mg-spinel indicates Mg-spinel should represent a new critical member in the lunar crust.

2) Results in Chapter 2 reveal that that the petrogenesis of Mg-spinel is related to the Mg-suite magmatism (plutonism and assimilation) rather than impact projectile remnants or shallow impact melts. The assimilation of Mg-suite magma with the anorthositic crust is most possibly responsible for the origin of Mg-spinel in the FHT. The Mg-suite plutonism most likely represents the source of Mg-spinel in PKT. The observed extents of Mg-spinel in the lunar crust and the Mg-suite associated petrogenesis suggest that Mg-spinel lithology represents a new member of Mg-suite rocks.

3) The global distribution of olivine-bearing central peaks has been determined in Chapter 3. Only about 5% of the investigated central peaks show the presence of olivine (14 olivine-bearing central peaks). All three olivine abundant central peaks (Copernicus, Eratosthenes, and Theophilus) are located within the middle layer of the lunar crust beneath the PKT. Seven olivine - bearing central peaks appear to be associated with impact basins. Olivine was not found in SPAT the central peaks. The coexistence of crystalline plagioclase and pyroxene has been detected in the most of olivine - bearing central peaks.

4) Olivine identified in the central peaks should represent the product of post-LMO magmatic evolution rather than an exogenic origin or mechanical excavation from the mantle. We propose a hybrid magmatic origin scenario including post-LMO plutonism and magmatic transport. The post-LMO plutonism is responsible for the origin of olivine in the olivine-rich central peaks. The small scale plutonism or magmatic transport is related to a small amount of olivine in other central peaks.

5) The observations described in Chapter 4 provide direct and indirect evidence demonstrating that the lunar crust is extremely anorthositic and relatively homogeneous. The results presented in this chapter indicate the lunar crust represents floatation cumulates which were generated by LMO initial differentiation and provided the critical evidence to support the existence of LMO. However, the compositional diversity in the lunar crust is primarily produced by post-LMO activities including continuous impact cratering and post-LMO magmatism.

6) Combining the results in Chapter 2 and Chapter 4 with respect to SPA, we suggest that SPAT might not be a crustal terrane and should represent the upper mantle rather than the lower crust. The major composition within the SPA is orthopyroxene instead of olivine, implying an enrichment of the upper lunar mantle in orthopyroxene rather than olivine.

7) In Chapter 4, a new three-layer compositional model for the lunar crust has been proposed. The uppermost layer is anorthositic or noritic megaregolith generated by heavily impact cratering; the middle layer contains Mg-suite equivalent materials and has been heavily modified by post-LMO magmatism which is concentrated in PKT; the lowermost layer possess a pure ferroan anorthositic layer which represents the primitive crustal composition generated by LMO.

2. Future directions

It is noteworthy that the conclusions from this study is primarily based on the analysis of M^3 images. To validate these conclusions, other currently available datasets (e.g. Chang’e, SELENE, Lunar Reconnaissance Orbiter, and Diviner) need to be analyzed in future. Additionally, in order to validate the new three-layer crustal model, additional geochemical parameters (e.g. An, Mg') and other regions which could represent exposure of the lunar crust and mantle (e.g. basin inner ring, crater wall and ejecta) should be included in future analysis.

2.1. Mg number

Mg number (Mg') is the ratio of Mg to the sum of Mg and Fe. It can be used to determine the degree of differentiation of the magma ocean at the time of its solidification, and is an important discriminator to distinguish Mg-suite rocks from other igneous rocks because while the concentration of MgO in Mg-suite rocks is in a wide range, the Mg' of Mg-suite rocks is usually relatively higher than other lithologies.

For the perspective of remote sensing, Mg' is a key factor controlling the spectral properties of lunar mafic silicates [Lucey et al., 1998; Lucey et al., 2004] such as orthopyroxene and olivine, and can be derived from Hapke’s radiative transfer model as presented in Lucey et al. [1998]. The derived Mg' could help us to further improve our understanding regarding the petrogenesis of common lunar minerals and the evolution of the lunar crust. For example, the high value of Mg' can be used to exclude the exogenic origin of olivine in the central peaks, because the olivine with exogenic origin usually contain high siderophile elements (e.g. FeO) which may lower the value of Mg'. Relatively low Mg' can be used to distinguish post-LMO lithologies from the LMO cumulates because the primitive cumulates from LMO are commonly Mg-rich compared with post-LMO compositions. Additionally, a Mg' map could benefit the characterization of the lunar crustal composition. Even though the Mg' for the major lunar lithology groups can be determined on the basis of lunar sample analysis, the value of Mg' of the lunar sample unrepresentativity. The Mg' derived from global remote sensing data could provide a critical evidence for the range of Mg'. Certainly, the petrology experimental constraints are necessary to be required.

2.2. Impact basins

Craters larger than 200 km in diameter are known as impact basins. Lunar impact basins excavated vast amounts of materials and redistributed them across the lunar surface. The impact basins could also excavate the lunar interior and serve as a window to explore the deep composition of the Moon. In general, the innermost ring may represent the deepest materials excavated by impact basins and the outer ring may represent the shallow crustal materials relative to the inner ring.

In this study, only the central peaks of impact craters less than 200 km in diameter were examined, and the corresponding depth of investigated central peaks is from ~5 km to ~30 km. Although this depth range is enough to cover the entire lunar crust in the vertical direction on the basis of the crustal thickness map derived from GRAIL, it is a little doubtful whether the lunar crust is such thin. Two investigated large craters Humboldt and Petavius in this study have been identified to have a large amount of crystalline plagioclase which is consistent with the composition of the lowermost crust based on the new three-layer model. However, the D/T value is ~1.5 for Humboldt central peak and 1.2 for Petavius central peak, which means these two craters have definitely excavated the mantle materials based on the current crustal thickness estimate. It is impossible that the lunar mantle has a large amount of crystalline plagioclase, and the presence of crystalline plagioclase implies that the crustal thickness based on GRAIL is possibly too thin in Humboldt and Petavius regions. Hence, investigation of the lunar interior deeper than 30 km is helpful to refine the crustal thickness as well as the boundary of the lunar crust and the upper mantle. The depth range of the lowermost layer in new three-layer model is probably modified through analysis of the composition of impact basin rings.

References

Lucey, P. G., Blewett, D. T., & Hawke, B. (1998). Mapping the FeO and TiO_2 content of the lunar surface with multispectral imagery. *Journal of Geophysical Research: Planets* (1991–2012), 103(E2), 3679-3699.

Lucey, P. G., Gillis, J. J., & Steutel, D. (2004, March). Global images of Mg-number derived from Clementine data. *In Lunar and Planetary Science Conference* (Vol. 35, p. 1717).

CURRICULUM VITAE

Ying Sun

Education

- **Ph. D.** Applied Earth Sciences, IUPUI, U.S.A., Aug. 2015.
- **B. Sc.** Geology, Jilin University, China, Jul. 2008.

Research and Professional Experience

- **2010-2015 Research Assistant** in the department of Earth Sciences, IUPUI, U.S.A.
- **2008-2009 Voluntary Teacher**, Duhuang High School. China
- **2006-2008 Research Assistant** in the department of Earth Sciences, Jilin University, China.
- **2006-2007 Teaching Assistant** in the department of Earth Sciences, Jilin University, China.

Conferences

- 44th Lunar and Planetary Science Conference, March 18-22, **2013**, Woodlands, TX. **Oral presentation.**

- 45th Lunar and Planetary Science Conference, March 18-22, **2014**, Woodlands, TX. **Oral presentation**.
- IUPUI Imaging Research Symposium, October 3, **2014**, Indianapolis, IN. **Poster presentation**.
- 46th Lunar and Planetary Science Conference, March 16-20, **2015**, Woodlands, TX. **Oral presentation**.

Publications

- **Sun, Y.**, Li, L. and Zhang, Y., (**2015**). Detection of Mg-spinel bearing central peaks using M^3 images: Implications for the petrogenesis of Mg-spinel. ***Journal of Geophysical Research: Planets***, (to be submitted).
- **Sun, Y.**, and Li, L., (**2015**). Distribution and Origin of Olivine on the Moon: New Insights from M^3 images of Crater Central Peaks. ***Earth and Planetary Science Letters***, (to be submitted).
- **Sun, Y.**, Li, L., and Liu, D., (**2015**). Characterization of Lunar Crust Mineralogy with Moon Mineralogy Mapper Images: A New Crustal Compositional Model. ***Journal of Geophysical Research: Planets***, (to be submitted).
- Liu, D., Li, L., **Sun, Y.**, (**2015**). An improved radiative transfer model for estimating mineral abundance of immature and mature lunar soils. ***Icarus***, 253, 40-50, DOI:10.1016/j.icarus.2015.02.013.
- Song, K., Li, L., Tedesco, L., Clercin, N., Hall, B., Li, S., ... and **Sun, Y.**, (**2013**). Remote estimation of phycocyanin (PC) for inland waters coupled with YSI PC

fluorescence probe. ***Environmental Science and Pollution Research***, 20(8), 5330-5340.

- **Sun, Y.**, Liu., Y., et al., (**2008**). Structural feature and uplift age of the southern part of Daheishan horst in Jinlin, China, ***Global Geology***, Vol.27 No.1.
- **Sun, Y.**, Zheng, C., (**2007**). Re-discussing moonstone characters. ***Jinlin Geology***, Vol.26 No.4.

Abstracts

- **Sun, Y.**, Li, L., and Zhang, Y., (**2013**). Detection of Mg-Spinel Bearing Central Peaks Using M^3 Images. In ***Lunar and Planetary Science Conference*** (Vol. 44, p. 1393).
- **Sun, Y.**, and Li, L. (**2014**). Global Investigation of Olivine Bearing Crater Central Peaks with M^3 Images. In ***Lunar and Planetary Science Conference*** (Vol. 45, p. 1653).
- **Sun, Y.**, and Li, L. (**2015**). Characterization of Lunar Crust Mineralogy with M^3 Data. In ***Lunar and Planetary Science Conference*** (Vol. 46, p. 2941).